Development and Evaluation of Multifunctional Colloidal Composite Nanoparticles for Potential Combined Cancer Cell Diagnosis and Therapy

Submitted by

Pablo Martinez Pancorbo

to the University of Exeter as a thesis for the degree of

Doctor of Philosophy in Physics and Engineering

September 2020

I certify that all material in this thesis which is not my own work has been identified and that no material has previously been submitted and approved for the award of a degree by this or any other university has been acknowledged.

(Signature) ……

Pablo Martinez Pancorbo

Abstract

Nanomedicine includes detection, diagnosis and treatment of diseases at the cellular level and can be a valuable tool for highly specific medical interventions by utilising nanoscale objects. Cancer nanomedicine is one of the most successful research fields for exploring cancer at the cellular level. To find a suitable candidate for cancer theranostics (therapy and diagnosis) at an early stage and post-treatment (remission), the cytotoxicity, imaging, and therapeutic capabilities of various classes of nanoparticles were investigated.

Firstly, various nanoparticles were first obtained from WO_x and iron oxides being processed under hydrogen (H_2) + argon (Ar) gas heat treatment and membrane filtration. A colouration process from yellow to blue colour was obtained for WO_3 nanoparticles (NPs) and an oxygen reduction process that led us to obtain metallic Fe NPs from γ-Fe_2O_3 NPs. Additionally, membrane filtration methods using ultrathin nanoporous membranes in microfluidic platforms were performed on γ-Fe_2O_3 polydisperse NPs. This novel application showed a consistent reduction in size distribution from these magnetic polydisperse NPs after filtration at 37 nm and 60 nm membrane pore sizes. Tangential and normal flow filtration (TFF and NFF, respectively) were used with ethanol and water solvents which showed the need to work at low concentrations for dense nanoparticles. TFF presented a higher degree of filtration at the cost of complexity, time and price.

Secondly, these NPs were then investigated for their incorporation as the core in core-shell structures. Novel core-shell NP structures were designed with an intermediate tunable SiO_2 layer (3-60 nm) using the Stober process and also a tunable Au outer shell (15-30 nm approximately) formed from 3.5 nm Au seeds obtained from

the Turkevich method. WO_3-SiO_2-Au NPs were synthesised which are a new class of NP that contains a first in it class WO_3 core with potential electrochromic functionalities. Coherent anti-Stokes Raman spectroscopy (CARS) and near-infrared (NIR) surface-enhanced Raman spectroscopy (SERS) were performed as a proof of concept for potential medical imaging to locate the nanoparticles achieving single-cell resolution. SERS enhancement factor (EF) using 785 nm was approximately 10^3 for a 30 nm thick Au shell in a silicon wafer. Additional Raman signals were measured in liquid samples to evaluate obtaining a SERS EF of 771 with WO_x core and 33 using γ-Fe_2O_3 core. It presented low toxicity at concentrations under 100 µg/mL after 24 h using human isolated at M D Anderson from a pleural effusion of a patient with invasive ductal breast carcinoma breast cancer cells (MDA-MB 231) in vitro.

Finally, monodisperse γ-Fe_2O_3-SiO_2-Au nanoparticles displayed a promising negative contrast for MRI in both T1 and T2 modes along with strong contrast under microcomputed tomography (µCT). Monodisperse γ-Fe_2O_3 cores, which have an average diameter of 11 nm following a gaussian distribution with a standard deviation of 3 nm, in γ-Fe_2O_3-SiO_2-Au structures outperformed in all these imaging tests to polydisperse γ-Fe_2O_3 cores, which have a mode value at 31 nm following a Lorentzian distribution with a scale parameter of 29 ± 7 nm. Magnetic hyperthermia was achieved using γ-Fe_2O_3 cores confirmed the potential therapy functionality in water using AMFs at 515 kHz and 170 Oe, obtaining an increment of 7 °C in 23 min, which adds in total 4 functionalities with potential application for cancer nanotheranostics. Moreover, cell viability assays using monodisperse γ-Fe_2O_3-SiO_2-Au nanoparticles showed almost negligible cytotoxicity in different nanoparticle concentrations (0-2000 µg/mL) and cell types (pericytes, embryonic kidney HEK293A and MCF10A human cells) in vitro.

Abstract

In conclusion, the thesis was able to demonstrate that WO_3-SiO_2-Au NP and γ-Fe_2O_3-SiO_2-Au NP have the potential for further development as a tool in nanomedicine, although systemic toxicology and excretion pathways will have to be carefully studied next.

Acknowledgements

First, I want to thank my wife, Yuliana Lobay, who has supported me during my doctoral journey and has been my rock-solid pillar in the most critical times of my life, particularly during my cancer treatment in 2018-2019. I would not have accomplished all that I did without your unconditional help.

I want to deeply thank my supervisors, Prof. Yanqiu Zhu and Prof. Nick Stone, for their guidance, friendliness and support during my entire Ph.D. degree. I cannot express fully with words the appreciation and respect I have for them. They believed in me and supported my choices to address complex situations and problems that arose at critical times. They showed me unquestionable support and flexibility in challenging times such as during the period I was diagnosed with cancer and had to undergo chemotherapy and during the COVID-19 world pandemic that stopped me from performing important experiments during my last year. Yanqiu, you always encouraged me to achieve better results and improve to be the best version of myself in every situation in the nicest and closest way possible. I have learned invaluable lessons working in your research group about materials science, laboratory safety and working in a highly multicultural environment. Nick, you have helped me to pursue challenging and ambitious goals while showing your friendly and honest nature. You have given me invaluable advice and guidance while I needed the most. Working in your group has allowed me to collaborate with many fantastic researchers that have been critical assets to achieve my research goals. Both Nick and Yanqiu, you have been not just my supervisors during my Ph.D., but also my mentors in multiple aspects related to the academic world. I feel I am prepared to deal with any challenge I face thanks to your invaluable lessons and advice. I truly believe I became a better and

wiser researcher and person because of you. I am also truly grateful for your support in achieving future milestones in my research journey.

I would also like to thank all my collaborators who made great contributions in my research allowing to achieve some of the most important results I obtained during my PhD. I am grateful for the support that multiple people have lend me from the Biophysics Labs, Functional Materials Lab and the EPSRC Centre for Doctoral Training in Metamaterials (CDT XM^2) at the University of Exeter.

Dr Kunyapat Thummavichai, you have been one of the most valuable colleagues and collaborators who helped me to get started with my research when I was lost. I am also grateful for all the great times we had in the lab and the office. Dr Louise Clark, your advice in Raman spectroscopy and SERS with gold nanoparticles made possible my first publication. I am thankful for your help with my initial Raman measurements and analysis when everybody else did not.

Thank you to Dr. Conor McKeever for the invaluable discussions in terms of magnetic nanoparticles behaviour and research ethics. You have been not just an excellent colleague, but also a great friend. Dr. Abdelmalek Benattayallah, your help in measuring magnetic resonance signals from my nanoparticles and its analysis has been an incredible contribution to my research. I am grateful for having the chance to meet you and for your outstanding support and guidance.

Dr. Hong Chang, you have been one of the key people to contact and work with during my doctoral studies. Without your knowledge and practical help in the Imaging Suite, I would not have obtained many of my best results. Dr. Ellen Green, you have been both moral support and an outstanding colleague. Thank you very much for the training and advice in the Biophysics Labs during my Ph.D.

Acknowledgements

Dr. Julia Sero, you have joined forces with me to investigate effects in cells from my nanoparticles in a key moment during my PhD. I truly thank you for the help and invaluable conversations we had about experimental details for cell-nanoparticles interactions at the University of Bath.

Marziyeh Belal, you have been both a good colleague and friend. Thank you for the great times we spent working together and for collaborating in my research project.

Dr. Kishan Menghrajani, thank you for being both a friend and a colleague. Your help and support are truly above and beyond. I cannot express you with words how much I appreciate your support during my time in the Harrison office.

Dr. Ben Gardner, your help with Raman maps and Raman signals in liquid samples has been incredibly important for me to publish. I have learnt a lot from your work ethics and rigour.

Thank you to all the organisers and participants of the PhD Summer School in Micro and Nano Sensors at DTU Nanotech in the Technical University of Denmark. I have learnt incredible lessons about research and commercialisation of micro and nano agents from biomedical applications that have helped me to shape this thesis.

Professor Jinquan Wei, thank you for welcoming to your lab in the School of Materials Science and Engineering at Tsinghua University. The short time I spent working with you was delightful. Yayu Huang, thank you for your help and guidance during my research visit at Tsinghua University. I would have been lost in Beijing without your help.

Acknowledgements

Prof. Kevin Webb, I want to thank you for your invaluable financial support that allowed me to go to the University of Rochester and perform the experiments in nanoparticles filtration presented in this thesis. I am also thankful for helping me to find the right people in Rochester to maximise the benefit from working there. Prof. James McGrath, thank you for making me feel welcome during my time in your lab at the University of Rochester and for your experience sharing during our meetings. My short time in your lab was meaningful and enjoyable. Kilean Lucas, thank you for your support, guidance and after work help during my research visit in Rochester. You made my time there valuable and enjoyable. You and your wife are amazing people and I wish we meet again.

Finally, I acknowledge financial support from the Engineering and Physical Sciences Research Council (EPSRC) of the United Kingdom, via the EPSRC Centre for Doctoral Training in Metamaterials (Grant No. EP/L015331/1).

Preface

This PhD thesis and its related work have been a complete odyssey from the beginning to the end. I immersed myself in a different culture and an area of research I was not experienced in; I got married, and I visited several countries worldwide. Unfortunately, I had to deal with undergoing chemotherapy, I got stuck in another country during a research visit due to extreme weather, and I was stopped from finishing many experiments by the COVID-19 pandemic that has wholly transformed today's society globally. However, I also got to live fulfilling research experiences such as synthesising novel nanoscale objects with promising biomedical features; winning several awards and grants related to these findings; and publishing my first related peer-reviewed paper in a prestigious scientific journal.

This thesis contains the work I performed in collaboration with many colleagues from different research groups and institutions since September 2016 until the COVID-19 pandemic affected the UK in March 2020. The work comprises primarily experimental studies, and it is focused on the development of multifunctional core-shell composite nanoparticles that can provide multiple diagnostic and therapeutic tools for early-stage cancer diagnosis and treatment.

Table of Contents

List of Figures

List of Figures

Definitions

4-MBA	4-mercaptobenzoic acid
Ag	Silver
AgNP	Silver nanoparticle
Au	Gold
$AuCl_4^-$	Chloroaurate
AFM	Atomic force microscopy
AMF	Alternating magnetic field
APTES	3-aminopropyltriethoxysilane
Ar	Argon
AuNP	Gold nanoparticle
AuNS	Gold nanoshell
B	Magnetic field
B cell	“Bursa of Fabricius” lymphocyte or B lymphocyte
CARS	Coherent Anti-Stokes Raman spectroscopy
CCD	Charge-coupled device
CH_2O(H-CHO)	Formaldehyde
CSF	Cerebrospinal fluid
CT	Computed tomography
d	Hydrodynamic diameter
D	Translational diffusion coefficient
DC	Direct current
DI water	Deionised water
DLS	Dynamic light scattering
DMEM	Dulbecco’s modified Eagle’s medium
DNA	Deoxyribonucleic acid
DOXIL™	Doxorubicin liposomal
EDS or EDX	Energy-dispersive X-ray microanalysis
EF	Enhancement factor
EPR	Enhanced permeability and retention
EtOH	Ethanol
fab	Antigen-binding fragment
FBS	Fetal bovine serum

FC	Field-cooled
FDA	United States Food and Drug Administration
FeO	Wüstite
Fe_3O_4	Magnetite
Gd-DTPA	Gadolinium diethylenetriaminepentaacetate
g-force	Gravity force
H	Hydrogen
H_2	Molecular hydrogen
$HAuCl_4$	Chloroauric acid
HRMRI	High-resolution magnetic resonance imaging
HRTEM	High-resolution transmission electron microscopy
IEC	International Electrotechnical Commission
IONP	Iron oxide nanoparticle
IR	Infrared
ITS	Insulin-Transferrin-Selenium
k	Boltzmann’s constant
K	Kelvin; potassium
K_2CO_3	Potassium carbonate
LSPR	Localised surface plasmon resonance
LUT	Lookup table
M	Magnetization
M_z	Longitudinal magnetization
Magnevist	Gadolinium diethylenetriaminepentaacetate
MSKCC	Memorial Sloan Kettering Cancer Center
MicroCT	Microcomputed tomography
MRI	Magnetic resonance imaging
MSN	Mesoporous silica nanoparticle
N	Nitrogen
NaOH	Sodium hydroxide
NH_3	Ammonia
NIR	Near-infrared
NF	Nanofiltration
NFF	Normal flow filtration

Definitions

NP	Nanoparticles
NPN	Nanoporous silicon nitride
NRS	Normal Raman spectroscopy
ns	No statistical significance
NS	Nanoshell
NTA	Nanoparticle tracking analysis
PC1	First principal component
PCA	Principal component analysis
$P(CH_2OH)_3$	Tris(hydroxymethyl)phosphine
PDMS	Polydimethylsiloxane
PEG	Polyethylene glycol
PET	Positron emission tomography
PM	Pericyte medium
pnc-Si	Porous nanocrystalline silicon
R	Organic substituent
RF	Radiofrequency
RNA	Ribonucleic acid
R-OH	Hydroxy or hydroxyl group
RRS	Resonance Raman spectroscopy
R-SH	Thiol group
SAM	Self-assembled monolayer
SAR	Specific absorption rate
SD	Standard deviation
SEM	Scanning electron microscopy
SepCon™	Separation container
SERS	Surface-enhanced Raman spectroscopy
SERRS	Surface-enhanced resonance Raman spectroscopy
SESORS	Surface-enhanced spatially offset Raman spectroscopy
SH	Carbon-bonded sulfhydryl
Si	Silicon
SiN	Silicon nitride
SiO_2	Silica
Si-O-Si	Siloxane bridge

sLL	Stochastic Landau-Lifshitz
STEM	Scanning transmission electron microscopy
STM	Scanning tunnelling microscopy
SNR	Signal-to-noise ratio
SORS	Spatially offset Raman spectroscopy
SPION	Superparamagnetic iron oxide nanoparticles
SP	Surface plasmon
SPR	Surface plasmon resonance
SQUID	Superconducting quantum interference device
t	Time
T	Temperature
T cell	Thymus-originated lymphocyte or T lymphocyte
T1	Proton spin-lattice or longitudinal relaxation time
T2	Proton spin-spin or transverse relaxation time
TE	Time to echo
TEM	Transmission electron microscopy
TEOS	Tetraethyl orthosilicate
THPC	Tetrakis(hydroxymethyl)phosphonium chloride
TI	Inversion time
TFF	Tangential flow filtration
TMP	Transmembrane pressure
TR	Repetition time
UF	Ultrafiltration
UV-Vis	Ultraviolet-visible
UV-vis-NIR	Ultraviolet-visible-near-infrared
VSM	Vibrating sample magnetometer
WO_2	Tungsten dioxide
WO_3	Tungsten trioxide
WO_x	Tungsten oxide
XRD	X-rays powder diffraction
ZFC	Zero-field-cooled
α-Fe_2O_3	Hematite
γ-Fe_2O_3	Maghemite

Definitions

ξ	Larmor frequency
λ	Wavelength
µCT	Microcomputed tomography
µTAS	Micro total analysis system
Ω	Difference of energy from ground state to a vibrational state
ω	Wavenumber

1. Introduction

Cancer is a disease of the genome in cells which typically leads to a reiterative process of clonal and subclonal expansion, genetic diversification, clonal selection, angiogenesis and tissue invasion[1–3]. When the tumour cells metastasise and migrate from a primary site to a distant organ, the survival rate of the patient with cancer is much lower. Hence, early diagnosis and treatment is a crucial element to minimise the impact of the malignancy. Current clinical in vivo diagnostic tools such as magnetic resonance imaging (MRI), X-ray computed tomography (CT), and positron emission tomography (PET) do not achieve a single-cell resolution. This issue prevents them from succeeding in early in-situ detections of tumours and validation after treatment for cancer patients in remission. They can only detect tumour tissues with a high number of tumour cells. Also, the effectiveness of most of these techniques is limited to certain types of cancer.

Raman spectroscopy is a powerful analytical technique that can measure the biochemical changes at a molecular level of complex biological samples, such as biofluids, cells and tissues [4]. Recent advances in the field of point-of-care medicine include in vivo Raman fiber-optic needle probes that measure the molecular fingerprints of the region where the needle tip is located to determine the presence of any type of cancer [5]. This minimally invasive Raman approach can reach deeper regions in the body and involve the use of either transmission illumination and collection geometries. Another approach is spatially offset Raman spectroscopy (SORS) in which the illumination and collection points are on different points of the tissue surface and can reach up to a few centimetres deep which has many application in various fields including point-of-care medicine [6–8]. These novel techniques allow

higher precision in vivo and ex vivo by measuring biomarkers in the microscale, such as microcalcifications in breast cancer tissue [9].

Alongside with these novel techniques, even more, precise diagnostic measurements are possible by obtaining images of labelled nanoscale contrast agents, achieving single-cell resolution via surface-enhanced Raman spectroscopy (SERS) for truly early-stage cancer detection [10,11]. Furthermore, an improved method to optimise the signal intensity is surface-enhanced resonance Raman spectroscopy (SERRS) which looks to match the wavelength of the excitation and the wavelength of an electronic transition within the reporter molecule used on the metal surface of the nanoparticles. Alternatively, fluorescent can also be used for single-cell detection but not for in vivo measurements in deeply buried tissue. However, its signal is several orders of magnitude weaker than those obtained in SERRS, although it is much simpler to get.

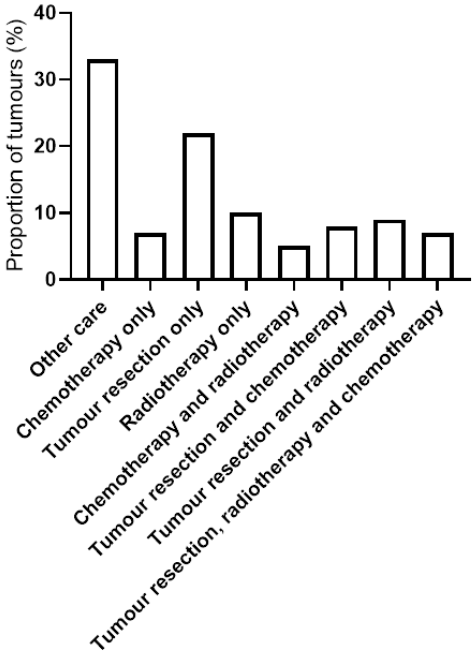

Figure 1.1 | Statistics of cancer treatments in England from 2013 to 2016 obtained by the National Cancer Registration and Analysis Service (NCRAS) in partnership with Cancer Research UK (CRUK) [12].

Once the diagnosis locates the tumour tissue and identifies the cancer type, clinicians choose the best available therapeutic procedure to treat the malignancy. Among potential therapies, the most common approaches are surgery, radiotherapy and chemotherapy or a combination of them depending on the pathological context and local regulation. Figure 1.1 shows statistics of the percentages of tumours diagnosed in England in 2013 - 2016 recorded as receiving radiotherapy, chemotherapy or tumour resection (surgery). Cancer surgery is not only the oldest oncological discipline but also the gold standard for localised tumours by excising the tumour with a surrounding margin of healthy tissue, such as lumpectomy in breast cancer [13]. Surgery is the most common line of defence against cancer, but often also requires to be used in combination with other therapies (as shown in Figure 1.1) due to potential extravasation of the tumour.

Radiotherapy aims to deliver as much dose to the localised tumour whilst sparing healthy tissue; however, there are intrinsic risks of developing additional tumours due to using ionising radiation [14]. X-rays were first used as a cancer treatment by Emil Grubbe who used against a recurrent breast carcinoma in 1896, called Roentgen rays at that time. This type of technique was called radiotherapy or radiation therapy because it is a therapy based on the exposure of cancer cells to high doses of X-rays radiation (ionising radiation) which damages the DNA of the cell and leads to cell death and miotic failure [15]. This damage can be direct or indirect ionisation of the atoms and molecules that are part of the cellular DNA. It is well known

that ionising radiation induces DNA breaks, particularly, double-strand breaks in the chromosome. It also generates reactive oxygen species that oxidise proteins and lipids, and induce several damages to DNA, like the generation of abasic sites and single DNA strand breaks. In radiotherapy, DNA damage is targeted to only the cancer cells. Usually, it includes the use of multiple X-rays beams at a lower intensity that converge into the tumorous area to maximise the dose received in the cancer cells while minimising the exposure of healthy cells. This technique aims to shrink the tumour mass or eliminate residual tumour cells.

A similar approach was also adopted in 1896 by Niels Finsen in the so-called phototherapy whose first trial in skin cancer used UV light which is also ionising radiation, but much less energetic than X-rays. Sixty years later, thanks to previous satisfactory clinical electric muscle stimulation, electrotherapy appeared published in Science to combat skin cancer cells with reported total tumour destruction in the 60% of the subjects in 1959. Furthermore, in 1985, Edwin Smith precisely described the concept of hyperthermia, for the first time in history. However, hyperthermia has not an agreed definition yet [16]; it has been defined as a core temperature above 38.2 °C, irrespective of the cause. In the context of treatment, it is defined as temperatures ranging between 40–48 °C [17]. Examples of external stimuli are shown in Figure 2.6.(2).

Chemotherapy is the most common line of treatment for metastasised tumours and blood cancer due to their usually high growth and cancer cell division rates along with tumour delocalisation [18]. This type of therapy in most cases uses combinations of chemotherapeutic drugs with critical anticancer effects such as preventing drug resistant cancer cells, inhibiting angiogenesis and disrupting all possible stages of the cancer cell reproduction cycle [19,20]. Chemotherapy is often used in combination with

other treatments such as surgery, radiotherapy and immunotherapy. Unfortunately, most chemotherapy drugs are highly dependent on the type of tumour and cannot be applied to other types. Therefore, in case of facing specific unexpected behaviour or high heterogeneity in the cancer cells, the therapy might fail for a subset of cells and require a second round of chemotherapy or an alternative treatment. Survivor cancer cells will have adaptive advantages that will make them harder to kill, the longer it takes to start a secondary effective therapeutic approach. Multifunctional nanoparticles (NPs) can address most of these demanding tasks for either detection, imaging or diagnosis by interacting at the nanoscale with single cells. There has been keen interest during the last decade in finding different NPs that tackle specific clinical limitations, including in vivo single cancer cell imaging and treatment of aggressive brain cancers such as glioblastoma [21].

Nevertheless, the interest has been even more substantial in finding those that can provide multiple highly valuable functionalities in the same device. Some very promising magneto-plasmonic NPs, those that have both magnetic and plasmonic behaviour, have previously been presented over the last years by other authors as multifunctional platforms [22–26]. However, most of these do not provide multiple translational applications to the clinic and are limited to only the areas of the body where the diagnostic technique is effective and safe. For instance, for MRI, different regions have different MRI contrast for both T1 and T2; consequently, the nanoparticle needs to be tuned to be distinguishable in the desired region in a particular mode [27]. Raman signals from nanoparticles can only be measured up to a penetration depth of approximately 15 mm in the best-reported scenario using SORRS [28], due to light attenuation in complex media, which is not enough to detect deep regions. Also, to obtain these signals, infrared light must be used, which usually requires large

nanoparticles to match the maximum absorption peak with the excitation wavelength. For similar reasons, effective photothermal ablation from NPs is only available for skin cancer and the heating rate is typically very high which limits the control in the hyperthermia region and the laser beam diameter tends to be 3 mm which provides low precision. Organs are susceptible to potential toxicity after exposure to NPs; some of the most critical areas are the respiratory system[29], the renal system[30] and the brain [31].

Additionally, there is a lack of cytotoxicity tests with different cell types - including healthy and malignant – for most NPs; they are usually performed in one cell type only. And many impactful studies on NPs for cancer diagnosis and treatment [24,25,32–39] did not include or discuss the effects of NP aggregation since it is an unwanted scenario, despite being a recurrently reported case during NP synthesis. It may happen in a diverse physiological environment as found in the human body; with changes in pH, pressure and temperature [40,41].

Moreover, most magnetoplasmonic structures use magnetite (Fe_3O_4) magnetic components that display powerful magnetic properties useful for faster and stronger responses to external magnetic fields, particularly with SPIONs [42–45]. Unfortunately, these strong magnetic properties also lead to a tendency to aggregate, even when coatings are used to reduce this effect [46]. In the worst scenario, the presence of NP aggregations can be critical for both efficiency and safety [47,48].

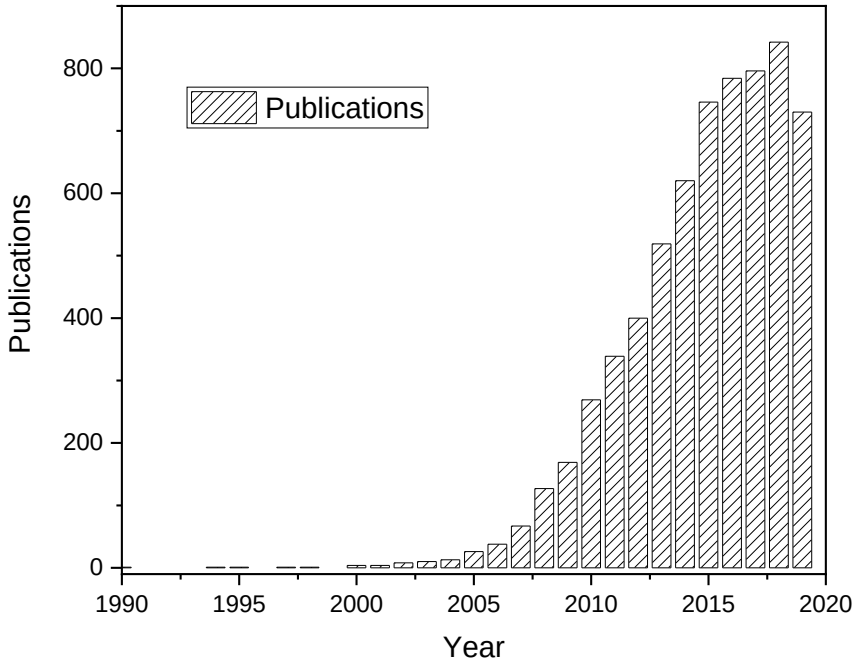

Figure 1.2 | Statistics of publications on nanomedicine/NPs used to find and treat cancer cells.

Figure 1.2 presents the number of publications per year listed in PubMed under the search query “nanoparticles treatment diagnosis cancer cells”. There is a clear exponential trend that represents the growing interest, development implementation and lately maturation of NPs for both diagnosis and treatment of cancer. Some of the breakthroughs in the field of NPs for cancer diagnosis and treatment include selective cell targeting, immunotherapy, fluorescent imaging, SERS imaging, surface-enhanced SESORS, computed tomography (Computer tomography) contrast agents, MRI contrast agents, magnetic drug targeting, photothermal hyperthermia and magnetic hyperthermia [49–54]. These functionalities arising from NPs have provided a better understanding of what can be introduced during the design of a nanoscale agent to overcome some current clinical limitations. However, most of these technological solutions are vaguely presented in the clinical context, yet with just a few undergoing clinical trials that are not fully approved for commercial use. In these examples, the

NPs involved are very simple, with minimal biomedical functionalities. Most initial clinical trials are blind controls or double-blind randomization to compare the evaluate dosage, and then efficacy and side effects. The main evaluated aspects for NPs are clearance and toxicity for specific NP concentration, which are mainly dependent on the size, shape, density, hydrophobicity, pH stability, surface charge and surface chemistry [55]. In terms of NP clearance, hydrophilicity (charge-polarized and capable of hydrogen bonding) usually leads to direct excretion by the kidneys, while the hydrophobicity undergoes biotransformation before excretion.

To get NPs approval by regulatory agencies, NPs need to undergo product-specific technical assessments, taking into account the effects of NPs in the particular biological context and pharmacodynamics of each product and its intended use. To regulate medical NPs, the US Food and Drug Administration (FDA) implements two regulatory pathways as mandated by the Medical Device Regulation Act of 1976: the most common is the 510 (k) process, and the other is the PMA process. The PMA process requires clinical trials to demonstrate the safety and effectiveness of NPs. Before beginning clinical research, an Investigational New Drug (IND) application must be submitted to the FDA, which must include: animal study data and toxicity data, manufacturing information, clinical protocols for studies to be conducted, data from any prior human research and information about the investigator. The 510 (k) process requires a submission to the FDA demonstrating that the NP to be sold is similar to, and at least as safe and effective as, a previously legally marketed NP that is not subjected to PMA [56]. For the European Medical Agency (EMA), the only route for the NP approval is performing human clinical trials whose data are evaluated by EMA scientific committees as stated by the new EU regulation (536/2014) for clinical trials

of medicinal products for humans. The clinical trials can be performed outside of the EU, but they need to adhere to equivalent standards.

In this thesis, experimental work is primarily presented with the aim to design, synthesise, and evaluate multifunctional core-shell composite NPs for combined cancer imaging and treatment capabilities. The main focus of this work is obtaining high quality and biocompatible nanomaterials that combine as many functionalities as possible, with the capacity for cancer diagnosis along with therapeutic capabilities that are externally activated and effective for many types of cancer. This thesis also aims to obtain materials suitable for in vivo single-cell imaging applications using SERS in conjunction with contrast imaging from clinically available diagnostic tools for cancer detection such as MRI and CT.

2. Background

2.1. Single-cell detection

Single-cell detection is essential for early diagnosis of health conditions that can quickly escalate if not detected early enough. Figure 2.1 shows the different methods used for single-cell detection.

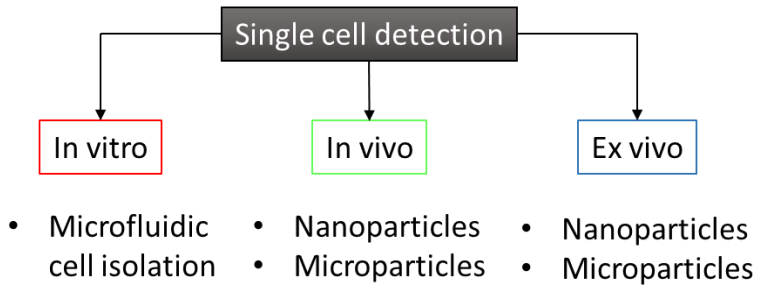

Figure 2.1 | Current approaches under investigation to single-cell detection for disease diagnosis.

While microfluidic cell isolation (detection) and subsequent single-cell sequencing (analysis) are relatively common oncological techniques in the clinic, the in vivo and ex vivo single-cell detection approaches are still under investigation.

In vitro methods are very popular to isolate cells and subsequently perform advanced analysis, including cell genomics and surface cells proteomics. Unfortunately, these methods require a sample biopsy from the patient, which is always invasive, with different degrees depending on the sample origin. This requirement makes in vitro systems less appealing for cell detection, especially when the exact tumour location is unknown.

For in vivo measurements, both microparticles and NPs overcome this problem by being able to target cells in any region of the body without the need for a biopsy from the patient. However, injecting micro- and NPs into a human body is a highly invasive procedure which requires very low toxicity and excretion of these foreign

objects. These features are usually not achieved by microparticles due to their size, which is in the same order of magnitude as the human cells, which are 4-40 μm. NPs, on the other hand, can achieve higher excretion percentages if their size is tailored appropriately to be in the size range of human proteins and virus (5-120 nm), enabling their ability to travel. However, only NPs smaller than 5 nm are readily excreted by the kidneys into the urine. Invasiveness can be minimised by localising a region of interest where the suspected disease exists, which is highly effective in the case of cancers since most of them exist in specific locations and display features characteristic of those regions. An example of this is the microcalcifications which are detected in breast cancers. These are biomarkers that indicate a potential malignancy, which can be further confirmed by using NPs in the breast area.

Diagnosis is the most critical aspect in oncology. The prognosis of patients whose cancer is detected early is drastically improved compared to those with later detection. Besides the fact that there are some cancer biomarkers that can be detected just by taking blood or urine samples, a comprehensive diagnosis is usually required to fully understand the illness or disease and follow with the treatment that has the highest likelihood of success. For this reason, there exist a wide range of molecular imaging options for this purpose that includes magnetic resonance imaging (MRI), computer tomography (CT), positron emission tomography (PET), single-photon emission CT, ultrasounds imaging, fluoroscopy and recently Raman spectroscopy (via SESORRS). 7-T MRI machines can resolve up to 0.5 mm, while 21.1-T high-resolution MRI (HRMRI) can resolve as small as 120 μm[57]. Microcomputed tomography (microCT) can have a resolution of 1 μm. However, in vivo, human CT imaging is restricted to a voxel size of 82 μm (with an actual spatial resolution of approximately 130 μm) due to technical limitations and radiation dose

considerations [58]. Positron emission tomography (PET) can obtain a resolution of 0.67 mm for pre-clinical studies (small non-human animals) and 1.83 mm for clinical imaging [59]. All these values are beneficial for clusters of cells or tissues, but they cannot detect single human cancer cells which typically range from 20 to 30 µm and even reach sizes smaller than 6-7 µm to navigate through blood vessels [60]. Therefore, these techniques cannot provide a single-cell resolution. For most types of cancer, detection in the early stage is the key to success in the treatment. Particularly in cancer research, early diagnosis has become the focus of attention in the scientific community.

There are some commercially available techniques to destroy cancer locally at the cellular level, but not for in vivo imaging. Most cancers are diagnosed when there is a significant volume of tumour tissue, and therefore the malignant cells are likely to have spread around the whole body, which decreases notably the probability of success for most treatments. Hence, single-cell detection is essential to find and analyse cancer at its earliest stage possible. However, single-cell detection has some physical barriers for most commercially available traditional techniques which make it not possible to achieve. Here is where nanotechnology comes to bring a new set of tools for unlocking the cellular and subcellular scale, particularly with the use of NPs.

NPs are objects smaller than 1 µm, usually in the range of approximately 1 to 100 nm, much smaller than any human cell (4-40 µm). Their relatively small size is what makes them so desirable for cancer cell imaging. Depending on the antigens expressed on the cancer cell surface (e.g. oestrogen, progesterone, her2, egfr), there is a unique type of antibody that links to each cancer cell antigen. Antigens are typically proteins, peptides, or polysaccharides. Different antibodies can be used to target the same cancer cell depending on the relative expression either raised or reduced for

different cells. With protein antigens, the antibody molecule contacts the antigen over a broad area of its surface that is complementary to the surface recognised on the antigen. Functionalisation of the NP surface with the right antibody enables it to target the surface of the malignant cells that present the binding antigen, which can occur as a consequence of electrostatic interactions, hydrogen bonds, van der Waals forces or hydrophobic interactions [61]. This targeting brings the possibility of performing diagnostics in single cells.

One essential point to consider is the biocompatibility and circulation time in the bloodstream of these NPs. This includes cytotoxicity but expands the considerations to NPs accumulation in undesired areas, inflammation, and cellular behavioural changes such as oxidative stress. These aspects must be considered while designing the nanomaterial for single cell detection. In this regard, gold nanoparticles (AuNPs) are truly biocompatible and non-cytotoxic at low concentrations for a wide range of scenarios because of their high stability and being a noble metal.

2.1.1. Raman spectroscopy

Spontaneous Raman spectroscopy, usually referred as Raman spectroscopy in the literature, is a molecular spectroscopic technique based on an inelastic light scattering, which provide spectroscopic information of the energy transitions of electrons that are excited from the molecular valence state to virtual molecular states and subsequently decay inelastically. This technique, combined with surface plasmons generated near the vibrating reporter molecules, results in the so-called surface-enhanced Raman spectroscopy (SERS). In SERS imaging, AuNPs have been widely used because of their ability to generate plasmons with visible and NIR light that boost the signal of Raman reporter molecules placed chemically on or within few

nm of the NPs surface. Raman reporter molecules are molecules are used to provide a known signal spectrum which are typically amplified using SERS. Plasmons are collective sinusoidal oscillations of the electron clouds in metals which boost the intensity of the Raman reporter molecular vibrations up to 10^6 on average and 10^{10} or higher in localised areas for low wavelengths such as UV light while using SERRS and matching the plasmon resonance frequency. SERRS is one step beyond SERS in which the analyte has a chromophore with the excitation energy of its electronic states close to the respective the frequency of the excitation that is utilised to excite the surface plasmons in SERS. Another approach is deep Raman spectroscopy; this type of Raman uses spatially offset Raman spectroscopy (SORS) to collect the Raman photons that have been generated more deeply in complex media when NIR illumination is used. SORS has been demonstrated for the detection of Raman spectra from calcifications (breast cancer biomarkers) and cancerous tissues under a deep soft tissue but at much higher concentrations than the required for a SERRS signal to be detected. Recently, silicated RGD-coated gold nanostars with an average diameter of 120+/-9 nm and a silica shell of 23 ± 4 nm have been used to perform a combination of SERRS and SORS called SESORRS obtaining measurable signals through stacked plastic barriers of 4.5, 6 and 7.5 mm thick each and being dispersed in ethanol [28]. By changing the offset, there is a substantial change in the depth of the detected signal. This can be used to obtain a higher contrast when displaying a heat map of the signal. Larger offsets provide weaker signals due to photons penetrating longer paths in the plastic barrier.

Figure 2.2 summarises the underlying physical principle of Spontaneous Raman spectroscopy which is commonly used to describe the molecular band energy transitions where Ω is the energy difference from the ground state and a vibrational

state [62]. This type of Raman-scattering receives the name of spontaneous because it takes place spontaneously, i.e., this scattering occurs randomly, and only a small number of scattered photons undergo this process. The potential vibrational energy states that the molecules can go to or depart from can be obtained by solving the vibrational Schrödinger equation.

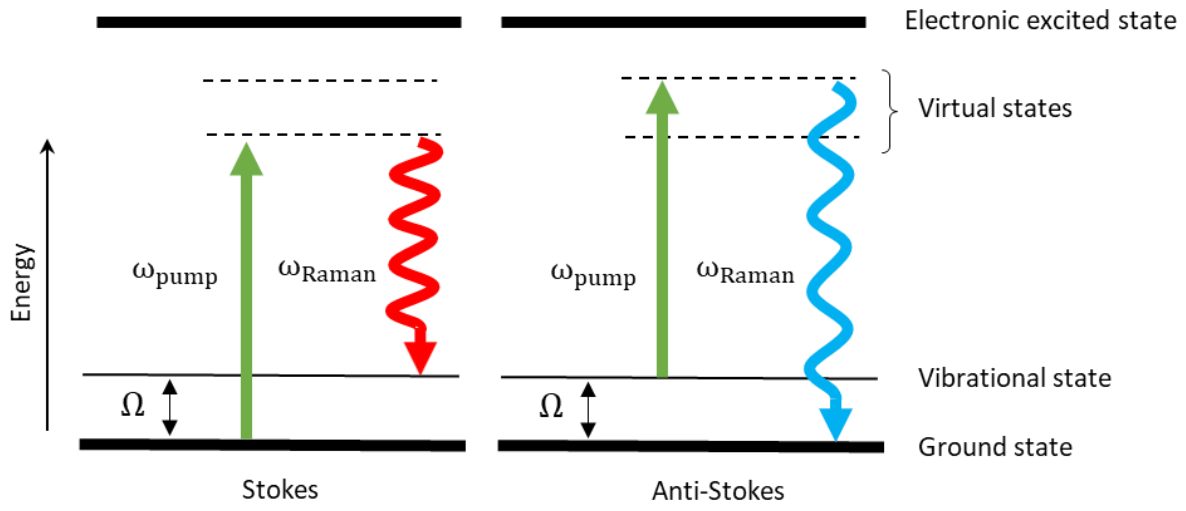

Figure 2.2 | Jablonski diagrams of Spontaneous Raman Spectroscopy. The fundamental physical principle of the Raman scattering in terms of energy levels. The Stokes mode is described in the left side, and the Anti-Stokes mode is described on the right side.

The Raman spectra contain the intensity of each decay present in Figure 2.2, which are expressed in terms of Raman shifts:

$$\Delta\omega = \left(\omega_{\mathrm{pump}} - \omega_{\mathrm{Raman}}\right) \tag{2.1.1}$$

where $\Delta\omega$ is the Raman shift, ω_{pump} is the excitation wavenumber and ω_{Raman} is the scattered wavenumber.

Background

In Raman spectroscopy, a monochromatic laser beam interacts with the molecules of the sample and produces scattered light. This scattered light contains spectroscopic information of the molecular interactions. However, most of the scattered photons are elastically scattered via Rayleigh scattering. This type of scattered photons contains no information about the light-matter interaction. Only a small fraction of the scattered radiation has a different frequency from the frequency of the monochromatic incident radiation. This small contribution of scattered radiation constitutes the Raman spectra. In Raman scattering, there is a molecular excitation caused by the incident radiation and a decay via inelastic photonic scattering through its interaction with vibrating molecules[63]. A Raman spectrum is presented as an intensity-versus-wavelength shift with a typical Raman spectra range of 4000-400 cm^{-1} which is the region of Raman active normal modes of vibration for organic molecules[64].

Low sensitivity due to weak Raman scattering is the major problem associated with this technique. However, sensitivity can be enhanced using Resonance Raman Spectroscopy (RRS) and SERS. The basic idea of RRS consists of matching the frequency of incident radiation with an electronic transition of the molecule, which increases the intensity of the obtained Raman spectrum drastically. RRS also allows working with very diluted samples.

For in vivo imaging of cancer cells, Raman spectroscopy should be performed in the NIR to penetrate human soft tissue deeper, red light (650 nm) is extinguished at 4–5 mm penetration depth and shorter wavelengths penetrate even less. Detection of NPs that target cancer cells using NIR SERS requires larger spherical NPs to redshift the maximum of local surface plasmon absorption peak and improve the SERS

enhancement factor (EF). However, the problems related to toxicity associated with large NPs and their low excretion rate make them less ideal for safe diagnosis. Moreover, large NPs tend to aggregate more quickly due to potential larger electrostatically charged surfaces, to be more massive than smaller counterparts and, if magnetic, to presenting ferrimagnetic behaviour that attracts other magnetic nanoparticles around. For these reasons, they eventually can form aggregates heavy enough to undergo gravitational decantation inside of the human body if they are in an area with a slow or null flow which will lead to potential tissue damage and will prevent their excretion. Furthermore, different shapes of nanoparticles also provide different absorption profiles which can be tuned for the optimal maximum of localised surface plasmon resonance (LSPR) absorption.

There are other methods for single-cell detection, such as NIR fluorescence. For instance, Dong *et al.* 2019 successfully developed NIR-to-NIR two-photon excited fluorescent CaF_2: Tm^{3+}, Yb^{3+} NPs (with a diameter of 11 nm and size dispersion of ±2 nm) for highly penetrating fluorescence bio-imaging which were tested using in vitro HeLa cells which are an immortal cervical cancer cell line [65]. Additionally, autofluorescence in the NIR region from human tissue is very low. This low NIR cellular autofluorescence background allows this technique to perform in vivo fluorescence of the entire body. This is particularly relevant in pharmacokinetics and guided tumour surgery [66]. Unfortunately, this technique does not provide molecular information from the fluorophores. For detailed molecular information, additional ex vivo studies can be performed from the excised tissues and organs after surgery.

Hence, finding the right NP that brings reliable single-cell detection in vivo, while causing minimal or zero toxicity, is the main goal in terms of diagnostic properties in this thesis.

2.1.1.1. SERS imaging and detection

Raman spectroscopy is a spectroscopic technique that shows the inelastic light scattering after interacting with the vibrational bands in the targeted molecules. These transitions between vibrational levels in molecules provide information of their chemical structure in the form of peaks for specific wavenumbers whose distribution is unique for every molecule. The Raman spectra can be understood as the “molecular fingerprints” of any molecule. This revolutionary discovery made in 1928 by Chandrasekhara Venkata Raman about the analysis of molecular structure resulted in his Nobel prize in physics in 1930 ‘for his work on the scattering of light and for the discovery of the effect named after him’.

SERS is a powerful method to measure the vibrational band fingerprints of single molecules which are adsorbed on top of a jagged metal (see Figure 2.3). SERS can stand for either scattering to emphasise the optical effect or spectroscopy to emphasise the technique and its applications. The signal obtained from Raman scattering is enhanced by surface plasmons that move across the metal substrate of noble metals such as Au, silver (Ag) and copper nanostructures. However, other plasmons can also be generated in periodic 2D structures such as graphene. These plasmons are activated by the coupling between photons and charge density oscillations of the electrons in the conduction band in metals. On the other hand, spectroscopy is a measurement technique of the interaction between matter and light. Typically, the standard way to analyse how matter interacts with electromagnetic

radiation is using light beams in the form of laser with approximately one single wavelength or by using white light. For Raman spectroscopy, a laser is used to excite the vibrational bands with different wavelengths depending on the purpose. The range of lasers commercially available involves ultra-violet (UV) from 244 nm to 364 nm, visible from 457 nm to 660 nm and near-infrared from 785 nm to 1064 nm. Conversely, it is an important issue to assess the appropriate laser power to ensure the NPs are activated strongly enough to enhance the Raman signal but not so high that they produce heat.

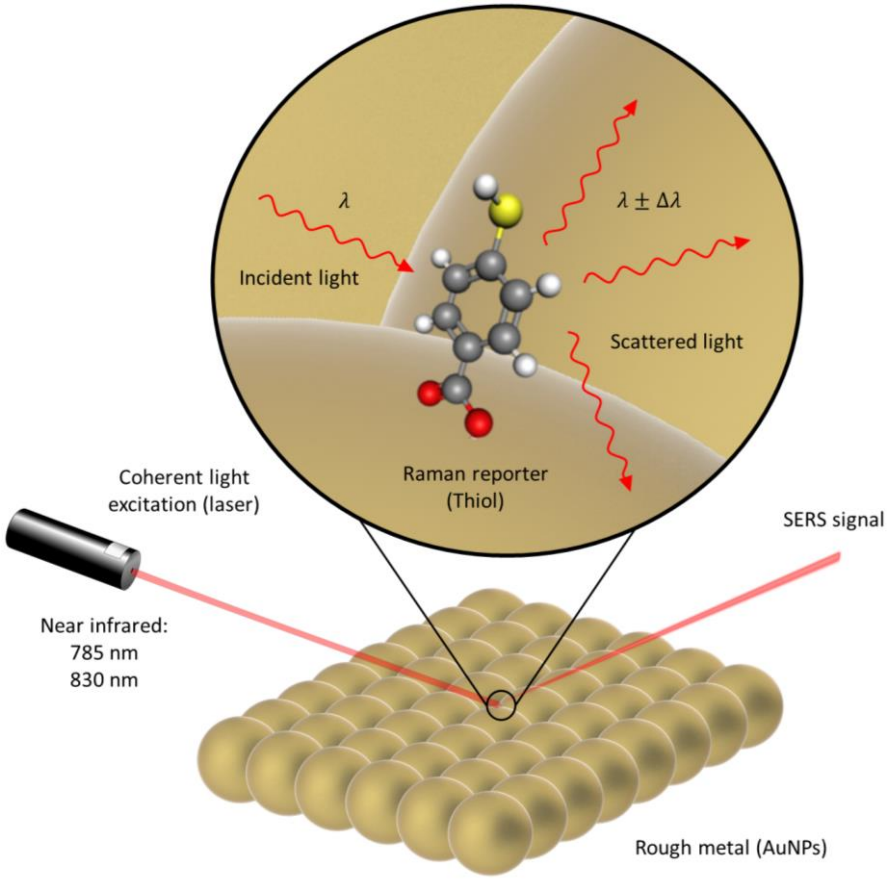

Figure 2.3 | Diagram of SERS effect where the Raman molecule reporter is a thiol (4-Mercaptobenzoic acid) on top of an Au layer that acts as a metallic substrate, and the laser photons are in the Near-Infrared. λ refers to the incident light and $\lambda \pm \Delta\lambda$ are the scattered wavelengths (“ + “ in Stokes and " – " in Anti-Stokes).

Figure 2.3 shows the very well-known bond between AuNPs and the sulphur of the thiol molecule obtaining a self-assembled surface structure of thiol-capped AuNPs. The selection of 4-mercaptobenzoic acid (4-MBA) among all the other possible thiolated marker provides the potential benefit of both a strong SERS signal and a peak shift with pH. Despite the fact that the bonding between one single sulphur atom and Au is robust, other chemical structures contain more than one sulphur that can bind with the same AuNPs and, therefore, can produce a much more stable final material. Also, 4-MBA only contains one aromatic ring that generates much weaker peaks than other thiols with several rings.

SERS is a surface spectroscopy technique, by definition. Hence, the reporting molecules must be close to the surface (<10 nm). This means that a bond or attachment between the metallic surface and the molecules is required for continuous, reproducible and optimised signals. To implement SERS in many practical applications, transferring the molecules from the bulk to a surface is needed and can be achieved in different ways that can affect the final enhancement efficiency. This step must be taken into careful consideration in advance to ensure the best performance for each case. The surface can present a variety of shapes, SERS can be performed from redispersed metallic colloids in a solution to uniform substrates fabricated by nano-lithography. However, roughened surfaces providing points of electric field enhancement, related to the lightning rod effect, provide areas of greatest enhancement.

The enhanced signal is due to plasmon resonances in the metal substrate. For both applied and fundamental SERS approaches, measuring how much the signal can be boosted is a vital aspect of this technique. Usually, this increment in the signal is

quantified by using the enhancement factor (EF). On average, the best enhancements in a sample can be up to 10^6, usually called 'average SERS'; while in localised areas it is possible to obtain an EF of 10^{10} or higher using UV light. However, there are some issues to compare and predict EFs of different SERS substrates for a specific application. Due to the significant number of possible scenarios in which SERS can appear, a single general definition for the EF is impossible. There has been a growing controversy during the last 15 years about the possible contribution for the origin of the SERS enhancement due to the effect of the electronic interactions between the metal and the adsorbate, typically called chemical enhancement factor [67]. While the electromagnetic enhancement makes it possible to see the enhancement in the signal, the chemical mechanism determines what is observed. When the molecule is directly attached to the surface, the highest EM enhancement is obtained. This enhancement is differential across large molecules, with a higher enhancement for the molecules closer to the metal surface. Then, there is a possibility of including in this enhancement a multiplicative contribution due to the excitation into a charge transfer (CT) excitation between the metal and the adsorbed molecules which can provide an enhancement of $\sim 10^2$ in the peaks [68]. SERS spectrum contains the information about the adsorbate, its environment and its interaction with the enhancing NP, its spatial orientation, and the polarization properties of the local electric field. Almost 20 years after the initial ideas about the physical origin of the magnitude increment in SERS, the possibility of single molecule (SM) Raman spectroscopy via SERS was proposed [69]. Since then, SERS became a dominant tool for SM laser spectroscopy competing with the traditional well-established fluorescence. Still much remains to be learned about SERS, in recent years, a better understanding of the SERS background was studied proposing new theories such as the physicochemical dependence of the background

on plasmons, the identity of the adsorbate, adsorbate coverage and electrochemical potential [70].

By using NIR lasers, non-dissipative light transmission in tissues can be achieved while keeping a strong SERS effect. This is the foundation of deep tissue Raman imaging for cancer cells. An excellent example of this is the SERS-active gold nanoshells (AuNSs) of 100 nm in diameter with built-in hotspots with SERS EF higher than their gold sphere counterparts of the same size for 633, 785, and 830 nm [71]. These structures reached NIR SERS EF over 200 for diluted colloidal samples in water using acquisition times of 10 s and 5 mW of power.

The key concept behind the SERS signal peaks' boost is the coupling of electric fields from the plasmon waves with the vibrational modes in the molecules. These electric fields are a consequence of the dielectric environment formed by the electron cloud oscillation around the metallic nucleus, i.e. plasmons. Therefore, a dipolar localised surface plasmon resonance (LSPR) is responsible for the excitation of the metallic NP (see Figure 2.4). One crucial aspect is the fact that plasmons are in principle only generated in metals due to the need for conductive electrons. However, there exist exceptions to this rule that were found during the last decade, such as carbon nanotubes that can generate LSPR as well.

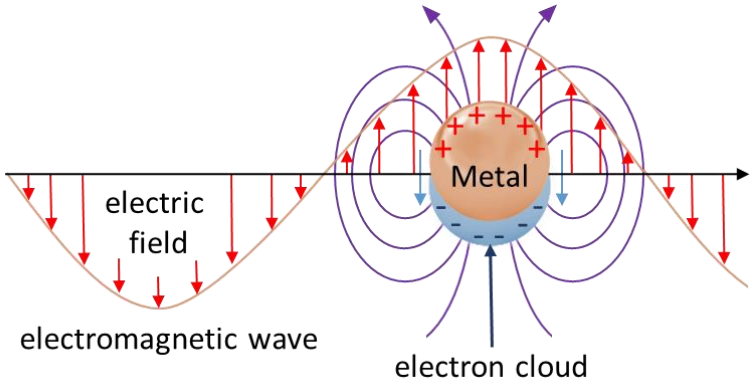

Figure 2.4 | Electromagnetic enhancement in SERS activated by excitation of a dipolar LSPR.

The SERS EF of a molecule within SERS is controversial and varies drastically depending on the considerations taken in account. A general expression of the SERS EF for the same Raman reporter concentration in the bulk sample solution is given by the following equation [72,73]:

$$\text{SERS EF} = \frac{I_{SERS}/N_{SERS}}{I_{NRS}/N_{NRS}} \quad (2.1.2)$$

where I_{SERS} and I_{NRS} refer to the peak intensities of the SERS and normal Raman Spectroscopy (NRS), respectively. N_{SERS} and N_{NRS} correspond to the number of probe molecules excited in the SERS and NRS tests given. Basically, N_{SERS} and N_{NRS} are equal in the concentration of molecules is the same, homogenously distributed in the region to excite and to use the same volume of sample to excite. However, this measurement might mislead. When comparing intensities, a refinement from this measurement includes considering a background signal that will be equally excited in both measurements and normalise the signal so that both backgrounds have equal intensities. Then the formula (2.1.2) can be considered correct. However, when the sample presents hot spots that vary under environmental changes, it will not be. Because of this unique Raman signal boost, many applications have been devloped to exploit the capabilities of this effect in a wide variety of fields. In medical diagnosis, deep Raman spectroscopy has supposed an innovative approach to measure molecules through a thick tissue layer. This technique, combined with the SERS enhancement is currently one of the most promising approaches to detect illnesses,

bacteria and viruses inside of the human body. However, there still is a debate about the consequences of introducing nanostructures in the organism in the long term.

2.1.1.2. Coherent anti-Stokes Raman spectroscopy

Coherent anti-Stokes Raman spectroscopy (CARS) is a nonlinear four-wave mixing Raman spectroscopy technique that typically uses two powerful collinear synchronised lasers, pump and Stokes, to irradiate a sample. CARS is particularly useful for enhancing the weak (spontaneous) Raman signals. CARS microscopy is frequently used to study cancer cell behaviours in vivo and in vitro [74].

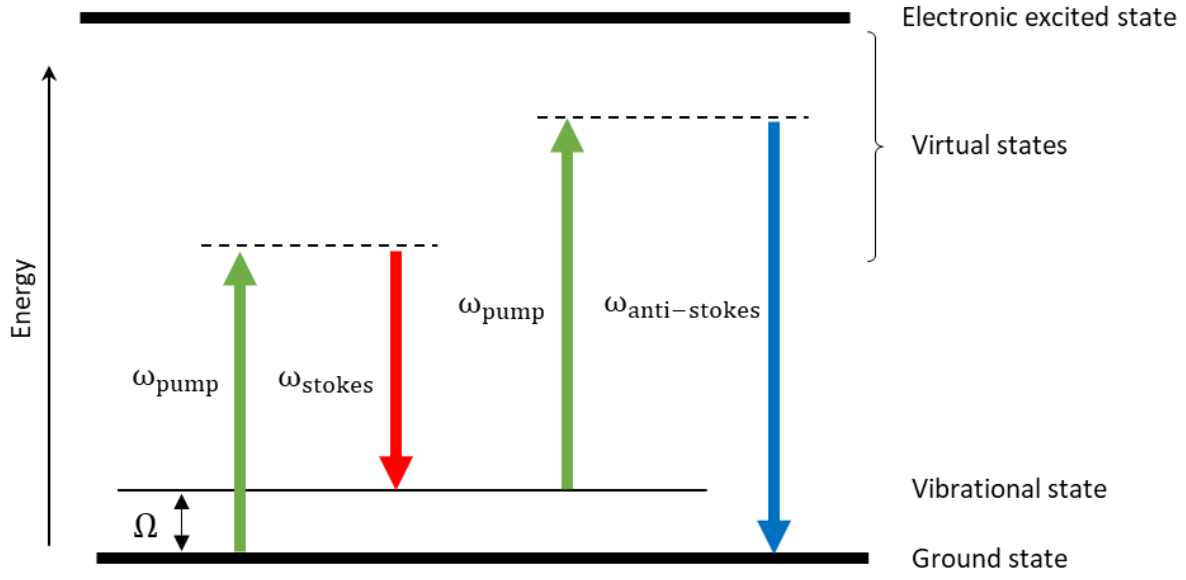

Figure 2.5 | Jablonski diagram of the Coherent Anti-Stokes Raman Spectroscopy in terms of energy levels following the same terminology used in Figure 2.2.

In a generic CARS process, three lasers at the pump (ω_{pump}), Stokes (ω_{stokes}), and probe ω_{probe}) frequencies interact with a medium to generate a new field at the anti-Stokes frequency [75] obtaining

$$\omega_{anti-stokes} = (\omega_{pump} - \omega_{stokes}) + \omega_{probe} \quad (2.1.3)$$

In most experiments, the pump field and probe field come from the same laser beam, and therefore, $\omega_{\text{pump}} = \omega_{\text{probe}}$ which leads to

$$\omega_{\text{anti-stokes}} = 2 \times \omega_{\text{pump}} - \omega_{\text{stokes}} \quad (2.1.4)$$

The frequency of the pump is usually kept constant, and the Stokes laser is tuned to ensure that the frequency difference between the two lasers equals the vibrational frequency of the Raman-active mode of interest (see Figure 2.5).

To obtain a strong Raman signal, the Stokes laser frequency is tuned to the difference between the pump and the vibrational frequency of the Raman-active mode of interest. Consequently, the scattered light frequency is higher than the excitation frequency, which leads to conclude that anti-Stokes scattering is occurring.

CARS microscopy provides spectroscopically high-resolution confocal mages cell and insights of cellular structures. Coherent Raman imaging techniques have demonstrated high-speed, high-spatial-resolution imaging, but with contrast limited to single or few Raman peaks [11,76–78].

2.2. Cell Targeting

Cell targeting is the delivery of a particular agent to a cell, and can also be used for its identification. There are primarily two subtypes of targeting modalities: active and passive. Both active and passive targeting promotes NPs' accumulation in the location of interest. Targeted cancer delivery of therapeutics or diagnostic agents involves systemic administration in passive targeting or localised delivery of the nanoscale agents to the diseased tissue active targeting [79]. The main controlling factors of the targeting are the surface functionalization, physicochemical properties

of the bare nanoparticles, and pathophysiological characteristics of the tumour microenvironment.

In passive targeting, the success of nanoscale object excretion relies on having a prolonged circulation time. This can be achieved by coating the NP with some highly biocompatible and non-reactive substance such as polyethylene glycol (PEG)[80]. The first clinically approved passively targeted nanocarrier was PEGylated liposomal doxorubicin (DOXIL™) in 1996 [81]. Long circulation time also maximises the chances of NPs excretion. On the other hand, active targeting is essential for the effective delivery of drugs, genes and theranostics to the location of interest, avoiding the healthy tissues and minimising side effects. Active delivery maximises the number of nanoscale object delivered to the target cell [82]. To achieve this, proteins on the surface of the cell are being targeted via antibody-antigen interaction. In this type of interaction, the antigen-binding fragment (fab) of the antibody binds to the epitope of the antigen. Epitopes or antigenic determinants are outer regions of proteins that can trigger an immune response from T or B cells [83]. The antigen can display multiple epitopes of which the antibody needs to recognise at least one to achieve the binding. By functionalising the surface of the NPs with these antibodies, the NPs can target the surface of the desired cell.

Despite the antibody targeting approach which the main route to delivery nanoscale objects to a cell, it is also possible to obtain NPs selectively uptaken by cancer cells via anionic surface functionalization [84].

There have been reported some highly successful cases of NPs for cancer in recent years, most of which are nab type (NP albumin-bound) tested for cancer treatment, some of which lead to patents [80,85–89]. Among this success, some of the

most notable examples are Doxil®, a liposomal system for doxorubicin delivery and treatment of ovarian carcinoma; Abraxane®, albumin NP taxol conjugate for the treatment of metastatic breast cancer; nanoliposomal irrinotecan, a SPIO Feridex I.V.® (ferumoxides injectable solution) to diagnose the pre-operative stage of pancreatic cancer with MRI with passive targeting[90]; a transferrin targeted cyclodextrin polymer-based NP for siRNA delivery CALAA-01 which uses multiple antibodies including anti-RRM2, anti-GAPDH, anti-hTfR and anti-*β*-actin [91]; and lyso-thermosensitive liposomal doxorubicin (Thermodox®) as a novel activated therapy using radiofrequency ablation [92,93].

2.3. Cytotoxicity

Cytotoxicity is the ability of any agent or process to kill cells. The cytotoxicity test is one of the most critical biological evaluation tests that use cultured tissue cells in vitro to observe the cell growth, reproduction and morphological effects by exposure to a certain drug or medical device. Cytotoxicity investigations of engineered NPs are particularly relevant in drug and gene delivery, biosensors, cancer treatment and diagnostic tools [94]. Recent studies showed varied in vitro cytotoxicity of NPs concerning size, shape, material composition, surface charge and cell type [95]. For instance, macrophages are highly susceptible to nanomaterial toxicity. At the same time, 3T3 fibroblasts are more resistant, the viability of 3T3 cells slightly decreases as the concentration of nanomaterials is increased and, in telomerase-immortalised bronchiolar epithelial cells, multi-wall carbon nanotubes <8 nm are substantially more toxic than similar materials with bigger diameters (20-30 nm and >50 nm). One reason for these effects is the correlation between particle size and surface area. Also, there are certain materials such as Au, SiO_2 and iron oxide that have shown remarkably low

cytotoxicity compared to other mainstream materials and lead to their approval for clinical use by drug regulatory agencies.

Most human cells are actively maintained neutral or slightly positive charge at the cell surfaces via the ion pumps and channels on the plasma membrane. Significant amounts of surface charge on cells are usually generated by an abnormal movement of mobile ions across the plasma membrane [96]. Cancer cells are distinctively characterised by having a negatively charged surface as a consequence of their unique metabolic processes [97]. The surface charge is measured using the zeta potential. Positively charged NPs will rob electrons from cells which can cause damage to them. Furthermore, positively charged NPs could easily enter any cell, not just diseased cells, in contrast with negatively charged and neutral NPs [97]. This is potentially very dangerous for healthy cells because cells contain negatively charged DNA that will bind to them. Moreover, positively charged NPs have an enhanced capacity to adsorb proteins, including antibodies, albumin and fibrinogen. Proteins binding to NPs alters the protein structure, which may lead to various diseases, such as amyloidosis [40]. Some studies have shown that there is a tendency to accumulate positively charged and neutral NPs by all cell types while negatively charged NPs are primarily uptaken by cancer cells [84]. NPs enter the cells by endocytosis, which is divided into phagocytosis for larger particles (>500 nm) and pinocytosis for smaller NPs [98].

Many studies have shown that more advanced in vitro toxicity assays allow more accurate representations of the physiological tumour microenvironment. For instance, a 3D cancer microfluidic cell culture for studying onco-nanomedicine efficacy was recently proposed by Carvalho *et al.* 2019 [99]. This study shows a real-time

response of malignant human colon carcinoma cells in a gradient-like fashion, as occurs in a physiological concentric tumour microenvironment, for several concentrations of GEM-loaded CMCht/PAMAM dendrimer nanoparticles as they penetrate the cancer hydrogel in a gradient fashion. Another relevant example is the dynamic multi-organ-chip for long-term cultivation developed by Wagner *et al.* 2013 [100]which obtained crosstalk between the tissues in 14-day co-cultures exposed to fluid flow.

2.4. Nanotherapy

The most important idea about therapy is that there is a need to find the therapeutic window where the treatment kills the cancer cells without killing too many healthy cells and therefore impact on the recovery or survival of the patient. This is the pillar on which all the different techniques are based.

The intrinsic limits of most cancer therapies require a better delivery control, total elimination of the selected NPs after therapy and safer treatment. Most of the current clinical chemotherapies include chemical agents that have a low molecular weight with the high pharmacokinetic volume of distribution that leads to increasing their cytotoxicity. Also, the low molecular weight of these chemicals promotes their fast excretion; hence more doses are required, which ends up with a higher net concentration. This contributes to the notable increase in toxicity. Therefore, the current pharmacological approach is being challenged by many other novel alternatives that currently present lower known risks. Examples of these are nanotechnology structures that can generate lethal effects such as absorbing oxygen (hypoxia), invading the inside of cancer cells, heating single cancer cells (hyperthermia) or carrying some dangerous substance to be intracellularly released.

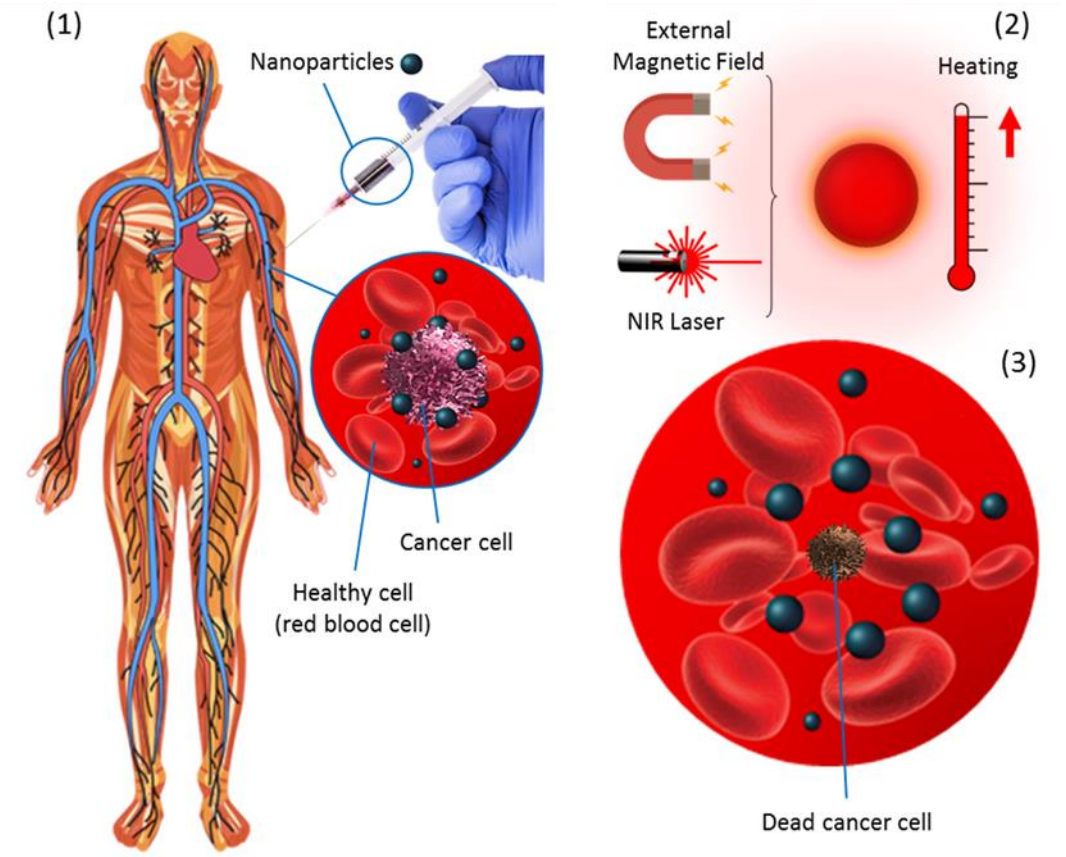

Figure 2.6 | Diagram of the hyperthermia treatment procedure. (1) NPs injection. (2) Heating treatment activation by increasing the NPs temperature. (3) The result of the hyperthermia treatment.

Recently, innovative magnetic hyperthermia has been implemented (see Figure 2.6), where the temperature increment is generated by the action of an alternating magnetic field to the magnetic material. The most common example is ferrite NPs, with sizes from 10 to 100 nm[101–105]. However, there is some concern about the toxicity of this type of NP since the human body cannot efficiently excrete sizes closer to 100 nm or larger, and most of the IONP used until this decade exceeds 100 nm without including any additional coating or aggregation. These giant magnetic NPs produce heat via two main mechanisms: hysteresis loss (multimagnetic domain) and relaxational losses (single magnetic domain). The combination of these mechanisms usually leads to very high temperatures in short periods. Remaining in the safe and

effective hyperthermia range of 42-48°C under these fast heating processes is hardly controllable. When the IONPs are small enough, close to 10 nm, their superparamagnetic behaviour becomes dominant and the single domain approximation becomes valid. And therefore, the only heat arises from relaxation losses that can be either Neel or Brown, which can be monitored and easily controlled to remain at 42-48°C to deliver magnetic hyperthermia. For Fe_3O_4 NPs, the dimensional limit for domain walls is in the order of 50 nm [106]. Moreover, most composite versions of these NPs bring this size issue.

Some of the most innovative approaches to combat cancer with NPs are hypoxia-activated drug treatment [107] and hyperthermia-induced by some external energy sources such as applied magnetic fields or NIR lasers. The hyperthermia treatment is described in Figure 2.6. Hence Figure 2.6.(1) shows the first step of this procedure, the nanotechnological agent introduced into the blood vessel. This agent has been previously functionalized with antibodies specifically selected for the unique antigens of the targeted cancer cells. In Figure 2.6.(2), the two most common external sources of heating are shown. The applicability of any of them depends on the type of NP selected. In oncology, the term hyperthermia refers to sustained therapeutic heating of a region of interest to temperatures above 40°C produced by some external source of energy. These two sources provide the possibility to activate the destructive temperature-dependent effect only when required and switch it off after. Finally, once the method ends the outcome results in the total or partial thermal damage and destruction of the cancer cells. The most important considerations before injecting the NPs for this kind of treatments are: right functionalization of the external surface with antibodies for the specifically targeted cancer cells, small size to avoid obstructions in the kidney (below 100 nm), high biodegradation and low or null cytotoxicity [108,109].

Some relevant examples of antibody functionalisation for cancer cells surface antigen targeting on the external NP surface of NPs similar to ours include the following. In 2003, Artemov *et al.* successfully implemented anti-HER2/neu antibody Herceptin (Genentech) functionalized SPIO which are MR contrast agents to target MCF-7, MDA-MB-231, and AU-565 human breast cancer cells [110]. In 2010, Day *et al.* produced anti-HER2 antibody-conjugated Au-Au_2S sulphide nanoparticles as multifunctional agents that specifically binds SK-BR-3 human breast carcinoma cells that over-express the HER2 receptor, enabling the cells to be imaged via multiphoton microscopy with an incident laser power of 1 mW [111].

2.5. Nanotheranostics

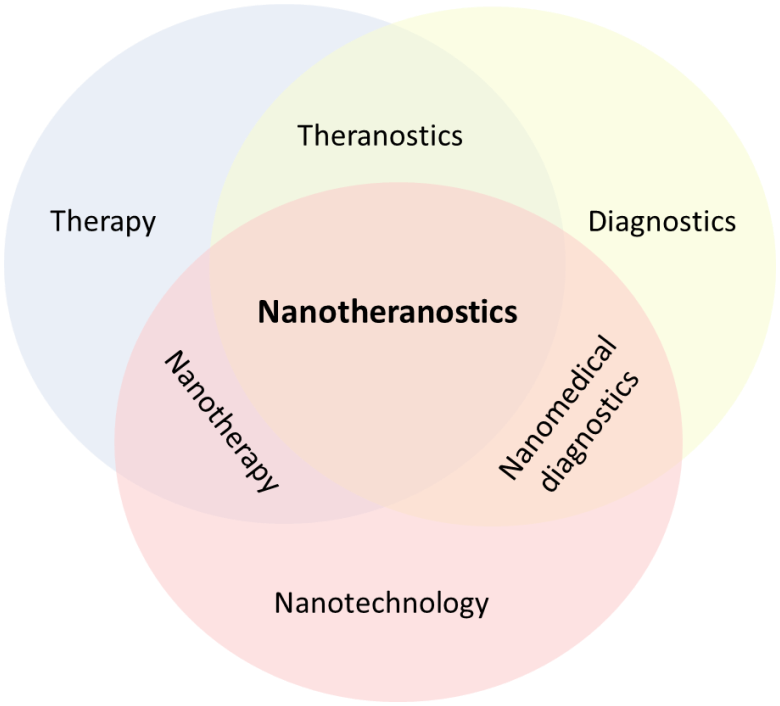

Figure 2.7 | Venn diagram showing the combination of fields that constitute nanotheranostics.

"Theranostics" is a combination of therapy and diagnostics that focuses on patient-centered precise treatment of cancer or infection sites to improve the prognosis

of the patient. A theranostic system couples the therapy with diagnostic information specific for the intended target [112]. Materials that, by having a multiphase structure, can be used for diagnosis and therapy (like our final material) are theranostic materials. Particularly, nanotheranostics is the most common type of theranostics and it utilises nanomaterials as a single platform to deliver both diagnostics and therapy [113–116]. Figure 2.7 shows the main concepts that involve this new field.

There exist nanoplatforms that can deliver imaging and therapeutic functions with higher precision than their bulkier counterparts. Over the last decade, a vast development in this area has been undertaken primarily for characterization of subtypes of cancer cells, identification of the cancer stage, analysis of the patient characteristics through imaging and having a complete solution to find and destroy cancer. Therapy personalisation to each specific case while imaging is one of the keys to each success. Therapy arising from NPs can be generated more generically, e.g. cellular hyperthermia or hypoxia. Then, by functionalising their surface with the right antibody, targeting cancer cells unlocks the potential to a cell by cell treatment.

2.6. Nanoparticles fate

The fate of the NPs in the body is crucial to minimise toxicity and side effects. Hence, NPs clearance is one of the most critical aspects to consider when designing NPs, but also can be a burden since optimising safety sometimes is at expenses of losing useful properties for either diagnosis or therapy. NP excretion and toxicity are highly dependent on many parameters including NP concentration, size, shape, density, hydrophobicity, pH stability, surface charge and surface chemistry [117]. The overall idea is that NPs that have long circulation time in the blood and low organ retention tend to be excreted better and faster [118]. The renal clearance occurs

because the kidney is capable of rapidly removing molecules from the vascular compartment such as the injected NPs and starting a renal clearance for final elimination through urinary excretion. Different strategies can be combined to accomplish prolonged circulation of NPs in blood and target specific clearance pathways.

When the NPs are intravenously administered, they encounter several sequential obstacles hindering efficacious, site-specific delivery to tumours [119]. Firstly, NPs undergo opsonization and subsequent uptake by resident macrophages of the mononuclear phagocyte system, which leads to high NP accumulation in healthy organs, such as the spleen and the liver. Secondly, under normal flow conditions in blood vessels, NP size and geometry influence margination dynamics to vascular walls. Small spherical NPs migrate far from endothelial surfaces in a cell-free layer, which limits both active targeting and accumulation through passive targeting mechanisms. Additionally, high intratumoural pressure in tumours is an important barrier to NP accumulation due to interrupted vasculature, the aggressive nature of cellular growth, fibrosis, a dense extracellular matrix, and impaired lymphatics. Moreover, cellular internalization and endosomal escape are critical barriers, dependent on size and surface functionalisation. Endosomal compartmentalization of internalized NPs is detrimental to cargo, especially to genetic material.

The fate of NP/cell interaction can be divided into particle/cell interaction and NP internalization. The interactions between NPs and cells are usually mediated by the formation of the protein corona on the NP surface when in biological environments, and these interactions are vital to predict the NPs bioactivity [120]. There is experimental evidence of potential membrane damage, DNA cleavage, mitochondrial damage,

frustrated phagocytosis, induction of oxidative stress, and inflammation related to the interaction of NPs with biological processes [121]. Cellular uptake depends at a large extent on the size and shape of the NPs to be internalized. While spherical shape seems the optimal shape to maximise cellular uptake, there is no consensus on the optimal size [122]. The wrapping of NPs is usually accompanied by the deformation of the cell membrane, which is induced by bending and stretching of the membrane [98]. It has been shown that positively charged NPs ranging from 50 nm to 100 nm display higher toxicity and cell uptake, and lower transport efficiency than its negatively charged counterparts [123]. NP hydrophilicity (charge-polarized and capable of hydrogen bonding) usually leads to direct renal excretion, while the hydrophobicity undergoes biotransformation before NP excretion [124].

The NP shape is also an important parameter. Several studies have shown that, during renal excretion, spherical NPs were cleared faster than rod NPs [125,126]. Non-spherical nanostructures can have distinct and unwanted enhanced permeability and retention (EPR) effects due to differences in the in vivo hydrodynamic behaviours such as circulation, transport in blood flow, and extravasation into the tumour. The EPR effect occurs when high–molecular weight nontargeted drugs and prodrugs accumulate in tissues which have increased vascular permeability, such as in sites of inflammation or cancer [127]. Enhanced vascular permeability via angiogenesis is the primary mechanism used by tumours to sustain an adequate supply of nutrients and oxygen for rapid tumour growth, which can lead to high NP uptake. At the same time, tumours display impaired lymphatic drainage, which leads to retention of the permeated NPs. Unfortunately, this effect can also happen non-tumorous inflammations, which will also tend to accumulate more nanoparticles than the rest of the tissues. This can present a high risk for patients that have chronic systemic

inflammatory diseases such as rheumatoid arthritis, systemic lupus erythematosus, multiple sclerosis and many others that are common in elderly patients.

In terms of size dependence, NPs smaller than 5 nm are cleared by glomerular filtration in the kidneys while bigger than 200 nm are cleared by the spleen [109]. A recent study showed that ≤5 nm inhaled Au NPs for 4 h were still present in blood and urine of the volunteers three months after exposure, at levels higher than the initial 24-h period, pointing towards systemic retention and delayed urinary excretion. Lee et al. have reported that particles smaller than 20 nm are cleared more rapidly than larger 100 nm particles [128]. Cho *et al.* [108] showed that 50 nm dye-labelled nonporous silica NPs cleared faster in the urine and bile than its 100 and 200 nm counterparts, and 200 nm NPs have a lower excretion ratio. Therefore, optimal sizes to maximise NP excretion rate and ratio are typically smaller than 50 nm but larger than 5 nm. However, it has been have shown that spherical NPs of 50–100 nm in diameter present maximized tumour accumulation due to the EPR effect and minimized the subsequent clearance [125,126].

However, Au NPs present long-term retention within many organ systems, most notably the liver and spleen. Some studies in mice have found that Au NPs from 20 to 40 nm showed high liver accumulation after several months from intravenous injection [129]. These results raise some concerns about the fate of these NPs used at these sizes, mainly because they are not biodegradable. Nevertheless, one of the most significant limitations of the research data in NP excretion is that most studies are performed in mice and not in humans, which differ on important physiological features such as organ dimensions and barriers.

2.7. Gold nanoparticles

2.7.1. History

AuNPs are finding uses in a wide range of applications. They are very well known in the literature for their excellent biocompatibility, ready bioconjugation and optical properties via plasmons[130]. Even before they were fully understood, AuNPs were used to exploit their optical properties in coloured glass with historical examples such as the Lycurgus Cup. The first person who accidentally found them was Michael Faraday. He described them and reported his particular reduction method of chloroaurate ($AuCl_4^-$) in a water solution by using phosphorus with CS_2 to synthesise them on his lecture at the Royal Society in London on 1857[131]. Almost one century later, in 1951, Turkevich[132] found a robust method to synthesise different sizes of AuNPs and the most relevant parameters that characterise their size and colour. Hence, this is the method by which our composites are based on this work. For colloidal Au (reddish colour), plasmon peaks are observed in the visible region and can, therefore, be excited at optical frequencies (10^{14}–10^{15} Hz). Combining this discovery with the theory developed by Pines and Bohm in 1952 of “plasma oscillations” so-called plasmons, a full branch of knowledge has been developed and made possible to obtain exciting applications in diverse areas such as biomedical imaging, hyperthermia, drug delivery, biosensing, nanoelectronics and energy harvesting.

2.7.2. Morphology and dimensions

Au nanostructures have obtained a remarkable interest in the scientific community due to their unique surface plasmon resonance (SPR) properties. By the exposure to light, the conduction electrons in an Au nanostructure are synchronised

with the electric field to generate collective oscillations at a resonant frequency relative to the lattice of positive ions. The frequencies at which the plasmons resonate are those when light absorption is produced. Some photons excite optical phonons that propagate along the surface. Therefore, the generation of plasmons can be quantified with UV-vis spectrophotometer by analysing the absorption. However, not all the incident light will be absorbed—a fraction of the incoming photons that are scattered in all directions.

One of the most critical aspects of using different shapes and sizes of Au nanostructures is their unique plasmon resonance frequency, i.e. unique maximum absorption in the UV-vis spectra. Monodisperse AuNPs (Figure 2.8.a) with spherical-like shape have their SPR wavelengths from 510 nm to 572 nm for the size from 3 nm diameter to 100 nm diameter, respectively[133]. There is a redshift of increasing sizes. This is one of the reasons why bigger particles are more useful for getting an excellent SERS enhancement, but they become less biocompatible since their toxicity grows. One step beyond is the synthesis of Au nanoshells (AuNSs) which coat other materials to combine their properties (Figure 2.8.g)[133]. These AuNSs are surface plasmon resonant NPs forming a shell that surrounds a nanoscale core. They have many previously studied properties [134–136] by using different cores and thicknesses, different outcomes can be achieved. Also, including internal sub-shells between the core and the external AuNS, exciting new materials can be found with promising functionalities such as robust fluorescence. However, these are not the only Au nanostructures that can be fabricated, a range of typical shapes is displayed in Figure 2.8.

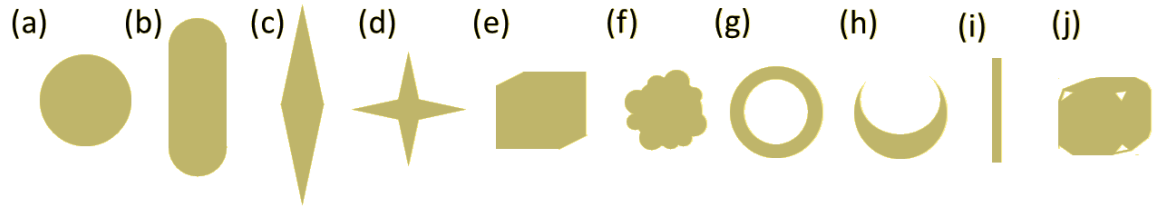

Figure 2.8 | Typical shape of Au nanostructures under transmission electron microscopy imaging: (a) spherical NPs (b) nanorods (c) nanobipyramids (d) nanostars (e) nanocubes (f) nanotruffles (g) nanoshells (h) nanocrescents (i) nanowires (j) nanocages.

For nanorods (Figure 2.8.b), there are 2 modes: transverse mode and longitudinal mode. The transverse mode provides a smaller peak in the UV-vis absorption and is approximately fixed for one specific nanorod diameter for any length. The longitudinal mode displays the strongest peaks, which are lower in energy compared to the transverse mode peaks. Its wavelength depends on both diameter and length. For example, for a diameter of 10 nm and lengths of 34 nm to 51 nm, the transverse mode plasmon resonance is at 508 nm, and the longitudinal mode is from 750 nm to 850 nm, respectively[133]. There is a redshift of increments in both diameter and length. In the case of assembled nanorods, the maximum intensity decreases drastically.

Au nanobipyramids present a similar behaviour to Au nanorods, as shown in Figure 2.8.c. However, in this case, it is not easy to increase the diameter without increasing the length at the same time. For nanobipyramid diameters from 20 nm diameter to 45 nm, the respective longitudinal and transversal mode wavelengths are from 700 nm to 850 nm, and from 506 nm to 517 nm, respectively[133]. There is redshift for bigger sizes one more time.

Au nanostars (Figure 2.8.d) have very similar UV-vis spectra compared with nanobipyramids with slightly redder shifted peaks for the longitudinal mode. Au nanocubes (Figure 2.8.e) show similar shape than AuNPs, but much more limited in terms of wavelengths when increasing size. Once again, assembled nanostructures end in a lack of intensity for the SPR peak. The Au nanotruffles or popcorn-like (Figure 2.8.f) have presented a redshift compared form the original seed. However, it is not clear how its absorption changes since it is an irregular shape that can grow in different ways. In a general approach, the bigger popcorns, the redder shift. For Au nanoshells or hollowed nanospheres (Figure 2.8.g), the UV-vis spectra are different compared with its counterpart. This structure shows a blue-shifted for thicker shells while keeping constant the core diameter. However, if the thickness is fixed and the core grows, then the redshift effect appears again. In the case of nanocrescents (Figure 2.8.h), the blue shift also occurs by growing the thickness. However, this structure requires considering not only the diameter of both hollow and NP but also the distance between both centres. Nanowires (Figure 2.8.i) behaves as nanorods with minimal diameter. The hollowed Au nanocages (Figure 2.8.j) structure shows a similar UV-vis absorption compared to the Au NPs, but much redder shifted for similar sizes.

When the Au NPs are chemically synthesised in a solution phase, the shape tends to be spherical-like that is the configuration in which the smallest surface area is achieved. However, as reported by many researchers, the shape is never wholly spherical. For the most accurate spherical shape, a pH 7.0 is highly recommended at room temperature or temperatures over 80°C depending on the specific method applied. Usually, the synthesis is assisted by ultrasonication to ensure a good redispersion and final monodispersed AuNPs. To obtain Au nanorods, it is necessary to use a more acidic pH with values that range from 2.5 to 4.8. Moreover, for more

unusual shapes such as hollowed microspheres, nanostars, nanowires or nanocrescents require more complex procedures, including customised working temperatures or customised surfactants rather than deionised water. Moreover, in all the previous cases, the introduction of polymers in the surfactant can substantially improve the size, stability, and distribution of particles.

In contrast, AuNPs can also be synthesised by laser ablation. This technique is based on extracting material from a surface (generally solid, but also liquid) by irradiating it with a laser beam. Through this method, the generation of AuNPs with several useful properties such as high purity, easily functionalisable surface and complex structure is achieved. The kind of structures achieved by laser ablation includes doped nanocrystals, core−shells nanocomposites, hollow microspheres, nanotruffles, and nanocrescents. Also, changes between structures such as from nanorods to nanospheres or from nanospheres to nanocrescents are possible, by laser ablation. However, obtaining more unusual shapes such as nanostars have yet to be found by the laser ablation technique. This sets a limitation on the possibilities that this technique offers.

A third method would be metal deposition on previously shaped surfaces. This method has been extensively used to fabricate a wide range of Au nanostructures from nanowires to spherical Au NPs. By combining the metal deposition with some UV irradiation, it is possible to have high control of the final morphology and atomic structure, achieving even single crystallite based AuNPs. This technique is usually called UV-induced photochemical synthesis of Au. Other methods very similar to this one are photothermal reduction and lithography through which an easy and fast preparation is obtained but lacking shape control.

One of the main applications of AuNPs was discovered in 1974. SERS was first observed by Fleischmann et al. when measuring the Raman spectra of pyridine adsorbed at a silver electrode [137]. The substantial enhancement in the signal was firstly estimated but not linked to plasmonic excitations in 1977 [137]. After then, many other researchers tried to understand the reason for such signal enhancement. Soon Au became a better choice for biomedical applications, due to its better biocompatibility than silver.

2.7.3. Thiol group

Thiols (R-SH) are compounds which contain a carbon-bonded sulfhydryl (SH) group. Its structure is analogous to alcohol by exchanging the oxygen atom with sulphur[138]. And therefore, its name is the combination of "thion", that means sulphur; and "alcohol". The -SH functional group designates both thiol and sulfhydryl groups. The term thiol is sometimes substituted by the term mercaptan that was introduced in 1832 by William C. Zeise.

The primary applicability of this functional group is their strong electronegativity, similarly, as explained by the amine group. Hence, metals such as Au are good candidates to act as donors and fulfils the two remaining unfilled orbitals which create a very strong covalent bond. Some thiols are more complex than others and can have, for instance, a bond with another sulphur that binds with Au. This also allows a better transference of vibrational energy across the Au-S-R bond chain[139]. Different organic substituents can be included with desirable properties such as benzene (aromatic group). This type of organic structure provides a unique Raman signature or fingerprint and very strong peaks in the Raman spectra that can be used to identify the sample. Indeed, there are more advanced structures with several rings interconnected or

disconnected, rings with additional carbon bonds and a different number of carbon atoms contained in the rings (five or six).

2.7.4. Toxicity

One crucial aspect in biomedicine is the toxicity, and therefore, there is a limited number of options to form the nanocomposites that are injected inside the human body[140]. Some of the most common NPs used for biomedical approaches are noble metals such as AuNPs [141] or silver NPs (AgNPs) [142], SiO_2, polymers and transition metal oxides [33]. There is not enough research to determine the cytotoxicity of AuNPs or AgNPs, and to conclude which one is the better candidate in each scenario; both are exciting candidates due to their unique antibacterial activities [141–145]. However, there are indications of higher induced cell necrosis by AgNPs independently on the size and surface charge while AuNPs have only shown specific toxicological effects for small or large sizes, high concentration and high surface charge [146]. Cytotoxicity is the ability of certain chemicals to kill or destroy healthy living cells, i.e. toxicity for cells. One of the most desirable scenarios is that after the injected NPs end their function, a renal excretion process occurs without producing cytotoxicity during the removal process. This is possible because the kidney is capable of rapidly removing molecules from the vascular compartment such as the injected NPs and starting a renal clearance for final elimination through urinary excretion. One of the biggest limitations of the research results in NP excretion is that most of the tests until now have been implemented in mice. Therefore the conclusions of these non-human studies do not provide any certainty of useful, practical or translatable to the clinical outcome for improving the understanding of human toxicology. Dimensions and blood chemical composition in humans are substantially different from mice; hence more studies in humans need to be carried out for a realistic, ethical, and proper analysis.

The recent literature contains conflicting data regarding the cytotoxicity of Au NPs for specific sizes and backgrounds. Several studies have shown that spherical Au NPs with a large number of surface functionalizations are generally not cytotoxic to human cells even when they are incorporated intracellularly in the cells [147,148]; although some NP sizes in specific cell types have shown notable cytotoxicity such as 1.4 nm diameter Au_{55} clusters [149]. Very small NPs with sizes < 2 nm have caused rapid cell death by necrosis in 12 h or forced the programmed cell death (apoptosis) while size > 15 nm is not cytotoxic [150]. The limit of the smallest convenient size for Au NPs is 5 nm not to produce any toxicity and 30 nm not to be endocytosed by cells, i.e. absorbed into the cell. However, different concentrations of particles have been used, and non-conclusive results have been found yet. All these considerations depend on the type of procedure followed to deliver the AuNPs. For a local injection, sizes bigger than 5 nm could be a good candidate while a long delivery anything below 12 nm can constitute a significant risk in terms of cytotoxicity. Also, NPs smaller than 5 nm are cleared by glomerular filtration in the kidneys while bigger than 200 nm are cleared by the spleen [109]. It has been found that smaller sizes tend to be excreted faster (a couple of hours for minimal diameters) than bigger sizes (up to a week for extra-large diameters).

2.8. Silica nanoparticles

2.8.1. History

Stöber *et al.* discovered an effective method to synthesise monodispersed SiO_2 particles with a tuneable size in 1968, via hydrolysis of alkyl silicates and subsequent condensations of silicic acid in a mixture of alcohol and water using ammonia as a catalyst [151]. The particle sizes obtained in that suspension ranged from less than 50

nm to 2 μm in diameter. This original work has since been improved by others [152–156], performed the synthesis of colloidal spherical SiO_2 NPs via polymerization, nucleation, and growth. All current sol-gel methods to synthesise highly stable colloidal SiO_2 NPs are mainly or partially derived from this method as described in Figure 2.9. Further advances were made with the discovery of mesoporous SiO_2 NPs (MSN), which allowed the development of the concept of MSN as drug delivery vehicles in cancer therapy [157–159]. MSNs are mesopores of SiO_2 with pore sizes from 2 to 50 nm that display favourable physicochemical properties for high biocompatibility [160]. The extension of the Stöber process to nanoshells [161–163] is almost immediate and was previously achieved by following a different route [164]. In the hydrolysis and condensation, there are precursor species and the necessary supersaturation for the formation of SiO_2 particles over the former core to generate the shell.

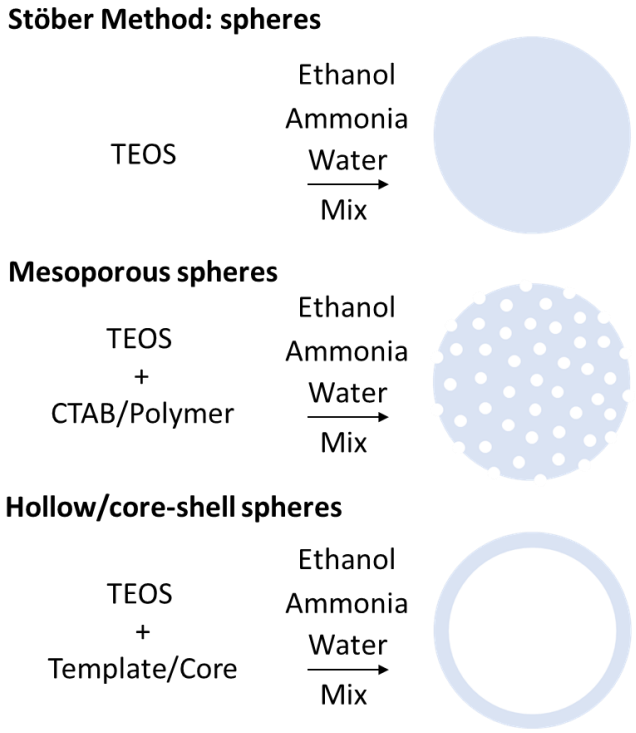

Figure 2.9 | Common techniques in SiO_2 NP synthesis.

2.8.2. Morphology and dimensions

SiO_2 NPs are being considered for several biomedical applications due to their biocompatibility, low toxicity, and scalable synthetic availability. It is possible to precisely control SiO_2 particle size, porosity, crystallinity, and shape to tune the nanostructure for diverse applications. Furthermore, the many possible surface modifications of SiO_2 NPs allow precise control of surface chemistry to modulate drug or chemical loading, NP dispersion, blood circulation, and site-specific targeting. The ability to combine these properties makes SiO_2 NPs a desirable platform for biomedical imaging, assaying, therapeutic delivery, monitoring, and ablative therapies. With the use of various dopants, surface group modifications, and assembly techniques, it is possible to create multimodal NPs with theranostic applications, such as including an imaging component along with a therapeutic payload or ablative component within the particle.

The most common type of SiO_2 NPs are spherical NPs, but there are other shapes frequently used in the literature such as SiO_2 nanoshells or hollow NPs. The mechanism of growing SiO_2 shells over iron oxide cores is based on the physicochemical mechanism of the silane agent on the surface of the IONP according to Arkles [165] and refined by De Palma *et al*. [166]. MSN nanocarriers are prepared in a variety of sizes and shapes, including nanohelices, nanotubes, nanozigzags, and nanoribbons aiming for tunable optical, electrical, and mechanical along with pH sensitivity [167,168]. Several synthesis techniques have been developed which produce particles with a narrow range of sizes and nearly uniform composition. Figure 2.9 shows the techniques that are commonly used to synthesise SiO_2 NPs. Most of the synthetic techniques employ sol-gel processing at 25 °C with careful control of the reactant to solvent ratios or the use of templates to control particles sizes.

2.8.3. Amine surface functionalisation

Amines are organic compounds (hydrocarbons) and functional groups that are made of one or more atoms of nitrogen (N) with a lone electron pair in each. The molecular structure resembles ammonia (NH_3) where one, two or three alkyl or aryl groups replace one, two or three hydrogen atoms, respectively. There are basically 3 types of functional groups: primary amines (RNH_2) which have an alkyl or aromatic group (R) and a N attached to two H; secondary amines (R_2NH) that contain a pair of alkyl or aromatic groups (R_2) and a N attached to a H; and the tertiary amines (R_3N) have three alkyl or aromatic groups (R_3) attached to a N. There are also other so-called cyclic amine groups that are any of the previous types bonding with some aromatic group that contains carbon rings such as benzene. Hence, surface amine functionalisation is the addition of amine groups on the surface for a subsequent effect related to this functional group. For our specific context, the importance is about the strong ligand generated between Au and N. This happens since Au is a noble metal, so it can donate electrons, and N has one of the highest electronegativity. Therefore, N will incorporate three electrons from Au to be more stable by filling its d orbitals. Only if there is some process that transfers higher energy than the one to fill these orbitals, then the bond will break.

In SiO_2 platforms, APTES is the most common option for Au seeding. The critical aspect of this functionalization is the NH_2 ending on top that needs one electron to become energetically stable. At the same time, the AuNPs have a tendency to share their electrons, forming a covalent bond [169]. These NH_2 ligands can also react with Au after breaking it in two parts by heating: first releasing H_2 when the H atoms absorb higher energy than the bond; and, in the other side, a firm bond is generated between the N and the Au atoms that are close enough. This fact makes it possible to attach

Au nanoseeds and subsequently grow Au on top stably and homogeneously. Immobilization of Au NPs has received interest in biomedical applications during the last decades. To ensure the AuNPs are homogeneously distributed on top, a redispersion of Au NPs and SiO_2 NPs or nanoshells need to be done during the entire process. Controlling the immobilization step, especially NPs dispersion and coverage, is an essential issue for all of these communities. Moreover, APTES can be attached easily to any hydroxyl group (-OH) on top of the surface, some examples of easy hydroxyl groups functionalization materials are SiO_2 or magnetite (Fe_3O_4).

2.8.4. Toxicity and clinical approval

SiO_2 is generally accepted as a safe material by the United States Food and Drug Administration (FDA) [170]. Cytotoxicity of SiO_2 NPs has been found closely related to multiple factors including their size, dose, the cell type in the study, treatment time, surface area, and structural discrimination [171]. It was found that SiO_2 particles at low dose present small retention, which is dependent on the particle size and organ [172]. In terms of toxicology, there are many reports for various formulations showing that SiO_2 NPs are generally well tolerated with a large maximum tolerated dose. However, the synthetic method profoundly influences the cytotoxicity. Fumed/pyrolytic SiO_2 NPs heat-treated between 1,200 and 1,400 °C show much higher cytotoxic behaviour than the Stöber counterparts[173].

Cornell Dots or C Dots are inorganic SiO_2 NPs that were developed at Cornell University as a diagnostic and therapeutic tool in cancer treatment [174]. These SiO_2 NPs have undergone FDA-approved trials at the Memorial Sloan Kettering Cancer Center (MSKCC) since 2011 for imaging detection of HER2-overexpressing breast

cancer [175]. They have lately been working with antibody functionalization to help to target a renal clearance.

2.9. Iron oxide nanoparticles

2.9.1. History

Iron oxides are commonly found in nature as rust and can be easily synthesised in the laboratory. This magnetic material has been used for centuries [176]. IONPs as a contrast agent for in vitro diagnostics has been produced and used for a wide diverse range of applications for nearly half a century [177–179].

Eight iron oxides are known [180]. In the last decades, increased investigations with diverse types of IONPs have been performed, particularly Fe_3O_4 (magnetite, $Fe^{II}Fe^{III}_2O_4$, ferrimagnetic, superparamagnetic when the size is less than 15 nm), α-Fe_2O_3 (hematite, weakly ferromagnetic or antiferromagnetic), γ-Fe_2O_3 (maghemite, ferrimagnetic), FeO (wüstite, antiferromagnetic), ε-Fe_2O_3 and β-Fe_2O_3) [181], among which magnetite and maghemite are the most promising and popular candidates due to their biocompatibility, strong magnetic magnetization and polymorphism involving temperature-induced phase transition [178]. Each of these iron oxides has unique biochemical, magnetic, catalytic, and other properties which provide suitability for specific technical and biomedical applications. In cancer research, IONPs have been used for two main applications: magnetic hyperthermia [103,104,182–186] and MRI [187–195], both owing to their magnetic properties.

The synthesis of IONPs has been extensively studied in the last decades, obtaining many different routes for efficient synthesis approaches to produce the shape-controlled, stable, biocompatible, and monodispersed IONPs. The most

common methods including co-precipitation, thermal decomposition, hydrothermal synthesis, microemulsion and sonochemical synthesis to obtain high quality of IONPs. The most conventional method for obtaining Fe_3O_4 or γ-Fe_2O_3 is by co-precipitation. In 1981, Massart reported the synthesis of magnetic NPs in acid and alkaline media [196], which were IONPs. This result triggered different modified versions of the procedure that are widely used today.

2.9.2. Morphology and dimensions

Different sizes display different magnetic properties. There is a transition from the single magnetic moment (one spin) to single magnetic domain (several spins that behave like one) to multi magnetic domain (several single magnetic domains). These transitions confirm the growth of sizes of the NP, which also leads to a transition from superparamagnetic to ferromagnetic or ferrimagnetic behaviour. Multi domains occur in highly ferromagnetic or ferrimagnetic samples with large NP diameters. When the diameter is small enough, the magnetic behaviour corresponds to a single domain, which present superparamagnetism.

Strongly ferrimagnetic samples usually aggregate, which can have two main side effects. On the one hand, the hydrodynamic radius of these NPs is vast and therefore not suitable for excretion once injected in the body. On the other hand, aggregated ferrimagnetic NPs have shown drastically decreased hyperthermia capabilities [197]. These NPs also are not suitable for core-shell structures since a potential multicore structure might happen, which would undervalue the potential not only in hyperthermia capabilities but also as an MRI contrast agent. These significant issues have prompted many efforts in finding suitable substitutes that can be easily eliminated from the body after being used.

Moreover, the best Fe_3O_4 sizes for MRI are the ultra-small magnetic IONPs (3-4 nm). This has been shown to have longer dwell time, and therefore, can activate macrophages. Macrophage phagocytosis leads to non-excretion and therefore, high toxicity. For this reason, seeking for a more reliable imaging method than MRI by using different composite nanostructures such as SERS in AuNPs is in high demand.

2.9.3. Toxicity and clinical approval

Currently, ferumoxytol is the only FDA-approved SPION and is used for the treatment of iron-deficiency anaemia in patients with chronic kidney disease. However, ferumoxytol is also being used off-label as an MRI angiography agent in patients with renal failure who cannot be given gadolinium, and in clinical trials for the characterization and mapping of metastatic lymph nodes and hepatic masses. The advantages of ferumoxytol include its size relative to other SPION formulations (<40 nm) and its long circulating half-life (~15 h).

MagForce received FDA investigational device exemption approval to conduct a clinical trial with NanoTherm® therapy as a focal ablation treatment for intermediate-risk prostate cancer.

2.10. Tungsten oxide

The combination of materials that possess different properties (such as metals, semiconductors, magnetic materials, polymers and biomolecules) in specific size, morphological and spatial configurations in a single nanoscale object has led to a revolution in materials and chemistry, creating an enormous impact in physical, biological and medical fields.

Metal oxides are crucial materials for the development of many advanced functional materials and smart devices due to their multiple potential functionalizations and dopings. Tungsten oxides (WOx) are unique materials that have been rigorously studied for their chromism, photocatalysis, and sensing capabilities. However, they exhibit further important properties and functionalities that have received relatively little attention in the past[198].

WO_x is a transition metal oxide with a wide range of applications. Interest in WO_x can be dated back to the 17th century when the properties of $LiWO_3$ and the techniques for the synthesis of WO_3 and $NaWO_3$ were first studied [199]. More recently, renewed research interest in WO_x was sparked by the discovery of its electrochromic (EC) effect [200,201]. Examples of WO_3 based fibre-optic sensors can also be found in a report by Ito *et al.* [202]. Based on the principles of H_2 sensing, WO_x was also explored in biological sensing [199]. Recently some authors have been working with infrared lasers in tungsten oxide nanostructures to the unlock electrochromic mechanism in this regime [11,199,203–209]. Therefore, WO_x to be a promising candidate for sensing applications, such as in cancer imaging.

2.10.1. Electrochromism

The first electrochemical reduction of a solid, WO_3, that displayed a colour change mediated by hydrogen (H) ions was reported by Kobosew and Nekrassow in 1930 [210]. When WO_3 was coated on an electrode, immersed in aqueous acid and possibly the electrode substrate was inert (there is no explicit record of this but it seems to be the most likely case), colouration occurred. They described the colouration reaction by the Eq. (2.9.1).

$$WO_3 + x(H^+ + e^-) \rightarrow H_xWO_3 \quad (2.10.1)$$

where x is the insertion coefficient that takes values from 0 to 0.03. This colour change from the oxidised form of WO_3 in a very pale yellow to its reduced form in an intense blue is due to the formation of H_xWO_3. Instead of introducing H in the Eq., another electro-inactive positive ion can be used instead. This ion is usually designated as a counter ion (positively charge, cation) and its main function is to preserve or maximise electroneutrality within the solid oxide film[201].

Electrochromism with arbitrary ion species in thin films of WO_3 was found in 1969 by Deb, and then the crusade for fabricating electrochromic devices started. During the following decades, several companies developed commercial products to exploit this effect such as Gentex Corporation's self-darkening rear-view mirrors for cars, adjustable opacity windows at the Boeing's 787 Dreamliner, Gyricon electrochromic paper developed by Xerox for electronic books, NTera's coloured electrochromic paper-quality displays and Skugga's electrical sunglasses with adjustable tint. Nowadays, the leading industrial interest in these technologies is focused on large-scale screens that tolerate living conditions for buildings. The state-of-the-art in this research field is more focused on novel applications such as self-powered electrochromic windows for smart management of the optical transmission of the visible and near-infrared in solar cells harvesting.

Electrochromic materials display a reversible and persistent change of visible optical properties (colour, transparency) by using a small electric field that causes electrochemical redox reactions. This means creating different visible light absorption bands by switching to different redox states via different voltages applied. An electroactive species in a redox reaction can undergo an electron uptake for reduction

or electron release for oxidation at an electrode. An electroactive material may be an atom, ion, molecule or radical, in some cases multi-bonded in a solid film. The electroactive material is usually a uniform film on an electrode submerged in a solution or a material embedded in a matrix that is in contact with an electrode substrate for an effective electron transfer. In case it is a solution, it needs to be close enough to the electrode substrate and provide the necessary conditions to achieve the activation energy for the electron transfer. Also, the electroactive material can be a solid or being dispersed within a solid matrix. In this matrix, the part of the electrochromic component that is physically in contact with the electrode substrate undergoes a redox reaction much faster than the rest of the component. The electrode is usually defined by the oxidised form, the reduced form and the metallic or quasi-metallic conductor. An electrode is a metallic conductor that in electrochromism is usually an adequately conductive semiconductor usually deposited as a thin film on top of a glass. This conductive glass surface is called the optically transparent conductor. In between two of these, the reversible change of colour and opacity occurs. This shift in optical properties happens when the inflow of charge-balancing electrons enters the electrochromic material and changes the valency of its atoms. The ion flow is in many cases held by an electrolyte that promotes the charge exchange. An electrolyte is a substance that dissolved in a polar solvent, such as water, yields ions, and therefore converts the solution into electrically conducting.

When an atom or molecule causes the colour of a compound, this part is called a chromophore. The mixture of all the visible colours results in white light. Only when some chromophore absorbs some specific wavelength in the visible region, its complementary colour is displayed as the dominant. For instance, when some materials display a reflected red colour under white light illumination such as some

AuNPs; this means that the maximum absorption is actually at the wavelength that corresponds approximately to green (532 nm). The absorption of light is produced by the electrons in the atoms that comprise the material, whose energy levels are quantised. Therefore, the energy absorbed by the atoms is invested in electrons jumping to more energetic levels. The original stable distribution is called the ground state, and the promoted levels are called excited states. The wavelength of maximum light absorption, λ, is governed by the energy gap, E, between these states and follow the Planck's Law,

$$E = h\nu = \frac{hc}{\lambda} \tag{2.10.2}$$

Where h is the Planck's constant, c is the speed of the light, and ν is the frequency. The change in the absorption spectra in an electrochromic material after a redox reaction is not visible if the optical absorptions of the two redox states are in the UV or NIR regions. So the traditional definition of electrochromism only includes changes in the absorption for visible spectra, but this has been changing in recent years towards exploring infrared light interactions [199,203–209].

In contrast to the above definition, there is an alternative approach for the term electrochromism. When some polarizable molecules suffer a molecular Stark effect in which their UV-vis bands show a spectroscopic shift in the presence of a strong electric field, these compounds are also called electrochromic [211]s.

2.11. Multifunctional nanoparticles

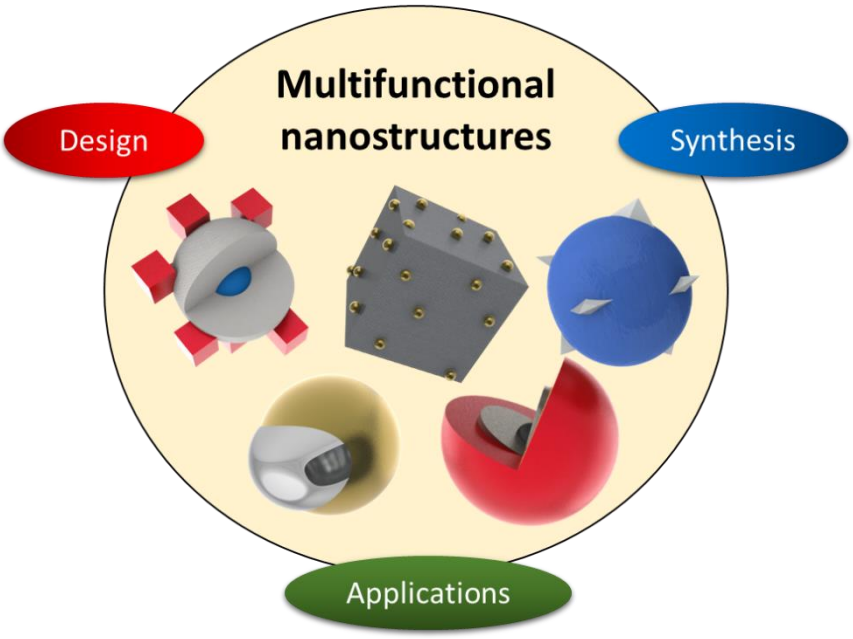

Figure 2.10 | Diagram of the main aspects of multifunctional materials.

The development of multifunctional nanostructures is a challenging process due to the need for chemical and molecular stability from the synthesis until the multiphase activation. The multifunctional NPs have developed a degree of maturity in some areas where there was an urgent need of finding new alternatives such as bionanotechnology that involves medical imaging, drug delivery and illness therapy. In nanooncology, due to the small size, surface functionalizations, variable shape and tuneable porosity of these nanostructures, they can stably bind, absorb, and carry nanometric and subnanometric biological objects such as molecule drugs, DNA (deoxyribonucleic acid), RNA (ribonucleic acid), proteins, and organic dyes which can be used for cancer linking and medical imaging techniques.

There are three main ideas behind the concept of multifunctional nanomaterial: design, synthesis and applications (see Figure 2.10). There is no one single and unique order to start, but typically, deciding the targeted application and designing the

nanomaterial are considered first. Then, the fabrication process begins. However, multifunctional NPs are used for many different applications, for instance, biomedicine, sensors, catalysis, energy harvesting and water treatment. Sometimes, multifunctional NPs can find more approaches to their usability than the previously expected and targeted. Also, the design is in many cases modified as well to analyse possible improvements.

2.12. Magnetic heating

Substantial hysteresis losses occur in large magnetic IONPs which possess multiple magnetic domains while subjected to external alternating magnetic fields (AMFs). Below approximately 128 nm, the number of magnetic domains is approximately reduced to one, single magnetic domain [212]. When reached, the NPs present a superparamagnetic behaviour. Magnetic field heating of small IONPs is typically accomplished by either Néel relaxation, Brownian motion, or perhaps, particle-particle interaction in super-paramagnetic NPs at frequencies between 100 and 300 kHz [213]. The precise mechanism is still controversial at this point, but it is understood that pure superparamagnetic NPs (below 30 nm) tend to relax through Néel relaxation, ferrimagnetic NPs (close to 100 nm) through Brown relaxation and materials presenting a hybrid behaviour may present a combination of these, and perhaps other, mechanisms [105,214]. In all cases, the heating field is highly local, and effective treatment depends on clustering and the spatial distribution of particles in strategically advantageous locations.

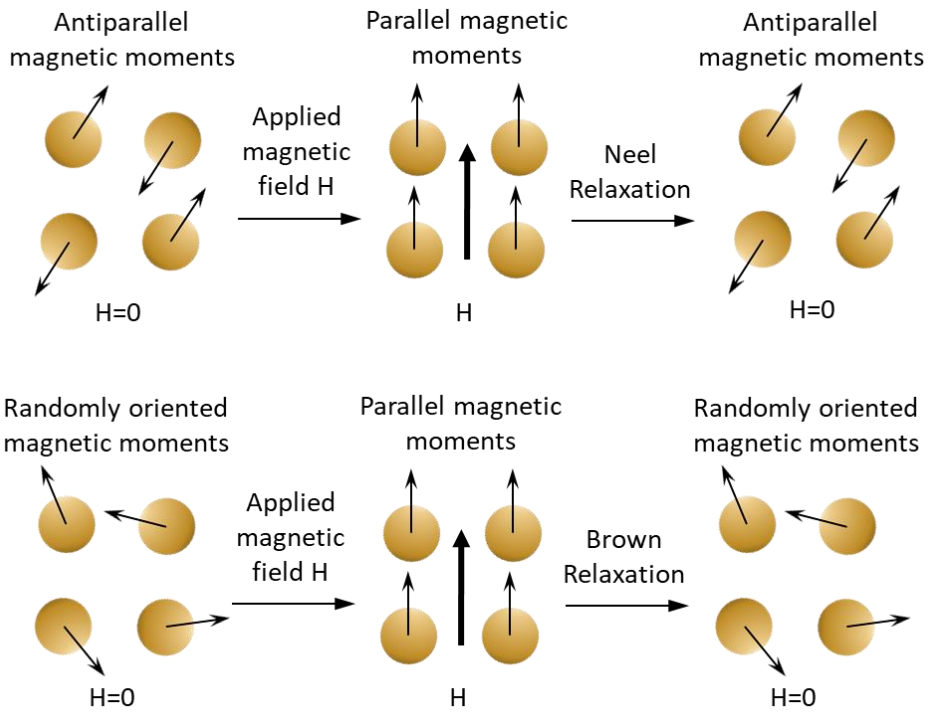

Figure 2.11 | Comparison between Neel and Brownian relaxations for single domain magnetic moment networks. The Neel relaxation diagram is based on the Nobel lecture of Neel [215].

Brownian relaxation occurs when the NP and the magnetic moment rotate together. This results in a frictional heat generated from the physical rotation of particles within a supporting medium when the particles attempt to realign themselves with the changing magnetic field [216]. On the other hand, Néel relaxation occurs when the magnetic moment rapidly rotates with respect to the crystal when exposed to AMF. The rapid realignment is opposed by the particle's crystalline structure, resulting in heat generation (see Figure 2.11). The type of behaviour can be extracted from the hysteresis loop. When the hysteresis loop has linear transitions, this is indicative of a Brown relaxation. Neel relaxation typically leads to curved profiles that intersect with the x-axis perpendicularly. The complexity arises when none of these behaviours is

dominating the overall magnetic behaviour, but a mixture of them or even other more complex behaviours.

The temperature profile over time will be dependent on the area formed by the hysteresis loop. Larger areas will increase the magnetic material temperature faster. The loop requires to correctly completed to maximise its heating performance, which implies reaching the saturation magnetization of the sample. Of course, to perform effective and safe hyperthermia, the most essential feature is the heat transferred to the cells. When working with materials that have layers on top of the magnetic component, this result is much more complex to understand, particularly at the nanoscale.

2.12.1. Magnetic hyperthermia

The oldest written record on the use of increased temperatures in cancer treatment was found in the Edwin Smith surgical Egyptian papyrus, dated around 3,000 BC [217]. Hippocrates (460–370 BC) introduced a hyperthermia method in one of his aphorisms. In the 19th and 20th centuries, fever therapy has been used as a method to increase temperatures, while other investigators in recent times started to apply radiofrequency techniques [218]. Worldwide interest in hyperthermia research was initiated by the first international congress on hyperthermia oncology in Washington in 1975. In the first decade, there was an exponential increase in the number of papers and participants at meetings. Later, it slowed down due to disappointing clinical results from some of the first randomised trials. Nowadays, there is a renewed interest thanks to successful randomised studies that show improvements in hyperthermia treatment outcomes [101,219,220].

Background

Hyperthermia therapy for cancer treatment seeks to destroy tumours through heating alone or combined with other therapies at elevated temperatures in the range of 41.8-48 °C. Generally, there is no difference between hyperthermia sensitivity of normal and tumour cells, except for haematological malignancies. However, selective tumour cell killing effect is achieved at temperatures in the range of 40-44 °C, which is related to structural differences between normal and tumour physiology. For instance, in solid tumours, the vasculature is chaotic, which leads to hypoxic and low pH regions [218,221] that are not found in healthy tissues. These environmental factors make cancer cells more sensitive to hyperthermia which means that this method is a promising approach to treat cancer at the cellular level.

Various forms of cell death, including apoptosis and necrosis, occur depending on temperature and heating time. At temperatures above 42.5-43 °C, the exposure time can be halved with each 1 °C temperature increase to achieve the same number of cell deaths [222]. Most normal tissues are undamaged by treatment for 1 h at a temperature of up to 44 °C [223]; only nervous tissue appears more sensitive. For the central nervous tissue, irreversible damage was found after treatment at 42-42.5 °C for longer than 40–60 min [224]. Treatment of peripheral nervous tissue for >30 min at 44 °C, or an equivalent 'dose', results in temporary functional loss, which recovers within 4 weeks [225]. The primary mechanism for cell death is probably protein denaturation, observed at temperatures >40 °C, which leads to, among other things, alterations in multimolecular structures like cytoskeleton and membranes, and changes in enzyme complexes for DNA synthesis and repair [226].

Magnetic fluid hyperthermia has been intensively investigated since Jordan *et al*. [182] reported in 1993 on the potential applications of colloidal subdomain ferrite

particle suspensions (“magnetic fluids”) subjected to an alternating magnetic for hyperthermia. Magnetic NPs have been under experimental investigation in recent years to provide a favourable therapeutic ratio for local hyperthermia; however, the number of practical numerical models that can be used to study the underlying mechanisms is still limited. Magnetite and maghemite NPs have been used successfully to localise tumour heating in vitro and in vivo [102,227–234].

2.13. Magnetic resonance imaging

2.13.1. Basics

MRI is a non-invasive medical diagnostic technique that uses alternating magnetic fields to create radiofrequency (RF) pulses that interact with nuclei with magnetic nuclear spin such as ^{1}H to obtain multiple cross-sectional 2D RF signals in the Fourier domain that can be transformed into a 3D image with high contrast between specific tissues and materials. A big part of this technique success lies in the avoidance of exposure to potentially harmful ionising radiation as in other medical imaging techniques such as CT and PET.

All atomic nuclei consist of protons and neutrons, with a net positive charge. Specific atomic nuclei, such as the hydrogen nucleus (^{1}H), sodium nucleus (^{23}Na) or phosphorus nucleus (^{31}P), possess a property known as “spin”, dependent on the number of protons and neutrons. This can be conceived as the nucleus spinning around its own axis, although this is a mathematical analogy. If the number of neutrons and the number of protons are both even, then the nucleus has no net spin. Otherwise, there is a net nuclear spin that can be an integer or half-integer.

Application of a strong, external magnetic field (B_0) aligns the nuclear spin either in parallel with or perpendicular to the external field. A liquid solution containing many nuclear spins, placed within the B_0 field, will contain nuclear spins in one of two energy states: a low-energy state (oriented parallel to the magnetic field) or a high-energy state (orientated perpendicular to the magnetic field direction). The nucleus has an angular momentum similar to a tiny magnet due to its rotation, so it will precess around the B_0 trying to align with or against the field. The nucleus is then bombarded with a perpendicular radiofrequency (RF) field usually at $10^{-5}B_0$ intensity and at certain resonant frequencies, the proton spins flip to the high energy state. When the RF energy is turned off, the new high energy excited nucleus may revert to its low energy spin state, producing an RF signal in the process called relaxation. The resonant frequency at which this happens is called the Larmor frequency (ξ) and is proportional to the field strength:

$$\xi = B_0 \times \gamma \qquad (2.13.1)$$

where γ is the "gyromagnetic constant" of the material. A typical field strength B_0 used in MRI is 1.5 Tesla. At this field strength, the Larmor frequencies ξ for Hydrogen and Carbon 13 (the atoms most relevant in medical imaging) are 63.9 MHz and 16.1 MHz, respectively. Probing with different frequencies of RF energy enables us to build a spectrum of what is in the sample.

There are two major relaxation processes: proton spin-lattice or longitudinal (T1) relaxation and proton spin-spin or transverse (T2) relaxation [235]. Shortening T1 and T2 increases the corresponding relaxation rates, 1/T1 and 1/T2, producing hyperintense and hypointense signals respectively in shorter times. Moreover, the signal-to-noise ratio can be improved with the acquisition of many measurements [236].

Background

T1, called the spin-lattice relaxation time, relates to how fast the magnetization parallel to the static magnetic field recovers after a perturbation is applied to the system. Protons that relax rapidly (short T1) recover full magnetization along the longitudinal axis quickly and produce high signal intensities. For protons that relax more slowly (long T1), full magnetization along the longitudinal axis is not recovered before subsequent RF pulses, and so they inherently produce a lower intensity signal.

The usual inversion recovery sequence begins with a 180°-inverting pulse, which reverses the longitudinal magnetization (M_z) for all tissues. The repetition time (TR) is the amount of time between successive pulse sequences applied to the same slice, from the start of one RF sequence at 180° until the next sequence. The inversion time is period from the start of one RF sequence at 180° inverting pulse until the 90° pulse. During the inversion time (TI) interval, M_z increases via T1-relaxation seeking to restore its equilibrium alignment in the z-axis. A spin-echo (or more commonly a fast spin-echo) sequence then generates a signal based on the longitudinal magnetization of each tissue at time TI. Time to echo (TE) is the time between the delivery of the RF pulse and the receipt of the echo signal.

T1 is calculated by using the following well-known formula for the longitudinal signal amplitude is proportional to the longitudinal magnetization derived in the literature [237]:

$$S = S_0\left(1 - 2e^{-\frac{TI}{T1}} + e^{-\frac{TR}{T1}}\right) \qquad (2.13.2)$$

where S is the MRI signal amplitude, and S_0 is the the MRI gnal amplitude at t=0. Where This formula is proportional to the longitudinal magnetization.

On the other hand, T2 relates to how rapidly the magnetization in the plane perpendicular to the static magnetic field loses coherence. During an RF pulse, proton

nuclei spin in phase with each other, whereas after the pulse, the magnetic fields of all the nuclei interact with each other, and energy is exchanged between them. Consequently, the nuclei lose their phase coherence and tend to spin in a random fashion. Because T2 decay is the result of the exchange of energy between spinning protons, it is referred to as spin–spin relaxation. A long T2 happens when the signal decay slowly. Therefore, substances with long T2 have stronger signals and appear brighter than substances with short T2.

T2 is calculated with the following well-known formula for the transversal signal amplitude [238]:

$$S = S_0 e^{-\frac{TE}{T2}} \tag{2.13.3}$$

Longitudinal and transverse relaxation processes are executed independently and simultaneously, although T2 is usually much shorter than T1, and this difference allows tissues to be differentiated.

The stronger the magnetic field, the higher the signal-to-noise ratio, which means the body can be imaged either at higher resolution, or at the same resolution, but faster. At 3 T, MRI machines can resolve details of the brain as small as 1 mm. That resolution can be as subtle as 0.5 mm in a 7-T machine. The nature of the image contrast is based on relative contributions from different tissues.

Specific Absorption Rate (SAR) is a measure of the rate at which energy is absorbed by the human body when exposed to a radio frequency (RF) electromagnetic field. Unit of SAR: watts per kilogram (W/kg). It can also refer to absorption of other forms of energy by tissue, including ultrasound. Radiofrequency pulses used in MR deposit RF power in tissue, which can be described by the SAR:

$$\mathrm{SAR} = \frac{\sigma\left|\vec{\mathrm{E}}\right|^2}{\rho} \qquad (2.13.4)$$

with the tissue conductivity σ, the root mean square of the electric field and the tissue density ρ. However, this formula is valid for materials that are monophasic and would not represent more complex materials such as composite NPs. Hence, SAR needs to be calculated experimentally by using the magnetic heating profile during the initial linear slope. Excessive SAR levels might lead to elevated temperature levels, making a careful SAR evaluation mandatory to confirm compliance with the RF power deposition limits given by the International Electrotechnical Commission (IEC) standard 60601-2-33:2010 Ed.3 for the safe operation of transmitting RF coils tailored for UHF-CMR. The IEC 60601-2-33:2010 Ed.3 technical standard defines limits for whole-body averaged SAR (normal mode: 2 W/kg, first-level controlled mode: 4 W/kg), which is used for large-volume body RF coils commonly used for transmission at 1.5 T and 3 T. RF power deposition of local transceiver RF coil arrays used for UHF-CMR is limited by a more restrictive local SAR of 20 W/kg for the trunk in first-level controlled mode.

2.13.2. Contrast-enhanced magnetic resonance imaging

Image contrast is the difference in brightness between an area of interest and the surroundings. The more significant the difference in brightness between different tissue types, the easier it usually is to differentiate them from each other. In MRI, this difference is critical since the spatial resolution of standard MRI images is quite low, in the range of 1.5 to 2.0 mm. Therefore, magnetic resonance imaging (MRI) contrast agents are an integral component of modern radiology. An additional reason to use contrast agents is that it reduces the need for more powerful machines to achieve higher contrast. This is crucial since MRI is exponentially more expensive for higher

magnetic field intensities. The primary type of MRI contrast agents is gadolinium-based. Gadolinium is one of the metals in the Lanthanide series, the metal of the chelate complexes, has a 4f7 sub-orbital configuration and a spin quantum number of 7/2. This implies a coordination number of 8 and seven unpaired electrons. Gadolinium-based contrast agents are paramagnetic; that is, these atoms act like ferrimagnetic and superparamagnetic substances, and have a positive magnetic susceptibility. The effect of paramagnetic substances is several orders of magnitude weaker than that of other substances with much higher positive susceptibility. The first patented MRI contrast agent was made of gadolinium diethylenetriaminepentaacetate (Gd-DTPA or Magnevist) and was filed in 1981. Until today, this remains as the most widely used contrast agent [239,240]. Although, since then, contrast-enhanced MRI has played an increasingly important role in diagnostic medicine and other alternatives have been heavily investigated, and a dozen contrast agents have been approved by the US Food and Drug Administration (FDA) for intravenous use [241].

Alternatives to gadolinium-based contrast agents are crucial since elevated toxicity was identified from gadolinium-based contrast agents in the past few decades. However, contrast agents made of non-gadolinium-based materials are not widespread yet. Among the most promising options, SPION covered in dextran or carboxydextran has gained substantial recognition for their biocompatibility and strong magnetic properties. However, most of them have not been approved for clinical use yet. There currently exists a scientific quest to find the best candidate to substitute gadolinium-based MRI contrast agents. Some of the most notable examples for T2 contrast clinically approved are ferumoxides with a particle size of 120 to 180 nm with SPION cores of 5 nm approximately dextran coated; ferucarbotran with a particle size of about 60 nm with SPION (γ-Fe_2O_3 and Fe_3O_4) cores of 4.2 nm carboxydextran

coated; and ferucarbotran with a particle size of about 17-31 nm with SPION (Fe_3O_4) cores of 6.8 nm carboxydextran coated [242,243]. Ferumoxides have displayed contrast 30 minutes after administration. A significant challenge today is to design all-in-one contrast agents that can be detected by multimodal techniques, as many as possible. The optimal MRI contrast agents would need to display a long T2 and short T1 to be high contrast in both modes.

2.14. Microcomputed Tomography

X-ray microcomputed tomography or computerised microtomography (microCT or µCT) is a non-destructive 3D imaging technique that uses X-rays record tomographic cross-sections of a physical object to recreate it virtually without destroying the original object. The non-destructive nature of microCT, combined with three-dimensional visualization and analysis, allows for a complete internal and external view of material geometry and composition at both macro and microscale. The nanoscale, however, is not accessible with conventional microCT scanners and requires the recently developed high-resolution X-ray micro-computed tomography (HRmicroCT or HRµCT) [244]. Applications include product quality checking, damage or defect analysis, porosity analysis, composite and laminate materials.

2.14.1. CT contrast agents

Contrast agents are pharmaceuticals that increase the sensitivity and specificity of diagnostic images. Among the most clinically used CT contrast agents, water-soluble barium- and iodine-based are the most common [245].However, the gold standard in X-rays CT contrast and safety is Au [246], AuNPs have the most promising candidate as an x-ray contrast agent due to their high x-ray opacity (attenuation), non-toxicity and facile synthesis and surface functionalization for colloidal stability and

targeted delivery. Beyond these properties, other essential parameters are vascular retention time and biodistribution [247]. All these physical, colloidal, and biological properties are consequences of the structural characteristics, including the NP composition, mass concentration, size, morphology and molecular functional groups.

2.15. Heat treatment for nanopowders

The conversion of certain materials to different materials using high temperatures has existed for centuries. Working at very high temperatures in a highly controlled environment, however, is a new experimental set up that has been only possible over the last century. Nanomaterials have also gained momentum over the last 50 years thanks to improved synthesis techniques. In this regard, during the last 20 years, researchers have made significant progress in combining both high temperatures in specific environments using nanomaterials. Most of these materials were treated in the form of thin-film but not nanopowders due to technical difficulties in preventing large samples lose. In the last decade, heavy NPs have been thermally treated in gaseous environments thanks to a better understanding of the characteristics that NPs need to meet to efficiently be treated without sample loss. Conversion of NPs is essential to unlocking novel properties and functionalities for diverse applications. Even though, today, most powder samples are up to the microscale [248,249].

2.16. Microfluidics

The history of microfluidics dates to the 1950s, in inkjet printer manufacturing. The mechanism behind these printers is based on microfluidics; it involves the use of tiny tubes carrying the ink for printing. First true micropumps were reported in 1976 [250]. Spencer et al. presented in 1978 an early example of the first technical micropump

designs based on actuation of both, the pump diaphragm and the valves [251]. Jan Smits developed MEMS micropumps in 1990 to control insulin delivery systems for maintaining diabetics' blood sugar levels without frequent needle injections [252]. All these examples represent microfluidic systems since they enable the precise control of the decreasing fluid volumes on the one hand and the miniaturization of the size of a fluid handling system on the other. Today, much more advanced tests are performed, such as organ-on-a-chip developments for drug testing and NPs membrane filtration for enhancing nanoscale samples purity.

2.16.1. Microfluidic pump

Microfluidics exploits the small size of channels and laminar flow of fluids inside them, due to the low Reynolds number. Microfluidic pumps or micropumps are devices that supply fluid from syringes in small doses continuously, for a defined period or in pre-set intervals. These pumps usually operate fluids in the range of 500 μms^{-1} in 20 µm deep and 100 µm wide. Microfluidics µL (10^{-6} L) to pL (10^{-12} L). The first applications of microfluidic technologies have been in the areas of biological and chemical analysis. Most micropumps found today can roughly be divided into two groups: The so-called “reciprocating micropumps” use the oscillatory or rotational movement of mechanical parts to displace fluid. Micropump development has started with “piston type” reciprocating micropumps like micro diaphragm pumps and peristaltic micropumps that do still form the main representatives of this class in the MEMS world.

2.16.2. Nanoparticles membrane filtration

Nanomaterials membrane filtration is the process of filtering nanoscale solid material redispersed in a liquid by using membranes[253]. Filtration of nanomaterials

can be two-dimensional (2D) with nanoporous membranes or three-dimensional (3D) with nanoporous scaffolds. For tangential flow filtration (TFF) mode, depending on the molecular weights, particle size and pressure during the filtration can be subdivided in ultrafiltration (UF) and nanofiltration (NF). Both UF and NF are heavily used for water purification and waste management, and over the last decades have been used for many more applications, including pharmaceutical applications and biotechnology [254–256]. Traditionally, synthetic nanoporous membranes have found biological and medical applications that involve sorting, sensing, isolating, and releasing biological molecules [257]; but just lately for NPs separation [258–262]. Normal flow filtration (NFF), also known as dead-end filtration, is the other filtration mode available using nanoporous membranes and has been primarily used for laboratory and medical filtration [263]. Unlike TFF membrane processes, the fluid to be filtered in NFF is fed perpendicularly to the filter element, and all the fluid passes through the filter element with retained solids forming a cake layer on the element surface.

High control of thickness, porosity, and pore size in nanoporous membranes production is essential to achieve excellent performance during the nanofiltration. Striemer et al. in 2007 published the first ultrathin porous nanocrystalline silicon (pnc-Si) membranes fabricated via crystallization of amorphous silicon thin films deposited by radio frequency sputtering [264]. Achieving a genuinely thin membrane is essential to reduce the effect of the membrane in the flow and maximise control during filtration and capture of nanomaterials during the filtration process. After this scientific breakthrough, many others used similar kinds of technology to achieve ultrahigh performance desalination by filtering reactive NPs [265], pH stimuli-responsive devices based on ionic current rectification [266] and removal of insoluble and soluble organic pollutants from water using superwetting materials [267].

3. Methodology

3.1. High-temperature gas treatment

This chapter showcases performed heat treatment using an Elite single-zone horizontal tube furnace to change the oxidation state of WO_3 and γ-Fe_2O_3 nanopowders. This furnace has a theoretical accuracy of 0.1 °C and can operate up to 1200 °C. The heat-treating processes require the precise control of temperature over the heating cycle. The heating rate is 5 °C per minute, and dwell time is 60 minutes, with variable target temperatures from 200 °C to 400 °C. The addition of a mixture of H_2 and argon (Ar) gas was used to perform redox reactions in metal oxides which could not usually happen in nature at these heating rates and target temperatures due to being highly endothermic. To achieve this purpose, our Elite gas furnace oven brings the capabilities to control with high precision the reaction's environmental parameters. The main drawback of this method is that it requires a dry sample and in the case of NPs, this leads to aggregation, which in some cases might be irreversible.

The sample is placed in alumina boats of 70 mm x 20 mm x 20 mm to hold it while interacting with the gas and to prevent damage to the quartz glass of 50 mm of diameter. Alumina boats are commonly used due to their strong heat resistance to very high temperatures and smooth surface that allows easy cleaning for long-lasting reusability. The external calibration thermometer is not necessary if the furnace is very well-calibrated, but it is recommended to use it every time to verify the calibration is correct. Once tightly closed, the gas continuously enters the quartz glass tube through the inlet, interacts give the sample exposed local atmosphere and leaves the tube through the gas outlet. Several minutes pass to ensure the atmosphere is filled with

the gas, no air remaining. Once the atmosphere is homogenised, the furnace is turned on pointing to the target temperature at a certain speed and dwell time. The speed is how fast the temperature will rise, and the dwell time is how long the furnace will remain at the target temperature once reached.

3.2. Massart procedure

Coprecipitation from aqueous solutions is one of the most frequently used methods. The first controlled preparation using an alkaline coprecipitation of $FeCl_3$ and $FeCl_2$ of superparamagnetic magnetite NPs was performed by Massart [196]. This is the method user the Massart method to obtain Fe_2O_3 NPs presented in this report.

Most synthetic routes on the literature to obtain IONPs are based on the Massart procedure. In this procedure, an aqueous solution of ferrous (Fe^{2+}) and ferric (Fe^{3+}) ions in a 2:1 stoichiometry is mixed with ammonia solution giving gelatinous precipitate. Since that time, many other modifications have been examined. The coprecipitation of very fine maghemite NPs using citrate stabilising ions was described by Bee et al.[268] The size and shape of the IONPs depend on the type of salt used (such as chlorides, sulfates, nitrates and perchlorates), the ferric and ferrous ions ratio, the reaction temperature, the pH value, ionic strength of the media, and the other reaction parameters (e.g. stirring rate, dropping speed of basic solution) [269].

The average size of the resulting NPs in this thesis is 11 nm approximately. To achieve, this size, 0.09 mol of iron (III) chloride hexahydrate and 0.054 mol of iron (II) chloride tetrahydrate were mixed in a total volume of 488 mL of distilled water. This mixed was added at rate of 0.2 mL/s into 75 mL of NH4OH 25% while heating at 90ºC for 1 h.

3.3. Stöber process

In this thesis, the Stöber process is used to create silica nanoshells that cover the NP cores in a core-shell structure. The Stöber process is a sol-gel method that involves consecutive hydrolysis and condensation of alkoxysilanes in an aqueous-alcoholic solution in the presence of a base catalyst, whose most popular version uses tetraethyl orthosilicate (TEOS) as alkoxysilane and ammonia as a base catalyst. In the course of the hydrolysis reaction, the ethoxy group of TEOS reacts with the water molecule to form the intermediate $[Si(OC_2H_5)_{4-x}(OH)_x]$ where the hydroxyl group is replacing ethoxy groups. Ammonia serves as a fundamental catalyst for the hydrolysis and condensation, so the hydroxyl anions break the silicon bonding on TEOS molecules [270]. Nevertheless, the role of ammonia is also to protect the newly formed SiO_2 from undesired aggregation; in other words, it helps to obtain monodisperse SiO_2 core-shell composite NPs. Immediately after the hydrolysis reaction, the condensation process occurs, and the hydroxyl group of intermediate $[Si(OC_2H_5)_{4-x}(OH)_x]$ reacts with the ethoxy group of other TEOS and the hydroxyl group of another hydrolysis intermediate steps where temporary Si-O-Si bridges are formed. K. S. Kim et al. stated that the rate of water condensation is thousands of times faster than the alcohol condensation [271–275]. Figure 3.1 shows the overall reactions.

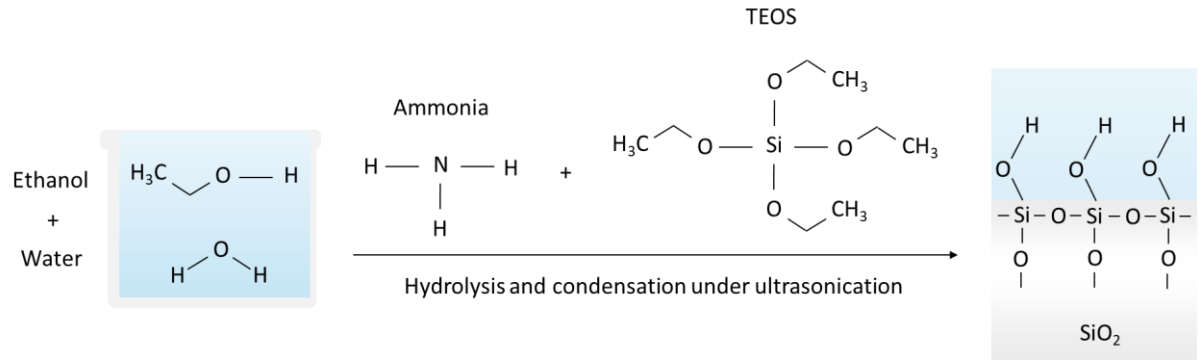

Figure 3.1 | Illustration of the Stöber process overall reaction and formation of SiO_2 structures.

The hydrolysis can be expressed as the following:

$$Si(OC_2H_5)_4 + xH_2O \rightarrow Si(OC_2H_5)_{4-x}(OH)_x + xC_2H_5OH \quad (3.3.1)$$

The sol-gel process can be described more in detail as water condensation in Eq. (3.3.1) and alcohol condensation in Eq.

$$\equiv Si - O - H + H - O - Si \equiv \rightarrow \equiv Si - O - Si \equiv + H_2O \quad (3.3.2)$$

$$\equiv Si - OC_2H_5 + H - O - Si \equiv \rightarrow \equiv Si - O - Si \equiv + C_2H_5OH \quad (3.3.3)$$

During this process, TEOS molecules form silanol groups, and the polymerization/nucleation between silanol groups and ethoxy groups creates the siloxane bridges (Si-O-Si) that integrate the SiO_2 structure as described in Figure 3.1. SiO_2 reacted with hexamethyldisilazane (HMDS) to form non-stable trimethylsilyl groups which have high reactivity with the SiO_2 surface silanols; therefore, the product is hydrophobic as shown in Eq.:

$$2(\equiv Si - OH) + 2((CH_3)_3 - Si) - NH \rightarrow 2(\equiv Si - O - Si - (CH_3)_3) + NH_3 \quad (3.3.4)$$

TEOS concentration is the main parameter on the SiO_2 particle size[276]. The more TEOS in the reaction, the thicker the SiO_2 shell in the product. For each core, the main differences rely on the stirring method. For WO_3[277], a robust ultrasonic redispersion during the SiO_2 coating process is necessary to avoid that they stick together.

3.4. Turkevich Method

Colloidal AuNPs can be obtained following different methods[278]. In our research, colloidal Au NPs were obtained by using the reduction of Au salts in the presence of surfactants, reduction of chloroauric acid with tetrakis(hydroxymethyl)phosphonium chloride (THPC, $C_4H_{12}ClO_4P$). There exist other very famous methods such as the trisodium citrate (NaCtr, $Na_3C_6H_5O_7$) and sodium borohydride ($NaBH_4$).

The THPC starts by dissolving chloroauric acid hydrate or Au (III) chloride trihydrate ($HAuCl_4$) in water described by the overall reaction

$$\mathrm{HAuCl_4 + H_2O \rightarrow AuCl_4^- + OH^- + H_2^+} \tag{3.4.1}$$

$HAuCl_4$ can be dissolved in water or another polar organic solvent. Using the citrate reduction method, reduction reaction between $HAuCl_4$ with sodium citrate ($Na_3C_6H_5O_7$) the reaction (3.4.2) or the reaction (3.4.3) in case of using different citrate can be written as

$$\mathrm{2AuCl_4^- + C_6H_5O_7^{3-} + 2H_2O \xrightarrow{100°C} 2Au + 3CH_2O + 3CO_2 + 8Cl^- + 3H^+} \tag{3.4.2}$$

$$\mathrm{6AuCl_4^- + C_6H_8O_7^{3-} + 5H_2O \xrightarrow{100°C} 6Au + 6CO_2 + 24Cl^- + 18H^+} \tag{3.4.3}$$

The Eq. (3.4.3) is the previously mentioned sodium citrate method developed by Turkevich. Here, 1 mM $HAuCl_4$ is dissolved in deionised (DI) water in which Au^{3+} cations are reduced. The colour change to dark blue/purple happens because the sodium citrate is reducing the $HAuCl_4$ and produces very small AuNPs that are dispersed in the solution rather than precipitate out. This is why they are called colloidal Au NPs. The disadvantages of this method are the additionally required

heating during the whole procedure, and the sizes are over 20 nm on average which is inconvenient for coating.

Another common alternative for the AuNPs formation is the sodium borohydride reduction[279] expressed as given in (3.4.4) and the scheme for the reduction reactions of Au ions can be written by the equation (3.4.5):

$$4[HAuCl_4] + 3NaBH_4 + 9H_2O \rightarrow \frac{4}{n[Au^0]_n} + 3NaCl + 3H_3BO_3 + 13HCl + 6H_2 \quad (3.4.4)$$

$$2Au^{2+} + BH^{4-} + 4H_2O \rightarrow 2Au^0 + B(OH)^{4-} + 2H_2 + 4H^+ \quad (3.4.5)$$

This method is highly stable and has been previously performed, obtaining good results[280]. The main disadvantage is the high average deviation in size, which is inconvenient for a subsequent Au coating.

Finally, a version of Turkevich method with THPC by Baiker et al.[281] was also reproduced. The first reaction is

$$[P(CH_2OH)_4]Cl + NaOH \rightarrow P(CH_2OH)_3 + H_2O + H_2C = O + NaCl \quad (3.4.6)$$

The product, tris(hydroxymethyl)phosphine ($P(CH_2OH)_3$), is used to synthesise AuNPs by treating it with aqueous sodium hydroxide ($NaOH.xH_2O$) what is necessary to generate the reduction reaction given by equation

$$3P(CH_2OH)_3 + 2AuCl_4^- + 6OH^- \rightarrow 3O = P(CH_2OH)_3 + 2Au + 8Cl^- + 3H_2O \quad (3.4.7)$$

This method allows the generation of ultra-small diameter Au NPs and high stability in aqueous solution for long periods [282]. If the solution were stored in the presence of NaOH, THPC could progressively decompose, thus reducing its ability to stabilise the Au NPs formation. Therefore, cleaning after the synthesis is essential.

During the formation of the metallic sol and the storage time, a considerable excess of NaOH is present. The reactions of THPC with NaOH performs the role of the reducing agent via the formation of formaldehyde, a well-known reducing agent for Au under standard conditions, following the mechanism. The modification of the Turkevich method via THPC resulted in the most appropriate one for the NPs and nanoshell synthesis because a bigger tunability in terms of the particle size and also very high reproducibility was obtained. However, some authors previously reported some limitations in the tunability of small-diameter Au nanoshells[283,284].

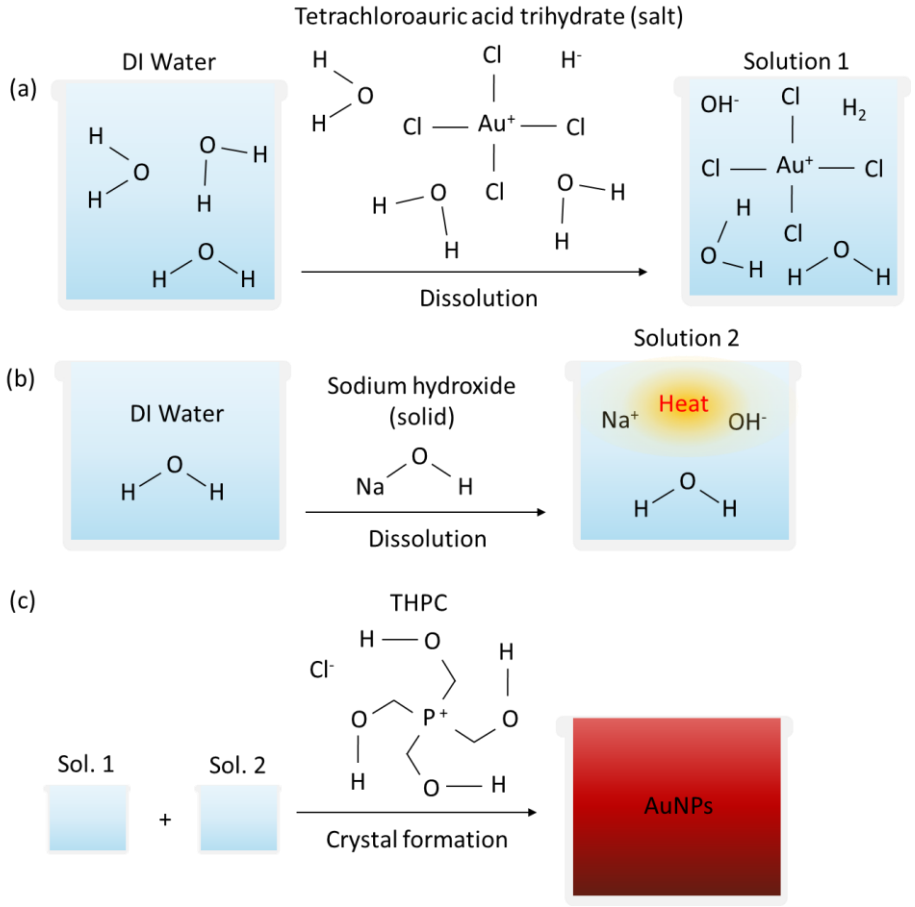

Figure 3.2 | Illustration of the Turkevich method steps using THPC.

Finally, the growth of Au on top of the SiO_2 is a pivotal element to improve the plasmon enhancement desired in SERS. Different thicknesses of the metal layers can

tune the LSPR peak position to match the excitation wavelengths from the incident laser, which optimise the SERS enhancement. This method can be the approach in different ways but in the end, follows the same fundamentals than the original Au NP formation. One of the most reliable and easily reproducible approaches is the reduction of the Au stock solution with potassium carbonate dissolved in an alkaline solution. This method leads to a smooth Au nanoshell growth.

3.5. Surface functionalization

3.5.1. Amine group

There are significant optical and chemical properties of AuNPs that depend strictly on the type of ligand and ligand-metal bond. 3-aminopropyltrimethoxysilane ($NH_2(CH_2)_3$-Si-$(OCH_3)_3$), APTS or APTES) is one of the most common chemicals used to amine functionalised surfaces for successive Au attachment due to its stable bonding with Au, fast attachment and low price. The amine functionalisation technique is applie din this thesis following the standard heating while stirring procedure to the surface of our SiO_2 nanoshell for the attachment of gold nanoparticles on top as described in Figure 3.3.

SiO_2 is formed by strong covalent bonds where one atom of SiO_2 is connected to 4 atoms of oxygen, and each oxygen is connected to 2 Si atoms. The amine functionalisation provides the same type of periodic molecular structure which make it very stable. However, due to potential defects and a higher degree of disorder, small variations from the formulas presented in Figure 3.3 may appear as described by Pasternack *et al*. [285]. The defects can be minimised by controlling specific parameters such as the temperature during the condensation process.

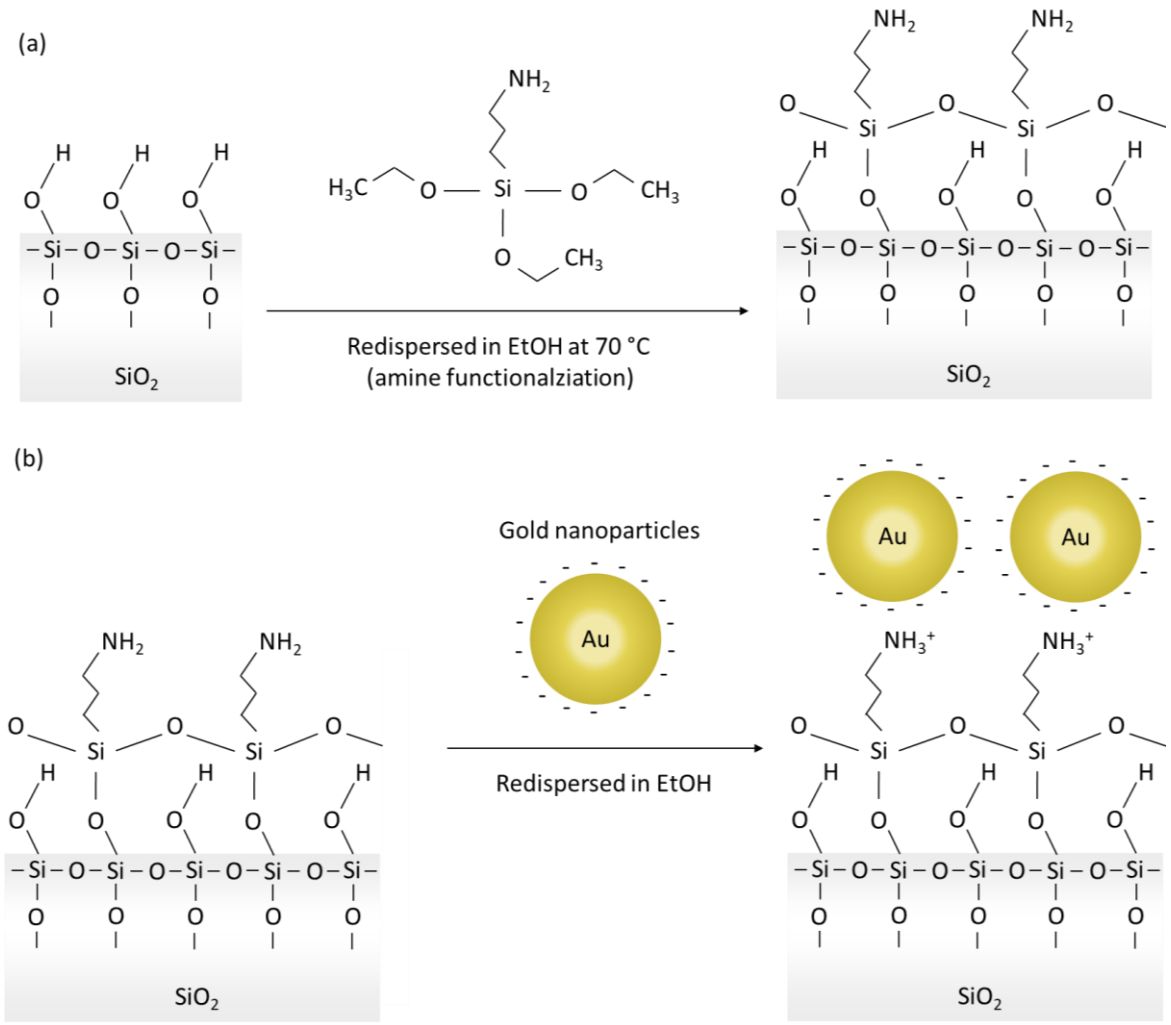

Figure 3.3 | Illustration of the amine groups interactions with nanostructures. (a) Amine surface functionalization of SiO_2 dispersed in ethanol by using APTES. (b) Amine functionalised surface of SiO_2 bonding with Au NPs.

3.5.2. Thiol group

Self-assembled monolayers (SAMs) of organic molecules provide an inexpensive and adaptable surface coating for a wide range of applications; and, in the case of noble metal substrates such as Au, thiol moieties are commonly used as end groups because of the strong affinity of sulphur with these metals. There is a profound debate in the field regarding the fate of the hydrogen from thiol molecules when thiols bind to Au in SAMs. This understanding is fundamental to explain and

predict their physical, spectroscopic, and chemical-structural formation properties. Traditionally, it was understood that thiol moieties are chemisorbed to planar Au surfaces, with the loss of hydrogen during the formation of the bond. Ipken *et al.* probed recently that the Au-thiol SAMS bond does unexpectedly not have chemisorbed character, which means the hydrogen atom is probably retained [286]. This comparison is portrayed in Figure 3.4, where R refers to any functional group. This new model indicates that the Au-thiol bond is maybe not as strong as initially thought.

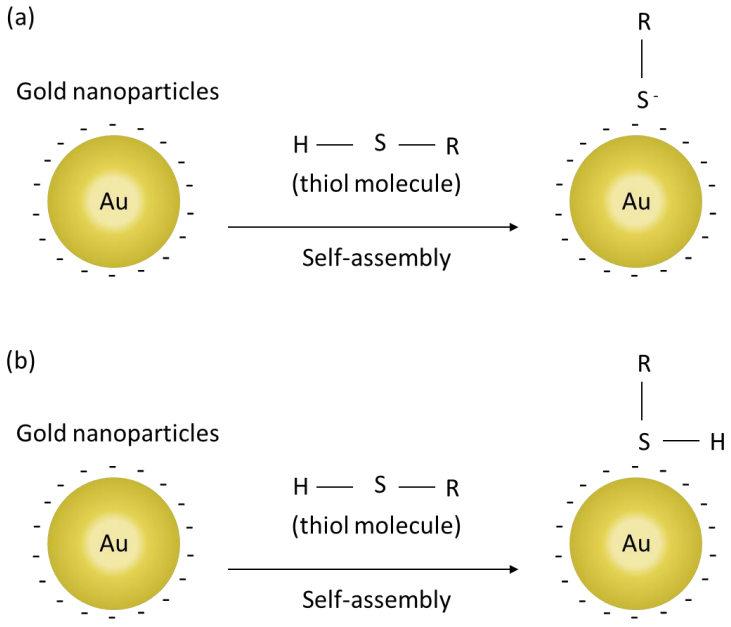

Figure 3.4 | Illustration of a SAM on an Au(111) monolayer. (a) Traditional model. (b) New model.

The -SH binds to Au at temperatures in the range of 20-70°C. In this thesis, the binding was performed at room temperature (approx. 24°C). Combining this with a structure that includes at least an aromatic ring which has vibrational modes, the -SH functional group provides an affordable option for SERS enhancing the aromatic

ring peaks. Price and biocompatibility are the most important factors taken into consideration when choosing the thiol molecule.

4-MBA ($HSC_6H_4CO_2H$) is one of the best options as a Raman reporter for biomedical applications. This molecule contains one benzene ring, a thiol and a carboxylic group. The main reason to choose 4-MBA is its extensively proven performance in the literature for SERS and being cost-effective. Raman scattering shows that the two most important peaks that should be used as a reference for this molecule are at 1078 cm^{-1} and 1590 cm^{-1}. However, once a good SERS effect is proven with the coupling between the Au surface plasmons and this thiol molecule, many other thiolated molecules with alternate marker peaks can be subsequently tested if required for biomedical imaging purposes.

3.6. Electron microscopy

3.6.1. Scanning electron microscopy

An SEM scans a focused electron beam over the surface of a micro- and/or nano- structured solid material to create an image such as micro and NPs. The resolution of SEM is approximately 10 nm in standard machines and 2.5 nm in advanced versions [287]. In this thesis the SEM models used were TESCAN VEGA3 SEM with the best resolution of 2 nm at 30 kV in high-vacuum mode and 2.5 nm at 30 kV in low-vacuum mode; and Zeiss Auriga FIB-SEM capable of resolutions of 1.0 nm at 15 kV and 1.9 nm at 1 kV.

SEM can also be used to obtain information about the surface composition by using it in conjunction with other related techniques of energy-dispersive X-ray

microanalysis (EDX, EDS, EDAX), for the determination of the composition or orientation of individual crystals or features [288].

One of the significant advantages of SEM against other electron microscopy techniques is the simplicity of the specimen preparation techniques. In the same line as the rest of electron microscopy techniques, it is necessary to have a conductive material or partially conductive material. When working with non-conducting or poorly conducting materials, and additional nanocoating is added on top of the material surface to enhance the SEM imaging. However, this coating will interfere with the composition analysis when using EDX.

3.6.2. Transmission electron microscopy

Transmission electron microscopy (TEM) is a microscopy technique in which a beam of electrons is transmitted through a specimen to form an image [289]. This specimen is a TEM grid that contains the sample scattered over the grid holes frequently suspended on a holey carbon film. The TEM specimen usually range the 2-3 mm and contains a mesh of copper (Cu) covered in a thin film of carbon (C) sometimes holey. The mesh usually has from 200 to 400 sub-regions or wholes where NPs or other nanomaterials can be seen and analysed. In this thesis, most images are obtained using the JEOL 2100 TEM which operates at 200 kV, providing point resolution of 0.25 nm and ideal lattice resolution of 0.14 nm, generating atomic resolution images of nanomaterials. It can operate in bright field (BF) and dark field (DF) modes and in both TEM and scanning transmission electron microscopy (STEM) modes. Moreover, the nanofiltration studies of this thesis are performed using an FEI Tecnai G2 TEM which has 0.24 nm resolution (Twin lens) with ±70˚ sample tilt (±30˚ on second tilt) and operates at 100-300 kV.

TEM achieve higher resolution than other electron microscopy modalities such as STEM or SEM. When the atomic structure of the sample is visible and can be imaged via TEM imaging, it is called HRTEM. HRTEM is a powerful tool to study the atomic scale of NPs or 2D nanomaterials such as graphene.

3.6.3. Scanning transmission electron microscopy

STEM is a type of TEM that includes SEM functionalities that which permits a fine electron probe to be scanned across the specimen. In many ways, STEM is like SEM. Scattered electrons are detected, and their intensity plotted as a function of probe position to form an image. In contrast to an SEM, where a bulk sample is typically used, the STEM requires a thinned, electron-transparent specimen usually less than 100 nm in thickness [290]. The most used STEM detectors are therefore placed after the sample and detect transmitted electron.

STEM can also perform atomic spectra analysis using EDX. The critical difference between performing EDX analysis in the STEM as opposed to the SEM is the improvement in spatial resolution. The increased accelerating voltage and thinner sample used in STEM leads to an interaction volume that is some 10^8 times smaller than for an SEM.

3.7. X-rays powder diffraction

Atoms in solid materials are arranged into crystalline and amorphous structures [291]. Amorphous materials are isotropic, i.e., present irregular atomic arrangements and possess the same properties in all directions. In contrast, the crystalline materials are anisotropic because their atoms are arranged in a regular and repeated pattern, and their properties vary with direction. There are many types of crystalline structures which can contain different atoms.

XRD is a rapid and powerful non-destructive analytical technique for phase identification of crystalline material. The X-ray diffraction pattern is distinct for each different phase, and it can provide information on unit cell dimensions. Amorphous materials, like glass, do not produce sharp diffraction peaks but broad peaks. The material to analyse needs to be flatly homogenised typically in a glass slide, and then an average bulk composition is determined. X-ray diffraction peaks are produced by constructive interference of an incident monochromatic beam of X-rays scattered at specific angles from each set of lattice planes in a sample. The peak intensities are determined by the distribution of atoms within the lattice. Consequently, the X-ray diffraction pattern is the fingerprint of periodic atomic arrangements in each material. The diffraction pattern of a mixture is a simple sum of the diffraction patterns of each individual phase.

In this thesis, the XRD spectra are obtained using a Bruker D8 that can analyse powders, bulk and thin-film materials for phase composition, quantitative phase analysis, unit lattice parameters, crystal structure, and average crystallite size of nanocrystallites. The spectra were obtained working at 0.03° step per second of 2θ from 10° to 80° at room temperature.

3.8. Ultraviolet-visible-near infrared spectrophotometry

Ultraviolet-visible-near infrared (UV-vis-NIR) or ultraviolet-visible (UV-VIS) spectrophotometry is a device developed to analyse the light scattering or absorbance characteristics of matter. For this purpose, the wavelength of collected light dispersed into its constituent wavelengths with a diffraction grating. To calibrate these measurements, a new measurement is always performed with the solution in which

the sample in redispersed to subtract the effects of the liquid medium and the cuvette absorption properties.

The nanoparticles were characterised by using the Thermo Scientific Evolution Array UV–vis spectrophotometer to obtain the light absorption spectra of the colloidal composite nanoparticles suspended in ethanol at mild conditions using plastic cuvettes. This UV-vis system uses light sources of pre-aligned Deuterium and pre-aligned Tungsten which can measure a full spectrum every 20 milliseconds, have a wavelength reproducibility < 0.02 nm (ten consecutive scans) and can scan in the range of 190 to 1100 nm.

3.9. Dynamic light scattering

Dynamic light scattering (DLS), also known as quasi-elastic light scattering or photon correlation spectroscopy (PCS), is a technique that determines the size of spherical particles from the nanoscale to the microscale [292]. DLS measures the Brownian motion of particles suspended within a liquid and correlates this to the particles' size. The Brownian motion of particles in solution arises due to collisions with solvent molecules and depends on the particle's size, temperature, and solvent viscosity [293]. If the particles are large, their Brownian motion will be slow. The molecules from the solvent push the smaller and lighter particles, which increase their speed. The translational diffusion coefficient (D), which is concentration-dependent is the property that defines the velocity of the Brownian motion. Additionally, temperature must be stable to prevent convection currents which induce non-random movements that will lead to wrong results. Moreover, the viscosity of the solvent is required for the calculation, and this value is dependent on the temperature.

The hydrodynamic diameter is measured by applying the Stokes-Einstein equation for the diffusion of spherical particles through a liquid at low Reynolds number[294]:

$$d(H) = \frac{kT}{3\pi\eta D} \tag{3.9.1}$$

where d(H) is the hydrodynamic diameter of the particles, k is the Boltzmann's constant, T is the absolute temperature of the liquid, η is the liquid's viscosity and D is the translational diffusion coefficient.

This calculation is useful but might mislead for particles that has forces that drive aggregation such as in the case of magnetic NPs. The actual measured hydrodynamic diameter is not the value of the single magnetic NPs but the aggregates. The electric surface charge can also lead to aggregation and modified diffusion speed which will lead to a change on the apparent size of the particle. When clusters occur, they sometimes do not form spherical shapes which will also contribute to misidentification of the hydrodynamic diameter. Also, heavy particles might eventually precipitate, which will drastically modify the number of NPs dispersed in the medium and the concentration of them. Therefore, multiple readings at different densities are usually recommended to find the region in which the results are consistently reproducible for prolonged periods of time.

The colloidal NP size and hydrodynamic radius were analysed using the NanoSight NS300 and Zetasizer Nano ZS for DLS from Malvern to measure the colloidal NP hydrodynamic radius. All samples where measured at concentrations between 10 to 400 ug/mL to obtain reproducible readings. The specific concentration for each batch was found following the standard methodology that uses a range of

concentrations until it goes from too concentrated to too diluted, in a range of consistent DLS results.

The scattered light in both systems is detected at 173-175º, it is called backscattered detection. Light is also detected at 90 and correlated with the backscattered detection to discard incorrect measurements by using the Mie theory of NPs size scattering at 90º and 173-175º degrees [292,295]. Also, when the optics are not in contact with the sample, the detection optics are called non-invasive. Measuring in these conditions is very important to measure without needing the light to travel across the entire sample. Otherwise, some issues may arise, such as multiple scattering, where light from one particle is itself scattered by other particles. This configuration also allows measuring the hydrodynamic radius of higher concentrations. Other problems such as contamination are avoided by measuring backscattered light since most of these contaminants scatter in the forward directions only. Using the correlator is essential to discard this kind of measurements discrepancies.

3.10. Nanoparticle tracking analysis

Nanoparticle tracking analysis (NTA) is a new technology commercialised in 2006 that visualises and analyses particles in liquids by relating the rate of Brownian motion to particle size. NTA combines laser light scattering microscopy with a charge-coupled device (CCD) camera to obtain visualization and recording of NPs in solution. In this thesis, NTA is performed using a NanoSight NS300 from Malvern Panalytical which can rapidly record particle sizes and concentration of samples ranging approximately from 10 to 1,000 nm in particle diameter and 10^6 – 10^9 particles/mL in concentration, with the lower detection limit being dependent on the refractive index of the NPs. The volume that can be recorded is 250 – 750 µL in real-time. In these

experiments, 500 µL were used. The NanoSight NTA software identifies and tracks individual NPs moving under Brownian motion and relates the movement to a particle size according to the Stokes-Einstein equation given by equation (3.9.1) [296].

3.11. Vibrating sample magnetometer

A vibrating sample magnetometer (VSM) is a magnetometer that measures the magnetic properties of liquid and solid samples including powder by vibrating the sample while applying a constant uniform external magnetic field which induces sample magnetization. The vibrations create perturbations in the external magnetic field, which can be detected using a magnetic field sensor such as a gaussmeter. To achieve a good reading, it needs to be calibrated first the saturation magnetization so that the sample indeed undergoes a hysteresis loop [297]. The intensity of the field must be tuned by knowing this parameter.

In this thesis, the VSM model is MicroSense EZ7 VSM which can reach fields up to 21.5 kOe at a sample space of 4 mm and fields above 17.5 kOe with the temperature chamber in place; can operate at temperatures from 4.2 K to 450 K; has a field resolution of 0.001 Oe in the lowest field range; a 1% moment accuracy when calibrated with calibration sample identical in shape and size to the measurement sample; and repeatability better than 0.5% at constant temperature and if sample position is not changed. Its highest sensitivity (lowest noise) without signal averaging: 125 nemu (125 nOe·mL) at a 3.5 mm sample space and 500 nemu (500 nOe·mL) with the single-stage temperature option in place. This VSM model can measure liquid, powder, solid, bulk, and thin-film samples. Approximately, 1 mL of powder sample was used; thus the sensitivity was close to 0.5 µOe.

3.12. Superconducting Quantum Interference Device

Superconducting quantum interference device (SQUID) is a very sensitive type of magnetometer used to measure extremely subtle magnetic fields, based on superconducting loops or rings containing Josephson junctions. In this thesis, a SQUID direct current (DC) was used. This device is based on using two Josephson (superconducting-insulating-superconducting) junctions instead of one that is used in the RF type. This device operates at cryogenic temperatures with quantum-limited sensitivity, and it has demonstrated field resolution at the 10^{-17} T (10^{-13} Oe) level [298].

For SQUID measurements, 1 mL of the colloidal sample was pipetted into a transparent glass vial with 12 mm diameter x 32 mm height. The increment of temperature was measured by using optical fibres. For powder samples, a known mass of sample is added to a flat surface like a petri dish and the increment of temperature is measured by using and infrared (IR) camera, FLIR E53

To measure the hysteresis loop of a sample, the sample was placed in the centre of the ring, which is the location where the field is the most intense and homogeneous. The SQUID performs as a flux-to-voltage transducer that converts small changes of magnetic flux into a voltage. These changes are due to magnetic properties of the materials such as ferrimagnetism or superparamagnetism and can be translated to hysteresis loops which present the magnetization of the sample when exposing it to a magnetic an alternating magnetic field. Additionally, a SQUID can detect the magnetization of the sample while cooling it while applying or not non-alternating magnetic field.

Zero-field-cooled (ZFC) were also obtained by cooling the samples without any applied magnetic field to ensure its magnetization or static susceptibility shows a peak

at the transition temperature. This process is generally reversible for ordered magnetic materials such as ferromagnets and antiferromagnets. In contraposition, field-cooled (FC) is obtained by cooling the samples with an applied magnetic field. The two susceptibilities are related to each other through the coercivity, which is a measure of the anisotropy. The ZFC susceptibility can be calculated from the FC susceptibility (or vice versa) and the coercivity [299].

3.13. Spontaneous Raman spectroscopy

In this thesis, the 2D Ramana maps were obtained using a inVia™ Reflex confocal Raman microscope from Renishaw. This system can obtain micro-Raman mappings and uses 785 and 830 nm NIR laser sources, reaching 140 mW power at sample illumination. A Leica microscope was used with the following parameters: 5×/0.12 NA (numerical aperture) for large area surfaces which has spot sizes of 7.98 µm (785 nm) and 8.44 µm (830 nm); and 50×/0.75 for small areas which has spot sizes of 1.28 µm (785 nm) and 1.35 µm (830 nm), assuming uniform illumination. The spatial resolution of the system is approximately 1 µm. Samples are pipetted directly to a silicon wafer and dried at 70 °C for 8 h. Spontaneous Raman signals from liquid samples were also measured in a plastic cuvette with a 785 nm class-4 laser source.

3.14. Coherent anti-Stokes Raman spectroscopy

In this thesis, all CARS measurements were obtained using a broadband CARS custom-built microspectrometer from the CONTRAST facility at the University of Exeter that provides 2D and 3D mapping of Raman fingerprints of biomolecules. Based on broadband CARS, this system utilises a configuration of laser sources that probes the entire biologically relevant Raman window (500–3500 cm^{-1}). At the centre, there are two co-seeded fibre lasers (Toptica, FemtoPro), custom-designed

specifically for broadband CARS. The system provides synchronization of narrowband (~3.4 ps) flat-top laser pulses at 770 nm synchronised with supercontinuum pulses (~16 fs) spanning ~900–1400 nm (NIR). By utilising intrapulse three-colour excitation and non-resonant background, CARS heterodyne-amplifies weak Raman signals. The beams are temporally and spatially overlapped and delivered onto the sample via a 1.2 NA objective and the CARS signal collected in the forward's direction by an inverted microscope (Olympus IX73) with a 0.7NA objective. The anti-Stokes signal is spectrally isolated from the excitation wavelengths using band-pass filters and focused onto the entrance slits of a spectrograph (Princeton Instruments Isoplane 160) equipped with a fast CCD camera (Princeton Instruments Pixis).

3.15. Microcomputed Tomography

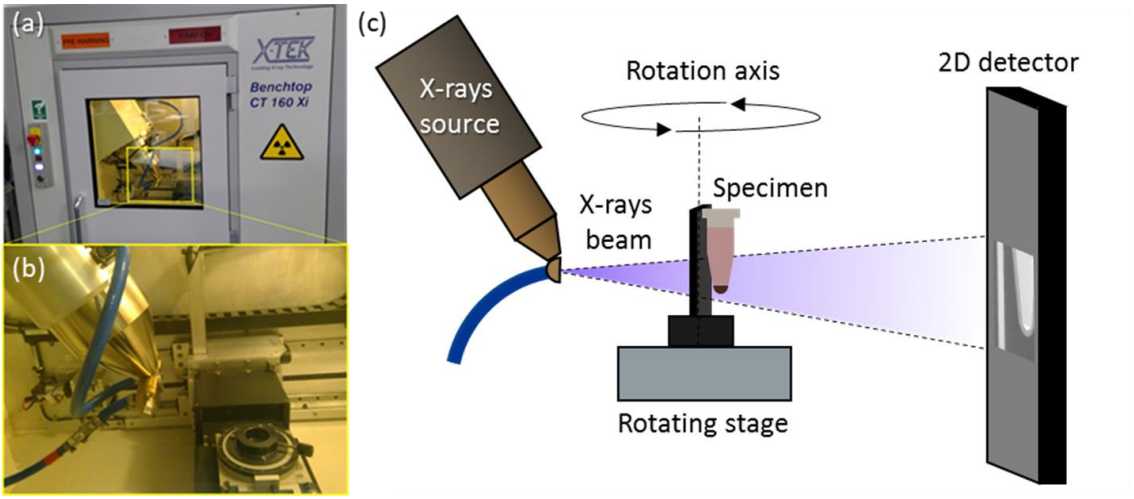

Figure 3.5 | (a) Picture of a X-TEK Benchtop CT 160 Xi and (b) zoomed image from the inside. (c) Diagram of the MicroCT imaging platform and basic operating principle to obtain the X-ray based tomographic image using aggregated nanoparticles precipitated at the bottom of a microcentrifuge tube.

In this thesis, all microCT measurements were obtained using the X-Tek Bench Top Computer Tomography (CT) 160 Xi (see Figures 3.8a and 3.8b) which produces

2D and 3D maps/structures of materials with a theoretical resolution of 3 micron in theory without damaging the samples. The re-constructed data/structure can be viewed from any 3D angle, sliced in any direction, accurately measured and even animated.

Aggregated or colloidal NPs are susceptible to absorbing X-rays and therefore being potential X-rays contrast agents depending on their size, volume, concentration, and material. Our samples were intentionally aggregated in the water at the bottom of microcentrifugation tubes to obtain aggregates more extensive than the resolution limit.

3.16. Magnetic heating

For our magnetic heating measurements, both NanoHeat from NanoScience Laboratories and MagneTherm™ from nanoTherics were used. The NanoHeat AC Magnetic Field Nanoparticle Heater can perform frequency response profiles readings in the frequency range 50 kHz to 1,000 kHz and offers 69 frequency points and field strengths up to 56 mT rms (79 mT peak). The NanoHeat employs continuous linear power control and provides an extremely homogenous (±5% homogenous field over 7ml volume) and well-defined AC field. On the other hand, the MagneTherm™ system can perform frequency response profiles experiments in the frequency range 110 kHz to 990 kHz and offers 10 frequency points and field strengths up to 25 mT. In this thesis, 1 mL of sample for both systems was used.

3.17. Micromagnetic simulations of magnetic nanoparticles

The numerical simulations were carried out by Conor McKeever using the stochastic Landau-Lifshitz (sLL) equation [300–304]. The LL equation describes the dynamics of the magnetization vector present in each cell of the NPs

$$\frac{\delta\vec{m}}{\delta t} = -\gamma_1\vec{\alpha}_i \times \left(\vec{H}_{ef,i} + \vec{H}_{th,i}\right) - \kappa_i\gamma_1\vec{\alpha}_i \times \left(\vec{\alpha}_i \times \left(\vec{H}_{ef,i} + \vec{H}_{th,i}\right)\right) \quad (3.17.1)$$

where γ is the gyromagnetic ratio, κ_i is the phenomenological damping parameter, $\gamma_1 = \gamma/1 + \kappa^2$, $\vec{H}_{ef,i}$ is the effective magnetic field and $\vec{H}_{th,i}$ is a thermal field. The local effective magnetic field acting on the magnetization vector $\vec{m}$ can be calculated as shown in equation (3.17.2),

$$\vec{H}_{ef,i} = -\frac{1}{\mu_0 M_S}\frac{\delta W}{\delta\vec{m}} \quad (3.17.2)$$

where W is the magnetic energy density. The total magnetic energy density of the interacting NP system is a sum of the Zeeman energy, nearest-neighbour exchange interaction, mutual magneto-dipole interaction, and the thermal energy.

For NPs with uniaxial anisotropy, the first-order magnetocrystalline energy density is given by equation (3.17.3),

$$W_{anis} = -K_{u1}(\vec{u}\cdot\vec{m})^2 \quad (3.17.3)$$

where K_{u1} is the first order uniaxial magnetocrystalline anisotropy constant.

The energy density due to the Heisenberg exchange interaction is evaluated as a six nearest neighbour small-angle approximation with energy density given by equation (3.17.4),

$$W_{exch} = -A(\nabla\vec{m})^2 \quad (3.17.4)$$

where the magnetisation $\vec{m}$ is taken as the central cell in the nearest-neighbour scheme.

The long-range magnetostatic field given in equation (3.17.5) is evaluated as a discrete convolution of the magnetization with a demagnetising field kernel $\widehat{\mathrm{K}}$

$$\vec{\mathrm{H}}_{\mathrm{ef,i}} = \widehat{\mathrm{K}}_{\mathrm{i,j}} * \vec{\mathrm{m}}_{\mathrm{j}} \tag{3.17.5}$$

The strong magneto–dipole interaction is known to significantly decrease the SAR of fractal clusters of interacting uniaxial NPs [305]. Finally, finite temperature is incorporated into the numerical simulations by means of a fluctuating thermal field $\vec{\mathrm{H}}_{\mathrm{th,i}}$ given by Brown [301],

$$\vec{\mathrm{H}}_{\mathrm{th,i}} = \vec{\eta}\sqrt{\frac{2\mu_0 \alpha \mathrm{k_b T}}{\mathrm{m_{sat}}\gamma \Delta \mathrm{V} \Delta \mathrm{t}}} \tag{3.17.6}$$

where $\mathrm{k_b}$ is the Boltzmann constant, α the damping parameter, T the temperature, m_{sat} the saturation magnetisation, γ the gyromagnetic ratio, ΔV the cell volume, Δt the timestep and $\vec{\boldsymbol{\eta}}$ a random vector computed from a normal distribution which varies after each timestep.

3.18. Magnetic resonance imaging

MRI measurements were taken by using nanoparticles redispersed in water inside of microcentifugation tubes of 2 mL. These tubes were placed inside of a silicon holder and then placed into a polystyrene box. The box was placed horizontally with the tubes oriented vertically, in the MRI Philips Gyroscan Intera 1.5T MRI.

3.19. Atomic Force Microscopy

Atomic force microscopy (AFM) can image almost any type of surface, including polymers, ceramics, composites, glass, and biological samples [306]. There are AFM techniques for almost any measurable force interaction – van der Waals, electrical,

magnetic, thermal. For some of the more specialised techniques, modified tips and software adjustments are needed. Typically, these micro-cantilever systems are operated in three open-loop modes; non-contact mode, contact mode, and tapping mode [307]. AFM works by raster-scanning a sharp tip over the sample surface using a feedback loop to adjust parameters needed to image a surface, and atomic forces are used to map the tip-sample interaction.

The AFM model used in this thesis is the Innova® AFM from Bruker which delivers accurate, high-resolution imaging and a wide range of functionality but is limited by the operation mode, type of probe and sample characteristics. The sample needs to be flat with rugosity not thicker than the maximum amplitude that the tip can undergo. In this thesis, an AFM was used to scan over the surface of the nanoporous silicon nitride (NPN) membranes that are approximately 50 nm thick, using average nanopore sizes of 37 nm and 60 nm. The full possible sample volume is 45 mm x 45 mm x 18 mm with a motorised Z-axis travel of 18 mm, with pitch and tilt capability. The resolution is not due to the system but to the tip and scanning mode.

3.20. Microfluidics

Materials: Polydimethylsiloxane (PDMS) sheets were obtained from Trelleborg Sealing Solutions Americas, Fort Wayne, IN. The following reagents were purchased from Sigma Aldrich: Iron (III) oxide (γ-Fe_2O_3) nanopowder, <50 nm particle size (BET) and pure ethyl alcohol (ethanol, EtOH) 200 proof, anhydrous. Deionised water was obtained at 18.2 MΩ and 24.1 °C from Q-POD® Ultrapure Water Remote Dispenser connected to a Milli-Q® Advantage A10.

Equipment: Silhouette Cameo digital craft cutter was purchased from Silhouette America, Oren, UT. NFF was performed using SepCon™ Spin Columns for Particle

Separation from SiMPore Inc. VWR High-Speed Microcentrifuge was used at ×500g centripetal force. Chemyx Fusion 100 Infusion Pumps were used in TFF to pump the solution at a rate of 25 µl/min as a supply and 12.5 µl/min during the ultrafiltration. These microfluidic pumps must be synchronised; otherwise, the vacuum pressure will break the membrane. For the electron microscopy images, the JEOL 2100 TEM/STEM, TESCAN VEGA3 SEM and Zeiss Auriga FIB-SEM systems were used. The colloidal NP size and concentration data were obtained using NanoSight NS300 and Zetasizer Nano ZS for DLS from Malvern. The XRD patterns were obtained with the Bruker D8 advanced XRD machine working at 0.03° step per second of 2θ from 10° to 90° at room temperature (300 K). Innova Atomic Force Microscope (AFM) from Bruker was used at 2 V setpoint, with a scanning mode RESP-20 tip of ~8 nm radius, 10-15 µm height and 17.5 º side angle to obtain the AFM profile of the membrane. The proportional (P), integral (I) and differential (D) gains for our system were of P=1, I=0.5 and D=0

3.20.1. Microfluidic pump

Two Chemyx Fusion 100 Infusion Pumps were used in TFF to pump the solution at a rate of 25 µl/min as a supply and 12.5 µl/min during the ultrafiltration. These microfluidic pumps must be synchronised; otherwise, the vacuum pressure will break the membrane. They can hold syringes from 0.5µL to 60 mL and operate at rates from 0.0001 µL/min to 140 mL/min which display a very high precision for our experiments.

Much attention has been focused over the last decades on miniature systems for chemical and biological analysis [308–311]. Miniaturization can reduce costs and enables portability. However, compatibility with the range of fluid volumes of interest

is necessary if micropumps are to become more widely used in micro total analysis systems (μTAS). Monitoring single cells may require manipulation of fluid volumes on the order of 1 pL — the volume contained in a cube 10 μm on a side [312–314]. It is possible to work with even smaller objects such as NPs and molecules disperse in the microfluidic media for many applications such as cytotoxicity assays, ELISA tests and size filtration.

3.20.2. Microfluidic filtration device

The fabrication of NPN Membrane performed by SiMPore Inc. following the fabrication steps for NPN membranes has been published previously by J.P. DesOrmeaux et al. 2014 [315]. Summarising the main steps, a double-side polished silicon wafer is coated with a three-layer stack made of 50 nm-thick silicon nitride (SiN), 40 nm-thick amorphous silicon, and 20 nm-thick silicon dioxide. Then, the wafers are then annealed using a rapid thermal process to transform the amorphous silicon into porous nanocrystalline silicon (pnc-Si) layer on top of SiN. The backside SiN is patterned using reactive ion etching while the SiO_2 layer acts as a protection for the pnc-Si and SiN films during the backside processing. The nanopores generated in the pnc-Si are transferred into the SiN layer by reactive ion etching after removing the SiO_2. Finally, to create the free-standing membranes, the backside of the silicon wafer was etched to the silicon nitride layer using ethylene diamine pyrocatechol. The final membranes developed following this method have 37 and 60 nm pore size each.

SepCon™ NFF device assembling was obtained as described in the following. The assembling process of the SepCon™ device follows the steps described below. In the first step, a flat and sticky PDMS piece U shaped gasket is added to the bottom element that will hold the filtered sample. Then, the NPN membrane is added by fitting

it in the square hollow and pressing in the edges against the sandwiched PDMS for adherence. Finally, this lower part of the SepCon™ is inserted in the top cylindrical part to finish the assembling. To collect the filtered sample, the SepCon™ is placed in a microtube before adding the sample and starting the centrifugation.

The TFF device fabrication was achieved by applying the following steps. Custom ordered 100 µm and 300 µm thick PDMS sheets are patterned using a Silhouette Cameo digital craft cutter. The patterned silicone sheets are assembled into layer stack devices by aligning the patterned layers as previously reported by M. Dehghani *et al* in 2019 [316]. Then, NPN membrane chips (300 µm thick) are sandwiched between the stacked layers. The final device is clamped to seal it and be ready for flow processes.

3.20.3. Tangential filtration

Tangential flow filtration (TFF) or cross-flow filtration is a type of filtration in which the solution to be filtered is pumped in parallel to the filtering membrane surface. In this configuration, part of the solution remains unfiltered and keeps flowing perpendicular to the membrane, and this is called retentate. It is possible to improve the quality of filtration by refeeding the retentate into the system as a sole feed or mixed with the original feed. Some of the most relevant parameters to achieve better filtration are the type of membrane used, the pressure in the upper side of the membrane versus the lower part of the membrane, the type of flow present in each region and the particles or molecules to be filtered. When working with nanoscale objects, this membrane must present permeability for the scale only, and it needs to receive minimal volumes of sample to filter, which is only achieved by using microfluidic pumps.

TFF NP filtration was applied following these steps: The two microfluidic pumps were connected to the TFF device. The pumps at a rate of 25 µl/min to supply the initial media background and avoid creating pressure differences that could damage the membranes. The flow rate was the same in both pumps – one pulling below the membrane and one pushing above. Then, a rate of 12.5 µl/min was used in both pumps during the ultrafiltration while adding 500 µl of the NPs solution at a concentration of 4 µg/ml (1:50,000 from stock). Once the entire volume is pulled through the membrane, the filtered solution was collected and analysed.

Heat treatment under H_2 gas atmosphere

4. Core material refinement

4.1. Introduction

In this chapter, two methods to refine and purify nanoparticles are being presented. The first method is a high-temperature gas treatment that uses a mixture of H_2+Ar gas to hydrogenate dry WO_x NPs which has been previously reported [317] and to reduce dry γ-Fe_2O_3 NPs. This method provides a simple and reproducible way to obtain alternative materials that be used for medical applications. A second method is a novel approach used later in the chapter to size filter colloidal γ-Fe_2O_3 NPs using nanomembranes in microfluidic devices that can be used to improve dispersity, purity and automate the synthesis of composite NPs.

4.2. Heat treatment of WO_3 and Fe_2O_3 nanoparticles under H_2 gas

4.2.1. Experimental setup

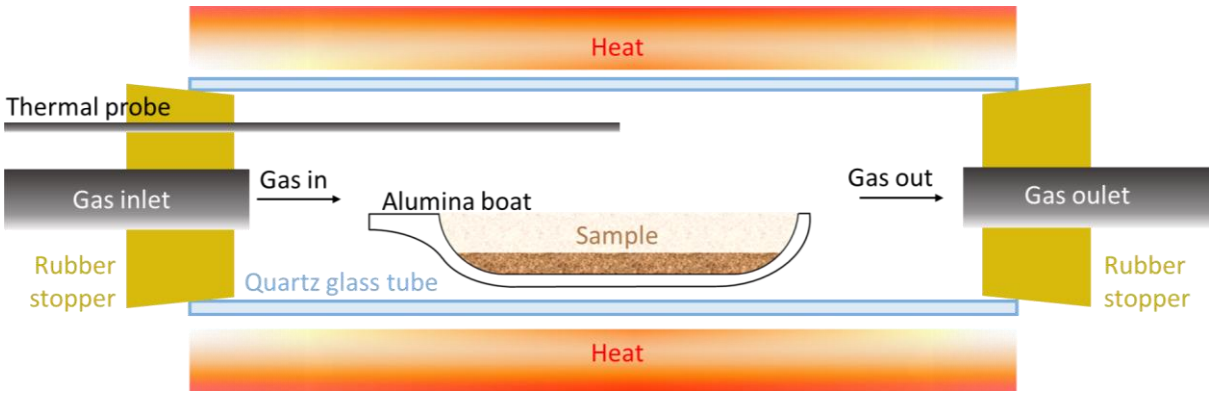

Figure 4.1 | Illustration of the high-temperature gas treatment using an electric furnace.

Figure 4.1 presents a diagram of the heat treatment set-up under controlled gas environment using an alumina boat to hold the powder sample. This configuration is a standard configuration for heat treatment with powders. Alumina is thermally stable up to 1750 °C. The speed of the gas flow cannot be high, or all the powder will be gone

quickly. Also, additional external thermometers are regularly used to calibrate the temperatures recorded in the internal thermometer using a thermal probe made of thermally conductive material with high plasticity to adopt different conditions.

4.2.2. WO_3 colouration

Materials: WO_3 NPs purchased from China, Chang Sha Na Ro Mei Nanomaterials Ltd, with a purity of 99.9% and an average size of 40 nm, Ar gas and H_2 gas.

The colouration of WO_3 via hydrogenation: WO_3 was thermally treated under a mixture of argon (Ar) and hydrogen (H_2) gas environment. Ar gas was pumped at 0.11 L/min and H_2 gas at 100 mL/min, using Aalborg gas mass flow controller for each gas. The temperature in the furnace was increased up to 400 °C displayed in the furnace (this temperature was additionally monitored using external thermometer) with a heating speed of 10 °C/min and a dwell time of 60 min. Then the procedure was repeated for different temperatures: 300 °C, 325 °C, 340 °C, 350 °C and 400 °C. By following these temperatures, a gradual colour change was observed, ranging from yellowish green to dark blue as displays in Figure 4.2.

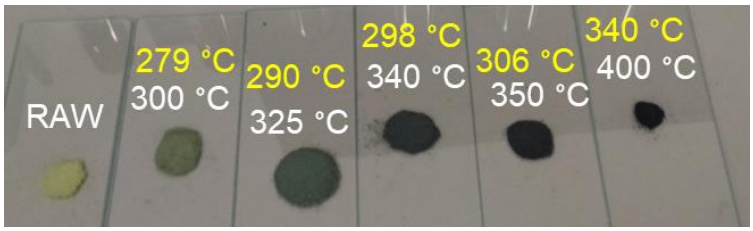

Figure 4.2 | Colouration process under different target temperatures for H_2 + Ar gas mixtu treatment. In yellow, the temperature from the external thermometer; in white, the temperature from the internal thermometer.

Heat treatment under H_2 gas atmosphere

This thermochemical colouration process has been previously reported in the literature, and it is understood that it is due to tungsten oxide bronzes formation, i.e. hydrogenation of the WO_x structure. It has been recently proven as hydrogen gas detector in thin films [318]. In Figure 4.2, the numbers in yellow are the temperatures measured with the external thermometer and in white the temperatures displayed by the furnace. There are minor discrepancies, but not the same temperature is recorded.

The samples displayed in Figure 4.2 were evaluated under XRD to understand their crystallographic structure, as seen in Figure 4.3. The main WO_3 characteristics 2θ diffraction peaks from Figure 4.3. appear at approximately 23.1°, 23.6°, 24.3°, 26.6°, 28.7°, 33.3°, 33.8° and 34.1° which are indexed as the (002), (200), (020), (210), (112), (202), (022) and (220) planes, respectively. These peaks are characteristic of monoclinic WO_3.

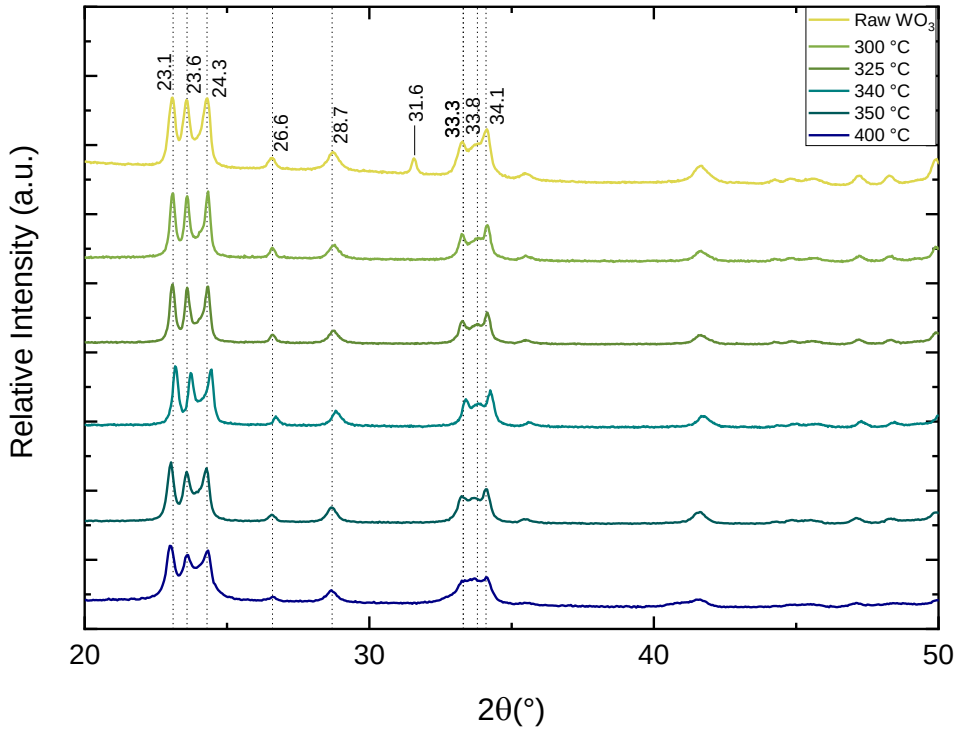

Figure 4.3 | XRD spectra of the sets of temperatures under which WO_3 has been hydrogenised.

Heat treatment under H_2 gas atmosphere

There are very small fluctuations for most peaks compared to the original WO_3 sample. However, there is a peak at 31.6 ° in the raw WO_3 that is gone already at 200 °C and does not reappear at different temperatures. It can be assigned to either (031) or (051) of monoclinic WO_3 structures. Figure 4.3 shows that once the Hydrogen starts to be absorbed by the WO_3, there is a peak that is missing. Even the darkest blue at 400 °C does not show any other distinguishable difference or pattern compared with the other XRD spectra. This peak has been multiple times dismissed in the literature due to its weak intensity, but it is present in many WO_3 profiles in the literature. Therefore, this might reflect a crystalline lattice orientation that is not trivially understood when looking at the WO_3 structure, and that is altered in the presence of hydrogen atoms. In 2018, Rinaldi et al. [317] reported an in-depth study following an almost identical experimental approach using variations of temperature of 100 °C. However, here there is a particular emphasis in seen changes at much smaller temperature increments. Therefore, the XRD results were measured at smaller angle increments to achieve higher precision at comparing the XRD patterns of each sample. Hence, the effect of small temperature changes is included in a small peak at 31 ° that Rinaldi missed probably due to lower spectral resolution. This peak could be the preeminent modification in the structure of WO_3 to induce a transition to other oxidation states. Controlling the colouration is essential to obtain also different material properties of WO_3 such as light absorbance and electrochromism.

Although this method seems very powerful for systematic oxidation state transition by oxygen reduction, there are some issues to obtain a homogeneous sample for intermediate states, as shown in Figure 4.4. There is a gradient of colouration in the final sample; therefore, only a particular region can be taken from the sample and variations in this region can limit the reproducibility of this technique.

Heat treatment under H_2 gas atmosphere

Figure 4.4 | Colouration gradient after hydrogen treatment at 340 °C.

4.2.3. γ-Fe_2O_3 transition to pure Fe

Materials: Iron(III) oxide nanopowder, <50 nm particle size (BET) from Sigma Aldrich (polydisperse commercial γ-Fe_2O_3 NPs), iron (III) chloride hexahydrate (ACS reagent 97% Sigma Aldrich), 0.054 mol of iron (II) chloride tetrahydrate (Alfa Aesar), iron (II) nitrate 9-hydrate (Sigma Aldrich), NH_4OH 25% (PanReac AppliChem), Ar gas, H_2 gas, Acetone (PanReac) and deionised (DI) water.

Synthesis of monodisperse γ-Fe_2O_3 NPs witn 11 nm in diameter: The synthesis method is the modified Massart coprecipitation method [196,214]. Briefly, magnetite NPs are prepared by mixing 0.09 mol of iron (III) chloride hexahydrate and 0.054 mol of iron (II) chloride tetrahydrate in a total volume of 488 ml of distilled water and adding all of it to 75 ml of alkaline medium. In particular, to obtain NPs around 11 nm it is necessary a slow addition (0.2 mL/s) of the aqueous solution into the base NH_4OH 25% and 1h of heating at 90ºC. After all, the black product is washed three times with distilled water using a permanent magnet to remove the supernatant. Maghemite (γ-Fe_2O_3) NPs are obtained by oxidising magnetite (Fe_3O_4) NPs previously synthesised. Fe_3O_4 NPs were synthesised by coprecipitation of 425 ml of a mixture of $FeCl_3 \cdot 6H_2O$ (0.09 mol) and $FeCl_2 \cdot 4H_2O$ (0.054 mol) in 75 ml of an alkaline medium. Slow addition rates (0.2 ml/s) and NH_4OH solutions were used to synthesise 11nm diameter NPs. After every synthesis, the particles were washed three times with distilled water and

the help of a permanent magnet. To oxidise the Fe_3O_4 to Fe_2O_3, 300 ml of HNO_3 (2 M) is added to the washed product and magnetically stirred for 15 min. After that, the supernatant is removed and 75 ml aqueous solution of iron (II) nitrate 9-hydrate ($Fe(NO_3)_3$, 1M) and 130 ml of distilled water are added. The mixture is heated until reaching the boiling temperature while magnetically stirring, and kept in these conditions after, for 30 min. When it cools down, the supernatant is removed by magnetic decantation again and 300 ml of HNO_3 2 M is added. After 15 min of magnetic stirring, the supernatant is removed and the brown product is washed three times with acetone. Finally, the acetone is evaporated and the sample is concentrated in distilled water.

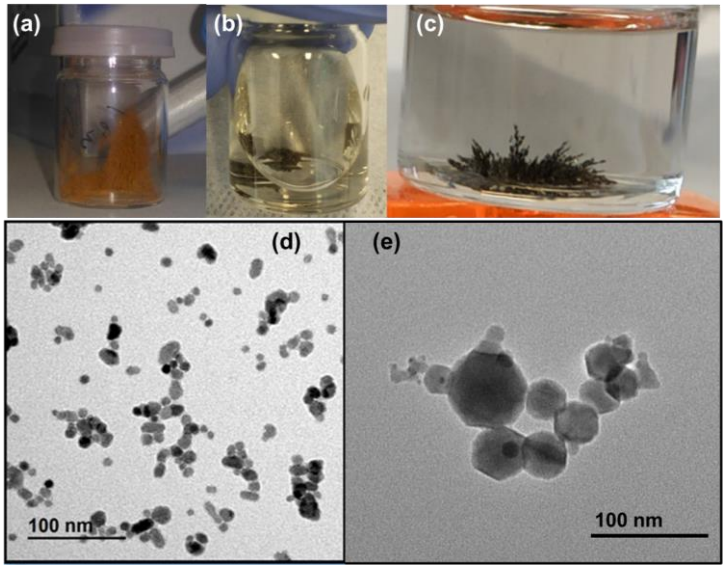

Figure 4.5 | (a-c) Pictures of raw polydisperse γ-Fe_2O_3 NPs (left) (commercially available) and treated samples under H_2 gas heat treatment; γ-Fe_2O_3 NPs treated at 240 °C (centre) and γ-Fe_2O_3 NPs treated at 380 °C (right). (d) TEM image of monodisperse γ-Fe_2O_3 NPs. (e) TEM image of polydisperse γ-Fe_2O_3 NPs.

Oxidation state change of iron oxide: γ-Fe_2O_3 was thermally treated following the same procedure described in section 4.1.2. Both polydisperse and monodisperse

Heat treatment under H_2 gas atmosphere

NPs were used to compare their different magnetic properties, further details including TEM images are presented in Chapter 6. The so-called “monodisperse” samples are not entirely monodisperse but present a minimal degree of dispersity while the so-called “polydisperse” samples are heavily polydisperse commercial γ-Fe_2O_3 NPs. The temperature was raised at a heating speed of 10 °C/min and a dwell time of 60 min targeting 240 °C to create magnetite and 380 °C to obtain pure iron. By following these temperatures, a gradual colour change was observed ranging from brown to black to shiny grey as displayed in Figure 4.5.

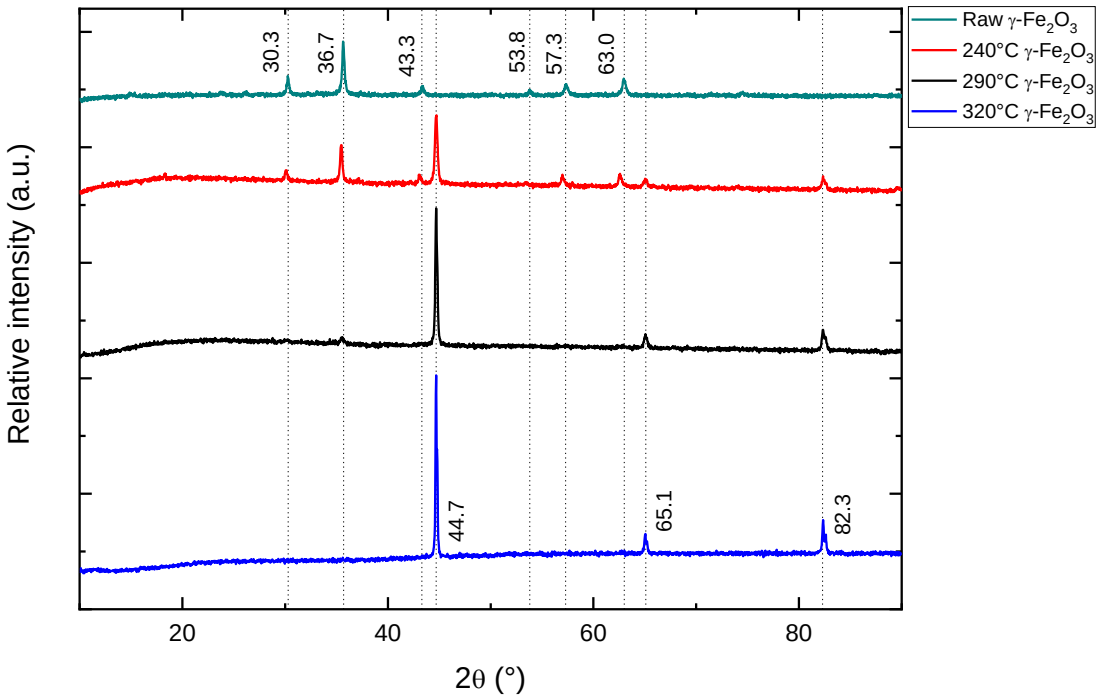

Figure 4.6 | XRD profiles of treated of γ-Fe_2O_3 and treated samples under H_2 gas heat treatment at 240 °C, 290 °C and 320 °C.

The main γ-Fe_2O_3 characteristics 2θ diffraction peaks from Figure 4.6. appear at approximately 30.3°, 36.7°, 43.3°, 53.8°, 57.3° and 63.0° which are indexed as the (220), (311), (400), (422), (511) and (440) planes, respectively. All of these peaks were the only peaks present in the raw nanoparticles before heat treatment under a

hydrogen environment. For pure body-centred cubic α-Fe, main characteristics appear at approximately 44.7°, 65.1° and 82.3°, which are indexed as the (110), (200) and (211) planes, respectively. Although, most Fe atoms would not be stable at room temperature, the samples that contained no oxygen atoms based on the XRD pattern were stable indefinitely at room temperature in dry powder and redispersed in DI water. This stability is possibly related to the fact that α-Fe, also known as ferrite, on bulk below 912 °C is a thermodynamically stable and relatively soft metal. α-Fe can be subjected to pressures up to 15 GPa, the pressure at which it transforms into a high-pressure hexagonal ε-Fe. During the reduction process under hydrogen, there is a transition from pure γ-Fe_2O_3 to pure α-Fe at 320 °C. The transition must be due to a partial reduction, which means part of the core has not undergone reduction and remains pure γ-Fe_2O_3. At the same time, there is a shell made of pure α-Fe that grows its ratio proportionally to the temperature at which the sample is exposed.

Magnetic properties measurements: IONPs magnetic properties were obtained from γ-Fe_2O_3 along with its treated counterpart at 240 °C (mixture of γ-Fe_2O_3 and α-Fe) for polydisperse samples and at 320 °C (pure α-Fe) for monodisperse samples.

Heat treatment under H_2 gas atmosphere

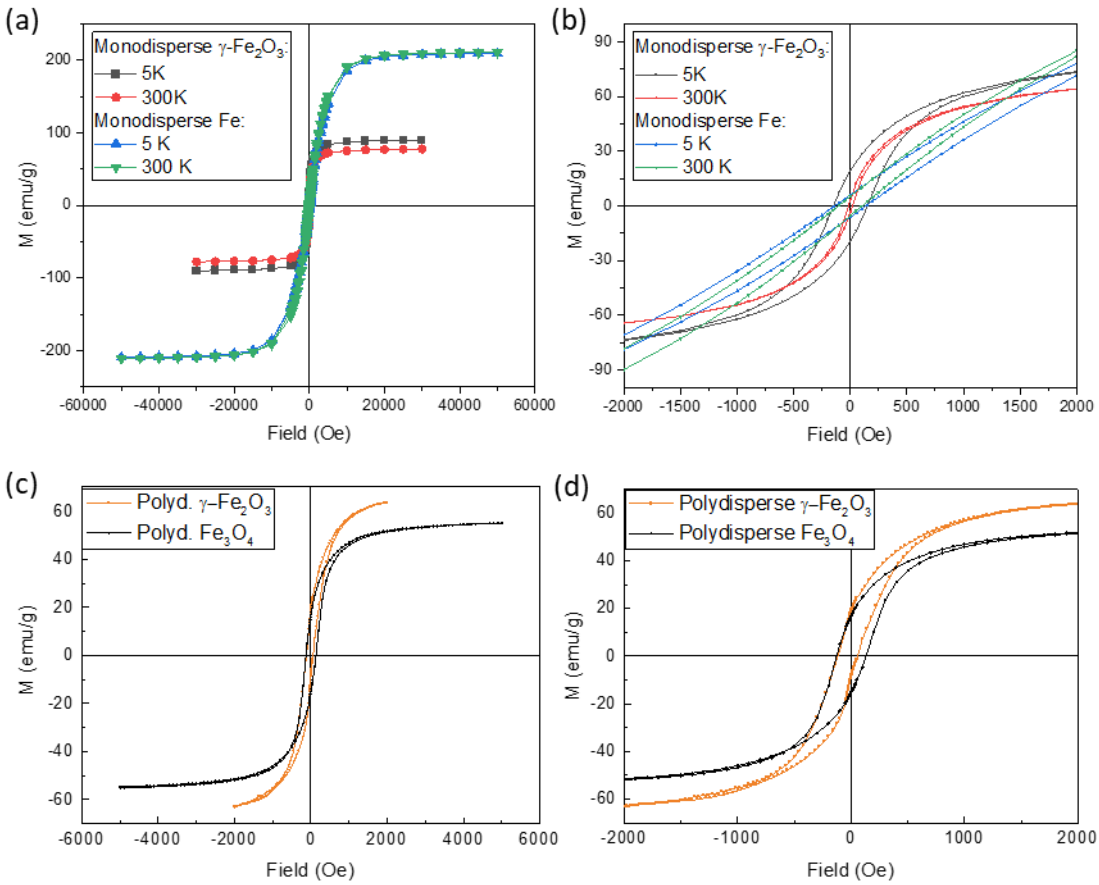

Figure 4.7 | Hysteresis loops of raw magnetic NPs and NPs under H_2+Ar gas heat treatment. (a,b) Monodisperse γ-Fe_2O_3 NPs in water solution and the treated version until reaching the Fe oxidation phase using Quantum Design MPMS-XL. (c,d) Polydisperse γ-Fe_2O_3 NPs in powder and the treated version until reaching the Fe_3O_4 oxidation phase using MicroSense EZ7 VSM.

For SQUID measurements, 1 mL of the colloidal sample was pipetted into a transparent glass vial with 12 mm diameter x 32 mm height. The increment of temperature was measured by using optical fibres. For powder samples, a known mass of the sample is added to a flat surface like a petri dish, and the increment of temperature is measured by using an IR camera, FLIR E53. Both SQUID and AFM magnetization results are displayed in Figure 4.7.

Heat treatment under H_2 gas atmosphere

These results show that the monodisperse NPs increase the magnetization power when reducing the oxidation state, while the polydisperse sample follows the opposite trend. The original loops of both polydisperse and monodisperse are very similar. However, the monodisperse sample presents a larger hysteresis loop area, and therefore better magnetic heating prospects. Moreover, the monodisperse sample presented almost no visible aggregation while kept in solution under room conditions. However, the polydisperse sample visibly aggregated at concentrations from 500 µg/mL to 30 mg/mL after short periods (from 10 min to 2 hours) which is not a desirable feature for in vivo biomedical applications.

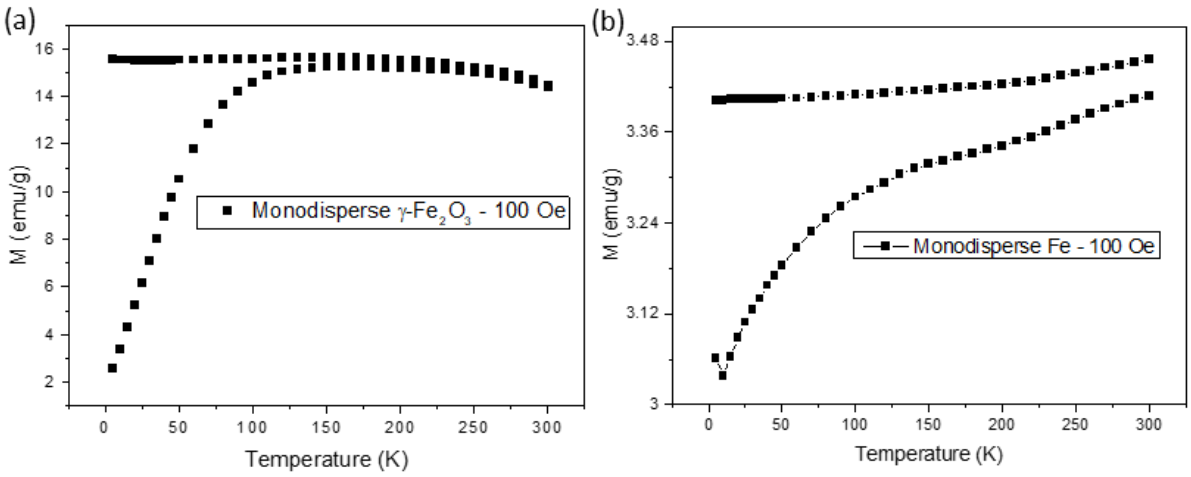

Figure 4.8 | SQUID at 100 Oe of sample curves (a) zero-field-cooled and (b) field-cooled.

Figure 4.8 shows how there is an anomalous region for pure Fe NPs at low temperatures. Also, Figure 4.8 shows how magnetization of the samples converges much faster in the γ-Fe_2O_3 sample than in the treated Fe sample. This might happen due to anisotropies generated during the conversion. Since the heat treatment is a surface-mediated technique, it is possible that some NPs were slightly less exposed to the gas and therefore are not fully converted to pure Fe but only a shell.

Heat treatment under H_2 gas atmosphere

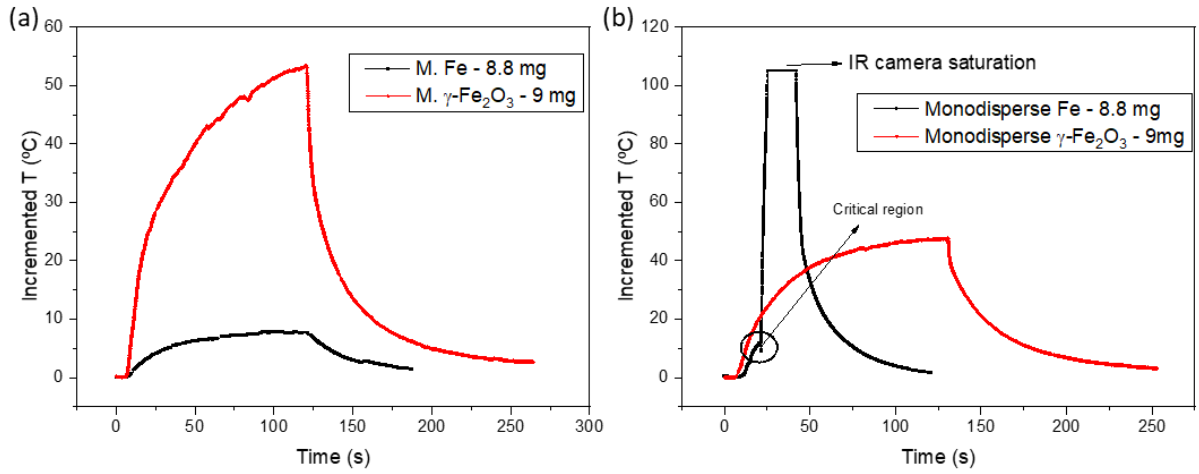

Figure 4.9 | Magnetic heat profiles using Magnetherm 1.5 from nanoTherics. (a) 525 kHz, 93 Oe. (b) 111.7 kHz, 170 Oe.

Figure 4.9 shows a rapid heat arising from the NPs which is highly dependent on the applied frequency and field intensity. For 111.7 kHz, 170 Oe if the external magnetic field increases slowly, after reaching a critical point close to the coercitive field, the heat increases very quickly until reaching the IR camera saturation.

Figure 4.9 shows that the sample containing pure Fe presents an apparent ferrimagnetic behaviour at 111.7 kHz and 170 Oe; a very high saturation magnetization around 200 emu/g (off charts) and a coercitive field of 100 Oe, which means it can be useful to reach very high temperatures in short periods. When applying fields below 100 Oe and 525 kHz, there is no intense heat for pure Fe while γ-Fe_2O_3 presents a reasonable heating rate. On the contrary, when applying fields over 100 Oe and 111 kHz, the pure Fe has a massive heat rate reaching 120 ºC in less than 10 seconds. There is a critical transition region at which the behaviour which initially would follow the single magnetic domain approximation is drastically modified probably as a result of strong Fe NPs aggregation.

4.3. Filtering nanoparticles

4.3.1. Context

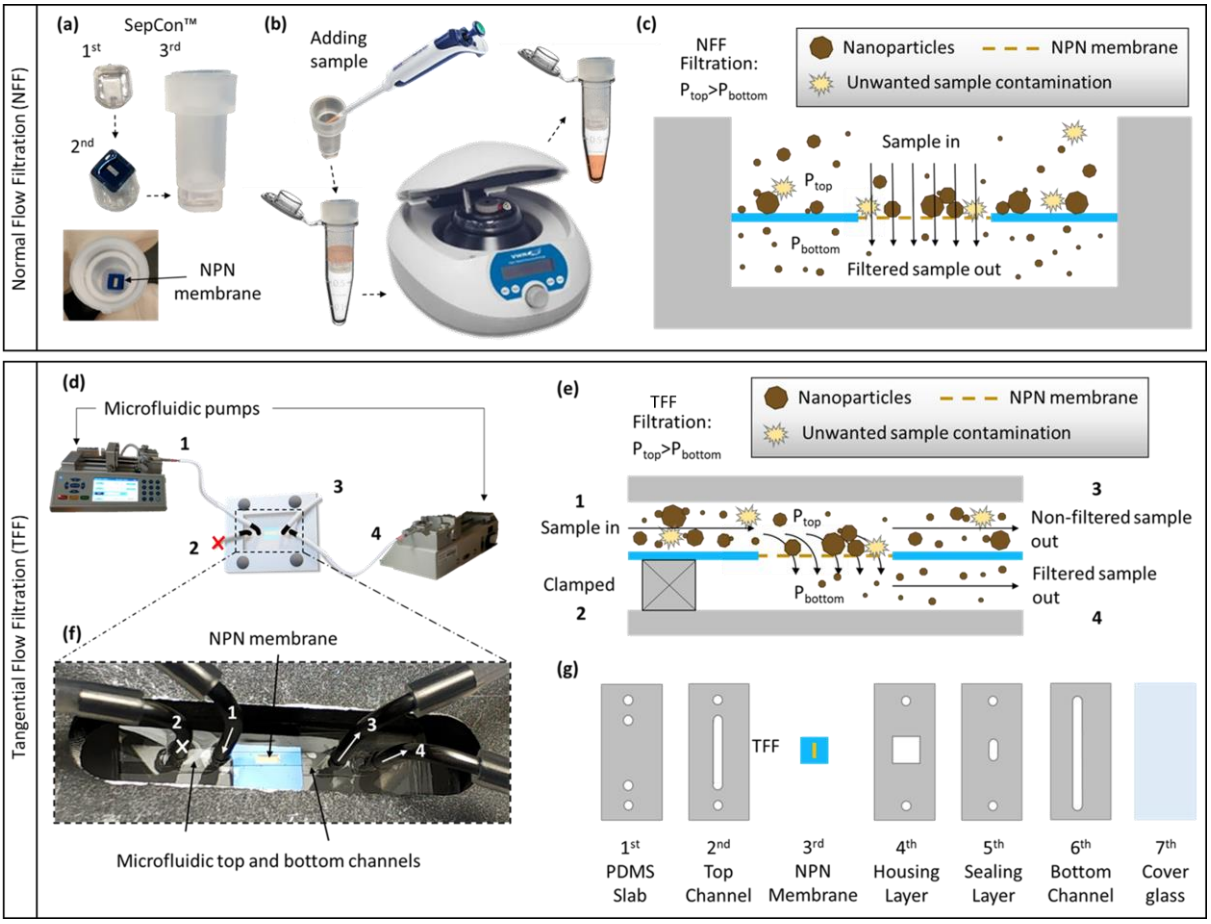

Figure 4.10 | a) Schematic of the assembly steps of the NFF separation container (SepCon™) for dead-end ultrafiltration. b) Diagram of the perpendicular flow nanosized particle separation in a SepCon™ under high-speed centrifugation. c) Schematic of the size-dependent filtration process in which the sample is passed across the surface of the nanoporous membrane. d) Schematic of the TFF microfluidic device. e) Diagram of the tangential flow filtration process in which the sample is passed across the surface of the nanoporous membrane. A transmembrane pressure (TMP) generated by syringe pumps drives the particle motion through the membrane while keeping large NPs and contaminating particles retained on the membrane surface or f) Close-up view of the membrane and microfluidic channels and other

features are patterned into PDMS sheets. g) Schematic of the stack of layers that form the TFF process, following the order in which they are assembled. These PDMS layers are assembled by stacking and clamping them.

In this chapter, the tangential and normal flows of colloidal NP solutions are studied by incorporating these nanoporous membranes in microfluidic platforms. This very high porosity is significantly better than the results reported by others in the literature [319–321]. For NFF, a fluid solution inlet containing polydisperse IONPs dispersed in water or ethanol flows perpendicularly through a selective nanoporous membrane designed to allow all the flow passing through the membrane while leaving large NPs and aggregates behind, as shown in Figure 4.10.a-c. Similarly, for the TFF design, a fluid solution inlet containing polydisperse IONPs dispersed in water flows tangentially over a selective nanoporous membrane with some fraction of the flow also passing through the membrane, as shown in Figure 4.10.d-g. These two filtration modes are designed to obtain partially purified and size-dependent filtered NPs. In this study, NPN based on pnc-Si (previously introduced in 2.16.2) were used because of the more than three times higher hydraulic permeability and its larger robustness compared to the original pnc-Si [258,322,323]. This membrane has robust chemical and mechanical properties that are inherited from the SiN, while keeping pores small enough for ultrafiltration (<100 nm) with a porosity reaching 40%.

UF has been widely used in the preparation and purification of NPs after synthesis, particularly for iron oxide and metallic NPs [324–326]. However, the primary purpose of this nanomaterial filtration was to separate the NPs from smaller molecules. Here this filtration is proposed for size selectivity of polydisperse maghemite (γ-Fe_2O_3) NPs to obtain monodisperse colloidal NPs in different ranges of sizes depending on the nanopore size. γ-Fe_2O_3 is frequently used for biomedical applications due to its

high stability and intense magnetic moment, which makes it a great candidate for both magnetic resonance imaging (MRI) and magnetic hyperthermia [43,327]. The size control using ultrathin nanoporous membranes can lead to physical nanosizing automatization, which can fundamentally transform the way NPs are synthesised and can accelerate their commercialization and end-use in the clinic. This goal requires the integration of fabricated thin, robust nanoporous membranefs into microfluidic platforms which allows a systematic filtration process that is simple, fast and reproducible.

4.3.2. Experimental setup

The experiments presented in this section were performed in collaboration with Kilean Lucas from the University of Rochester.

4.3.3. Before filtration

The sample used in this study was the highly polydisperse iron oxide (γ-Fe_2O_3, maghemite) from a commercial source from the previous section. These nanoparticles are highly polydisperse, as shown under TEM in Figure 4.11a and its interplanar distance is 0.25 nm displayed under HRTEM in Figure 4.11b. The NPs were used from a stock solution (200 mg/ml) at which they present strong aggregation and agglomeration due to the ferrimagnetic behaviour of the particles of the sample larger than 20 nm. Reduction of both polydispersity and aggregation are key challenges that most scientists working with magnetic NPs have to deal with, particularly those working with fully or partially ferrimagnetic samples. As a first step, to achieve a more monodisperse and less aggregated colloidal solution, the sample concentration was reduced and redispersed with ultrasound for over 10 min. This helped to reduce substantially visible agglomeration, but it was not strong enough to break the

aggregates. Hence, further membrane filtration steps were implemented to achieve higher purity and monodispersity.

The γ-Fe_2O_3 NPs have an average size of 34.3 ± 0.1 nm with an extremely high polydispersity (Figure 4.11c), analysed over a population of 250 NPs. As shown in Figure 4.11d, the sizes fit reasonably well to a Lorentzian behaviour with some deviation that can be due to not using a sample representative enough, having 1 nm bias and the roundoff error while removing all decimals for the bar plot representation.

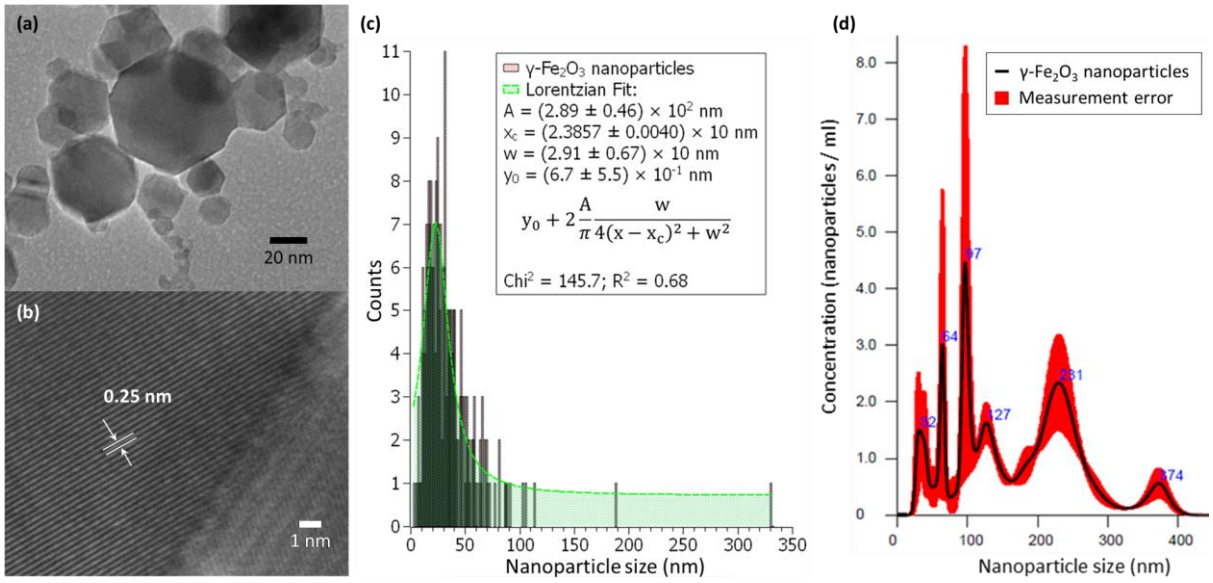

Figure 4.11 | a) TEM image of the polydisperse γ-Fe_2O_3 (<50 nm) NPs over a carbon-coated TEM grid. b) HR-TEM image of the γ-Fe_2O_3 material. c) Histogram of 250 NPs sizes counted from TEM images of the polydisperse sample before filtration. d) NanoSight measurements of averaged finite track length adjusted (FTLA) concentration (particles/ml) versus size (nm) of polydisperse γ-Fe_2O_3 (<50 nm) NPs before filtration. The average values were calculated from three measurements.

Therefore, this semi-Lorentzian trend achieves values in the right-side tail that deviates far from the mean value, mode (31 nm) and x_c. These relatively large NPs

are indeed a problem for any biomedical application since they act as highly intense ferrimagnetic attractors of the other magnetic NPs. The NanoSight measurements provide insightful information about the behavior of the NPs while they are suspended as colloidal NPs. Unfortunately, these results have significant uncertainty and a limited range of size readings. Further details of the crystallographic structure are displayed in the Figure 4.11b and 4.6. The peaks from the XRD pattern confirm that the iron oxide phase present in this material is solely maghemite (γ-Fe_2O_3).

The Lorentzian fit follows formula displayed below:

$$y_0 + 2\frac{A}{\pi}\frac{w}{4(x - x_c)^2 + w^2} \tag{4.3.1}$$

Lorentzian fit parameters from Figure 4.11c: A (amplitude) = 289 ± 46, x_c (center) = 23.8567 ± 0.040, w (width) = 29.1 ± 6.7, y_0 (offset) = 0.67 ± 0.55, R^2 = 0.68.

Comparing results from Figure 4.11c and d, it can be inferred that the NPs suffer high aggregation and agglomeration. Most of the NPs are found forming aggregates and agglomerated regions around 127 nm and 231 nm, while there is only a small number of non-aggregated NPs smaller than 50 nm. However, the NanoSight measurements only can detect NPs sized from 10 nm to 1 µm in optimal conditions which include non-aggregated samples and optimised concentration to differentiate NPs from each other. However, the TEM image in Fig 4.12.a shows that there exist NPs smaller than 10 nm. Therefore, these smaller NPs cannot be detected using NanoSight, neither some large magnetic NPs that are close to the micron range. Most aggregates are caused by large NPs that display stronger effective magnetization and ferrimagnetic behaviour which leads to permanent magnetic forces that attract magnetic particles. Agglomerations while in the colloid around 374 nm exist but

account for a small quantity of them; however, they are likely to be the many sources of both aggregation and subsequent agglomeration. For most biomedical applications, these large NPs will need to be removed before proceeding any further to prevent high toxicity. That is the reason for us to conduct the investigation of particle filtrations.

4.3.4. After filtration

To effectively filter these NPs, the NPN membranes displayed in Figure 4.12a and b were used. Mainly, to have two-step filtration that shows its effectiveness, the hole diameter profiles of each membrane must be significantly different from each other. This means minimised overlap between holes diameter distribution of all membranes and high monodispersity of each membrane individually.

Figure 4.12c,d shows how the holes present Gaussian distributions with minimal overlapping and low polydispersity. Moreover, our sample's distribution (Figure 4.11c) is broader and polydisperse enough to cover both hole diameter distributions. The approximated Lorentzian fit that the NPs size distribution follows in Figure 4.11c covers both Gaussian fits represented in Figure 4.12c and d.

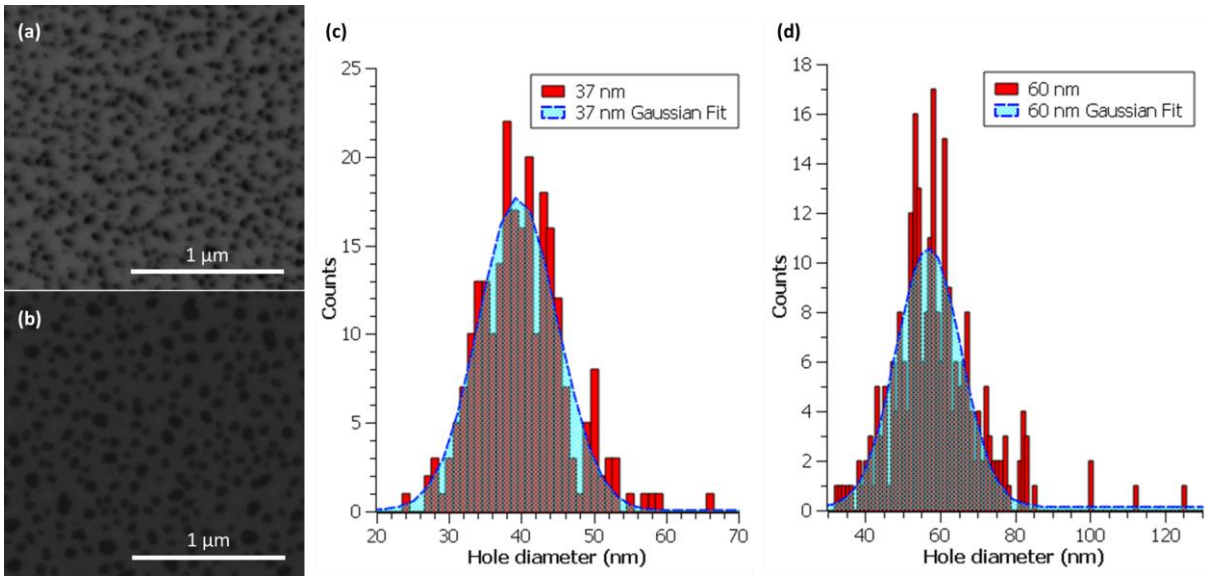

Figure 4.12 | a) SEM image of the NPN membrane with 37 nm average pore diameter. b) SEM image of the NPN membrane with a 60 nm average pore diameter. c) Histogram of 250 nanopores counted from SEM images of 37 nm nanopore size NPN membranes applying a gaussian fit under the scaled Levenberg-Marquardt algorithm. d) Histogram of 250 nanopores counted from SEM images of 60 nm nanopore size NPN membranes applying Gaussian fit under the scaled Levenberg-Marquardt algorithm. Results obtained with TESCAN VEGA3 SEM.

The Gaussian fit follows the formula displayed below:

$$y_0 + \frac{A}{w}\sqrt{\frac{2}{\pi}}\, e^{-2\left(\frac{x-x_c}{w}\right)^2} \tag{4.3.2}$$

The Gaussian fit parameters using scaled Levenberg-Marquardt algorithm with tolerance = 0.0001 in the range x = 1 - 200 nm for the 37 nm nanopore membrane are the following: A (amplitude) = 242.3 ± 6.3, x_c (center) = 39.53 ± 0.15, w (width) = 10.93 ± 0.31, y_0 (offset) = 0.039 ± 0.083, R^2 = 0.93. For the 60 nm nanopore membrane, the parameters are the following: A (amplitude) = 226 ± 13, x_c (center) = 56.95 ± 0.48, w (width) = 17.2 ± 1.0, y_0 (offset) = 0.12 ± 0.13, R^2 = 0.82.

Therefore, by filtrating this sample with first the larger pores, subsequently followed by the smaller pores, the sample can separate in different size ranges. Figure 4.13 from the supporting information provides further insights about the topology of the membrane. Besides the NPN membrane nanopores are not fully represented under the AFM profile, the depth of the membrane appears to be around 40 nm which is the same order of magnitude as 100 nm thick NPN reported previously [316,322]. The

difference in this value is due to high uncertainties in the tips due to their large diameter, similar to the holes themselves.

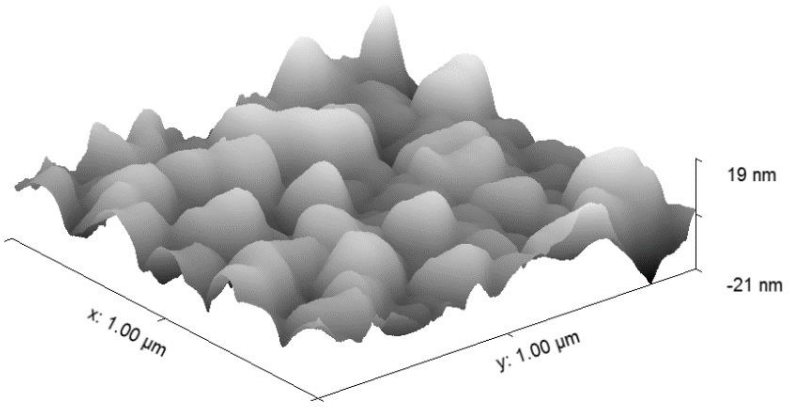

Figure 4.13 | 3D AFM topographic profile for the 60 nm nanoporous membrane obtained in collaboration with Iago Fernandez.

The NPN membranes shown in Figure 4.14 were used to filter the sample from Figure 4.13, and the resulting samples are displayed in Figures 4.14 and 4.15. Comparing the filtered samples from figure 4.12b-e and the original sample (Figure 4.12a), it is clear that the NPs were highly filtered through all the processes. Figure 4.12a shows how the hydrodynamic diameter of the colloidal magnetic NPs is significantly reduced from every filtration step in NFF. These results show a consistent and reproducible size filtration and agglomeration reduction in both normal and tangential flow filtration, but each of them present advantages in some aspects and drawbacks in others. Comparatively, to reduce agglomeration and the number of aggregates, the TFF results in one-step filtration in water with 60 nm pore size are as good as the two-step filtration in water with NFF SepCons^{TM} using first 60 nm and the 37 nm pore size, and better than using ethanol as the liquid media. Although the TFF device does a better job reducing agglomeration of NPs once filtered, this process is much slower, expensive and sophisticated compared to the using the SepCon^{TM} spin

columns, but it allows potential series tandem filtration. To maximise the quality of the filtration process, a reasonable approach would be applying a series of TFF filtration steps incorporated in a microfluidic device. On the other hand, cake formation played a significant role in both TFF and NFF in stopping the sample from being filtered. In NFF, this effect resulted in the membrane breaking due to accumulated mechanical stress as previously reported in these types of membranes [328]. Hence, all filtrations had to be performed at very low concentrations for both modes and solvents. Interestingly, ethanol, which has lower surface tension than water, offers slightly worse filtration but was found to be much faster and simpler by not requiring centrifugation. When using ethanol, gravity is strong enough to overcome the surface tension for the solution to pass through the membrane and perform the filtration of the sample. It would be beneficial to not only obtain the DLS results from the filtered samples but also their NP concentration versus size profiles from NanoSight. Unfortunately, this was not possible due to ending with a very diluted sample that was not readable using Nanosight. An iterative process of filtrating and concentration of the sample could be done in future studies to corroborate these results.

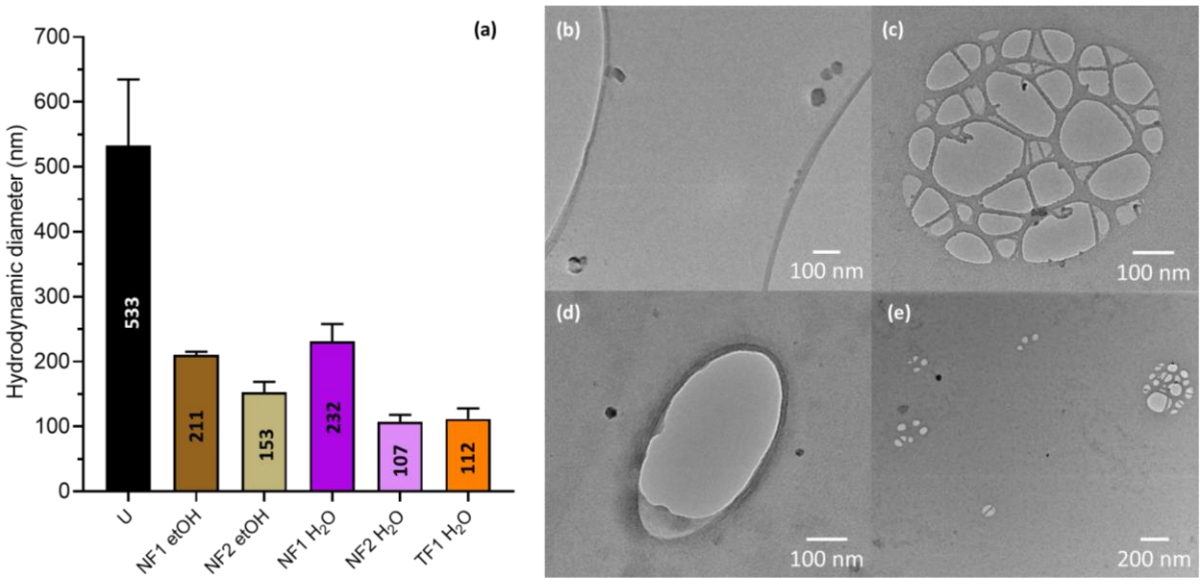

Figure 4.14 | (a) Bar chart of average dynamic light scattering (DLS) value of three measurements that represent the hydrodynamic diameter of polydisperse Fe_2O_3 (<50 nm) NPs at different filtration steps. The error bars presented are the standard deviation of 3 repeats for each value. U: Unfiltered NPs in EtOH. NF1 EtOH: Filtered gravitationally via SepCon™ with 60 nm nanopores in EtOH. NF2 EtOH: Filtered gravitationally via SepCon™ with 37 nm (gravity) in EtOH after 60 nm. NF1 H_2O: Filtered at 500g centrifugation speed for 4 minutes via SepCon™ with 60 nm nanopores in H_2O. NF1 H_2O: Filtered at a500g centrifugation speed for 4 minutes via SepCon™ with 37 nm in H_2O after SepCon™ after 60 nm. TF1 H_2O: Tangential flow 60 nm in H_2O. TEM images of polydisperse Fe_2O_3 (<50 nm) NPs resulting after filtration over a carbon-coated TEM grid: (b) SepCon™ of ~60 nm holes centrifuged at 500 g (g-force) in water; (c) SepCon™ of ~60 nm holes first and ~37 nm holes after centrifuged at 500 g (g-force) both in water; (d) Tangential flow with ~60 nm membranes in water; (e) SepCon™ of ~60 nm holes first and ~37 nm after without centrifuging in EtOH, filtered just by gravity.

By analysing multiple TEM images from the filtered NPs, 25 NPs were identified per filtered sample to compare relative filtration between two-step filtration in NFF SepCon™ and one-step filtration in TFF. These results can be seen in Figure 4.15.a-c and lead to a deeper understanding of the filtration process. The hydrodynamic radius from one-step TFF filtration in water with 60 nm nanopores is reduced similarly to two-step NFF filtration in water with 60 and 37 nm nanopores and better than in ethanol with 60 and 37 nm nanopores. However, the actual NPs appear to be significantly better filtered from both two-step SepCon™ NFF filtrations (see Figure 4.14a and b) than from one-step TFF filtration. The NP agglomeration and aggregates, therefore, were better removed from the filter in TFF, but the actual size filtration of

single NPs remain dependent exclusively on the size of the nanopores and not on the filtration mode.

Interestingly, in TFF using a 60 nm NPN membrane only (Figure 4.15c), no NP larger than 37 nm was found which suggests that larger NPs tend to aggregate and get captured on the nanomembrane surface and holes. Contrarily, using SepCon™ under two-step NFF filtration with 60 and 37 nm in series (Figures 4.15a and b), there exist some NPs larger than 37 nm which might be due to the excessive pressure when using water under centrifugation and low surface tension when using ethanol as a medium. Moreover, when using two-step filtration in NFF most NP sizes range from 4 to 24 nm in water with local maximum values at 10 nm and 20 nm, and 8 to 35 nm in ethanol with a maximum value at 11 nm. Meanwhile, after one-step TFF filtration, the sizes were concentrated in the range of 17 to 37 nm with a maximum value at 27 nm. These results emphasise the idea that the actual NP size filtration depends primarily on the nanopore size but seems better-filtered underwater which is consistent with the DLS results from Fig 4.15a.

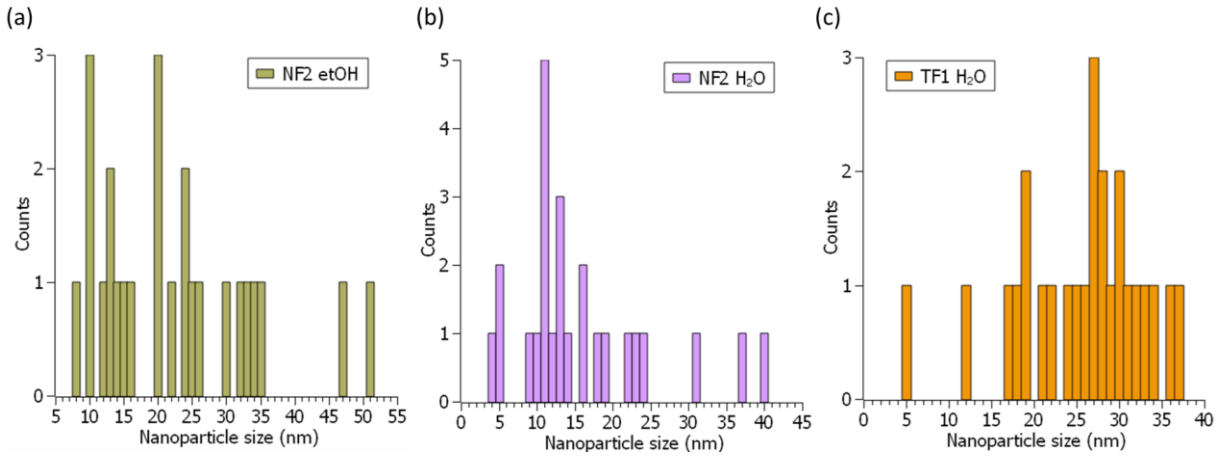

Figure 4.15 | Histogram of 25 NPs sizes counted from TEM images of the polydisperse sample after filtration for different filtration processes (counts of NPs against NP size):

(a) NFF SepCon^{TM} two-step filtration in ethanol by gravity under 60 nm nanomembrane followed by 37 nm nanomembrane. (b) NFF SepCon^{TM} two-step filtration in water by centrifugation under 60 nm nanomembrane followed by 37 nm nanomembrane. (c) TFF one-step filtration in water by centrifugation under 60 nm nanomembrane.

Moreover, a comparison between Figure 4.11c and Figure 4.15a-c shows the much lower concentration of filtered samples compared to the stock. Both filtration modes required low NP concentration before filtration and produced an even lower concentration after filtering the sample. Therefore, there are some limitations to apply this method at the early steps during the synthesis of NPs since most of them require high concentrations that would be diluted in the final steps. Working at low concentrations in early synthetic steps require a posterior concentrating method that might lead to further aggregation would substantially increase the synthesis time. Furthermore, washing steps during the synthesis of NPs by using decantation usually includes sample loss and reduction in concentration, therefore working at very low concentrations would be a risk and disadvantage if it were required after filtering using the membranes. However, this filtration would be beneficial for final steps during the synthesis when there is no need to work at high concentrations.

Finally, Figure 4.16 shows another important of the membranes - not only for the filtration of aggregates and selective reduction of NP sizes but also for purification of the samples by removing unwanted microscopic contamination. Figure 4.16 displays two zooming sequences of SEM images taken at different magnifications without coating the membranes with Au to achieve better contrast between different materials. Figure 4.14a-d displays a nanoporous membrane with a 60 nm average

nanopore size after filtration and was obtained after using a NP concentration of 20 mg/ml (1:10 from the stock solution). Figure 4.16 shows more in detail how the captured NPs on the membrane looks like after filtration.

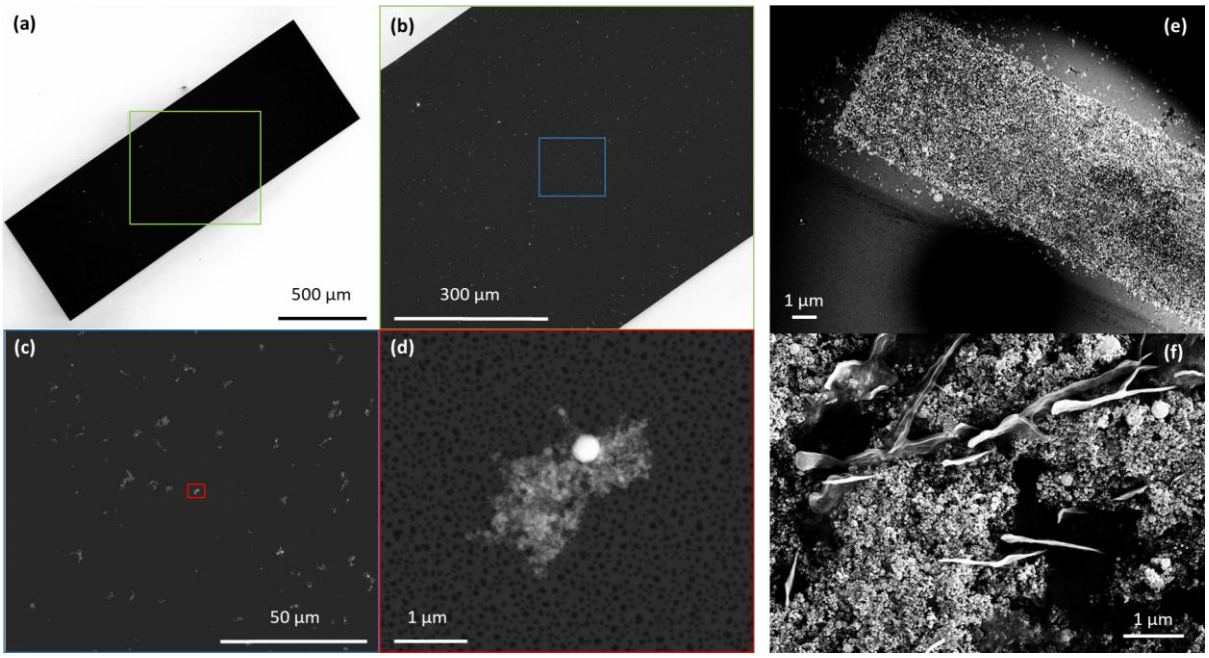

Figure 4.16 | SEM images of the bare nanoporous membrane after NP filtration in NFF SepCon^{TM} devices. Using TESCAN VEGA3 SEM: (a-d) 60 nm average nanopore size from low magnification to high magnification, respectively. Using Zeiss Auriga FIB-SEM and 4 nm Au coating: (e) Low magnification image of the full membrane covered on NPs. (f) Sample contamination.

4.4. Summary

In summary, WO_3 NPs were coloured by an apparent hydrogenation process by performing heat treatment under H_2+Ar gas atmosphere. The resulting NPs were stable for long periods of time. For γ-Fe_2O_3 NPs, following the same procedure, there is an apparent reduction to pure α-Fe NPs at 320 °C which contains a mixture of both materials for temperatures below 320 °C. These α-Fe NPs were also very stable for

as long as were tracked (over several months) and presented substantial magnetic properties compared to the original γ-Fe_2O_3 NPs. α-Fe NPs dispaly notably higher heat rate than γ-Fe_2O_3 NPs when applying fields over 100 Oe and 111 kHz, the pure Fe has a significant heat rate reaching 120 ºC in less than 10 seconds. This opens the door to tuned heat rate by obtaining particular ratios of γ-Fe_2O_3 and α-Fe in the same NP.

In terms of NP filtration, two nanoscale size-controlled filtration methods in NFF and TFF have been implemented and compared for polydisperse colloidal magnetic NPs using ultrathin nanoporous membranes in microfluidic devices. These methods can be applied for automated biomedical NP filtration during NP synthesis and purification purposes after the synthesis to obtain monodisperse samples with better biomedical applicability prospects. This filtration is effective when no high concentrations of NPs are required in subsequent synthetic steps. TFF brings a higher degree of filtration but at the expense of higher complexity for the assembly, longer filtration time and not currently commercially available. These advantages make these TFF and NFF filtration devices promising micro platforms for size selectivity and purification of biomedical magnetic NPs. Concretely, monodispersity can help improve consistency in various techniques including SERS, MRI, CT and magnetic hyperthermia. Different degrees of dispersity of magnetic nanoparticles are evaluated to play a role of magnetic cores in core-shell structures for these techniques in chapter 6.

5. Novel WO_3-SiO_2-Au

5.1. Introduction

This chapter presents the successive steps to produce a new composite NP (see Figure 5.2) that displays prominent biomedical properties. These composite NPs were prepared by following modifications of the Stöber process for the intermediate SiO_2 shell formation and the Turkevich method for the external Au coating generation. 4-mercaptobenzoic acid (4-MBA) molecules Raman reporters are attached over this Au final layer that enhance the Raman signal via surface plasmons (SP) over the metal substrate.

Currently, there is a lack of variety in diagnostic NPs to form the core of a diagnostic agent. The only clinically approved material is IONPs, although the body cannot break them down and need to be excreted to avoid toxic effects. Furthermore, this material has a toxicity problem related to strong magnetic NPs aggregation. This severe aggregation also appear when synthesising a single-core magnetite composite. Besides the fact that some methods can achieve very small individual monodisperse magnetite NPs which reduce the magnetization, the need for elaborating tuning of the physiochemical and surface properties generate complications to keep small sizes. This fact brings the needs of designing and synthesising new alternative composite NPs for diagnosis.

Combining different functionalities in the same nanoscaled object has become one of the main goals for nanotechnology medical applications, bringing the need to fabricate nanocomposites which are a combination of different NPs to merge their individual phases. Indeed, the most extended and reliable kind of nanocomposites for SERS is the colloidal core-shell nanocomposites with a magnetic core and

functionalized surface, as described in Figure 5.1[329]. A magnetic core is needed to achieve hyperthermia after SERS imaging and then having a theranostic material. WO_3 have shown low magnetic susceptibility, and thus a high magnetic field is required for magnetic heating. However, this could lead to better-controlled form of heating than high thermal damage produced with IONPs [330] which frequently also damage healthy cells [331].

WO_3 is a semiconductor what leads to the possibility of being easily doped to change several functional properties. Doped WO_3 species have displayed even more promising electrochromic and magnetic properties so an alternative core could be easily introduced in the scheme from Figure 5.2 to satisfy any particular need such as magnetic susceptibility for hyperthermia treatment and magnetic delivery[332]. The SiO_2 nanoshell reduces its cytotoxicity drastically, and the finally AuNS makes it non-cytotoxic while retaining the capacity of getting good SERS under near-infrared light. The external Au behaves in such a way that there is a significant Raman signal enhancement without generating photoinduced heating. Also, the chosen core could be electrically activated to display electrochromism if the SiO_2 shell is thin enough to let electron transmission or if some Au NPs were in touch with the core. Besides, some studies have shown certain links between colour change and static magnetic fields that need to be better understood. Moreover, big sizes (larger than 100 nm) are hard to excrete by humans and this increase drastically their toxicity as described in section 2.3. Liver accumulation suggests that the hepatobiliary system is the primary site for agent clearance for AuNPs from 10-250 nm [333]. It has been found that reduction in size for the most used type of iron oxide-based nanocomposites for delivery is challenging and, therefore, its toxicity is higher than for smaller composite NPs. Nonetheless, WO_3 that has been reduced to sizes of 20 nm with a significant reduction

in renal toxicity during the elimination process[334]. These are the main reasons to explore new possible options to overcome this critical issue such as WO_3.

Figure 5.1 shows the final composite core-shell WO_3-SiO_2-Au NP proposed for synthesis in this chapter that potentially will be attached to the cancer cells external surface or endocytosed in a human body for SERS imaging. For this configuration, the maximum of absorption in the Au surface is supposed to shift from 532 nm light, which would be plasmonic resonant for green light laser, to redder wavelengths closer to NIR. For biomedical imaging through biological tissue, it is necessary switching to NIR lasers in order to penetrate all the layers and reach the NPs.

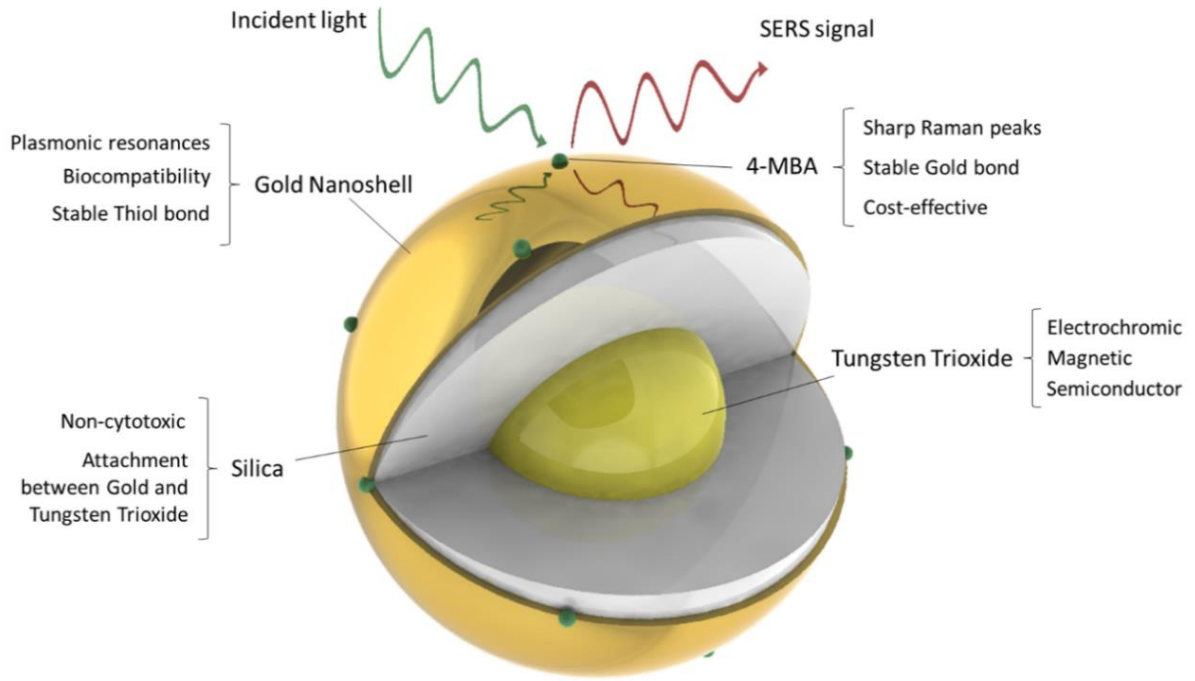

Figure 5.1 | Diagram of the final WO_3-SiO_2-Au NPs for SERS imaging and their most relevant characteristics for biomedical imaging.

In the last decade, AuNSs with SiO_2 cores have been prepared and characterised, obtaining desirable properties[335]. The SiO_2 synthesis was firstly

reported by Stöber[151], and our procedure is a modification of this method to wrap a third material core, the final nanocomposite is WO_3-SiO_2-Au NPs where WO_3 is the core. In Figure 5.2, the description of the full process is displayed. The election of a specific core relies on its individual properties such as small size, semiconductivity and magnetic susceptibility. WO_3 is an electrochromic material whose nanopowder non-calcinated version has a yellow colour, and in the presence of an electrical current can change it, this ability has been widely studied previously[336,337]. The WO_3 core can be easily substituted by other semiconductor material with for instance magnetic moment. Characteristics of toxicity, biocompatibility, light absorption, plasmonic generation, electrochromic effect and easy fabrication reproducibility need to be discussed in detail to understand the benefits of using this novel structure.

5.2. WO_3-SiO_2-Au synthesis method

Materials: All the following reagents were purchased from Sigma-Aldrich: Gold(III) chloride hydrate ($HAuCl_4.xH_2O$, 99.999% trace metals basis MW 339.79 g/mol), Tetrakis (hydroxymethyl)phosphonium chloride solution (THPC, 80% in H2O), (3-Aminopropyl)triethoxysilane (APTES), potassium carbonate (K_2CO_3, 99.995% trace metals basis MW 138.21 g/mol), sodium hydroxide (NaOH, Sigma-Aldrich), potassium carbonate (K_2CO_3), formaldehyde (CH_2O (H-CHO)), 4-mercaptobenzoic acid (MBA), deionised water, ethanol and formaldehyde solution. The WO_3 NPs were purchased from China, Chang Sha Na Ro Mei Nanomaterials Ltd, with a purity of 99.9% and an average size of 40 nm.

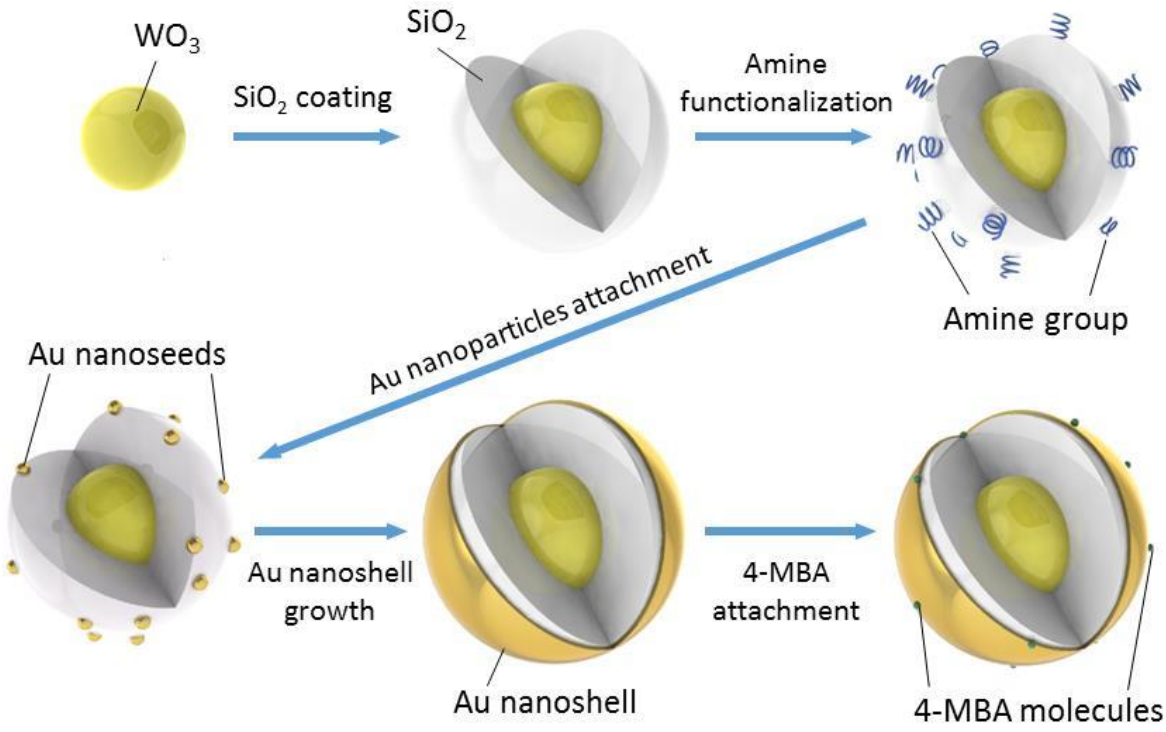

Figure 5.2 | Diagram of the WO_3-SiO_2-Au core-shell composite NPs synthesis process with 4-MBA Raman reporters.

SiO_2 nanoshell formation: The first step was the synthesis of the WO_3-SiO_2 core-shell nanocomposite NPs (Figure 5.2), following the Stober process. A liquid suspension made of 10 mL deionised (DI) water, 20 mL ethanol and 0.015 g WO_3 NPs were first prepared, then a modified Stöber process promoted the formation of the SiO_2 shell via the sol-gel method. In this method, consecutive hydrolysis and condensation of alkoxysilanes in an aqueous-alcoholic solution in the presence of a base catalyst was involved, using tetraethyl orthosilicate (TEOS) as alkoxysilane and ammonia as the base catalyst.

In this thesis, a different route from other Stöber-based versions was taken to perform the SiO_2 synthesis while in parallel coating the core. WO_3 NPs were coated with SiO_2 by adding 1 mL ammonia and 5 drops of TEOS while stirring the WO_3

suspension with a time interval of 10 sec between each TEOS drop. This was the key to create the SiO_2 coating because by changing the concentration of TEOS the SiO_2 thickness could be modified. After that, the mixture was stirred continuously for 30 more min. The ammonia concentration catalysed this reaction by increasing the reaction rate. Finally, the suspension was washed with deionised water and Ethanol by centrifugation to separate the NPs from the liquid in 50 mL Eppendorf tubes.

Amine functionalisation: The WO_3-SiO_2 core-shell nanocomposite surfaces were functionalized with an amine group. First, 0.015 g WO_3-SiO_2 core-shell nanocomposites (Figure 5.2) was dispersed in 20 mL of ethanol in a beaker and subjected to 30 min ultrasonic probe treatment. Then, 500 µL of APTES was added to the suspension which was heated to 70 °C under the magnetic stirring for 5 h. To remove the excess reactants, the suspension of 25 ml ethanol was centrifuged for 3 times (10 min per cycle at 6,000 rpm) without washing and redispersed by ultrasonic probe treatment.

The critical aspect of this functionalization was the NH_2 ending on top[169]. These NH_2 ligands reacted with Au after breaking it in two parts by heating. On one hand, H_2 was released on one side when the H atoms absorbed higher energy than the bond. On the other hand, a firm bond was created between the N and the Au atoms that were close enough to be attracted by the electric force of the N^{2-} ions and the Au electron cloud. This fact made it possible to attach Au nanoseeds and to stabilise subsequent Au growth on top with homogeneous distribution.

Colloidal WO_3-SiO_2-Au NPs fabrication: Colloidal Au NPs can be obtained following different methods, which are based on the work of Turkevich *et al.*[132]. Herein they were NP obtained by reducing Au salts ($HAuCl_4$) in the presence of surfactants,

tetrakis (hydroxymethyl) phosphonium chloride (THPC, $C_4H_{12}ClO_4P$)[282]. During the formation of the metallic solution, a massive excess of NaOH was formed. The reactions between THPC and NaOH produced formaldehyde as the reducing agent for Au. After the amine functionalisation, the Au coating process is implemented.

By dissolving 0.098 g of $HAuCl_4 \cdot 3H_2O$ in 10 mL of deionised water, a 25.0 mM Au stock solution was prepared, called chloroauric acid. By typical reducing the chloroauric acid with THPC, the colloidal Au NPs (13 nM) was prepared. In detail, 3 mL of 1 M NaOH (0.2 g in 5 mL deionised water) and 1 mL of diluted THPC (12 µL of 80% THPC per 1 mL of deionised water, 50mM) were added to 44 mL of deionised water while being stirred. The solution was magnetically stirred for 5 min and 2 mL of the 25 mM Au stock solution was rapidly added in and the colour quickly changed to dark red or brown. The final Au colloidal was stored at 5 °C for 12 h, prior to being used for later Au coating process.

5 mL of the amine functionalised SiO_2 core-shell nanocomposites suspension of 70 °C was added to 20 mL of magnetically stirred Au colloidal NP of 100 °C, and then continuously stirred for 10 min. The resulting colloidal suspension NP was washed with deionised water under centrifugation for 3 times at 6,000 rpm for 10 min each time, to remove the excess of reactants.

Au shell synthesis: Once the Au nanoseeds were attached to the SiO_2 nanoshell, the Au started to grow to form the final out layer[136]. The alkaline growth solution was prepared by dissolving 0.025 g potassium carbonate (K_2CO_3) in 100 mL deionised water (0.18 mM). Then 1.5 mL of 25 mM (1% w/v) of the Au stock solution was added to the growth solution, and the mixture was stirred until the yellow colloidal suspension became clear (transparent). 20 mL of this clear solution was injected with

1 mL of the WO_3-SiO_2-Au NPs suspension, then 100 µL of formaldehyde was added, and a colour change from colourless to purple was observed which is characteristic of the Au nanoshell formation. The resultant suspension was then centrifuged and redispersed in water, for later UV-vis spectrophotometry and Raman spectroscopy characterization.

Adding reporter molecule for SERS: The Au nanoshell bioconjugation was achieved by mixing 4-mercaptobenzoic acid (4-MBA) diluted in ethanol with the WO_3-SiO_2-Au nanocomposites[338]. After these synthesis steps, Thiolated WO_3-SiO_2-Au core-shell nanocomposites were obtained. Figure 5.2 (see additional information) describes the entire synthesis steps. 1 mM of 4-MBA solution was prepared by diluting an appropriate mass of the solid in ethanol. For the collection of SERS spectra, 100 µL of 1 mM solution of 4-MBA was mixed with 1 mL of colloidal Au NPs. After 5 min stirring, the mixture was centrifuged 3 times for 7 min at 4,000 rpm in 1.5 mL Eppendorf tubes, and the supernatant was re-dissolved in deionised water.

5.3. Characterisation

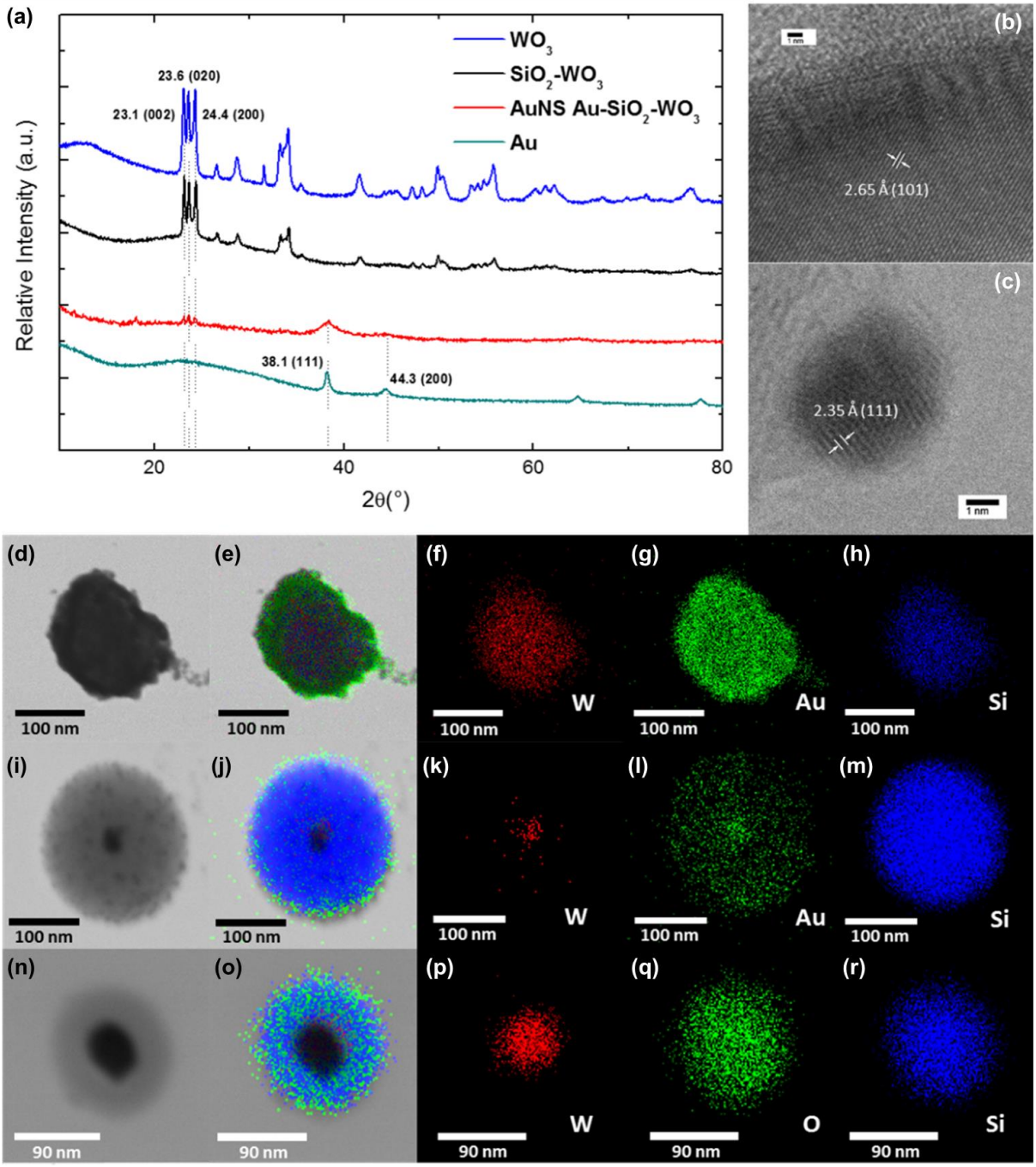

Figure 5.3 | Characterization of the nanocomposites. (**a**) XRD profiles of the WO_3, WO_3-SiO_2, WO_3-SiO_2-Au and Au. (**b**) HRTEM images of WO_3 and (**c**) Au. (**d-h**) STEM-EDX element mapping of Au nanoshell on WO_3-SiO_2-Au: STEM image, RGB overall, W, Au and Si, respectively. (**i-m**) STEM-EDX element mapping of Au nanoseeds on WO_3-SiO_2-Au: STEM image, RGB overall, W, Au and Si, respectively. (**n-r**) STEM-

EDX element mapping of WO_3-SiO_2: STEM image, RGB overall, W, O and Si, respectively.

Figure 5.3 displays the XRD patterns of the NPs from each synthesis step. The peaks in each XRD pattern reveal the crystal structure of these materials. Along with the progression, the original monoclinic WO_3 (Blue line) peaks are accompanied with lumps of the amorphous SiO_2 at 23.1° (002), 23.6° (020) and 24.4° (200) (black line), and then the cubic Au peaks appear (red line) in the composite, benchmarked against the plain Au NPs at 38.1° (111) and 44.3° (200) (Green line). The three main fingerprint peaks of monoclinic WO_3 at 23.1°, 23.6° and 24.4° are always present. This result confirms the bulk composite phase structures.

The phases identified by XRD are also verified by HRTEM imaging. The lattice spacing is 0.265 nm (Figure 5.3b) for the Monoclinic WO_3 (020) core, and 0.235 nm for the Au (111) on top of the intermediate SiO_2 shell (Figure 5.3b and c). Figure 5.3d-r shows the STEM images of the composite NPs and their corresponding energy-dispersive EDX elemental mapping results. These maps reveal the detailed distribution features of each element at the nanoscale. Figure 5.3n-r represents the first step of the synthesis and shows that the core contains W and O, while the first shell being Si and O. This is consistent with the expected WO_3 wrapped by SiO_2. Figure 5.3i-m is the Au seeding step, in which Au in green color is found surrounding the SiO_2 shell with a homogeneous distribution of small Au seeds. Figure 5.3d-h demonstrates the thick Au shell growth in green color as compared with that shown previously for the attached Au nanoseeds. Finally, the STEM-EDX and HRTEM results both confirm an average diameter of 3.5 ± 1.0 nm for the particulate Au nanoseeds.

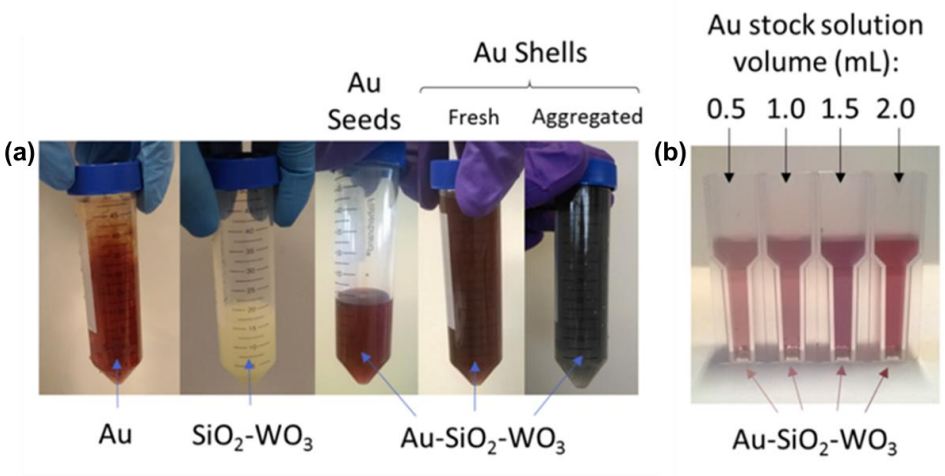

Figure 5.4 | a) Colloidal NPs solutions made of Au, WO_3-SiO_2 and WO_3-SiO_2-Au covered with Au seeds and Au shells within thick layers respectively. b) WO_3-SiO_2-Au NPs solutions with various Au thickness obtained by using different Au stock solution during the shell formation.

The WO_3 core used in this material is polydisperse and add a significant uncertainty in the final shape and size, especially for thin layers of SiO_2 and Au. Also, the purity of the source can be refined to avoid crosslinked WO_2 contamination or use WO_2 cores directly during the synthesis which has smaller energy bandgap for displaying electrochromic behavior. The reduction of the final overall size can help to improve excretion rates of the NPs after imaging [32–35].

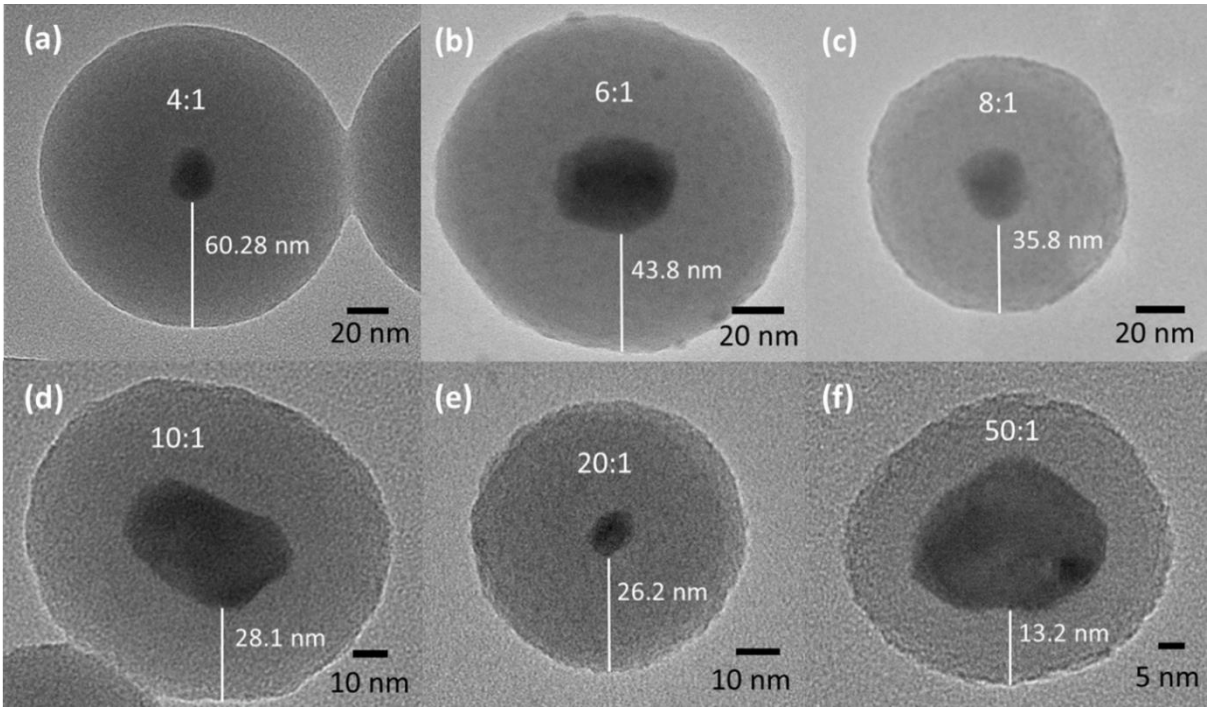

Figure 5.5 | TEM images of WO_3-SiO_2 samples with different ratios of ammonia:TEOS. a) 4:1, b) 6:1, c) 8:1, d) 10:1, e) 20:1 and f) 50:1.

Control of SiO_2 shell thickness: Figure 5.5 shows the SiO_2 thickness dependency on the ratio of ammonia:TEOS. To achieve thickness control, the volume of ammonia remains constant at 1 mL for all the displayed coatings in Figure 5.5. This follows the principles of the Stöber process that describes the growth of SiO_2 NPs [36]. When the amount of TEOS increases over the ammonia, the coating is thicker, and vice versa (Figure 5.5a-f). This has been previously addressed using different cores by several authors [37–39]. The thickness of the SiO_2 can be minimised down to 3 nm. However, the relationship between the thickness and the concentration of TEOS is non-linear. On the other hand, the current core has been found to exhibit some potential cytotoxicity for certain cells[40–42], so it needs to be wrapped thick enough to ensure it never directly interacts with healthy cells. TEOS concentration is the main parameter determining the SiO_2 layer thickness.

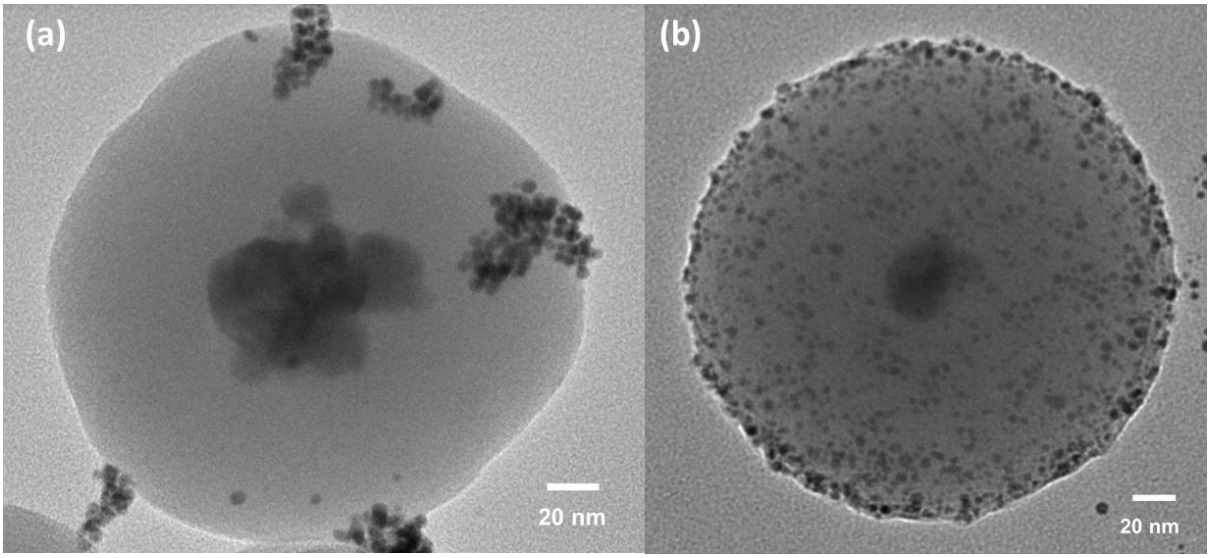

Figure 5.6 | TEM images of Au nanoseeds attachment. WO_3-SiO_2-Au NPs synthesised with different APTES additions: a) 50 µL. b) 200 µL.

Attachment of Au NPs: There are several very important optical and chemical properties of Au NPs that depend strictly on the type of ligand and ligand-metal bond. 3-aminopropyltrimethoxysilane (APTES) is one of the most common chemicals used to amine functionalised surfaces for successive Au attachment due to its stable bonding with Au, fast attachment, and low cost.

Figure 5.6a displays the sample prepared with 4 times lower APTES concentration than the one used to prepare the sample shown in Figure 5.6b during the amine functionalisation process. Figure 5.6b shows that an increment of the APTES content leads to a more homogeneous Au seeding over the SiO_2 surface. The concentration of APTES used in this study produced Au NPs of 3.5 nm ± 1.0 nm in diameter. Quantification of Au seeds from TEM images was attempted by counting the number of gold seeds visible in these images over many samples. Unfortunately, due to the high polydispersity of the core and the overall diameter, no consistent number of seeds was found for the same synthetic steps.

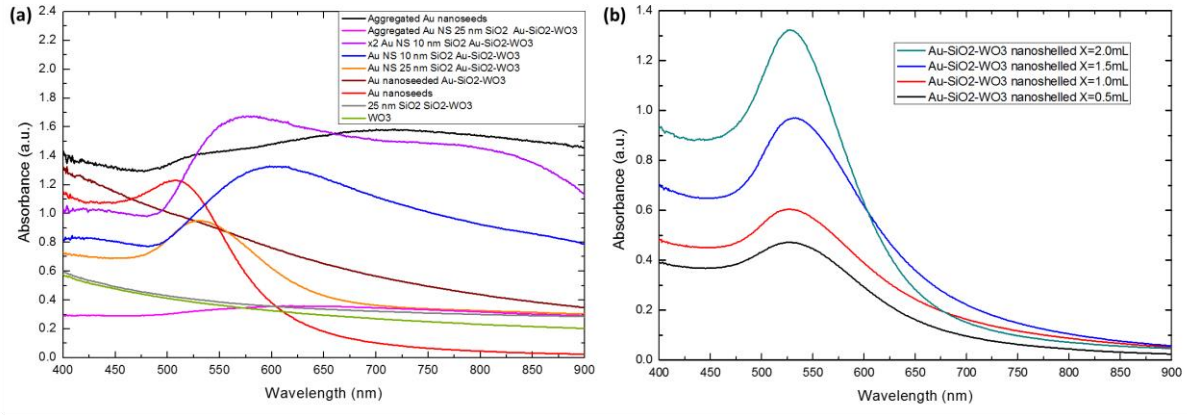

Figure 5.7 | UV-vis absorption spectra of various colloidal NPs: a) WO_3, WO_3-SiO_2, Au seeded WO_3-SiO_2-Au, Au shelled WO_3-SiO_2-Au (and aggregated batch, after 2 weeks stored in room temperature) and Au alone (and aggregated batch, after 2 weeks stored in room temperature). b) WO_3-SiO_2-Au shelled with different Au stock solution (X) used during the shell formation.

Plasmonic light absorption: Figure 5.7a shows the ultraviolet-visible (UV-vis) absorption spectra of various synthesis stages, which reveals the plasmon excitation wavelengths and the maximum absorption peak of Au, and the visible colour displayed by the colloid. The plain Au colloidal appears as red, with maximum absorption at 510 nm; whilst the colloidal nanoshell version of WO_3-SiO_2-Au appears purple with an absorption peak at 532 nm[43]. Figure 5.7b, which corresponds to the colloidal NPs displayed in Figure 5.3d, displays the evolution of the absorption spectra during the nanoshell formation in which X represents the volume of 25 mM Au stock solution as explained in the methods section. Also, there is a clear redshift when the aggregation of the Au and WO_3-SiO_2-Au NPs takes place. The optimal scenario is a maximum peak in the near-infrared regime to have the highest plasmonic oscillations for the SERS application with near-infrared laser illumination, which is analysed in Figure 5.8. There are no maximum local peaks for the non-metallic materials, as expected since

they do not have plasmon resonances. Also, the contribution of SiO_2 is negligible but starts to be relevant for increased wavelengths.

5.4. Cell viability

Materials: Dulbecco's Modified Eagle's Medium (DMEM), trypsin-EDTA solution and cell proliferation reagent WST-1. Culture cell serum-supplement and penicillin-streptomycin were purchased from Gibco.

Cell culture: The MDA-MB 231 human breast cancer cells were cultured in DMEM with 10% serum-supplement and 1% penicillin-streptomycin. Cells were grown under standard conditions of 5% CO_2 and 37 °C in a controlled humidified incubator to reach 70-80 % confluence. Cells were routinely sub-cultured using 0.25% trypsin-EDTA solution.

Cell viability: Cell viability experiments were performed in 96-well plates, and imaging experiments were performed in 6-well plate. Cells were seeded in 96-well plate at the density of 1 x 10^4 cells per well while cells were seeded onto the 6-well plates at a density of 1 × 10^6 cells per well and incubated for 24 h prior to the experiments. After overnight incubation, cells were treated with and without 100, 250, 500 and 1000 µg/ml of 4 types of NPs for 24 h. Cell viability after NP treatment was determined using WST-1 assay (Roche Applied Biosystems) according to the manufacturer's instructions with modifications to adapt for NP-treated cells. Briefly, cells were seeded in a 96-well plate with a density of 1 x 10^4 cells per well, differentiated and incubated with NPs (3 replicates per concentration). After 24 h, WST-1 reagent was added to the cells, and after the colour reaction, the plate was then kept for shaking and then absorbance was measured at a wavelength of 450 nm using a plate reader (Clariostar plate reader, BMG lab tech). The results were

expressed as percentage cell viability. Three independent experiments were performed for each study, and all measurements were performed in triplicate.

Statistical analysis: The data were statistically analysed using GraphPad Prism 5.04 to assess the effects of NPs treatment on cell viability and were expressed as % cell count ± SD, Mann Whitney. * ($p < 0.05$) was considered statistically significant. Results were presented as the mean ± standard deviation (SD).

Cytotoxicity profile in a triple-negative human breast cancer cell line MDA-MB 231: Figure 5.9a shows the in vitro cytotoxicity profile of the selected concentrations (100, 250, 500 and 1000 µg/ml) of four different batches (A1, A2, B1, B2) of WO_3-SiO_2-Au NPs in a triple-negative human breast cancer cell line MDA-MB 231. A1, A2, B1, B2 represent The NPs concentration range was selected from the minimum concentration showing low toxicity to concentration showing maximum toxicity. A live-dead assay for a period of 24 h was performed to confirm the suitability of the NPs for biomedical applications. Statistical analysis was performed with three batches per sample and concentration of which the mean and standard deviation were calculated. The results show no statistical significance (ns, $p \geq 0.05$) for concentrations 500 µg/ml, while for concentrations of 100, 250 and 1000 µg/ml the results are statistically significant (*, $p < 0.01$ to 0.05) as shown in Figure 5.9a. Among the statistically significant results, low cytotoxicity (>75% alive cells) after 24 h was found for concentrations of 100 µg/ml indicating their suitability for cell imaging purposes.

5.5. Raman spectroscopy applications

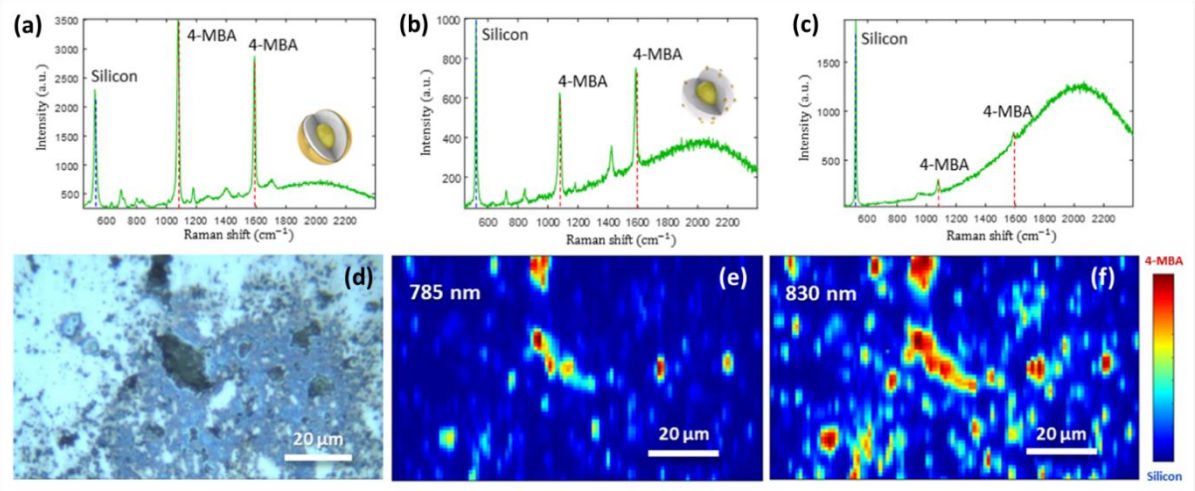

Figure 5.8 | (a-c) SERS spectra of 4-MBA molecule peaks at 1,078 and 1,589 cm^{-1} with 830 nm laser and d-f) Raman maps with 785 nm and 830 nm of different samples with 4-MBA Raman reporter over a silicon wafer with its characteristic reference peak at 520 cm^{-1}. (a) Au shelled WO_3-SiO_2-Au. (b) Au seeded WO_3-SiO_2-Au. c) Plain 4-MBA molecules. (d-f) Optical microscopy image, Raman maps under PC1 (66.09%) taken with 785 nm and 830 nm lasers, respectively.

SERS maps with 4-MBA reporter: Figure 5.8a-c shows the Raman spectra of 4-MBA molecules bound to the shelled WO_3-SiO_2-Au, seeded WO_3-SiO_2-Au and 4-MBA alone, respectively. 100 µL of sample at 1 mg/L was pipetted on a substrate and dried at 60 °C until the liquid fully evaporates. The substrate that holds the dried samples is a Si wafer and acts as a reference to control the intensity performance of the vibrational resonance peaks from the fixed concentration and volume of 4-MBA molecules, and therefore, the SERS effect quality. It is clear from Figure 5.8a-c that for Au content there is a boost in these peaks against the 4-MBA molecule alone in Figure 5.8c[44]. This boost could also be caused by local hot spots even though the work was performed at low concentrations. The maximum enhancement of 771 times

over the original signal is achieved for the core-shell NPs nanoshelled with Au twice as shown in Figure 5.10b. This factor is more than 4 times achieved value with the 3.5 nm Au nanoseeds on the SiO_2 surface from Figure 5.8.b. This implies that for better contrast, the complete nanoshell is essential. All the enhancement factor calculations have been carried out using the same Raman reporter molecule concentrations. A quick comparison with previous results using bare Au NPs for the same overall size shows that these composite NPs achieved lower enhancement factors, mainly due to the bluer maximum absorption peak position [45,46]. Smaller monodispersed cores and thinner SiO_2 shells can be the key for a substantial improvement to match the surface plasmon resonance wavelength. Larger enhancements can be more readily achieved by increasing the Au nanoshell thickness while keeping non-smooth surfaces. It can also be improved with the addition of another external Au layer on top of the Raman molecules to create hot spots.

4-MBA is a thiol that contains a benzene ring in the R part which forms the aromatic ring. This ring provides a substantial Raman scattering cross-section with characteristics peaks of 1,078 cm^{-1} and 1,589 cm^{-1} (see Figure 5.8). This molecule was chosen due to its features of stable sulfur bond with Au, easy attachment and pH sensitivity in the Raman spectra [47]. Depending on the intensity and position of the peaks, different thiolated reporter molecules can be investigated to find the most suitable Raman reporters for potential use when labeling specific cell types such as cancer cells. The NPs synthesised in this paper achieve easily improvable 10 and 10^3 SERS EFs for one Au shell and double Au shell, respectively, in dried samples over Si wafers (see Figures 5.8.a and 5.10.b). Also, several orders of magnitude were found for the double Au layer for liquid samples (see Figure 5.10.a), which is very promising for future in vivo applications due to including optical absorption similar to organic

human soft tissue. All these values were obtained by dividing the SERS signal by the background silicon peak to normalise them and subsequently measuring the ratio of the SERS peak versus the molecule without plasmonic enhancement. Moreover, no Raman enhancement from the Au seeds without attaching to the SiO_2 shell was included because the intensity of the 4-MBA peaks was as strong as the molecules alone for both near-infrared lasers.

PCA is an adaptive data analysis technique that combines conventional imaging and spectroscopy to simultaneously obtain both spatial and spectral information from an object by reducing a broad set of possibly correlated variables to a small set of uncorrelated variables, called principal components that still contains most of the relevant information from the broad set [48,49]. The origin of the new coordinate system is located in the center of the data points, the first PCA step includes the points in the direction of the highest variance, the second PCA step includes the ones for the second-highest variance and the rest follow this trend. Using the first PCA which describes the highest variance in the dataset (66.09%) in the Raman maps, the 4-MBA molecules location is found: dark red means 4-MBA and dark blue represents the Si wafer (Figure 5.8.e,f). This information is not obvious from the optical image (Figure 5.8.d); however, the Raman maps are able to identify the locations of these reporters. The SERS intensity of the aggregated areas is not only due to the 2D spatial distribution of the materials but also due to having several layers that lead to stronger hot spots [50] and cannot be seen with the optical microscope. After subsequent attachment of the NPs to or uptake into cancer cells, the cancer cells will be precisely located.

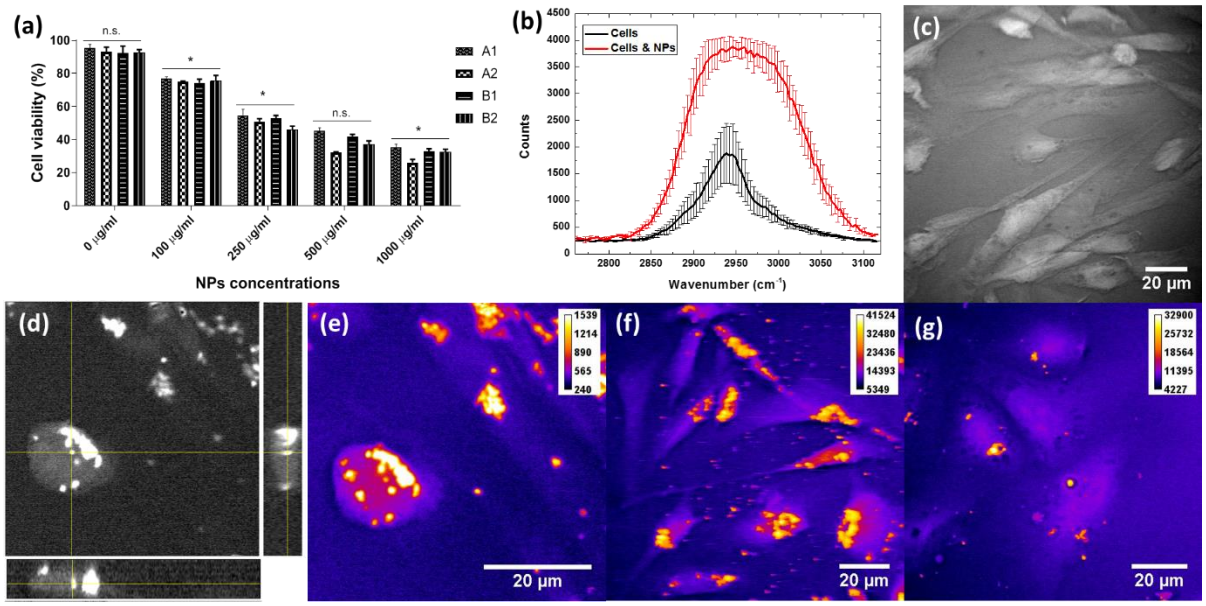

Figure 5.9 | (a) Cytotoxicity tests after 24 h of samples A1 (single layer of Au), A2 (single layer of Au coated with 4MBA), B1 (double layer of Au) and B2 (double layer of Au coated with 4MBA). The values represent the mean ± standard deviation of three experiments; * denotes $p < 0.05$ (statistical significance) and ns represent $p \geq 0.05$ (non-statistical significance). (b) Average values and standard deviations errors from CARS spectra from cells alone and cells with NPs. (c) Control cells CARS stack – z-projection image in greyscale. (d) CARS 3D demonstration of NPs B1 within the cell in greyscale and (e) its z-projection of the entire stack (recoloured intensity-dependent with fire LUT in ImageJ). (f) NPs A2 in cells CARS imaging (recoloured intensity-dependent with fire LUT in ImageJ). g) z-stacking of CARS images from cells and NPs stack A1 (recoloured intensity-dependent with fire LUT in ImageJ). The cytotoxicity results were obtained in collaboration with Dr. Tanveer Tabish and the CARS imaging with Dr. Jessica Mansfield.

Cell imaging using coherent Anti-stokes Raman spectroscopy: CARS imaging was carried by using dual-wavelength output from an InSight X3 ultrafast fs laser (Newport SpectraPhysics) with 800 nm for the pump and probe beam and 1045 nm as the Stokes beam. The beams where chirped to produced ps pulses and spatially

overlaid in the Spectral Focusing Timing and Recombination Unit (SF-TRU, Newport SpectraPhysics). The temporal overlap between the pump and Stokes beams was scanned via the SF-TRU unit to allowing us to rapidly change which Raman vibration was probed and acquire spectral data [58]. 3D submicron resolution imaging was performed on a modified confocal microscope (Olympus FV3000), with a 60 x water-immersion objective (1.2NA, UPlanSApo, Olympus). The anti-stokes light at 648 nm from CARS was collected in the forward direction using a water immersion objective (Olympus LUMPlanFLN 60 x). The anti-Stokes light was separated from the laser fundamentals by using a long pass dichroic beamsplitter (Chroma DC/T760lpxr) followed by 2 filters (Chroma ET650/45x) and detected using a PMT (Hamamatsu R3896). The samples were mounted between 2 coverslips. To avoid photo-damage to the samples the laser intensities were attenuated to give 9mW and 18mW for the pump and Stokes beams in the sample plane, respectively.

Cell imaging in human MDA-MB 231 breast cancer cells: The cancer cells were visualised by imaging the CARS signal generated from the CH molecular vibrations within the cells, this signal was chemically specific with a peak around 2940 cm^{-1}. The NPs within the cells also exhibited a very strong signal within the CARS channel, however, this was from a four-wave mixing process which was not chemically specific. Figure 5.9b compares the spectra of the cells to the spectral of the WO_3-SiO_2-Au NPs within the cells. The average value and standard deviation of three measurements were taken and plotted for both the cells only and the cells with the NPs. The intensity of the signal in cells with NPs is a few times higher than cells alone which indicates high sensitivity to locate the NPs. Figures 5.9c-g show the cell imaging results obtained with CARS. The control label-free human MDA-MB 231 breast cancer cells without NPs are shown in Figure 5.9c, this image is a z-projection of a CARS image

stack and the contrast is from the CH vibrations within the cells. Then, in Figure 5.9d, CARS 3D cross-sections of NPs with a double layer of Au (white color) within the cells (grey color) in grey confirms that the NPs were uptaken by the cells and can be seen from the inside of the cells. Additionally, the z-projection of the entire stack of CARS images was implemented in Figure 5.9e by applying the color filter fire LUT in ImageJ over the original intensity-dependent greyscale. This recolored image shows the NPs (white) located inside the cells (purple) at different z-positions. Similarly, Figure 5.9f and d show the z-projection of the entire stack with fire LUT recoloration for NPs with a single layer of Au coated with 4MBA and without 4MBA, respectively. These results along with the cytotoxicity profiles confirm the viability for these NPs to be used in cancer cell imaging.

Targeting and localization of cancer cells can be achieved in future studies by functionalising the Au nanoshell with cancer ligands such as antibodies which are customised for each type of cancer. One type of promising ligand is the anti-HER monoclonal antibodies for the treatment of various types of cancers including HER-2^+ metastatic breast, colorectal, NSCLC, pancreatic, breast, HNSCC, ovarian and renal tumours [51,52]. Should these core-shell NPs provide sufficient signals in combination with bright Raman reporters in the near-infrared, the SERS signals could be readout using microscopy in individual cancer cells. Moreover, they also could visualise in vivo tissues with Raman fibre probes or SESORS.

5.6. Raman in liquid samples

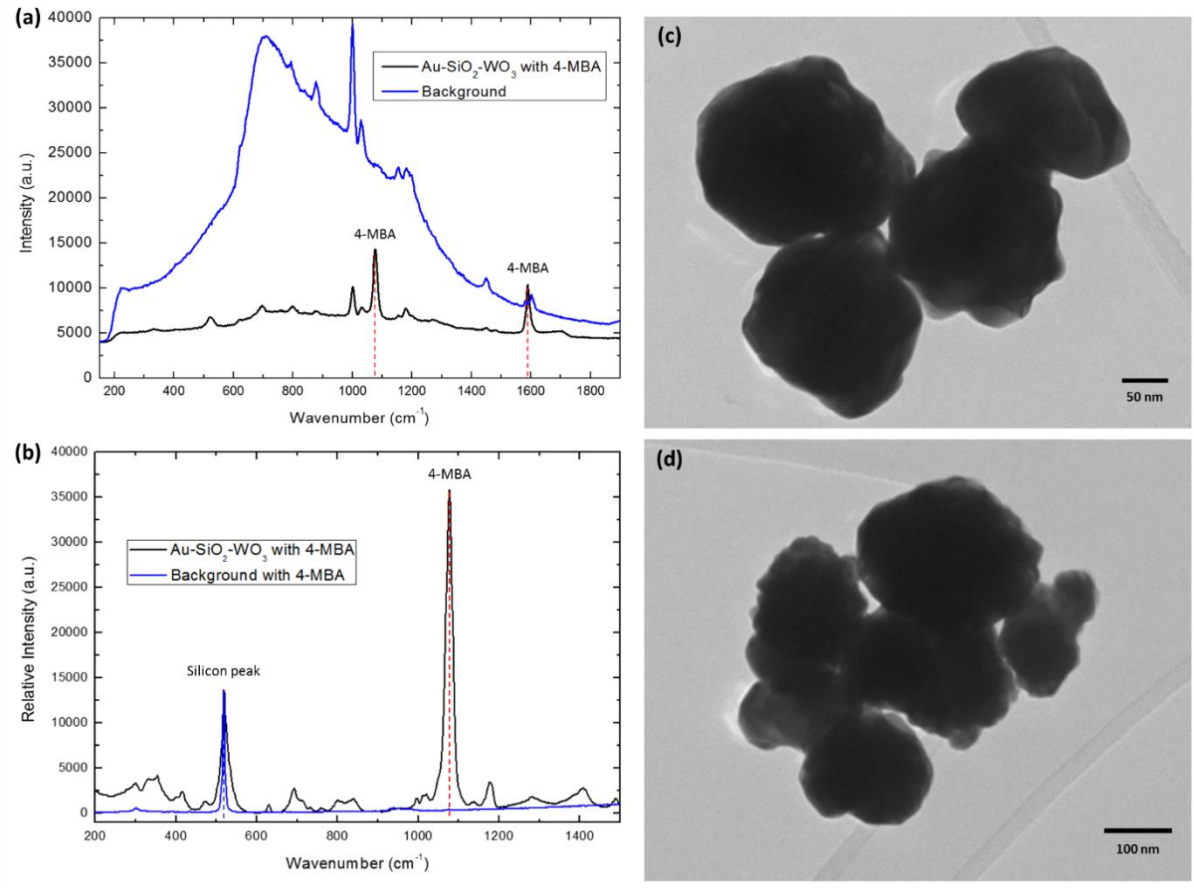

Figure 5.10 | Raman spectra of 4-MBA peaks which are boosted by the SERS effect on the external double Au shell of the colloidal WO_3-SiO_2-Au NPs with 10 nm SiO_2 intermediate shell thickness dispersed in a mixture of 80% water and 20% ethanol solvent. These measurements were performed in collaboration with Dr. Benjamin Gardner. a) Liquid sample that includes the background measurements of the plastic cuvette and solvent; b) dried sample over a silicon wafer with the characteristic 520 cm^{-1} peak. c,d) TEM images of the doubly Au shelled colloidal WO_3-SiO_2-Au NPs.

Figure 5.10a shows a strong SERS signal obtained in an aqueous liquid media, which does not attenuate light as much as human tissues but reduces substantially the concentration. Measurements with only 4-MBA molecules within the solution were also taken, but there was not visible signal compared to background only. Other

samples with thinner Au shells were measured, but no 4-MBA peaks were found for the liquid samples Raman spectra besides having visible SERS in their dried counterpart. Therefore, the Raman spectra from these WO_3-SiO_2-Au NPs in Figure 5.10.a is several orders of magnitude bigger than the bare molecules proving a truly strong SERS effect for both 4-MBA resonance peaks. Looking at dried samples over a silicon wafer with the well defined 520 cm^{-1} peak, it is easy to obtain accurately the enhancement factor. And for this batch the SERS EF is bigger than for measurements in liquid due to not having dilution from the aqueous media as displayed in Figure 5.10b. The SERS EF reached a value of 771 for the main 4-MBA peak at 1078 cm^{-1} without removing fluorescence due to being inexistent. This batch of NPs was prepared growing two layers of Au before to attach the 4-MBA molecules. The second layer was grown by repeating the Au shell synthesis step but using 0.050 g potassium carbonate and 3.0 mL of 25 mM of the Au stock solution. The NPs have a very thick double layer of Au and look as shown in Figure 5.10c and d, which is clearly enhancing both the plasmon generation and subsequently 4-MBA vibrations. Some hot spots for agglomerations may have also occurred in this batch and contributed to boosting the signal. This strong SERS signal for a liquid media leads to believe that other 3D liquid media such human organ-on-a-chips could also provide a fundamental understanding of 3D human cell behaviour and interactions in the presence of colloidal NPs.

5.7. Summary

In summary, these studies have demonstrated a size-tunable synthesis method to obtain novel WO_3-SiO_2-Au NPs. Higher APTES concentrations result in attachment of larger numbers of seeding Au NPs over the SiO_2 layer. Along with the synthesis, modifications in the intensity of the ultrasonication and speed in the centrifugation can be introduced to refine the washing process and avoid NPs agglomerations. On the

one hand, by repeating the Au shell growth step, several Au shells are created, and stronger SERS is achieved when using the 785 nm laser. This ability to increase the enhancement factor is crucial for translational biomedical applications that involve scattering media that attenuates the near-infrared laser intensity. On the other hand, the main parameter for the SiO_2 thickness growth is the ratio between TEOS and ammonia. Higher ratios of ammonia:TEOS lead to thinner SiO_2 thickness which reduces the potential toxicity in the human body through a faster excretion. The minimum thickness was down to 3 nm. The ratios 4:1, 6:1, 8:1, 10:1, 20:1 and 50:1 lead to SiO_2 thicknesses of 60, 44, 36, 28, 26 and 13 nm, respectively. However, it could increase the risk of displaying cytotoxicity related to partially uncoated WO_3 cores. The final WO_3-SiO_2-Au NPs have been systematically obtained in more than 10 batches by following the synthetic procedure; this reflects the high reproducibility of the synthesis.

The optimal thickness of the SiO_2 and Au nanoshells for both strong SERS and low toxicity has yet to be determined. However, preliminary results from various configurations show NPs detection in 2D human breast cancer cell culture and liquid media, which leads to believe in vivo cell imaging can be achieved.

Moreover, cytotoxicity tests after 24 h show >75% living cells (against approx. 90% in the control batch) from statistically significant cell viability at concentrations of 100 µg/ml which is higher than needed for detection. This is a promising translational result that encourages the use of these NPs in future live human cancer cells imaging and 3D human cell culture models such as spheroids, organoids and organ-on-a-chip technologies to have the full picture of how beneficial these NPs can be in the clinical stage. Further improvements could be obtained by using a monodisperse source for

the core and working with smaller NPs that present similar toxicity but can better penetrate the cell.

6. Magnetic-plasmonic composite nanoparticles

6.1. Introduction

In this chapter, a similar approach to the one used in the previous chapter is followed in terms of the NP synthesis design; the only difference lies in the core. Since most proposed magnetic NPs developed to replace the highly toxic gadolinium-based compounds used in the clinic are Fe_3O_4, the use of other magnetic NPs with slightly weaker magnetic properties such as γ-Fe_2O_3 can provide a safer approach thanks to a reduced aggregation tendency. Looking into biocompatibility, Au NPs are also clinically approved and bring high opacity (absorption) against X-rays for CT and plasmonic properties for SERS and potential light-induced hyperthermia. Therefore, composite NPs that contain both materials seem promising for both strong theranostic capabilities and clinical viability.

This chapter presents the design and critical synthetic steps for the creation of a new class of composite core-shell NPs, named Fe_2O_3-SiO_2-Au that displays desirable properties for cancer theranostics following the ideas mentioned previously. Figure 6.1 shows how the NPs could effectively use multifunctionality to image and kill cancer cells by combining clinically relevant functionalities. The NPs have a magnetic core made of γ-Fe_2O_3 which has a superparamagnetic or ferrimagnetic behaviour depending on the size, a SiO_2 coating over the surface and an external Au nanoshell which brings the plasmonic behaviour[32]

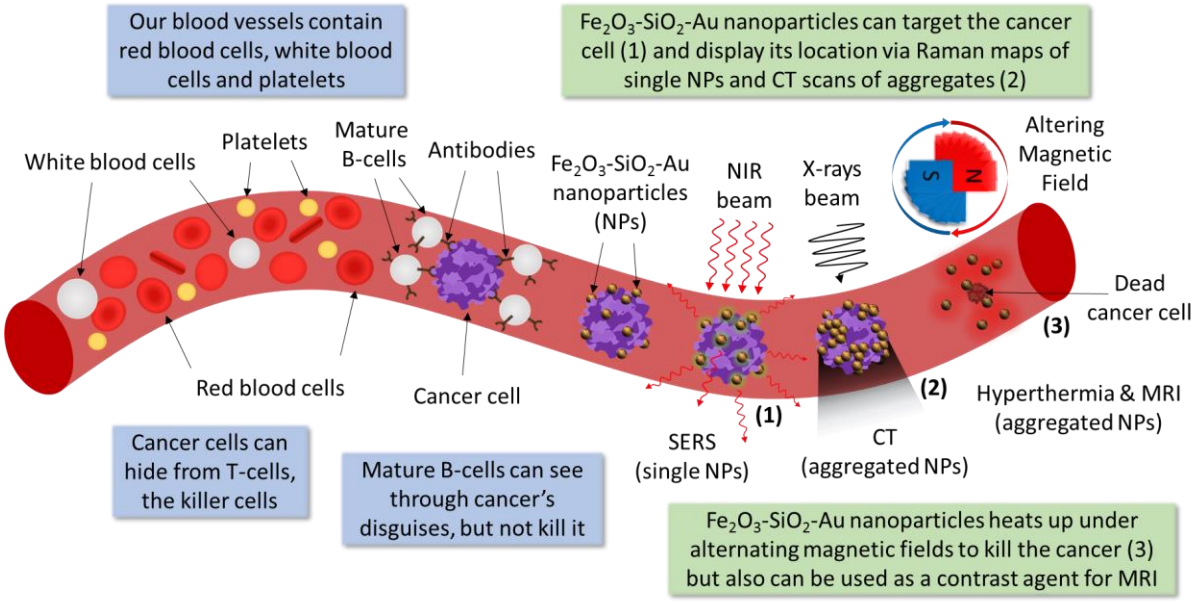

Figure 6.1 | Overview of the multifunctional NP in vivo applications for cancer nanotheranostics.

In cancer nanotheranostics, there are multiple routes to obtain fully operational and multifunctional agents by mixing properties that arise from the nanoscale. Concretely, SERS can be used to obtain single-molecule detection[339], in combination with CT and MRI for a multifunctional detection of malignant regions. On the other hand, magnetic heat is generated by flipping continuously and rapidly the material's nuclear spins inefficiently via external AMFs. Composite NPs made of both plasmonic and magnetic materials that combine these four functionalities are promising candidates for effective detection and treatment of early cancers.

6.2. Experimental synthesis

Materials: All reagents are purchased from Sigma-Aldrich: Gold(III) chloride hydrate ($HAuCl_4.xH_2O$, 99.999% trace metals basis MW 339.79 g/mol), Tetrakis (hydroxymethyl)phosphonium chloride solution (THPC, 80% in H2O), (3-Aminopropyl)triethoxysilane (APTES), potassium carbonate (K_2CO_3, 99.995% trace

metals basis MW 138.21 g/mol), sodium hydroxide (NaOH, Sigma-Aldrich), potassium carbonate (K_2CO_3), formaldehyde (CH_2O (H-CHO)), 4-mercaptobenzoic acid (MBA), deionised water, ethanol and formaldehyde solution. Pericyte Medium (PM) consists of 500 ml of basal medium, 10 ml of fetal bovine serum (FBS, Product Code SC-0010), 5 ml of pericyte growth supplement (PGS, Product Code SC-1252), and 5 ml of penicillin/streptomycin solution (P/S, Product Code SC-0503).

These NPs were prepared by modifying the Stöber process to create the intermediate SiO_2 shell over the core, amine functionalising the SiO_2 surface and using the Turkevich method to attach Au nanoseeds over the SiO_2 surface and grow them to form the external Au nanoshell. In terms of the core, two distinctive cores are presented in this chapter which were already analysed in Chapter 4: monodisperse and highly polydisperse commercial γ-Fe_2O_3 NPs. Moreover, the Au was thiolised with benzene rings to produce strong Raman signals. The resulting NPs were thoroughly characterised by transmission electron microscopy, powder X-ray diffraction, Raman spectroscopy and ultraviolet-visible spectrophotometry. Light absorption and plasmonic generation tests have been carried out to understand the benefits of these novel composite NPs.

SiO_2 nanoshell formation: The first step was the synthesis of the γ-Fe_2O_3-SiO_2 core-shell nanocomposites (Figure 6.2), NP following the Stober process. A liquid suspension made of 10 ml deionised (DI) water, 20 ml ethanol and 0.015 g γ-Fe_2O_3 NPs was first prepared, then a modified Stöber process promoted the formation of the SiO_2 shell via the sol-gel method. The Stöber-based process used follows the same steps described for WO_3-SiO_2 in section 5.2.

γ-Fe_2O_3-SiO_2-Au core-shell composite nanoparticles

Amine functionalisation: The γ-Fe_2O_3-SiO_2 core-shell composite NP surface was functionalized with an amine group following the same method used for WO_3-SiO_2 in section 5.2.

Colloidal γ-Fe_2O_3-SiO_2-Au NPs: Colloidal γ-Fe_2O_3-SiO_2-Au NPs with Au nanoseeds were obtained following the same method used for WO_3-SiO_2-Au in section 5.2.

Au shell synthesis: Colloidal γ-Fe_2O_3-SiO_2-Au NPs with Au nanoshells were obtained following the same method used for WO_3-SiO_2-Au in section 5.2.

Adding reporter molecule for SERS: The Au nanoshell bioconjugation with 4-MBA over γ-Fe_2O_3-SiO_2-Au core-shell nanocomposites was obtained following the same method used for WO_3-SiO_2-Au in section 5.2.

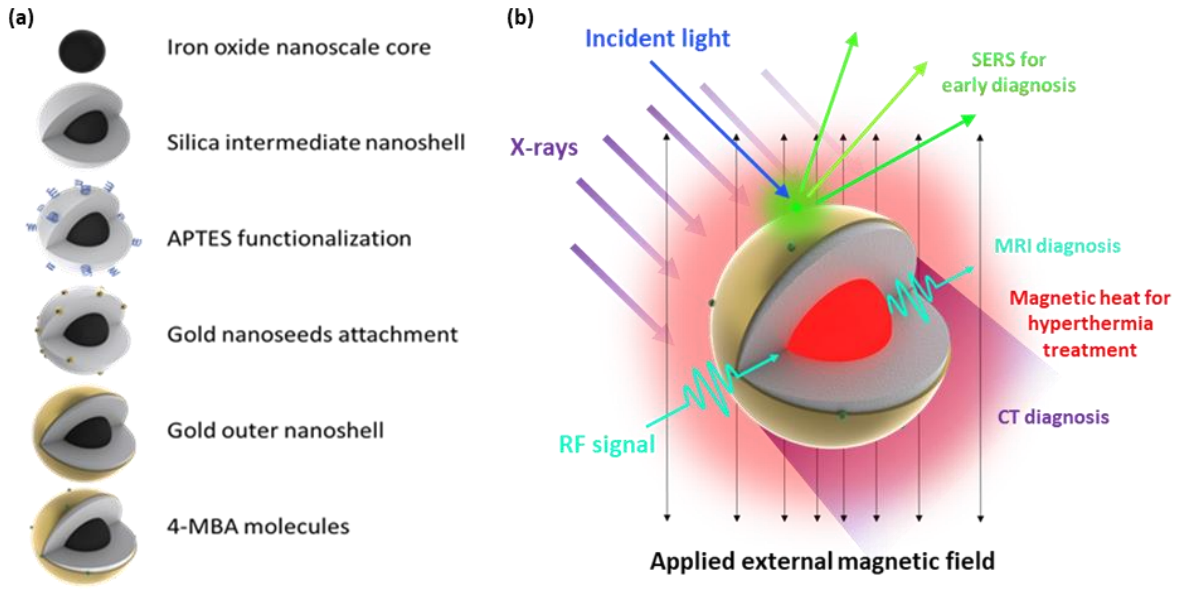

Figure 6.2 | Diagram of (a) synthetic steps and (b) the theranostic combination of functionalities: SERS, MRI, CT and magnetic hyperthermia.

To summarise, Figure 6.2a represents the synthetic process of these core-shell composite NPs where the core can be either monodisperse and polydisperse to fabricate two distinctive types of NPs, but the rest of the steps are identical for both. The idea is understanding if there are improvements or drawbacks of working with a highly monodisperse core against a polydisperse counterpart. Hence, the four functionalities described in Figure 6.2b are analysed for both cases.

6.3. Characterization

When trying to understand the composition, TEM images and XRD spectra are used to verify that the core-shell composite nanostructure is achieved following the same approach followed in chapter 5. Figure 6.3a presents the solutions obtained during the synthesis when creating 1 layer of Au and 2 layers of Au as performed in chapter 5. These solutions once again present a transition from dark red/purple to purple/blue when increasing thee Au content. Similar results are obtained for monodisperse and polydisperse in terms of solution apparent colour. This consistency is independent of the core material but dependent on substantial fluctuations of its size; which is a pivotal result to design and predict future NPs.

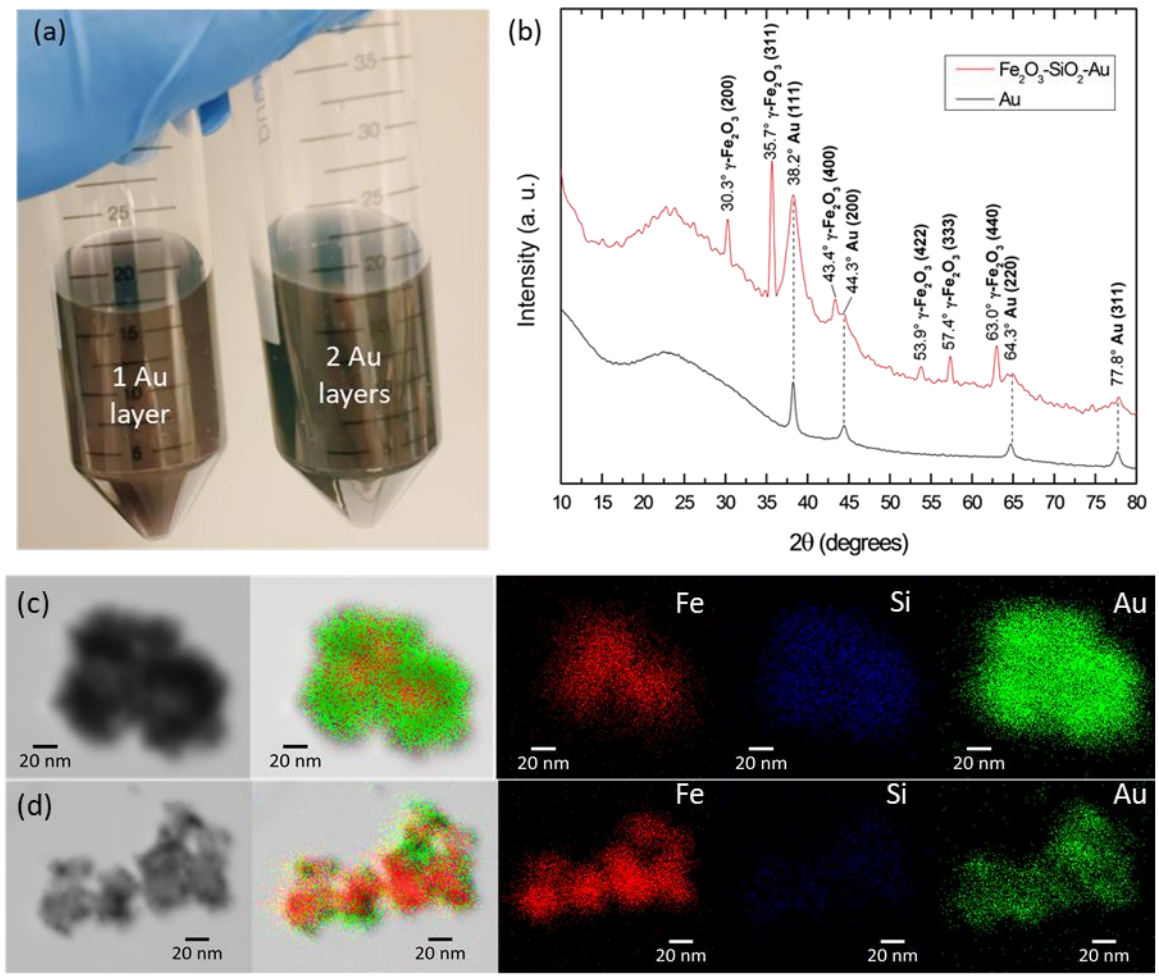

Figure 6.3 | (a) Photographs of the colloidal NPs solutions γ-Fe_2O_3-SiO_2-Au NPs with 1 Au layer and 2 layers (b) XRD spectra of γ-Fe_2O_3-SiO_2-Au NPs with 1 Au layer and γ-Fe_2O_3 NPs. (c) STEM element mapping analysis of γ-Fe_2O_3-SiO_2-Au NPs with 1 Au layer. (d) STEM element mapping analysis of γ-Fe_2O_3-SiO_2-Au NPs with Au nanoseeds.

NPs material composition: Figure 6.3b-d presents the analysis of the composition in the NP design, proving the correct configuration of the different layers portrayed in Figure 6.2. Figure 6.3a verifies that the colour change when growing the outer layer of Au follows the same procedure already reported in Chapter 5 and Figure 6.4 also corroborates that the plasmonic behaviour is almost identical as the displayed in chapter 5.

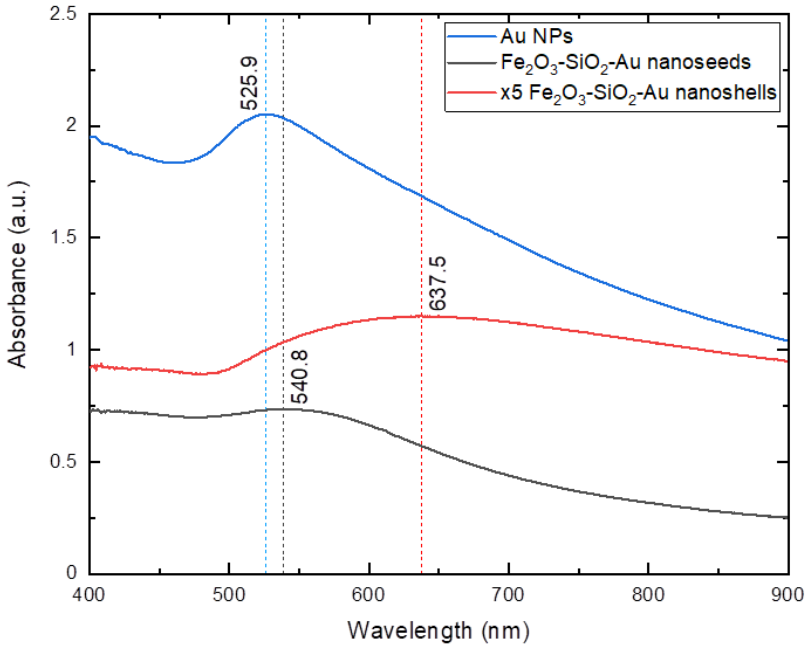

Figure 6.4 | UV-vis absorption spectra of various colloidal NPs: Au, γ-Fe_2O_3-SiO_2-Au nanoseeded and γ-Fe_2O_3-SiO_2-Au nanoshelled with one Au nanoshell step (multiplied 5 times the spectrum).

Plasmonic light absorption: Figure 6.4 shows the UV-vis absorption spectra of various synthesis stages, which reveals the plasmon excitation wavelengths and the maximum absorption peak of Au, and the visible colour displayed by the colloidal. The plain Au colloidal appears as red, with maximum absorption at 525.9 nm; whilst the colloidal of nanoshell version of γ-Fe_2O_3-SiO_2-Au appears purple with an absorption peak at 637.5 nm[43]. This shift will allow us to obtain a more efficient SERS when working at longer laser wavelengths.

6.3.1. Polydisperse commercial core

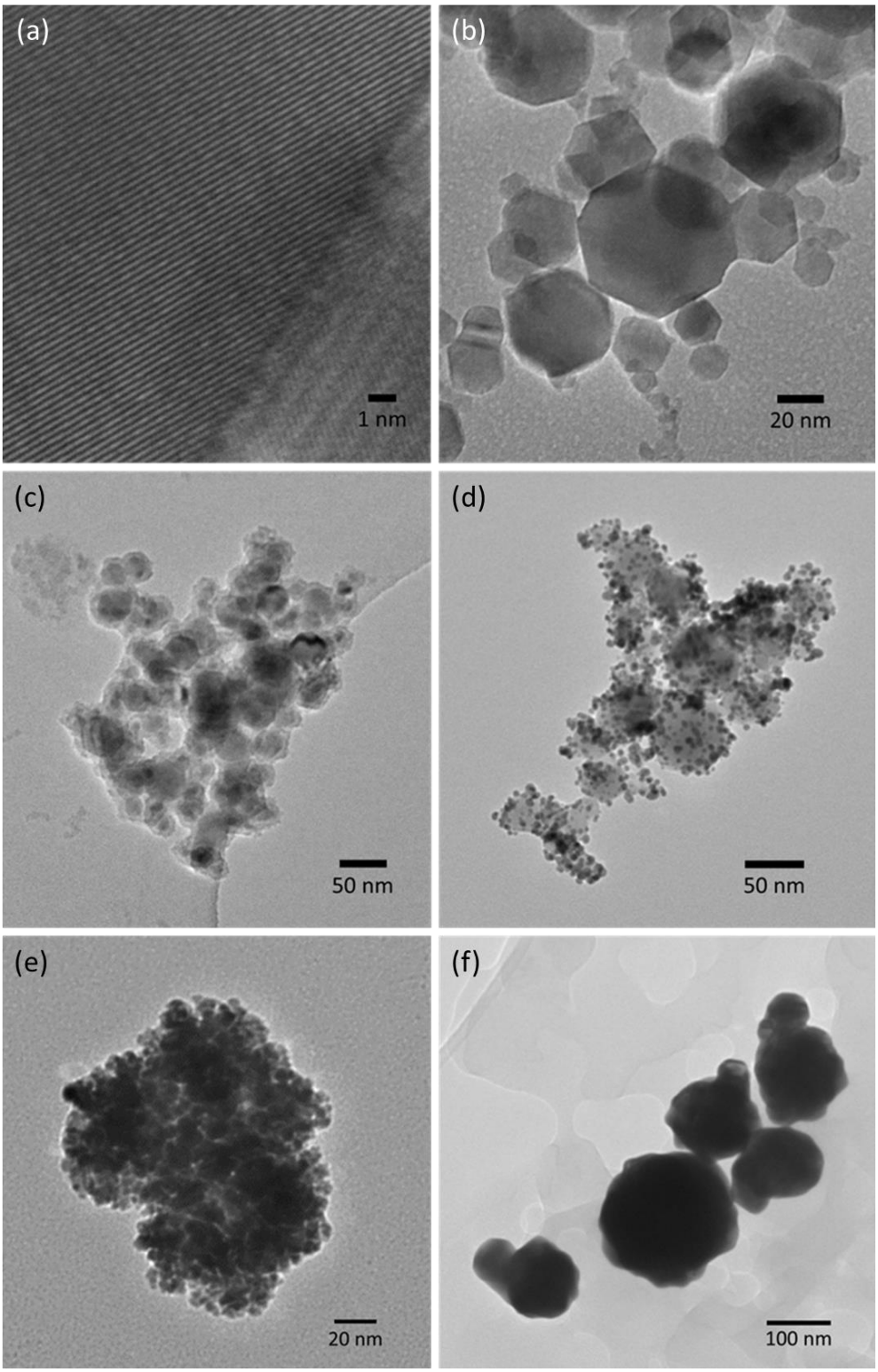

Figure 6.5 | (a) HR-TEM image of γ-Fe_2O_3 NPs (b) TEM image of γ-Fe_2O_3 NPs (c) TEM image of γ-Fe_2O_3-SiO_2 NPs (d) TEM image of γ-Fe_2O_3-SiO_2-Au NPs with Au

seeds (e) TEM image of γ-Fe_2O_3-SiO_2-Au NPs with 1 Au layer nanoshell (f) TEM image of γ-Fe_2O_3-SiO_2-Au NPs with 2 Au layers nanoshell.

The polydispersity of the core for these samples was already analysed in chapter 4. Here, the synthetic steps of the polydisperse γ-Fe_2O_3-SiO_2-Au NPs imaged under TEM are presented, including HR-TEM, to verify the atomic structure (see Figure 6.5).

6.3.2. Monodisperse core

First of all, it is necessary to understand these samples from the inside out, starting from the core. In chapter 4, a comprehensive study on dispersity for the commercial polydisperse γ-Fe_2O_3 cores. This chapter shows a more straightforward study of their monodisperse 11 nm NPs counterpart synthesised in the lab following the procedure explained chapter 4.

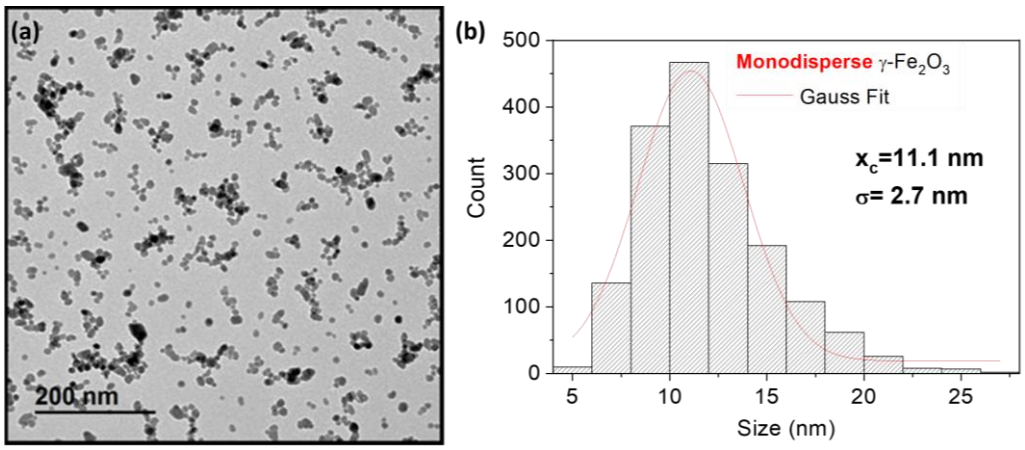

Figure 6.6 | (a) TEM images of monodisperse γ-Fe_2O_3 NPs. (b) Statistical analysis of the size distribution in the monodisperse γ-Fe_2O_3 NPs. These results were obtained in collaboration with Irene Morales and Prof. Patricia de la Presa.

Figure 6.6 displays a dispersity analysis under TEM. This image shows how NPs size range from 4 to 26 nm following a gaussian distribution with a centred

maximum peak value at 11 nm. This is a drastic reduction in dispersity compared to commercial NPs. Therefore, during the rest of this chapter, this NPs will be referred to as ‘monodisperse‘.

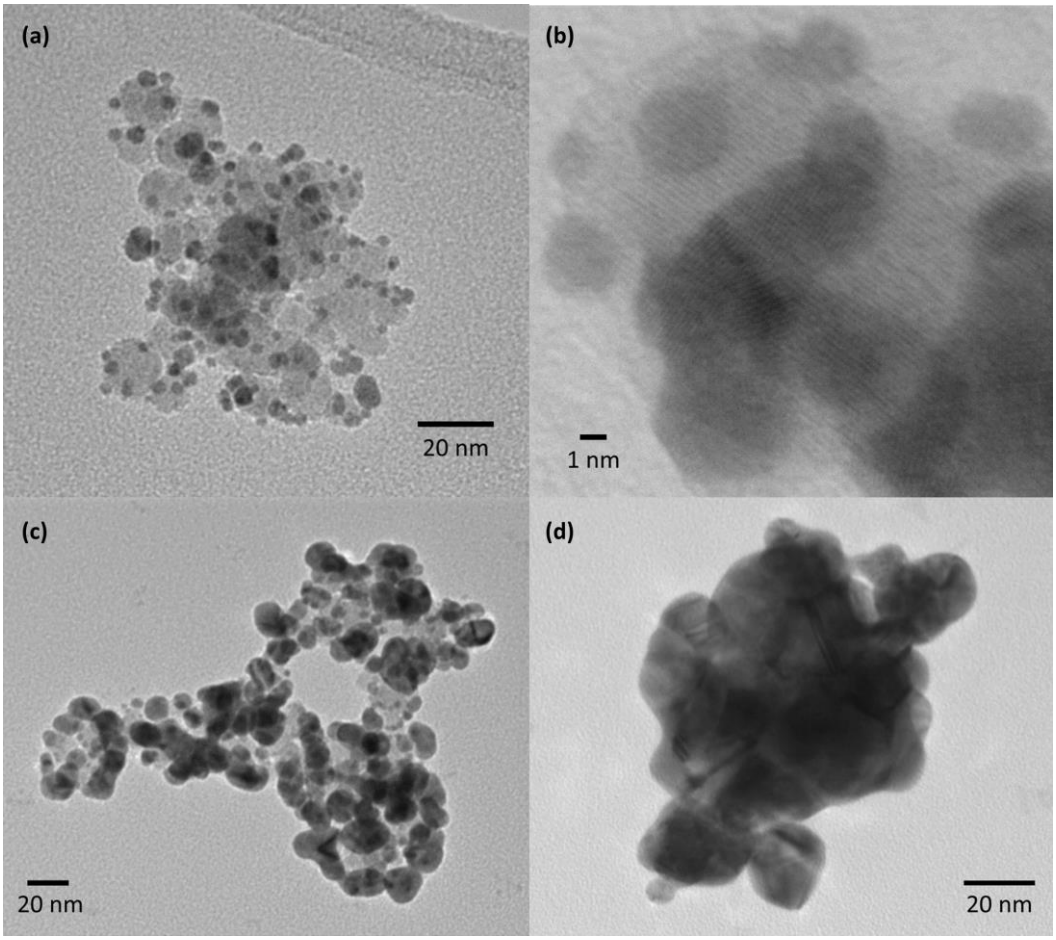

Figure 6.7 | (a) TEM image of γ-Fe_2O_3-SiO_2-Au NPs with Au seeds, (b) HR-TEM image of γ-Fe_2O_3-SiO_2-Au NPs with 1 Au layer nanoshell, (c) TEM image of γ-Fe_2O_3-SiO_2-Au NPs with 1 Au layer nanoshell, and (d) TEM image of γ-Fe_2O_3-SiO_2-Au NPs with 2 Au layers nanoshell.

Figure 6.7 shows how the growth of Au structures from seeds to seeded shell to Au shell has a redshift in the maximum of absorption as previously described in Chapter 6 and in the study published by Martinez Pancorbo *et al.* In 2019 [11].

γ-Fe_2O_3-SiO_2-Au core-shell composite nanoparticles

6.4. Detection Results

6.4.1. Liquid Raman

Raman spectroscopy measurements: The measured Raman signal follows the same procedure discussed in section 5.6. As shown in Figure 6.8, results confirm a strong SERS effect in liquid samples containing water, ethanol, and Raman reporters for the 1,077.8 cm^{-1} and 1,589.4 cm^{-1} peaks from 4-MBA.

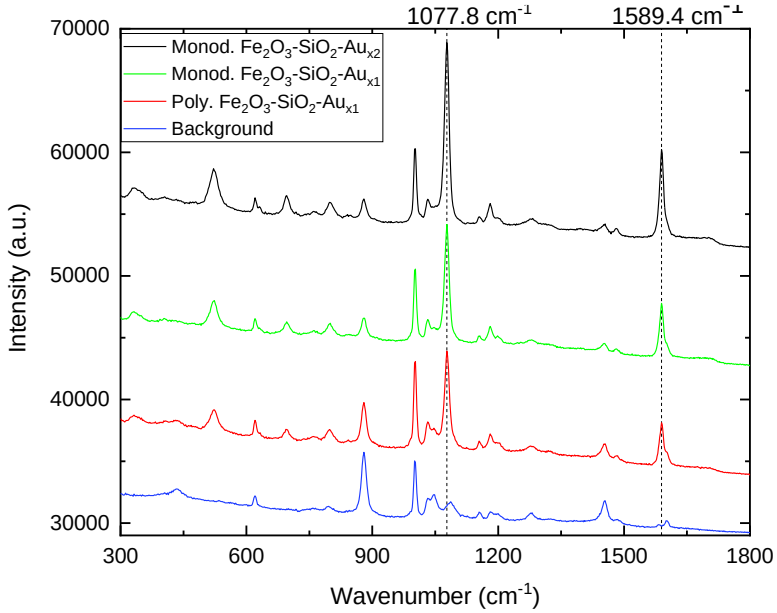

Figure 6.8 | Liquid sample Raman spectra of 4-MBA peaks which are boosted by the SERS effect on the external double Au shell of the colloidal γ-Fe_2O_3-SiO_2-Au NPs in a mixture of 80% water and 20% ethanol solvent in plastic cuvettes. These results were obtained in collaboration with Dr. Benjamin Gardner.

Figure 6.8 shows a strong SERS signal obtained in an aqueous liquid media that is easily overcoming the background signal. The solvent attenuates the Raman activity to mimic body fluids which are primarily made of water. These results show that monodisperse cores with double Au shell provide the best SERS effect reaching a SERS EF of 33 for removed fluorescence for the 1,077.8 cm^{-1} peak. Measurements with only 4-MBA molecules within the solution were referred to as “background”.

6.4.2. MicroCT

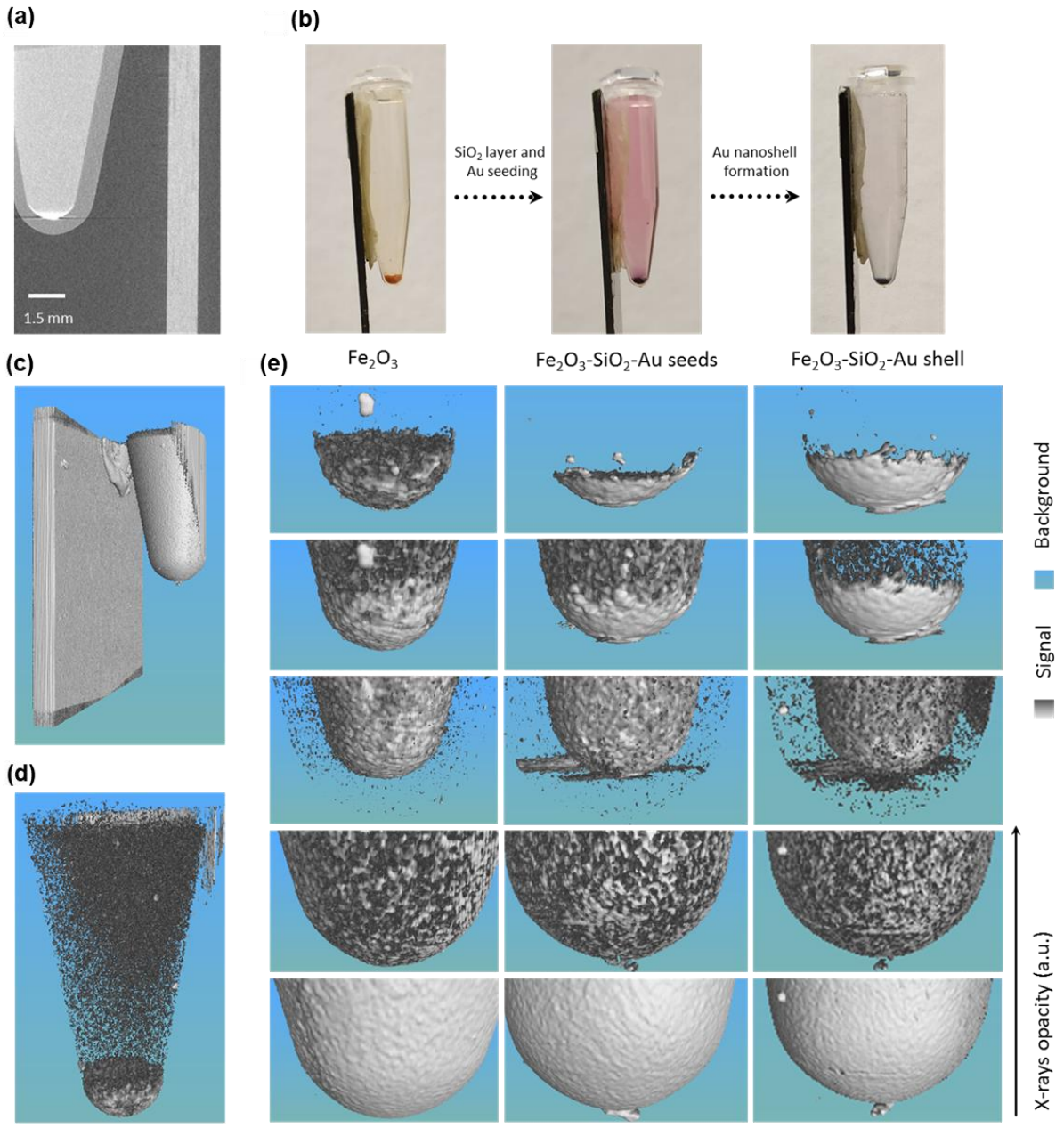

Figure 6.9 | MicroCT 3D imaging of aggregated samples from different relevant synthetic steps, all at the same mass (20 mg) and in the same volume (1.5 mL) of DI water. (a) Shadow cross-section of the aggregated γ-Fe_2O_3-SiO_2-Au NPs. (b) Photographs of the three synthetic steps samples used for MicroCT imaging. (c) Manipulable 3D volume at low X-rays opacity of both the carbon fibre, plastic sticky tape and sample in microcentrifuge tubes. (d) Manipulable 3D volume at medium X-

rays opacity of both the carbon fibre, plastic sticky tape and sample in microcentrifuge tubes. (e) Manipulable 3D volumes at variable X-rays opacity of both the three aggregated liquid samples in microcentrifuge tubes. All tomographical measurements were taken at 125 ms per projection; and for 2400 projections in total, from 0 to 360 degrees. These results were obtained in collaboration with Dr Hong Chang.

NPs materials' CT contrast: Results from Figure 6.9 confirm the capabilities of γ-Fe_2O_3-SiO_2-Au NPS to be used as CT contrast agents for aggregated NPs, not for single-cell imaging, due to their spatial resolution limitation. MicroCT measurements were performed following the configuration displayed in Figure 3.5. Standard CT usually provides less resolving power and, therefore, the results obtained from this experimental setup will outperform the spatial resolution from clinical CT measurements. However, any values obtained from MicroCT come from smaller voxels than in clinical CT, which carry a weaker signal per voxel for the same X-rays emitter intensity. Hence, the contrast per voxel will be higher in the 3D region of the NPs if the voxel size is not larger than the aggregates. Figure 6.9a-e compile the results obtained under MicroCT for γ-Fe_2O_3 NPs, γ-Fe_2O_3-SiO_2-Au NPs with Au nanoseeds and γ-Fe_2O_3-SiO_2-Au NPs with Au nanoshell. These results confirm that the more Au included in the sample, the better CT contrast agent, i.e., more Au absorbs Z-rays, and this creates X-rays contrast when performing X-rays CT. Unfortunately, to achieve strong contrast, the samples had to be aggregated at the bottom on the microcentrifugation tube. This issue makes this modality not suitable for single-cell imaging but still useful for submillimeter sized tumour regions which are still better than most current early-stage detections in the clinic, including not only CT but also using any other clinically approved in vivo imaging technique.

γ-Fe_2O_3-SiO_2-Au core-shell composite nanoparticles

6.4.3. MRI

All the MRI results in this section were obtained in collaboration with Dr Abdelmalek Benattayallah.

MRI measurements: The volume used for all the measurements is 600 uL while varying concentrations: 200, 100 ug/mL, 50, 20, 10 and 5 µg/mL. Results were measured for monodisperse γ-Fe_2O_3 NPs, monodisperse γ-Fe_2O_3-SiO_2-Au NPs and polydisperse γ-Fe_2O_3-SiO_2-Au NPs.

For fresh NPs, 3D signals without modality were taken at TE = 1 min, TR/TE=25/2 and with dimensions of the coronal slices to measure of 2x2x2 mm (spatial resolution). T2 measurements were taken with a total scan of 5 minutes. Dimensions of the coronal slices to measure: 1x1x5 mm (spatial resolution). TR=3000 ms. TE values are 13, 26, 39, 52, 65, 78, 91 and 104 ms. T1 measurements were taken with a total scan of time for each TI (point) is 2.5 minutes. Dimensions of the coronal slices to measure: 1x1x5 mm (spatial resolution). TR=10000 ms. TI values are 50, 100, 200, 300, 500, 800, 1000, 1300, 1500, 1800, 2000, 2500 ms.

For NPs after 2 months, 3D signals without modality were taken at TE = 1 min, TR/TE=.25/7. ms. Dimensions of the coronal slices to measure: 0.5x0.5x2 mm. For T1 measurements, the total scan time for each TI is 5 min 20 seconds. The dimensions of the coronal slices to measure are 0.5x0.5x5 mm (spatial resolution). TR is 10000 ms and eight TI measurements (50, 100, 200, 300, 500, 800, 1000, 1300, 1500, 1800, 2000 and 2500 ms) are performed. For T2 measurements, the total scan time is 9.6 minutes. The dimensions of the coronal slices to measure are 0.5x0.5x5 mm (spatial resolution). TR is 3000 ms, and TE values were measured at 14, 28, 42, 56, 70, 84, 98 and 112 ms.

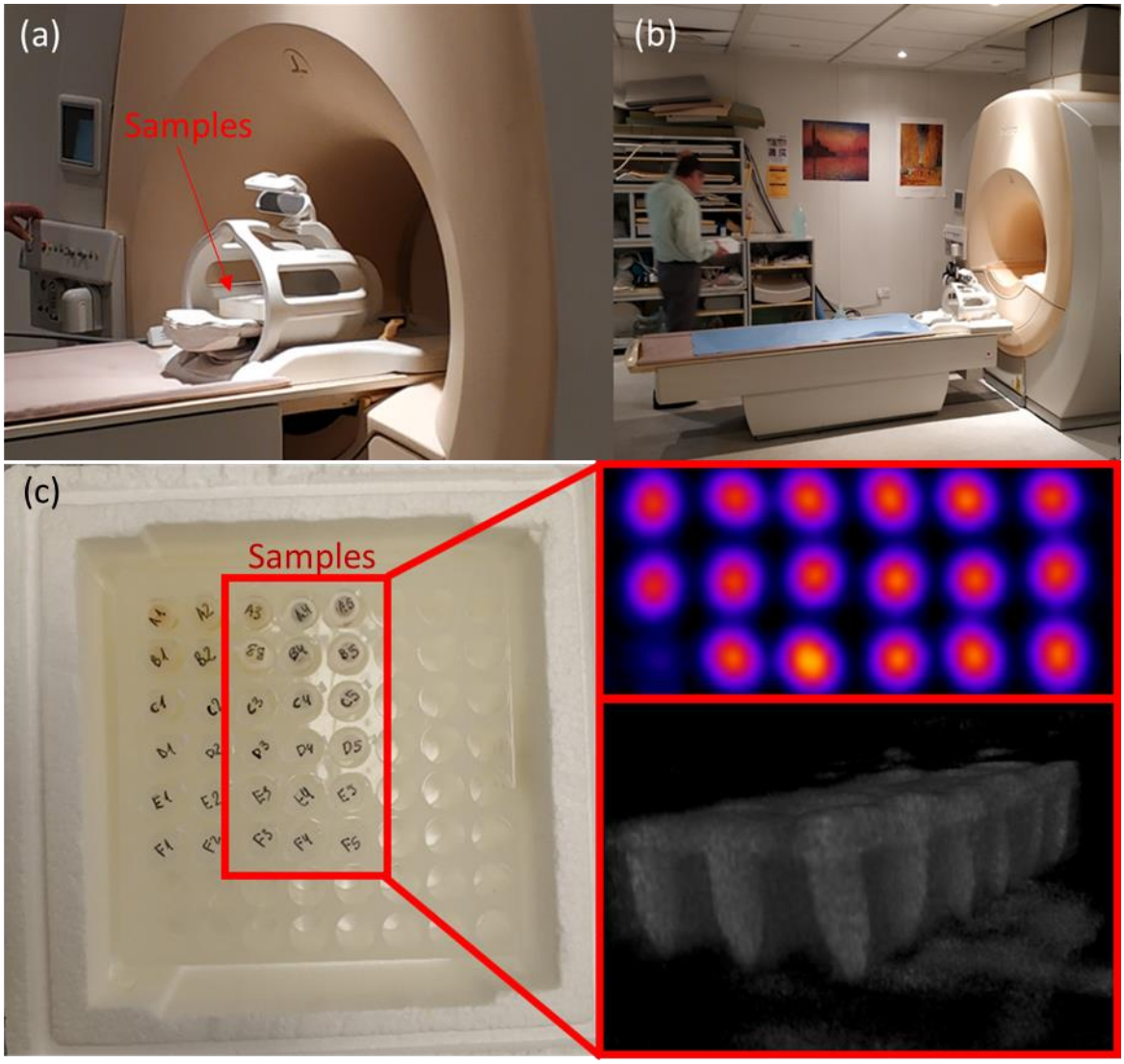

Figure 6.10 | (a) Zoomed area where our samples are placed during the MRI measurement, (b) Philips Gyroscan Intera 1.5T MRI, (c) Picture of the sample holder with a zoomed area over the samples analysed in this chapter, including 3D signals of the samples from the top recoloured intensity-dependent with fire LUT in ImageJ and from the side with no filter.

MRI was performed to evaluate whether the γ-Fe_2O_3-SiO_2-Au NPs are suitable for being MRI contrast agents. Figure 6.10a-b shows how the sample was located in the MRI to be measures and 6.10c displays that the liquid samples dispersed in DI water kept in microcentrifugation tubes are being measured using a silicon holder

encapsulated in a polystirine box. Moreover, the samples are imaged in 3D to verify the location and orientation of what is being detected.

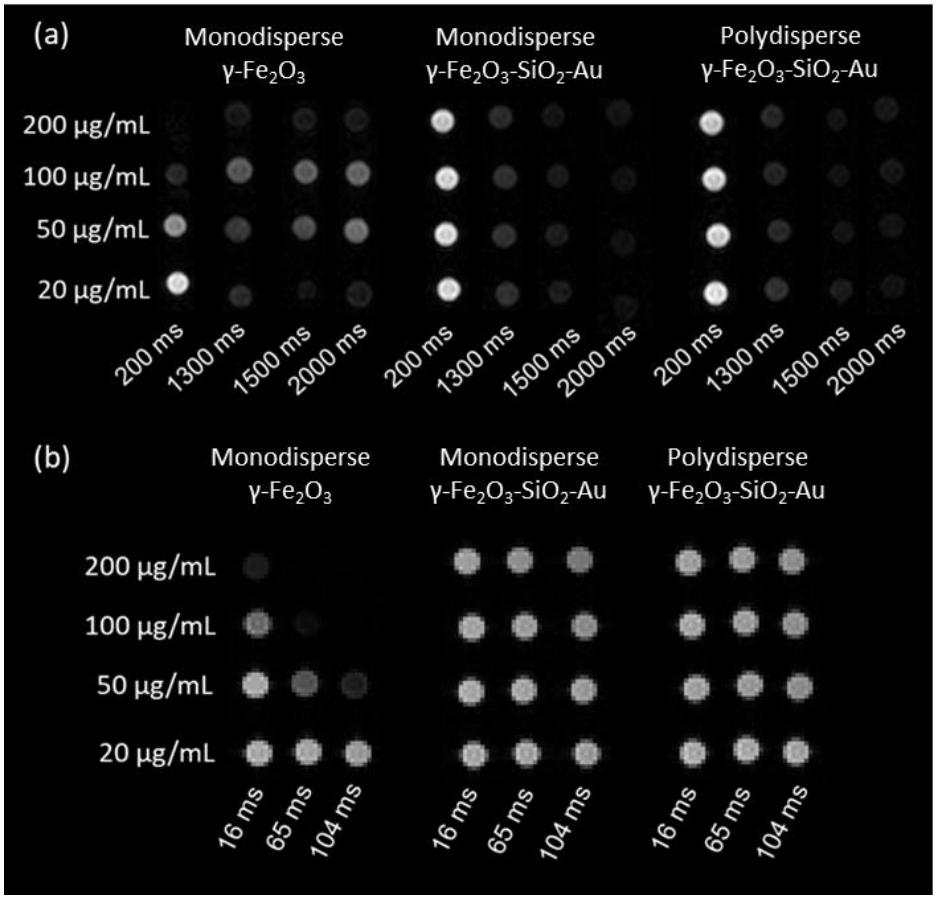

Figure 6.11 | (a) *T*1-weighted MR images at TI of 200 ms. 1300 ms, 1500 and 200 ms. (2) *T*2-weighted MR images at TE of 16 ms. 65 ms and 104 ms.

MRI T1 and T2 weighted images were taken and used for all the following calculations, some of these modal images are displayed in Figure 6.11 at various concentrations, all as low or below the concentrations used for cytotoxicity and cell viability tests so that the results obtained in MRI are automatically translated to a safe cellular exposure.

MRI T1-weighted images from 6.11 have high contrast for just the core and moderate contrast for full core-shell NPs independently of the core dispersity. However,

it is essential to consider that the core-shell NP have a minimal amount of magnetic material since the core present a small fraction of the entire NP. For the monodisperse core, this difference is bigger than for the polydisperse sample. Therefore, lower contrast in the sample cannot be inferred as a consequence of a weaker signal from each NP but an effect of having less magnetic material.

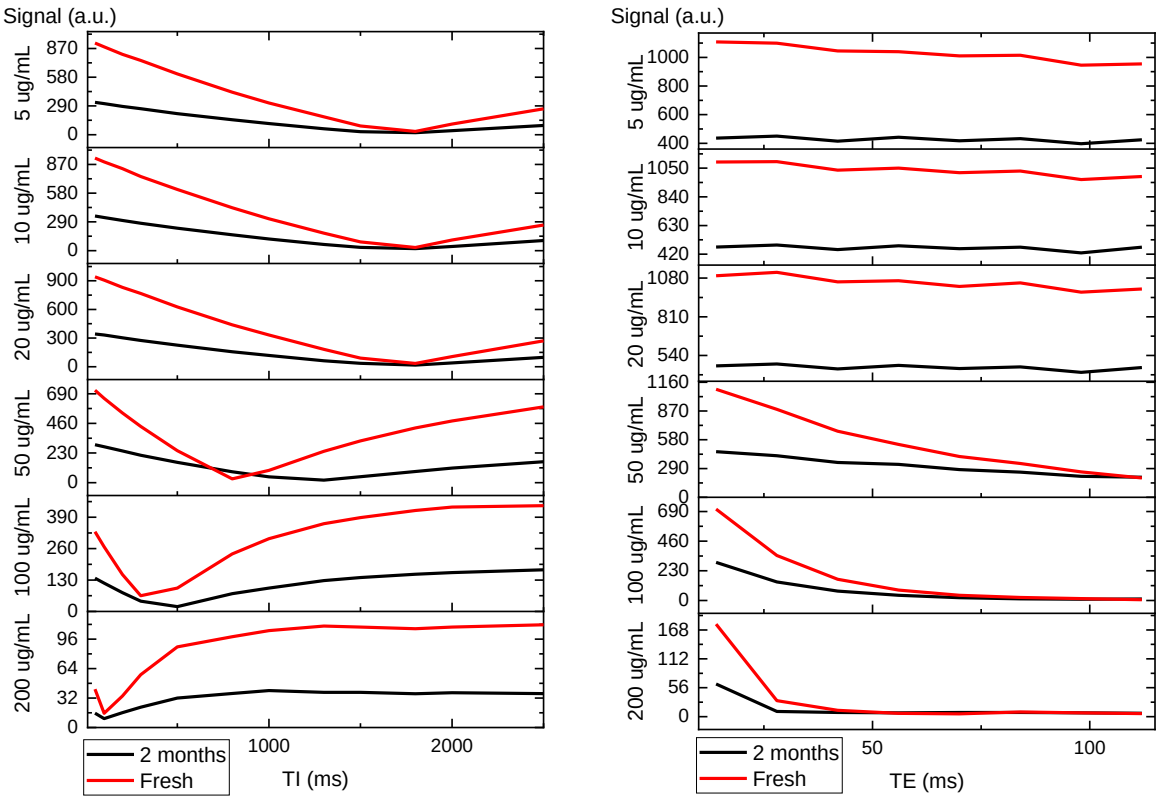

Figure 6.12 | T1 (left) and T2 (right) profiles from the center of the microcentrifugation tubes containing monodisperse γ-Fe_2O_3 NPs at concentrations of 200, 100, 50, 20, 10 and 5 µg/mL. (a) T1 measured at TI of 50, 100, 200, 300, 500, 800, 1000, 1300, 1500, 1800, 2000 and 2500 ms. (b) T2 is measured at TE of 14, 28, 42, 56, 70, 84, 98 and 112 ms.

Figure 6.12 displays the signal obtained for both T1 and T2 weighted images. There is an evident diminution in contrast for both modes when decreasing the signal. However, these concentrations are extremely low, therefore any contrast obtain from

them is already a promising result. “Fresh” means same day synthesis and ultrasonically redispersed. “2 months” means stored in the fridge at 5 °C for 2 months which resulted in most of the sample aggregated and decantated at the bottom of the microcentrifugation tube and strongly sonicated afterwards, plus allowing a few hours to seat at room temperature that will lead to decantation when the particles still remain aggregated.

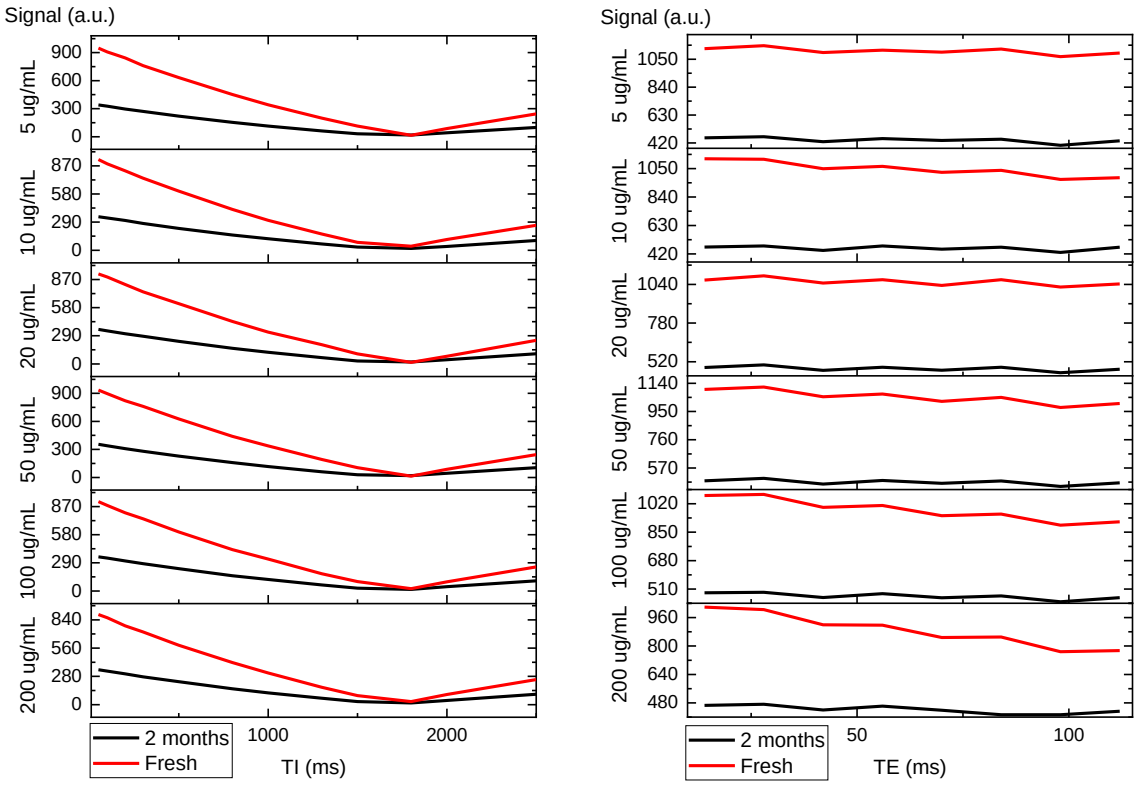

Figure 6.13 | T1 and T2 profiles from the center of the microcentrifugation tubes containing monodisperse γ-Fe_2O_3-SiO_2-Au NPs at concentrations of 200, 100, 50, 20, 10 and 5 µg/mL. T1 is measured at TI of 50, 100, 200, 300, 500, 800, 1000, 1300, 1500, 1800, 2000 and 2500 ms. T2 is measured at TE of 14, 28, 42, 56, 70, 84, 98 and 112 ms.

In the same line, Figure 6.13 shows moderate contrast at 200 µg/mL and low for any value below 50 µg/mL. This means that single cancer cells might not be detected using this NP but clusters of them could be detected.

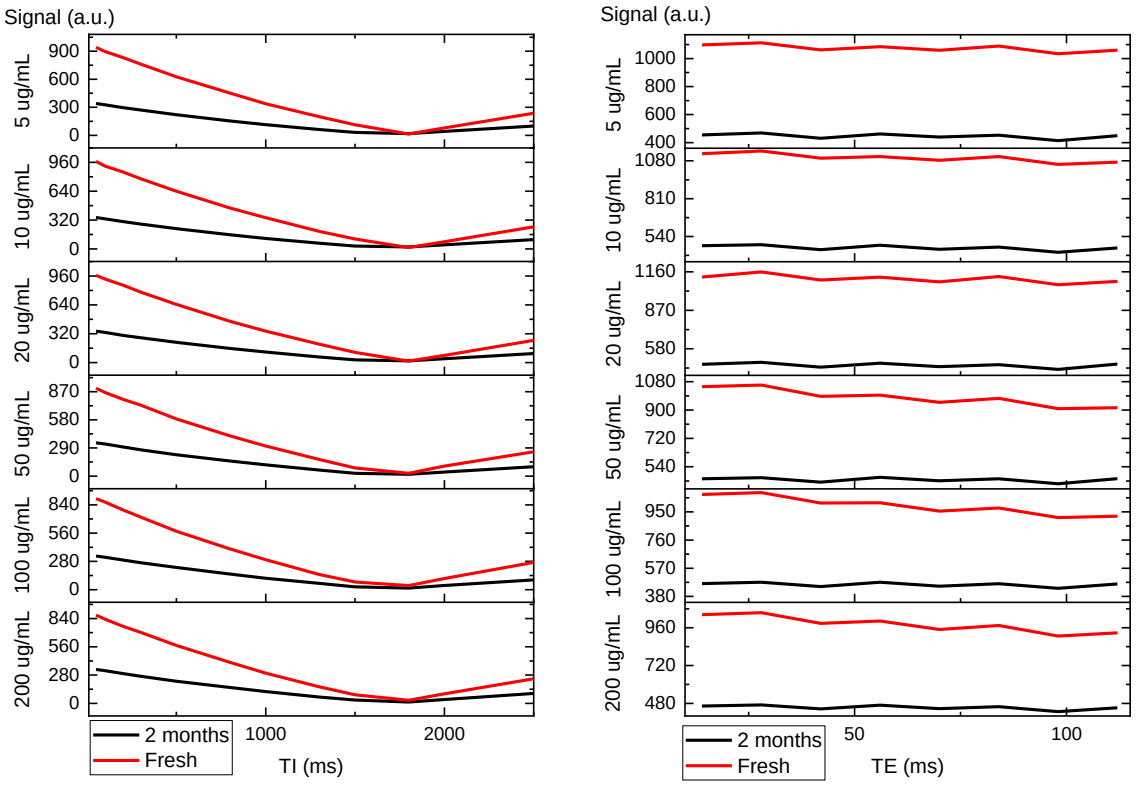

Figure 6.14 | First time T1 and T2 profiles from the centre of the micro centrifugation tubes containing polydisperse γ-Fe_2O_3-SiO_2-Au NPs at concentrations of 200, 100, 50, 20, 10 and 5 µg/mL. T1 is measured at TI of 50, 100, 200, 300, 500, 800, 1000, 1300, 1500, 1800, 2000 and 2500 ms. T2 is measured at TE of 14, 28, 42, 56, 70, 84, 98 and 112 ms.

Comparing these results from monodisperse nanoparticles with the polydisperse counterparts presented in Figure 6.14, it is clear that the polydisperse sample performs worse as a contrast agent than the monodisperse sample. Not only the results are worse, but also the polydisperse sample contains a higher magnetic material ratio per NP and should provide a stronger signal for the same concentration

to compensate. However, this is not the case, and therefore the performance is clearly poorer.

By using the profiles displayed in Figures 6.12-14, Table 1 was obtained where the T1 and T2 values are reported for each concentration in the fresh and 2 months formats using equations A3 and A5 from the Appendix, along with an estimation of how well the fit the exponential decay model.

The T1 and T2 obtained values are listed in the following table:

MRI samples		Concentration (μg/mL)	$T1_{mean}$ (ms)	R_{T1}^2	$T2_{mean}$ (ms)	R_{T2}^2
Monodisperse γ-Fe_2O_3	Fresh	200	0.97	0.32	36	0.62
		100	0.96	0.35	21	1.00
		50	3.89	0.01	57	1.00
		20	-0.37	0.73	883	0.79
		10	-0.37	0.72	837	0.84
		5	-0.22	0.72	615	0.93
	2 months	200	1.29	0.32	69	0.45
		100	1.07	0.27	28	0.94
		50	-1.09	0.14	114	0.99
		20	-0.40	0.74	1492	0.33
		10	-0.40	0.73	2099	0.17
		5	-0.25	0.72	1595	0.28
Monodisperse γ-Fe_2O_3-SiO_2-Au	Fresh	200	-0.37	0.73	328	0.95
		100	-0.35	0.73	526	0.90
		50	-0.32	0.72	870	0.78
		20	-0.32	0.74	2365	0.40
		10	-0.39	0.71	682	0.88
		5	-0.32	0.72	2279	0.45
	2 months	200	-0.39	0.71	824	0.65
		100	-0.40	0.69	1142	0.54
		50	-0.24	0.69	1732	0.31
		20	-0.40	0.72	1848	0.28
		10	-0.24	0.74	2753	0.11
		5	0.24	0.72	1172	0.40
Polydisperse γ-Fe_2O_3-SiO_2-Au	Fresh	200	-0.37	0.74	704	0.83
		100	-0.39	0.70	576	0.90
		50	-0.37	0.72	655	0.87
		20	-0.32	0.75	1938	0.43
		10	-0.32	0.74	1450	0.69

		5	-0.32	0.74	2108	0.47
	2 months	200	-0.38	0.64	2013	0.30
		100	-0.39	0.64	2852	0.14
		50	-0.40	0.66	3670	0.09
		20	-0.40	0.65	2417	0.13
		10	-0.42	0.66	3315	0.30
		5	-0.40	0.65	1925	0.19

Table 1: T1 and T2 values calculated using the linear regression included in the Appendix.

Previously, Jun *et al.* reported that the T2 results have an intrinsic relationship with the size of the Fe_3O_4 NPs. Concretely, they obtained values of 350-400 ms at 4 nm, 150-200 ms at 6 nm, 150 nm at 9 nm and 100 ms at 12 nm [340]. Similar NPs to the ones used in our study were synthesised before by other authors also for contrast-enhanced MRI without including an intermediate layer of SiO_2 (direct coating). That approach seems to decrease the saturation magnetization, hence reducing the relaxivity of the IONP core and reducing its ability to act as an MRI contrast agent [235,341,342]. Therefore, the intermediate thin SiO_2 shell plays a strategic role in preventing this avoidable loss in relaxivity.

Our composite NPs display strong contrast negative for both T1 and T2 modes. These results are consistent with the literature [343]; IONPs tend to display a negative contrast for T2. The T2 decay time of water and cerebrospinal fluid (CSF) is 2000-2500 ms while in fat is around 60-70 ms [344]. In contrast, the T1 decay time of water and CSF is about 4000 ms while in fat is 250 ms. Knowing the value is very important for medical imaging, but in our analysis, water is also essential to evaluate the contrast of the NPs since they are redispersed in deionised water. This means that negative contrast agents will be useful for water and CSF but not for fatty tissue. On the contrary, positive contrast agents will be more useful for both modes than negative contrast agents in theory. However, our T1 values from Table 1 are so low that they are close

to 0 in the approximated exponential fit and this can bring good contrast for both modes in water.

Dispersity in sizes for the magnetic core of a core-shell NP is not affecting significantly in the contrast capabilities at the same concentrations of the composite NP. However, since the polydisperse samples have much larger cores, the proportion of magnetic amount of magnetic material is much higher than in the monodisperse samples at the same NP concentrations. Therefore, the monodisperse samples seem to match the same contrast displayed in the polydisperse samples while having less magnetic material. This could be indicative of a higher contrast of the polydisperse sample. Overall, the concentration of the magnetic material in the composite structure is critical to obtain strong or weak contrast as seen by reducing the NPs concentration.

6.5. Magnetic nanoparticles' micromagnetic simulations results

All the following magnetic simulations in this section were performed by Conor McKeever using the micromagnetics theory with mumax[3]. The simulations were run on the GPU card: CUDA 9010 GeForce GTX 1080 Ti, from the online information there are 3584 CUDA cores.

Figure 6.15 shows the hysteresis loop using micromagnetics under single domain approximation for one maghemite NP. This result shows a high potential magnetic heat since thanks to the wide hysteresis loop area. However, these results are not an accurate representation of our system because there are many interacting NPs that will display emergent behaviour from these interactions.

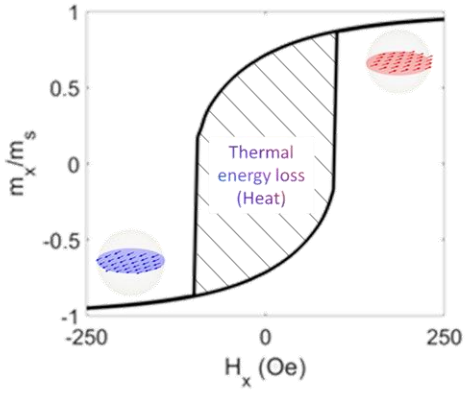

Figure 6.15 | Hysteresis loop Simulation of a 11 ± 1 nm NP using micromagnetics

Figure 6.16 shows a snapshot of 40 NPs like the ones used previously to obtain figure 6.15. Here, small variations in the size are introduced to include small polydispersity in the sample which is more realistic and adjust better to the monodisperse maghemite NPs used experimentally in this chapter.

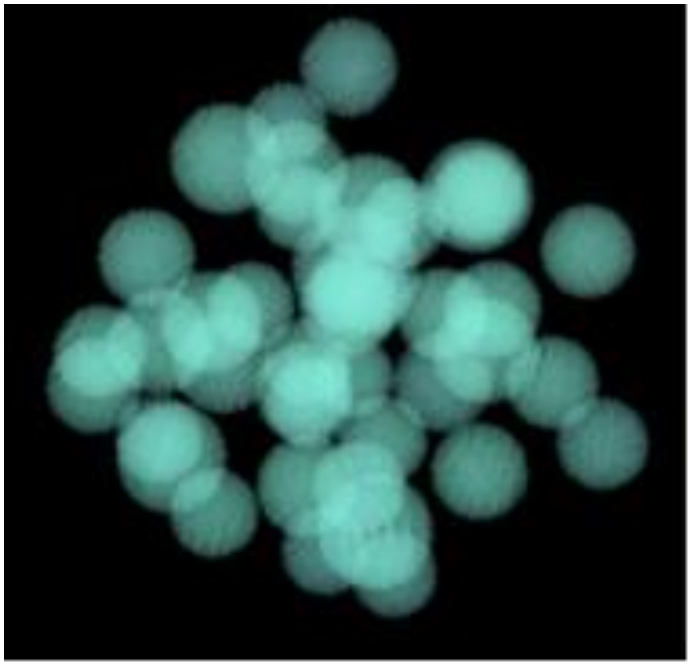

Figure 6.16 | High contrast simulation snapshot of 11 ± 1 nm NPs.

These simulated NPs present 11 ± 1 nm diameter. The polydispersity is included by adding up to 1 nm of random fluctuations around 11 nm, which is the average value of the monodisperse NPs used experimentally. This small

polydispersity is very similar to the experimentally present fluctuations in diameter from the experiments.

As a computationally affordable approximation, a single net magnetic spin is used to describe each NP within the ensemble, which is subject to both inter- and intraparticle magnetic interactions. Figure 6.17.(a-c) shows the hysteresis loop comparison between the simulations and the experimental results. Figure 6.17.(d) displays the spin direction of the single domain magnetic NPs at a different intensity of the applied magnetic field.

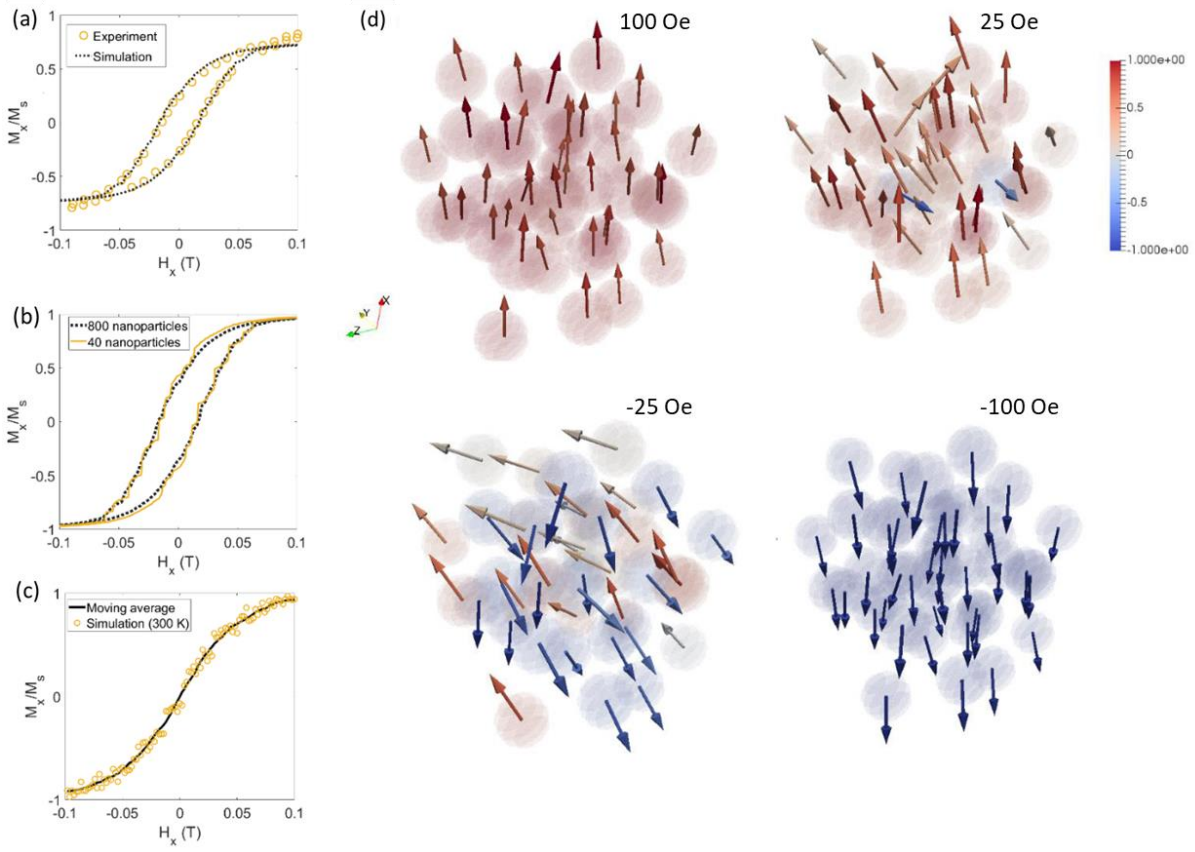

Figure 6.17 | (a) Comparison between simulated and experimental data for maghemite NPs, indicating close agreement between simulated and experimental values for the coercivity and remanence 5 K. (b) Comparison between numerical hysteresis obtained from a single simulation of 40 NPs and 800 NPs obtained by averaging over 20

simulations at 5 K. A smoothened hysteresis loop is observed due to particle averaging. (c) Hysteresis loop of interacting NP system at 300 K (room temperature). Superparamagnetic behaviour is observed at room temperature. (d) Magnetic configurations obtained for 40 strongly interacting maghemite NPs at different field strengths, corresponding to (b). The NPs are below the single domain limit allowing the magnetisation to be represented by a single net magnetic spin. These results were obtained by Conor McKeever using micromagnetics.

The saturation magnetization was that of maghemite at low temperatures [345] m_{sat} = 3.8 × 10^5 A/m with an exchange constant of C = 1 × 10^{-11} J/m in the magnetic regions and C = 0 in non-magnetic regions. Uniaxial magnetocrystalline anisotropy was used with an estimated value of K_u = 8 × 10^3 J/m^3 based on fitting to experimental data (see Figure 6.10.(a)), which is in reasonable agreement with the effective magnetic anisotropy of maghemite, e.g. 7.8 × 10^3 J/m^3 ± 12% for 13 nm maghemite NPs, which is known to be generally larger than the bulk magnetocrystalline anisotropy 4.6 × 10^3 J/m^3 [346–348]. The magnetocrystalline anisotropy axis was oriented along a direction chosen randomly on the unit sphere. To incorporate the material variation present in actual samples, a 10% uniform variation of the material parameters was introduced into the simulations. Moreover, due to the random choice of magnetocrystalline anisotropy direction for each particle, there is an infinite number of unique magnetic NPs which can be modelled. As a result, each simulation was repeated multiple times with different random number generator seed values, and the resulting hysteresis loops were averaged. The particles were randomly populated within the grid and prevented from overlapping to study a system of non-agglomerated particles. A cell-size of 0.4 nm was adopted for NPs of 11.1 nm in diameter, which is below the single domain limit for maghemite NPs [349,350]. A 10% uniform variation in

particle size was introduced to account for the size disparity of experimental samples. Brown's thermal equation was incorporated into the simulation by running the stochastic Landau-Lifshitz (sLL) equation in the time-domain with high-damping (α = 1.0). The impact of thermal energy on the hysteretic behaviour is very large at room temperature due to the small size of the NPs, leading to superparamagnetic behaviour (see Figure 6.10.(c)). At low temperatures, the simulated coercivity and remanence of the hysteresis loop are found to agree closely with experimental values (see Figure 6.10.(a)). However, the experimental measurements show a longer hysteresis tail. Such a discrepancy could potentially result from the effect of particle agglomeration leading to more complex domain configurations with larger nucleation fields [351].

6.6. Magnetic heating results

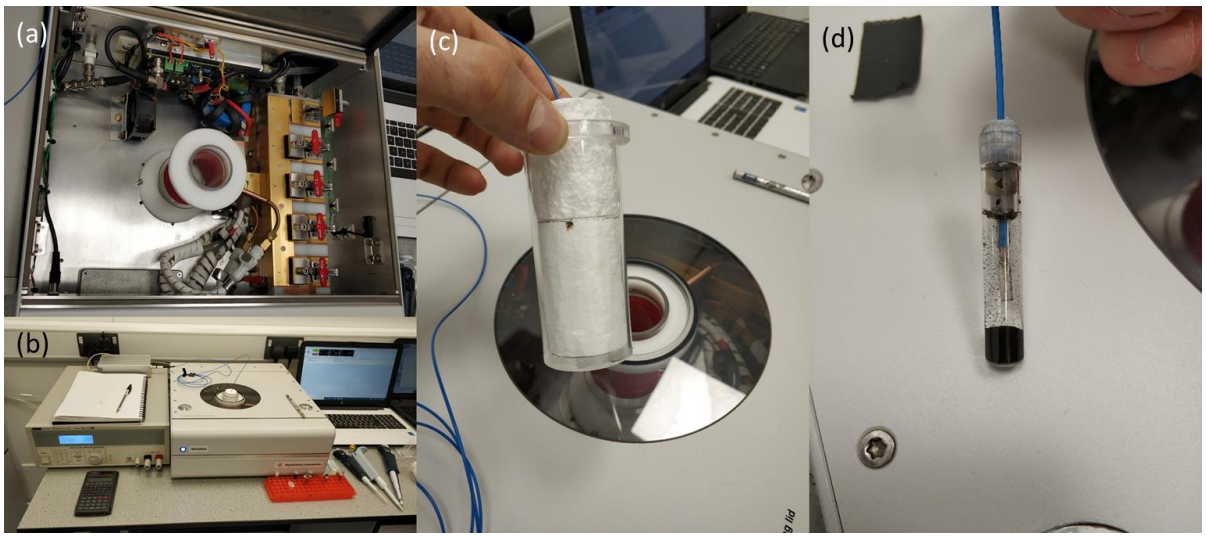

Figure 6.18 | NanoHeat from NanoScience Laboratories experimental setup (a) from the inside and (b) from the outside. (c) Polystyrene holder. (d) Sample configuration during readings.

Figure 6.18 displays the experimental setup used to obtain the magnetic heating profiles of the monodisperse core and its core-shell counterpart. The device

was calibrated before taking the measurements with a 9 nm magnetite sample. This system works in a range of 50kHz to 1,000kHz, which is optimal to cover most biologically relevant magnetic heating tests.

Figure 6.19 shows that the magnetic heating profiles of γ-Fe_2O_3 and γ-Fe_2O_3-SiO_2-Au NPs at 515 kHz and 170 Oe seem promising for cellular applications. The temperature rise is 30 °C in 18 min for γ-Fe_2O_3 and 7 °C in 23 min for γ-Fe_2O_3-SiO_2-Au. Human body temperature is usually at 37 °C in normal conditions, and magnetic hyperthermia is achieved at 40-48 °C. Therefore, both heating profiles quickly increase by 3 °C to reach the range.

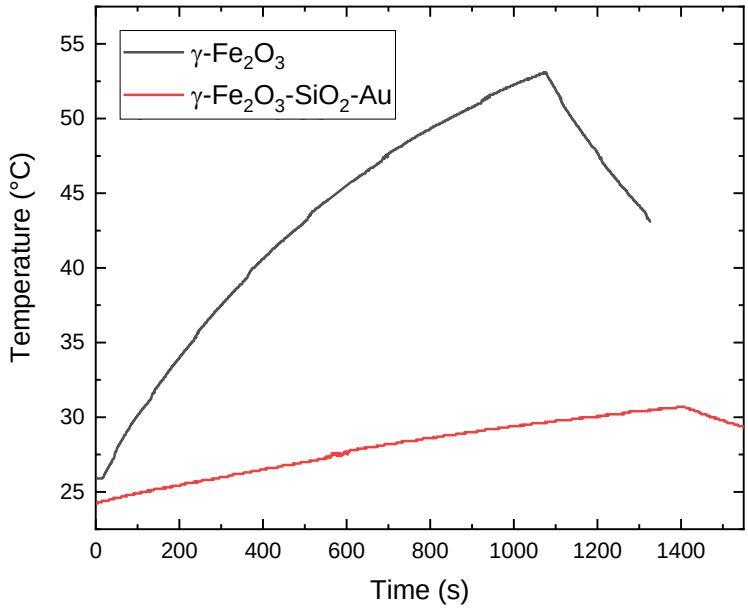

Figure 6.19 | Magnetic heating profiles of γ-Fe_2O_3 and γ-Fe_2O_3-SiO_2-Au NPs at 515 kHz and 170 Oe.

6.7. In vitro toxicity results

All the cell viability and toxicity assays are performed in close collaboration with Dr Julia Sero, Dr Dyan Ankrett and Marziyeh Belal.

γ-Fe_2O_3-SiO_2-Au core-shell composite nanoparticles

Cell viability in human kidney cells: Monodisperse Fe_2O_3-SiO_2-Au NPs cytotoxicity against eukaryotic cells was determined using human embryonic kidney HEK293A cells (ThermoFisher, UK) and utilising the MTT assay. HEK293A cells were sequentially adapted to serum-free media, followed by routine culture in Pro293™ chemically defined, serum-free media (Lonza, Slough, UK) and supplemented with 1% v/v Insulin-Transferrin-Selenium (ITS, Gibco, UK), 4.5 g/L glucose, 2 mM L-glutamine and 1% Penicillin Streptomycin (Sigma-Aldrich, Dorset, UK). Media and all supplements were free of animal-derived components. The cells were maintained 37°C in 5% CO_2. For cytotoxicity assays, HEK293A cells were seeded in 96-well plates at a density of 1×10^5 cells mL^{-1} and incubated for 24 hours at 37 °C in 5% CO_2.

NPs were diluted in Pro293™media to produce a final concentration range of 100 – 2000 µg/mL^{-1} when added to cells in individual wells (final volume, 200 µL per well). Cells exposed to NPs were then incubated for a further 24 or 48 hrs. Upon termination of the incubation time, MTT (20 µL of 5 mg/mL in PBS) was added to all wells and incubated for a further 4 hours. All wells were then aspirated, followed by the addition of 200 µL DMSO, at room temperature and under subdued light, for 15-20 minutes. DMSO solubilised the MTT formazan product, which was produced by live-cell mitochondrial succinate dehydrogenase. The absorbance of the solubilised formazan product was read at 590 nm using ClarioStar microplate reader (BMG LABTECH Ltd, Bucks, UK).

Cell viability in human pericytes: The pericyte cells derived from human foetus provided by ScienceCell Company were cultured in T75 flasks and maintained in 5% CO_2 incubator at 37 °C. After a few days of culturing once the flasks were fully covered by the cells and reached the confluency of >80% the monodisperse Fe_2O_3-SiO_2-Au

NPs were added to the flasks in series of dilutions. After 48 hours, the cell viability was evaluated using the Trypan blue exclusion method. The NPs added in the flasks were initially soluble in the Pericyte Medium but not anymore after being left for 48 hours. As a result, after the aspiration of the medium from flasks, the NPs were not present in the medium; instead, they were bound to the pericyte cells and make them look dark after centrifugation.

Cell viability in human breast epithelial cells: Cells were cultured in 96-well plates in 100 µL of growth medium were treated with 10 µL of DI H_2O or 1:10 dilutions of washed NP supernatant (carrier liquid) or NPs in suspension (for a final dilution of 1:100). The initial concentration of NPs prior to two washes was ~20 mg/µL. Plates were fixed and stained to label nuclei (DAPI), 5 fields of view per well were imaged at 20X using a high-content wide-field fluorescence microscope, (InCell Analyser 2000), and cells were detected and measured using automated image analysis (CellProfiler). The tube was centrifuged for 10 min at 4 ◦C, and the supernatant was removed.

MCF10A (non-tumour) human breast epithelial cell plate was incubated at 37 °C (5% CO_2) for 24 h. Then, it was fixed with 2% formaldehyde and permeabilised with 2% Triton X-100, washed with phosphate-buffered saline, and incubated with 10 ug/ml Hoeschst to stain DNA (label nuclei). Imaged 9 fields of view per well (20X) - most of the wells covered by these fields and automatically detected and counted nuclei/well using CellProfiler. Dead/dying cells not removed by washing were filtered out based on morphology and staining.

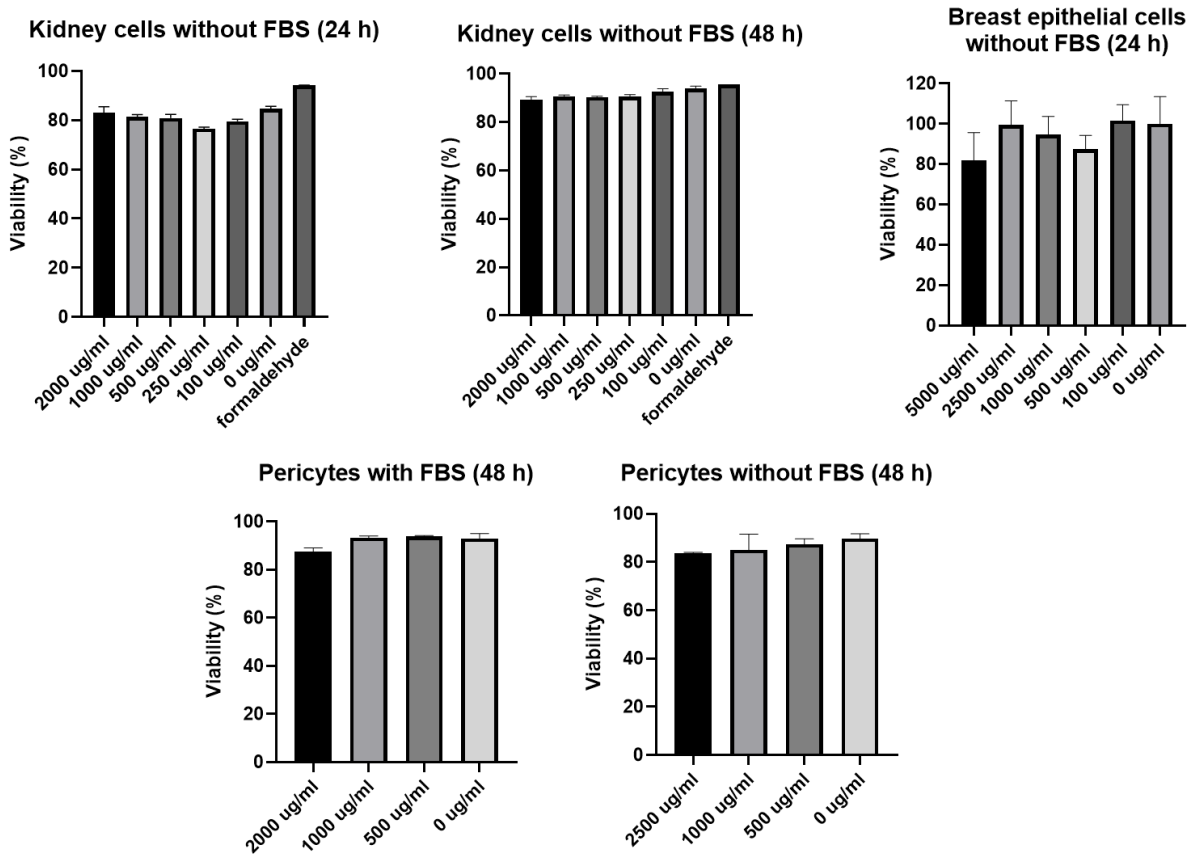

Figure 6.20 | Cell viability and cytotoxicity assays for monodisperse γ-Fe_2O_3-SiO_2-Au NPs in healthy cells. Cell viability assay in human kidney cells was performed by Dr. Dyan Ankrett, in human pericytes by Marziyeh Belal and in human breast epithelial cells was performed by Dr. Julia Sero.

Figure 6.20 displays the cell viability assays results from kidney cells and pericytes. None of the concentrations leads to high levels of cytotoxicity even at 2000 ug/mL, which is the high most drugs and NPs are usually tested at. This is incredibly encouraging since these are healthy cells that usually survive worse than cancer cells when exposed to nanoscale agents. Also, kidney cells died faster after 24 h than after 48 h which is beneficial for long term exposure and could be an effect NP corona formation. Breast epithelial cells showed very variable toxicity, but not significant since the standard deviation was high. Nevertheless, the no substantial cytotoxicity was found for these cells. For human pericytes, using single factor ANOVA, p-value is more

than 0.05% which shows there is no significant difference between groups in terms of the viability. Based on the pericyte assay, we can state that FBS does not display clear benefits.

The main issue with the use of NPs in vivo as a diagnostic or therapeutic tool is that it is an invasive technique which brings potential side effects to the patient. These concerns could be outweighed for terminal patients. However, high concentrations of NPs would be required to deal with the metastasised tumours, and high concentrations of any NPs also lead to longer excretion time and small excretion ratios. High concentrations that remain for more extended periods in the human organism have been found toxic even for safely engineered NPs[352]. Therefore, the primary target patient for the use of these NPs are those whose potential tumour is small, and subsequently, only small volumes at low concentration of these NPs would be required to find and treat the malignancy. The optimal patients that match these criteria are early stage and reemission patients. Hence, assessing their toxicity in physiologically relevant microenvironments is essential to pursue a commercialization plan while actively avoiding the use of non-human animals for preclinical trials.

6.8. Summary

In summary, chapter 6 presented magneto plasmonic core-shell γ-Fe_2O_3-SiO_2-Au NPs with monodisperse and polydisperse cores. The monodisperse sample presented a better performance in all the imaging techniques, and subsequently, its magnetic hyperthermia capabilities and cytotoxicity were analysed. These NPs displayed promising magnetic hyperthermia capabilities within the scope of 20 minutes of heating time. No significant toxicity was found in any of the three types of cells tested either. γ-Fe_2O_3-SiO_2-Au NPs have therefore shown combined capabilities for strong

SERS effect in liquid samples, CT contrast for aggregated NPs, MRI contrast at low concentration and hyperthermia capabilities without presenting significant toxicity at the cellular level for healthy cells. This NPs present a promising approach for cancer cell nanotheranostics.

7. Conclusions

In this thesis, several nanoparticles were designed and successfully synthesised, followed by the testing of their cancer nanotheranostics functionalities.

Multiple NPs were synthesised and compared in Chapter 4 to evaluate potential functionalities for a core in a core-shell structure. WO_3 and γ-Fe_2O_3 were reduced under heat treatment in an H_2+Ar gas atmosphere showing material transition at different temperatures. For WO_3, a colouration process to dark blue probably due to hydrogenation is achieved with complete colouration at approximately 340 °C. For γ-Fe_2O_3 NPs, a customizable mixture ratio of α-Fe and γ-Fe_2O_3 is obtained. This mixture presents different magnetic properties, obtaining only α-Fe as a product at approximately 320 °C. Filtration of NPs was performed with heavily polydisperse γ-Fe_2O_3 NPs to identify synthetic methods that improve sample homogeneity, purity and monodispersity. Consistent reduction in both hydrodynamic and NP diameter was found after filtration for both NFF and TFF using 37 nm and 60 nm pore size NPN. While TFF brings a higher degree of filtration than NFF, it is also more complex to assemble, requires longer filtration time, and it is not currently commercially available. These results bring valuable insights for automated microfluidic NP synthesis and purification platforms.

In chapter 5, a novel type of core-shell composite NP that contains WO_3 in its core was synthesised. This core was first shelled with SiO_2 and subsequently with Au that grew from an intermediate seeding step. This chapter reports how to control the SiO_2 shell formation, Au seeding process and Au shell formation over the WO_3 with SiO_2 and Au tunable shell thicknesses. SiO_2 was from 3 nm to 60 nm with potential to larger and thinner shells controlled by changing the ratio of ammonia:TEOS and Au

shell thickness by repeating the Au shell formation step and morphology is controlled by the varying the density of Au seeds on the SiO_2 shell which is increased by increasing the APTES concentration. These NPs displayed auspicious properties for clinical in vivo single cancer cell imaging. However, no therapeutic nor imaging capabilities were proven arising from the core. These NPs were tested using cell viability assays which showed low toxicity for concentrations below 100 µg/mL (after 24 h, >75% alive cells from statistically significant cell viability). These concentrations are low but still higher than the values other authors have used previously, which can go as low as 5 µg/mL.

The last multifunctional type of NP – the magnetic-plasmonic composite core-shell γ-Fe_2O_3-SiO_2-Au NP – combined effectively magnetic and plasmonic behaviours for cancer diagnosis and treatment while minimising toxicity and aggregation. This thesis showed a performance analysis of four different functionalities from this NP: SERS, MRI, microCT and magnetic heating. These functionalities are highly desirable for cancer theranostics from a clinical point of view. Furthermore, their cytotoxicity was analysed in various types of human cells, including healthy kidney cells, healthy pericytes and breast cells. These results showed extremely low toxicity in vitro using 2D assays for all the tested cells at all concentrations. These results lead to expect highly promising results in 3D in vitro models and human trials.

Refinement methods and material phase transitions were performed to study other potential NPs. Some of these methods display some limitations, such as the need to work at low concentrations or working with dried samples. Converting NPs from a higher oxidation state to a lower stable phase is highly demanded in materials science. However, our technique poses the risk of inducing irreversible aggregation of

these NPs during the heat treatment, particularly with magnetic NPs. On the other hand, working with nanoporous membranes brought to our attention some vital issues during the NPs' size filtration. The NPs need to be filtered at a significantly lower concentration to prevent aggregation that will accumulate on the membrane surface building the cake effect – which tends to break the membranes. Low concentrations during filtration translate to long filtration periods. Moreover, both tangential and normal filtration have low efficiencies – many NPs that could be filtered never cross the membrane, which leads to high sample loss. Moreover, future tests of electrochromic properties in realistic microphysiological mimicking environments could help to better understand the usefulness of the electrochromic behaviour.

In conclusion, the final type of NPs, monodisperse γ-Fe_2O_3-SiO_2-Au, presents highly desirable properties for potential cancer theranostics by offering a combination of SERS, MRI and CT imaging capabilities as well as extremely low cytotoxicity for all types of healthy and cancer cells in vitro tested which are representative of different regions of the human body. Furthermore, magnetic heat was obtained from these NPs using AMF at 515 kHz and 170 Oe, obtaining an increment of 7 °C in 23 min. Since a healthy human body is usually at 37 °C, in 23 min temperatures of 44 °C can be reached, which are in the optimal hyperthermia range (42-46 °C). This implies a potential combination of four functionalities (three diagnostic and one therapeutic) which could be used for in vivo scenarios to locate and treat cancer cells.

8. Future prospect

Further studies should be performed to understand their behaviour in a dynamical environment and without 2D movement restrictions as well as being under gradients of temperature, pressure, and pH. For a selective targeting, these NPs can be functionalized with antibodies that target specific antigens from the cancer cell surface. However, as long the surface is negatively charged, targeting can be achieved to only cancer cells [97]. This could be better in cases of dealing with multiple types of cancers or when the identification of the type of cancer is not possible. In this regard, working with personalised 3D microfluidic assays is the safest and most ethical approach to understand the future behaviour of the NPs for a particular cancer patient.

Additional functionalities can be further studied with the same materials used in this thesis such as NIR fluorescence, ultrasound and terahertz imaging along with photothermal treatment. This is possible thanks to the fact that the materials of types of core (WO_3 and γ-Fe_2O_3) and the Au shells used in this study are good contrast agents for ultrasound imaging and terahertz imaging, except SiO_2 which would bring a lower resolution in these imaging techniques but can be used to embed fluorescent dyes.

Bibliography

[1] M. Greaves, C. C. Maley, *Nature* **2012**, *481*, 306.

[2] M. W. Schmitt, L. A. Loeb, J. J. Salk, *Nat. Rev. Clin. Oncol.* **2016**, *13*, 335.

[3] N. Nishida, H. Yano, T. Nishida, T. Kamura, M. Kojiro, *Vasc. Health Risk Manag.* **2006**, *2*, 213.

[4] K. Kong, C. Kendall, N. Stone, I. Notingher, *Adv. Drug Deliv. Rev.* **2015**, *89*, 121.

[5] J. C. C. Day, N. Stone, *Appl. Spectrosc.* **2013**, *67*, 349.

[6] N. Stone, R. Baker, K. Rogers, A. W. Parker, P. Matousek, *Analyst* **2007**, *132*, 899.

[7] N. Stone, P. Matousek, *Cancer Res.* **2008**, *68*, 4424.

[8] S. Pahlow, K. Weber, J. Popp, B. R. Wood, K. Kochan, A. Rüther, D. Perez-Guaita, P. Heraud, N. Stone, A. Dudgeon, B. Gardner, R. Reddy, D. Mayerich, R. Bhargava, *Appl. Spectrosc.* **2018**, *72*, 52.

[9] D. I. Ellis, D. P. Cowcher, L. Ashton, S. O'Hagan, R. Goodacre, *Analyst* **2013**, *138*, 3871.

[10] J. P. B. O'Connor, E. O. Aboagye, J. E. Adams, H. J. W. L. Aerts, S. F. Barrington, A. J. Beer, R. Boellaard, S. E. Bohndiek, M. Brady, G. Brown, D. L. Buckley, T. L. Chenevert, L. P. Clarke, S. Collette, G. J. Cook, N. M. deSouza, J. C. Dickson, C. Dive, J. L. Evelhoch, C. Faivre-Finn, F. A. Gallagher, F. J. Gilbert, R. J. Gillies, V. Goh, J. R. Griffiths, A. M. Groves, S. Halligan, A. L. Harris, D. J. Hawkes, O. S. Hoekstra, E. P. Huang, B. F. Hutton, E. F.

Jackson, G. C. Jayson, A. Jones, D.-M. Koh, D. Lacombe, P. Lambin, N. Lassau, M. O. Leach, T.-Y. Lee, E. L. Leen, J. S. Lewis, Y. Liu, M. F. Lythgoe, P. Manoharan, R. J. Maxwell, K. A. Miles, B. Morgan, S. Morris, T. Ng, A. R. Padhani, G. J. M. Parker, M. Partridge, A. P. Pathak, A. C. Peet, S. Punwani, A. R. Reynolds, S. P. Robinson, L. K. Shankar, R. A. Sharma, D. Soloviev, S. Stroobants, D. C. Sullivan, S. A. Taylor, P. S. Tofts, G. M. Tozer, M. van Herk, S. Walker-Samuel, J. Wason, K. J. Williams, P. Workman, T. E. Yankeelov, K. M. Brindle, L. M. McShane, A. Jackson, J. C. Waterton, *Nat. Rev. Clin. Oncol.* **2016**, *14*, 169.

[11] P. Martinez Pancorbo, K. Thummavichai, L. Clark, T. A. Tabish, J. Mansfield, B. Gardner, H. Chang, N. Stone, Y. Zhu, *Adv. Funct. Mater.* **2019**, *29*, 1903549.

[12] “Chemotherapy, Radiotherapy and Surgical Tumour Resections in England: Treatment Breakdown, 2013-2016,” can be found under https://www.cancerdata.nhs.uk/treatments, **2020**.

[13] L. Wyld, R. A. Audisio, G. J. Poston, *Nat. Rev. Clin. Oncol.* **2015**, *12*, 115.

[14] R. Baskar, K. A. Lee, R. Yeo, K.-W. Yeoh, *Int. J. Med. Sci.* **2012**, *9*, 193.

[15] G. Borrego-Soto, R. Ortiz-López, A. Rojas-Martínez, *Genet. Mol. Biol.* **2015**, *38*, 420.

[16] E. J. Walter, S. Hanna-Jumma, M. Carraretto, L. Forni, *Crit. Care* **2016**, *20*, 200.

[17] Z. Behrouzkia, Z. Joveini, B. Keshavarzi, N. Eyvazzadeh, R. Z. Aghdam, *Oman Med. J.* **2016**, *31*, 89.

[18] J. West, P. K. Newton, *Cancer Res.* **2017**, *77*, 6717.

[19] A. E. El-Kenawi, A. B. El-Remessy, *Br. J. Pharmacol.* **2013**, *170*, 712.

[20] B. A. A. Weaver, D. W. Cleveland, *Cancer Cell* **2005**, *8*, 7.

[21] K. Mahmoudi, A. Bouras, D. Bozec, R. Ivkov, C. Hadjipanayis, *Int. J. Hyperthermia* **2018**, *34*, 1316.

[22] I. Urries, C. Muñoz, L. Gomez, C. Marquina, V. Sebastian, M. Arruebo, J. Santamaria, *Nanoscale* **2014**, *6*, 9230.

[23] V. Amendola, S. Scaramuzza, L. Litti, M. Meneghetti, G. Zuccolotto, A. Rosato, E. Nicolato, P. Marzola, G. Fracasso, C. Anselmi, M. Pinto, M. Colombatti, *Small* **2014**, *10*, 2476.

[24] A. M. Ahmed, A. Mehaney, M. Shaban, A. H. Aly, *Mater. Res. Express* **2019**, *6*, 85073.

[25] V. Hosseini, M. Mirrahimi, A. Shakeri-Zadeh, F. Koosha, B. Ghalandari, S. Maleki, A. Komeili, S. K. Kamrava, *Photodiagnosis Photodyn. Ther.* **2018**, *24*, 129.

[26] Y. Li, J. Zhao, W. You, D. Cheng, W. Ni, *Nanoscale* **2017**, *9*, 3925.

[27] J. Wahsner, E. M. Gale, A. Rodríguez-Rodríguez, P. Caravan, *Chem. Rev.* **2019**, *119*, 957.

[28] F. Nicolson, B. Andreiuk, C. Andreou, H.-T. Hsu, S. Rudder, M. F. Kircher, *Theranostics* **2019**, *9*, 5899.

[29] A. J. Ferreira, J. Cemlyn-Jones, C. Robalo Cordeiro, *Rev. Port. Pneumol.* **2013**, *19*, 28.

[30] I. Iavicoli, L. Fontana, G. Nordberg, *Crit. Rev. Toxicol.* **2016**, *46*, 490.

[31] A. Karmakar, Q. Zhang, Y. Zhang, *J. Food Drug Anal.* **2014**, *22*, 147.

[32] Y. Gao, Y. Li, Y. Wang, Y. Chen, J. Gu, W. Zhao, J. Ding, J. Shi, *Small* **2014**, *11*, 77.

[33] N. N. L. Quynh, L. Van Vu, C. D. Kiem, S. C. Doanh, C. T. Nguyet, P. T. Hang, N. D. Thien, L. Manh, *J. Phys. Conf. Ser.* **2009**, *187*, 12026.

[34] P. Puvanakrishnan, J. Park, P. Diagaradjane, J. A. Schwartz, C. L. Coleman, K. L. Gill-Sharp, K. L. Sang, J. D. Payne, S. Krishnan, J. W. Tunnell, **2009**, *14*, 24044.

[35] F. Nicolson, L. E. Jamieson, S. Mabbott, K. Plakas, N. C. Shand, M. R. Detty, D. Graham, K. Faulds, *Analyst* **2018**, *143*, 5358.

[36] A. R. Rastinehad, H. Anastos, E. Wajswol, J. S. Winoker, J. P. Sfakianos, S. K. Doppalapudi, M. R. Carrick, C. J. Knauer, B. Taouli, S. C. Lewis, A. K. Tewari, J. A. Schwartz, S. E. Canfield, A. K. George, J. L. West, N. J. Halas, *Proc. Natl. Acad. Sci.* **2019**, *116*, 18590 LP.

[37] J. Jose, R. Kumar, S. Harilal, G. E. Mathew, D. G. T. Parambi, A. Prabhu, M. S. Uddin, L. Aleya, H. Kim, B. Mathew, *Environ. Sci. Pollut. Res.* **2020**, *27*, 19214.

[38] D. T. T. Phan, R. H. F. Bender, J. W. Andrejecsk, A. Sobrino, S. J. Hachey, S. C. George, C. C. W. Hughes, *Exp. Biol. Med.* **2017**, *242*, 1669.

[39] H.-Y. Park, M. J. Schadt, Wang, I.-I. S. Lim, P. N. Njoki, S. H. Kim, M.-Y. Jang, J. Luo, C.-J. Zhong, *Langmuir* **2007**, *23*, 9050.

[40] A. Sukhanova, S. Bozrova, P. Sokolov, M. Berestovoy, A. Karaulov, I. Nabiev, *Nanoscale Res. Lett.* **2018**, *13*, 44.

[41] E. Demangeat, M. Pédrot, A. Dia, M. Bouhnik-le-Coz, F. Grasset, K. Hanna, M. Kamagate, F. Cabello-Hurtado, *Environ. Sci. Nano* **2018**, *5*, 992.

[42] WangWang, J. Luo, Q. Fan, M. Suzuki, I. S. Suzuki, M. H. Engelhard, Y. Lin, N. Kim, J. Q. Wang, C.-J. Zhong, *J. Phys. Chem. B* **2005**, *109*, 21593.

[43] S. Sabale, P. Kandesar, V. Jadhav, R. Komorek, R. K. Motkuri, X.-Y. Yu, *Biomater. Sci.* **2017**, *5*, 2212.

[44] Y. Zhai, J. Zhai, Y. Wang, S. Guo, W. Ren, S. Dong, *J. Phys. Chem. C* **2009**, *113*, 7009.

[45] W. Dong, Y. Li, D. Niu, Z. Ma, J. Gu, Y. Chen, W. Zhao, X. Liu, C. Liu, J. Shi, *Adv. Mater.* **2011**, *23*, 5392.

[46] J.-E. Bae, M.-I. Huh, B.-K. Ryu, J.-Y. Do, S.-U. Jin, M.-J. Moon, J.-C. Jung, Y. Chang, E. Kim, S.-G. Chi, G.-H. Lee, K.-S. Chae, *Biomaterials* **2011**, *32*, 9401.

[47] A. Nel, T. Xia, L. Mädler, N. Li, *Science* **2006**, *311*, 622.

[48] T. Xia, N. Li, A. E. Nel, *Annu. Rev. Public Health* **2009**, *30*, 137.

[49] T. Carter, P. Mulholland, K. Chester, *Immunotherapy* **2016**, *8*, 941.

[50] Z. Li, M. Wu, H. Bai, X. Liu, G. Tang, *Chem. Commun.* **2018**, *54*, 13127.

[51] N. Stone, M. Kerssens, G. R. Lloyd, K. Faulds, D. Graham, P. Matousek, *Chem. Sci.* **2011**, *2*, 776.

[52] O. S. Wolfbeis, *Chem. Soc. Rev.* **2015**, *44*, 4743.

[53] N. S. Aminabad, M. Farshbaf, A. Akbarzadeh, *Cell Biochem. Biophys.* **2019**,

77, 123.

[54] S. F. Karkan, M. Mohammadhosseini, Y. Panahi, M. Milani, N. Zarghami, A. Akbarzadeh, E. Abasi, A. Hosseini, S. Davaran, *Artif. Cells, Nanomedicine, Biotechnol.* **2017**, *45*, 1.

[55] R. Toy, E. Hayden, C. Shoup, H. Baskaran, E. Karathanasis, *Nanotechnology* **2011**, *22*, 115101.

[56] A.-A. D. Jones III, G. Mi, T. J. Webster, *Trends Biotechnol.* **2019**, *37*, 117.

[57] V. D. Schepkin, F. C. Bejarano, T. Morgan, S. Gower-Winter, M. Ozambela Jr., C. W. Levenson, *Magn. Reson. Med.* **2012**, *67*, 1159.

[58] A. J. Burghardt, T. M. Link, S. Majumdar, *Clin. Orthop. Relat. Res.* **2011**, *469*.

[59] W. W. Moses, *Nucl. Instruments Methods Phys. Res. Sect. A Accel. Spectrometers, Detect. Assoc. Equip.* **2011**, *648*, S236.

[60] S. Acharyya, L. Matrisian, D. R. Welch, J. Massagué, in *Mol. Basis Cancer (Fourth Ed.* (Eds.: J. Mendelsohn, J.W. Gray, P.M. Howley, M.A. Israel, C.B. Thompson), Content Repository Only!, Philadelphia, **2015**, pp. 269-284.e2.

[61] C. A. Janeway Jr, P. Travers, M. Walport, M. J. Shlomchik, in *Immunobiol. Immune Syst. Heal. Dis. 5th Ed.*, Garland Science, **2001**.

[62] L. Wei, W. Min, *J. Phys. Chem. Lett.* **2018**, *9*, 4294.

[63] G. S. Bumbrah, R. M. Sharma, *Egypt. J. Forensic Sci.* **2016**, *6*, 209.

[64] F. A. Settle, *Handbook of Instrumental Techniques for Analytical Chemistry*, Prentice Hall PTR, **1997**.

[65] N.-N. Dong, M. Pedroni, F. Piccinelli, G. Conti, A. Sbarbati, J. E. Ramírez-

Hernández, L. M. Maestro, M. C. Iglesias-de la Cruz, F. Sanz-Rodriguez, A. Juarranz, F. Chen, F. Vetrone, J. A. Capobianco, J. G. Solé, M. Bettinelli, D. Jaque, A. Speghini, *ACS Nano* **2011**, *5*, 8665.

[66] P. Wang, Y. Fan, L. Lu, L. Liu, L. Fan, M. Zhao, Y. Xie, C. Xu, F. Zhang, *Nat. Commun.* **2018**, *9*, 2898.

[67] A. Otto, *J. Raman Spectrosc.* **2005**, *36*, 497.

[68] R. Aroca, in *Surface-Enhanced Vib. Spectrosc.*, John Wiley & Sons, Ltd, **2007**, pp. 107–132.

[69] S. Nie, S. R. Emory, *Science* **1997**, *275*, 1102.

[70] S. Mahajan, R. M. Cole, J. D. Speed, S. H. Pelfrey, A. E. Russell, P. N. Bartlett, S. M. Barnett, J. J. Baumberg, *J. Phys. Chem. C* **2010**, *114*, 7242.

[71] M. Yang, R. Alvarez-Puebla, H.-S. Kim, P. Aldeanueva-Potel, L. M. Liz-Marzán, N. A. Kotov, *Nano Lett.* **2010**, *10*, 4013.

[72] M. Rycenga, M. H. Kim, P. H. C. Camargo, C. Cobley, Z.-Y. Li, Y. Xia, *J. Phys. Chem. A* **2009**, *113*, 3932.

[73] Q. Zhang, X. Li, Q. Ma, Q. Zhang, H. Bai, W. Yi, J. Liu, J. Han, G. Xi, *Nat. Commun.* **2017**, *8*, 14903.

[74] T. T. Le, T. B. Huff, J.-X. Cheng, *BMC Cancer* **2009**, *9*, 42.

[75] J.-X. Cheng, *Appl. Spectrosc.* **2007**, *61*, 197.

[76] C. L. Evans, X. S. Xie, *Annu. Rev. Anal. Chem.* **2008**, *1*, 883.

[77] C. H. Camp Jr, Y. J. Lee, J. M. Heddleston, C. M. Hartshorn, A. R. H. Walker, J. N. Rich, J. D. Lathia, M. T. Cicerone, *Nat. Photonics* **2014**, *8*, 627.

[78] R. R. Jones, D. C. Hooper, L. Zhang, D. Wolverson, V. K. Valev, *Nanoscale Res. Lett.* **2019**, *14*, 231.

[79] W. K. Johnson, C. Stoupis, G. M. Torres, E. B. Rosenberg, R. R. Ros, *Magn. Reson. Imaging* **1996**, *14*, 43.

[80] R. Bazak, M. Houri, S. El Achy, W. Hussein, T. Refaat, *Mol. Clin. Oncol.* **2014**, *2*, 904.

[81] Y. (Chezy) Barenholz, *J. Control. Release* **2012**, *160*, 117.

[82] M. F. Attia, N. Anton, J. Wallyn, Z. Omran, T. F. Vandamme, *J. Pharm. Pharmacol.* **2019**, *71*, 1185.

[83] R. Kogay, C. Schönbach, in *Encycl. Bioinforma. Comput. Biol.* (Eds.: S. Ranganathan, M. Gribskov, K. Nakai, C. Schönbach), Academic Press, Oxford, **2019**, pp. 952–971.

[84] A. Asati, S. Santra, C. Kaittanis, J. M. Perez, *ACS Nano* **2010**, *4*, 5321.

[85] X. Shi, S. Wang, S. Meshinchi, M. E. Van Antwerp, X. Bi, I. Lee, J. R. Baker Jr., *Small* **2007**, *3*, 1245.

[86] S. E. Zale, M. M. Ali, **2012**.

[87] S. E. Zale, M. M. Ali, **2013**.

[88] R. Bazak, M. Houri, S. El Achy, S. Kamel, T. Refaat, *J. Cancer Res. Clin. Oncol.* **2015**, *141*, 769.

[89] M. Wang, M. Thanou, *Pharmacol. Res.* **2010**, *62*, 90.

[90] J. A. Flexman, A. Yung, D. T. T. Yapp, S. S. W. Ng, P. Kozlowski, *Conf. Proc. ... Annu. Int. Conf. IEEE Eng. Med. Biol. Soc. IEEE Eng. Med. Biol. Soc.*

Annu. Conf. **2008**, *2008*, 851.

[91] M. E. Davis, *Mol. Pharm.* **2009**, *6*, 659.

[92] R. T. P. Poon, N. Borys, *Expert Opin. Pharmacother.* **2009**, *10*, 333.

[93] G. Kong, G. Anyarambhatla, W. P. Petros, R. D. Braun, O. M. Colvin, D. Needham, M. W. Dewhirst, *Cancer Res.* **2000**, *60*, 6950.

[94] B. Kong, J. H. Seog, L. M. Graham, S. B. Lee, *Nanomedicine (Lond).* **2011**, *6*, 929.

[95] S. K. Sohaebuddin, P. T. Thevenot, D. Baker, J. W. Eaton, L. Tang, *Part. Fibre Toxicol.* **2010**, *7*, 22.

[96] E. Fröhlich, *Int. J. Nanomedicine* **2012**, *7*, 5577.

[97] W. Le, B. Chen, Z. Cui, Z. Liu, D. Shi, *Biophys. Reports* **2019**, *5*, 10.

[98] J. Zhao, M. H. Stenzel, *Polym. Chem.* **2018**, *9*, 259.

[99] M. R. Carvalho, D. Barata, L. M. Teixeira, S. Giselbrecht, R. L. Reis, J. M. Oliveira, R. Truckenmüller, P. Habibovic, *Sci. Adv.* **2019**, *5*, eaaw1317.

[100] I. Wagner, E.-M. Materne, S. Brincker, U. Süßbier, C. Frädrich, M. Busek, F. Sonntag, D. A. Sakharov, E. V Trushkin, A. G. Tonevitsky, R. Lauster, U. Marx, *Lab Chip* **2013**, *13*, 3538.

[101] D. Chang, M. Lim, J. A. C. M. Goos, R. Qiao, Y. Y. Ng, F. M. Mansfeld, M. Jackson, T. P. Davis, M. Kavallaris, *Front. Pharmacol.* **2018**, *9*, 831.

[102] I. Hilger, W. Andrä, R. Bähring, A. Daum, R. Hergt, W. A. Kaiser, *Invest. Radiol.* **1997**, *32*, 705.

[103] A. Jordan, R. Scholz, P. Wust, H. Fähling, R. Felix, *J. Magn. Magn. Mater.*

1999, *201*, 413.

[104] F. Sonvico, S. Mornet, S. Vasseur, C. Dubernet, D. Jaillard, J. Degrouard, J. Hoebeke, E. Duguet, P. Colombo, P. Couvreur, *Bioconjug. Chem.* **2005**, *16*, 1181.

[105] P. de la Presa, Y. Luengo, M. Multigner, R. Costo, M. P. Morales, G. Rivero, A. Hernando, *J. Phys. Chem. C* **2012**, *116*, 25602.

[106] J. L. Dormann, D. Fiorani, E. Tronc, *Vol. XCVII, Eds. I. Prigogine y Stuart A. Rice, John Wiley Sons* **1997**, *283*.

[107] Y. Wang, Y. Xie, J. Li, Z.-H. Peng, Y. Sheinin, J. Zhou, D. Oupický, *ACS Nano* **2017**, *11*, 2227.

[108] M. Cho, W.-S. Cho, M. Choi, S. J. Kim, B. S. Han, S. H. Kim, H. O. Kim, Y. Y. Sheen, J. Jeong, *Toxicol. Lett.* **2009**, *189*, 177.

[109] S. Barua, S. Mitragotri, *Nano Today* **2014**, *9*, 223.

[110] D. Artemov, N. Mori, B. Okollie, Z. M. Bhujwalla, *Magn. Reson. Med.* **2003**, *49*, 403.

[111] E. S. Day, L. R. Bickford, J. H. Slater, N. S. Riggall, R. A. Drezek, J. L. West, *Int. J. Nanomedicine* **2010**, *5*, 445.

[112] D. Y. Lee, K. C. P. Li, *Am. J. Roentgenol.* **2011**, *197*, 318.

[113] R. G. Bai, K. Muthoosamy, S. Manickam, in (Eds.: S. Thomas, Y. Grohens, N.B.T.-N.A. for T.E. Ninan), William Andrew Publishing, Oxford, **2015**, pp. 195–213.

[114] S. A. Keek, R. T. H. Leijenaar, A. Jochems, H. C. Woodruff, *Br. J. Radiol.*

2018, *91*, 20170926.

[115] A. Carvalho, A. R. Fernandes, P. V Baptista, in *Micro Nano Technol.* (Eds.: S.S. Mohapatra, S. Ranjan, N. Dasgupta, R.K. Mishra, S.B.T.-A. of T.N.D. and D.S. Thomas), Elsevier, **2019**, pp. 257–295.

[116] S. Gul, S. B. Khan, I. U. Rehman, M. A. Khan, M. I. Khan, *Front. Mater.* **2019**, *6*, 179.

[117] C. Auría-Soro, T. Nesma, P. Juanes-Velasco, A. Landeira-Viñuela, H. Fidalgo-Gomez, V. Acebes-Fernandez, R. Gongora, M. J. Almendral Parra, R. Manzano-Roman, M. Fuentes, *Nanomater. (Basel, Switzerland)* **2019**, *9*, 1365.

[118] S. M. Moghimi, A. C. Hunter, J. C. Murray, *Pharmacol. Rev.* **2001**, *53*, 283.

[119] E. Blanco, H. Shen, M. Ferrari, *Nat. Biotechnol.* **2015**, *33*, 941.

[120] M. Lundqvist, J. Stigler, G. Elia, I. Lynch, T. Cedervall, K. A. Dawson, *Proc. Natl. Acad. Sci. U. S. A.* **2008**, *105*, 14265.

[121] H. Meng, W. Leong, K. W. Leong, C. Chen, Y. Zhao, *Biomaterials* **2018**, *174*, 41.

[122] J. Yue, T. J. Feliciano, W. Li, A. Lee, T. W. Odom, *Bioconjug. Chem.* **2017**, *28*, 1791.

[123] A. M. Bannunah, D. Vllasaliu, J. Lord, S. Stolnik, *Mol. Pharm.* **2014**, *11*, 4363.

[124] A. Z. Garza, S. B. Park, R. Kocz, **2019**.

[125] K. C. L. Black, Y. Wang, H. P. Luehmann, X. Cai, W. Xing, B. Pang, Y. Zhao, C. S. Cutler, L. V Wang, Y. Liu, Y. Xia, *ACS Nano* **2014**, *8*, 4385.

[126] Y. Zhao, Y. Wang, F. Ran, Y. Cui, C. Liu, Q. Zhao, Y. Gao, D. Wang, S. Wang,

Sci. Rep. **2017**, *7*, 4131.

[127] H. Maeda, J. Wu, T. Sawa, Y. Matsumura, K. Hori, *J. Control. Release* **2000**, *65*, 271.

[128] J.-A. Lee, M.-K. Kim, H.-J. Paek, Y.-R. Kim, M.-K. Kim, J.-K. Lee, J. Jeong, S.-J. Choi, *Int. J. Nanomedicine* **2014**, *9 Suppl 2*, 251.

[129] A. Al Zaki, J. Z. Hui, E. Higbee, A. Tsourkas, *J. Biomed. Nanotechnol.* **2015**, *11*, 1836.

[130] D. Barchiesi, *J. Opt. Soc. Am. A* **2015**, *32*, 1544.

[131] M. Faraday, *Phil. Trans. R. Soc. Lond.* **1857**, *147*, 145.

[132] J. Turkevich, P. C. Stevenson, J. Hillier, *Discuss. Faraday Soc.* **1951**, *11*, 55.

[133] M. Hu, J. Chen, Z.-Y. Li, L. Au, G. V Hartland, X. Li, M. Marquez, Y. Xia, *Chem. Soc. Rev.* **2006**, *35*, 1084.

[134] Z. L. Liu, X. Li, Y. Xie, Shunying, *Biomed. Mater.* **2014**, *9*, 25012.

[135] L. A. Dykman, N. G. Khlebtsov, *Biomaterials* **2016**, *108*, 13.

[136] M. L. Brongersma, *Nat Mater* **2003**, *2*, 296.

[137] M. G. Albrecht, J. A. Creighton, *J. Am. Chem. Soc.* **1977**, *99*, 5215.

[138] E. Pensa, E. Cortés, G. Corthey, P. Carro, C. Vericat, M. H. Fonticelli, G. Benítez, A. A. Rubert, R. C. Salvarezza, *Acc. Chem. Res.* **2012**, *45*, 1183.

[139] A. D. Pomogailo, V. N. Kestelman, *Metallopolymer Nanocomposites*, Springer Science & Business Media, **2006**.

[140] A. M. Alkilany, C. J. Murphy, *J. Nanoparticle Res.* **2010**, *12*, 2313.

[141] L. Ge, Q. Li, M. Wang, J. Ouyang, X. Li, M. M. Q. Xing, *Int. J. Nanomedicine* **2014**, *9*, 2399.

[142] Y.-W. Huang, C. Wu, R. S. Aronstam, *Mater.* **2010**, *3*, DOI 10.3390/ma3104842.

[143] M. M. Mohamed, S. A. Fouad, H. A. Elshoky, G. M. Mohammed, T. A. Salaheldin, *Int. J. Vet. Sci. Med.* **2017**, *5*, 23.

[144] S. Shamaila, N. Zafar, S. Riaz, R. Sharif, J. Nazir, S. Naseem, *Nanomater. (Basel, Switzerland)* **2016**, *6*, 71.

[145] M. Faried, K. Shameli, M. Miyake, A. Hajalilou, A. Zamanian, Z. Zakaria, E. Abouzari-lotf, H. Hara, N. B. B. Ahmad Khairudin, M. F. Binti Mad Nordin, *J. Nanomater.* **2016**, *2016*, 4941231.

[146] H.-J. Yen, S. Hsu, C.-L. Tsai, *Small* **2009**, *5*, 1553.

[147] E. E. Connor, J. Mwamuka, A. Gole, C. J. Murphy, M. D. Wyatt, *Small* **2005**, *1*, 325.

[148] M.-C. Senut, Y. Zhang, F. Liu, A. Sen, D. M. Ruden, G. Mao, *Small* **2016**, *12*, 631.

[149] A. D. Maynard, D. B. Warheit, M. A. Philbert, *Toxicol. Sci.* **2011**, *120 Suppl*, S109.

[150] Y. Pan, S. Neuss, A. Leifert, M. Fischler, F. Wen, U. Simon, G. Schmid, W. Brandau, W. Jahnen-Dechent, *Small* **2007**, *3*, 1941.

[151] Stober A. Fink W., *J. Colloid Interface Sci.* **1968**, *26*, 62.

[152] R. K. Sharma, S. Sharma, S. Dutta, R. Zboril, M. B. Gawande, *Green Chem.*

2015, *17*, 3207.

[153] C. C. M. C. Carcouët, M. W. P. van de Put, B. Mezari, P. C. M. M. Magusin, J. Laven, P. H. H. Bomans, H. Friedrich, A. C. C. Esteves, N. A. J. M. Sommerdijk, R. A. T. M. van Benthem, G. de With, *Nano Lett.* **2014**, *14*, 1433.

[154] H. Giesche, in *Med. Appl. Colloids* (Ed.: E. Matijević), Springer US, New York, NY, **2008**, pp. 42–66.

[155] A. Navrotsky, *Proc. Natl. Acad. Sci. United States Am.* **2004**, *101*, 12096.

[156] K. S. Rao, K. El-Hami, T. Kodaki, K. Matsushige, K. Makino, *J. Colloid Interface Sci.* **2005**, *289*, 125.

[157] T. Yanagisawa, T. Shimizu, K. Kuroda, C. Kato, *Bull. Chem. Soc. Jpn.* **1990**, *63*, 988.

[158] C. T. Kresge, M. E. Leonowicz, W. J. Roth, J. C. Vartuli, J. S. Beck, *Nature* **1992**, *359*, 710.

[159] A. Watermann, J. Brieger, *Nanomater. (Basel, Switzerland)* **2017**, *7*, 189.

[160] F. Tang, L. Li, D. Chen, *Adv. Mater.* **2012**, *24*, 1504.

[161] A. Guerrero-Martínez, J. Pérez-Juste, L. M. Liz-Marzán, *Adv. Mater.* **2010**, *22*, 1182.

[162] L. M. Liz-Marzan, P. Mulvaney, *New J. Chem.* **1998**, *22*, 1285.

[163] M. M. Y. Chen, A. Katz, *Langmuir* **2002**, *18*, 8566.

[164] V. R. K. Iler, *The Chemistry of Silica. Solubility, Polymerization, Colloid and Surface Properties, and Biochemistry*, John Wiley And Sons, **1979**.

[165] B. Arkles, *Chemtech* **1977**.

[166] R. De Palma, S. Peeters, M. J. Van Bael, H. Van den Rul, K. Bonroy, W. Laureyn, J. Mullens, G. Borghs, G. Maes, *Chem. Mater.* **2007**, *19*, 1821.

[167] A. Schulz, C. McDonagh, *Soft Matter* **2012**, *8*, 2579.

[168] B. Korzeniowska, R. Nooney, D. Wencel, C. McDonagh, *Nanotechnology* **2013**, *24*, 442002.

[169] A. Cossaro, M. Dell'Angela, A. Verdini, M. Puppin, G. Kladnik, M. Coreno, M. de Simone, A. Kivimäki, D. Cvetko, M. Canepa, L. Floreano, *J. Phys. Chem. C* **2010**, *114*, 15011.

[170] Y. Zhou, G. Quan, Q. Wu, X. Zhang, B. Niu, B. Wu, Y. Huang, X. Pan, C. Wu, *Acta Pharm. Sin. B* **2018**, *8*, 165.

[171] C. Zhong, M. He, K. Lou, F. Gao, in *Neurotox. Nanomater. Nanomedicine* (Eds.: X. Jiang, H. Gao), Academic Press, **2017**, pp. 227–257.

[172] A. Liberman, N. Mendez, W. C. Trogler, A. C. Kummel, *Surf. Sci. Rep.* **2014**, *69*, 132.

[173] H. Zhang, D. R. Dunphy, X. Jiang, H. Meng, B. Sun, D. Tarn, M. Xue, X. Wang, S. Lin, Z. Ji, R. Li, F. L. Garcia, J. Yang, M. L. Kirk, T. Xia, J. I. Zink, A. Nel, C. J. Brinker, *J. Am. Chem. Soc.* **2012**, *134*, 15790.

[174] D. Bobo, K. J. Robinson, J. Islam, K. J. Thurecht, S. R. Corrie, *Pharm. Res.* **2016**, *33*, 2373.

[175] F. Chen, K. Ma, B. Madajewski, L. Zhuang, L. Zhang, K. Rickert, M. Marelli, B. Yoo, M. Z. Turker, M. Overholtzer, T. P. Quinn, M. Gonen, P. Zanzonico, A. Tuesca, M. A. Bowen, L. Norton, J. A. Subramony, U. Wiesner, M. S. Bradbury, *Nat. Commun.* **2018**, *9*, 4141.

[176] R. K. Gilchrist, R. Medal, W. D. Shorey, R. C. Hanselman, J. C. Parrott, C. B. Taylor, *Ann. Surg.* **1957**, *146*, 596.

[177] A. K. Gupta, M. Gupta, *Biomaterials* **2005**, *26*, 3995.

[178] W. Wu, Q. He, C. Jiang, *Nanoscale Res. Lett.* **2008**, *3*, 397.

[179] Z. L. Liu, X. Li, Y. Xie, Shunying, *Biomed. Mater.* **2014**, *9*, 25012.

[180] W. Wu, Z. Wu, T. Yu, C. Jiang, W.-S. Kim, *Sci. Technol. Adv. Mater.* **2015**, *16*, 23501.

[181] R. M. Cornell, U. Schwertmann, *The Iron Oxides: Structure, Properties, Reactions, Occurrences and Uses*, John Wiley & Sons, **2003**.

[182] A. Jordan, P. Wust, H. Fähling, W. John, A. Hinz, R. Felix, *Int. J. Hyperth.* **1993**, *9*, 51.

[183] M. Shinkai, M. Yanase, H. Honda, T. Wakabayashi, J. Yoshida, T. Kobayashi, *Japanese J. Cancer Res.* **1996**, *87*, 1179.

[184] A. Ito, Y. Kuga, H. Honda, H. Kikkawa, A. Horiuchi, Y. Watanabe, T. Kobayashi, *Cancer Lett.* **2004**, *212*, 167.

[185] M. Suzuki, M. Shinkai, H. Honda, T. Kobayashi, *Melanoma Res.* **2003**, *13*, 129.

[186] Z. Nemati, J. Alonso, H. Khurshid, M. H. Phan, H. Srikanth, *RSC Adv.* **2016**, *6*, 38697.

[187] J. R. Herb, **1979**.

[188] D. J. Widder, W. L. Greif, K. J. Widder, R. R. Edelman, T. J. Brady, *Am. J. Roentgenol.* **1987**, *148*, 399.

[189] G. Marchal, P. Van Hecke, P. Demaerel, E. Decrop, C. Kennis, A. L. Baert, E. van der Schueren, *Am. J. Roentgenol.* **1989**, *152*, 771.

[190] C. J. Fretz, D. D. Stark, C. E. Metz, G. Elizondo, R. Weissleder, J. H. Shen, J. Wittenberg, J. Simeone, J. T. Ferrucci, *Am. J. Roentgenol.* **1990**, *155*, 763.

[191] J. T. Ferrucci, D. D. Stark, *Am. J. Roentgenol.* **1990**, *155*, 943.

[192] E. Schulze, J. T. Ferrucci, K. Poss, L. Lapointe, A. Bogdanova, R. Weissleder, *Invest. Radiol.* **1995**, *30*, 604.

[193] D. Pouliquen, R. Perdrisot, A. Ermias, S. Akoka, P. Jallet, J. J. le Jeune, in (Eds.: H.P. Higer, G. Bielke), Springer Berlin Heidelberg, Berlin, Heidelberg, **1990**, pp. 234–241.

[194] L. Babes, B. Denizot, G. Tanguy, J. J. [Le Jeune], P. Jallet, *J. Colloid Interface Sci.* **1999**, *212*, 474.

[195] D. Pouliquen, J. J. [Le Jeune], R. Perdrisot, A. Ermias, P. Jallet, *Magn. Reson. Imaging* **1991**, *9*, 275.

[196] R. Massart, *IEEE Trans. Magn.* **1981**, *17*, 1247.

[197] A. F. Abu-Bakr, A. Y. Zubarev, *Eur. Phys. J. Spec. Top.* **2020**, *229*, 323.

[198] H. Zheng, J. Z. Ou, M. S. Strano, R. B. Kaner, A. Mitchell, K. Kalantar-zadeh, *Adv. Funct. Mater.* **2011**, *21*, 2175.

[199] S. K. Deb, *Sol. Energy Mater. Sol. Cells* **2008**, *92*, 245.

[200] C. G. Granqvist, *Appl. Phys. A* **1993**, *57*, 19.

[201] G. A. Niklasson, C. G. Granqvist, *J. Mater. Chem.* **2007**, *17*, 127.

[202] K. Ito, T. Ohgami, *Appl. Phys. Lett.* **1992**, *60*, 938.

[203] K. Sauvet, L. Sauques, A. Rougier, *Sol. Energy Mater. Sol. Cells* **2009**, *93*, 2045.

[204] C. G. Granqvist, P. C. Lansåker, N. R. Mlyuka, G. A. Niklasson, E. Avendaño, *Sol. Energy Mater. Sol. Cells* **2009**, *93*, 2032.

[205] H.-J. Yen, K.-Y. Lin, G.-S. Liou, *J. Mater. Chem.* **2011**, *21*, 6230.

[206] K. Zhou, H. Wang, S. Zhang, J. Jiu, J. Liu, Y. Zhang, H. Yan, *J. Mater. Sci.* **2017**, *52*, 12783.

[207] C.-M. Wu, S. Naseem, M.-H. Chou, J.-H. Wang, Y.-Q. Jian, *Front. Mater.* **2019**, *6*, 49.

[208] X. Wang, O. S. Wolfbeis, *Anal. Chem.* **2020**, *92*, 397.

[209] M. Bourdin, I. Mjejri, A. Rougier, C. Labrugère, T. Cardinal, Y. Messaddeq, M. Gaudon, *J. Alloys Compd.* **2020**, *823*, 153690.

[210] N. Kobosew, N. I. Nekrassow, *Zeitschrift für Elektrochemie und Angew. Phys. Chemie* **1930**, *36*, 529.

[211] J. C. Powers, W. R. Heller, J. Kumamoto, W. E. Donath, *J. Am. Chem. Soc.* **1964**, *86*, 1004.

[212] T. K. Houlding, E. V Rebrov, *Green Process. Synth.* **2012**, *1*, 19.

[213] J. Pearce, A. Giustini, R. Stigliano, P. Jack Hoopes, *J. Nanotechnol. Eng. Med.* **2013**, *4*, 110071.

[214] P. de la Presa, Y. Luengo, V. Velasco, M. P. Morales, M. Iglesias, S. Veintemillas-Verdaguer, P. Crespo, A. Hernando, *J. Phys. Chem. C* **2015**, *119*, 11022.

[215] L. Néel, *Science* **1971**, *174*, 985 LP.

[216] E. Y. K. Ng, S. D. Kumar, *Biomed. Eng. Online* **2017**, *16*, 1.

[217] J. H. Breasted, **1930**.

[218] M. H. Seegenschmiedt, P. Fessenden, C. C. Vernon, *Thermoradiotherapy and Thermochemotherapy: Biology, Physiology, Physics*, Springer, **1995**.

[219] J. C. Peeken, P. Vaupel, S. E. Combs, *Front. Oncol.* **2017**, *7*, 132.

[220] N. R. Datta, H. P. Kok, H. Crezee, U. S. Gaipl, S. Bodis, *Front. Oncol.* **2020**, *10*, 819.

[221] H. S. Reinhold, B. Endrich, *Int. J. Hyperth.* **1986**, *2*, 111.

[222] S. B. Field, J. W. Hand, *An Introduction to the Practical Aspects of Clinical Hyperthermia*, Taylor & Francis Group, **1990**.

[223] L. F. F. LG, *Cancer Res.* **1984**, *44*, 4826s.

[224] P. Sminia, J. Van Der Zee, J. Wondergem, J. Haveman, *Int. J. Hyperth.* **1994**, *10*, 1.

[225] J. Wondergem, J. Haveman, V. Rusman, P. Sminia, J. D. P. Van Dijk, *Int. J. Radiat. Biol.* **1988**, *53*, 429.

[226] C. Streffer, in (Eds.: M.H. Seegenschmiedt, P. Fessenden, C.C. Vernon), Springer Berlin Heidelberg, Berlin, Heidelberg, **1995**, pp. 47–74.

[227] R. T. Gordon, J. R. Hines, D. Gordon, *Med. Hypotheses* **1979**, *5*, 83.

[228] S. Cassim, A. Giustini, A. Petryk, R. Strawbridge, P. Hoopes, *Proc. SPIE--the Int. Soc. Opt. Eng.* **2009**, *7181*, 71810O.

[229] N. Harris, M. J. Ford, M. B. Cortie, *J. Phys. Chem. B* **2006**, *110*, 10701.

[230] C. J. Gannon, C. R. Patra, R. Bhattacharya, P. Mukherjee, S. A. Curley, *J. Nanobiotechnology* **2008**, *6*, 2.

[231] M. Johannsen, U. Gneveckow, L. Eckelt, A. Feussner, N. Waldöfner, R. Scholz, S. Deger, P. Wust, S. A. Loening, A. Jordan, *Int. J. Hyperth. Off. J. Eur. Soc. Hyperthermic Oncol. North Am. Hyperth. Gr.* **2005**, *21*, 637.

[232] P. Hoopes, J. Tate, J. Ogden, R. Strawbridge, S. Fiering, A. Petryk, S. Cassim, A. Giustini, E. Demidenko, R. Ivkov, S. Barry, P. Chinn, A. Foreman, *Proc. SPIE--the Int. Soc. Opt. Eng.* **2009**, *7181*, 71810P.

[233] A. J. Giustini, R. E. Gottesman, A. M. Rauwerdink, A. A. Petryk, J. B. Weaver, P. J. Hoopes, in *Proc. SPIE*, **2011**.

[234] M. Hedayati, O. Thomas, B. Abubaker-Sharif, H. Zhou, C. Cornejo, Y. Zhang, M. Wabler, J. Mihalic, C. Gruettner, F. Westphal, A. Geyh, T. L. Deweese, R. Ivkov, *Nanomedicine (Lond).* **2013**, *8*, 29.

[235] K.-L. Chen, Y.-W. Yeh, J.-M. Chen, Y.-J. Hong, T.-L. Huang, Z.-Y. Deng, C.-H. Wu, S.-H. Liao, L.-M. Wang, *Sci. Rep.* **2016**, *6*, 35477.

[236] J. Estelrich, M. J. Sánchez-Martín, M. A. Busquets, *Int. J. Nanomedicine* **2015**, *10*, 1727.

[237] P. A. Gowland, V. L. Stevenson, in *Quant. MRI Brain*, John Wiley & Sons, Ltd, **2004**, pp. 111–141.

[238] P. A. Boulby, F. J. Rugg–Gunn, in *Quant. MRI Brain*, John Wiley & Sons, Ltd, **2004**, pp. 143–201.

[239] H. Gries, D. Rosenberg, H. J. Weinmann, *Pat. DE-OS* **1981**, *3129906*, A1.

[240] H.-J. Weinmann, R. C. Brasch, W.-R. Press, G. E. Wesbey, *Am. J. Roentgenol.* **1984**, *142*, 619.

[241] V. C. Pierre, M. J. Allen, P. Caravan, *J. Biol. Inorg. Chem.* **2014**, *19*, 127.

[242] Y.-X. J. Wang, *Quant. Imaging Med. Surg.* **2011**, *1*, 35.

[243] C.-Y. Yang, M.-F. Tai, C.-P. Lin, C.-W. Lu, J.-L. Wang, J.-K. Hsiao, H.-M. Liu, *PLoS One* **2011**, *6*, e25524.

[244] A. [du Plessis], C. Broeckhoven, *Acta Biomater.* **2019**, *85*, 27.

[245] H. Lusic, M. W. Grinstaff, *Chem. Rev.* **2013**, *113*, 1641.

[246] J. F. Hainfeld, D. N. Slatkin, T. M. Focella, H. M. Smilowitz, *Br. J. Radiol.* **2006**, *79*, 248.

[247] I. Brigger, C. Dubernet, P. Couvreur, *Adv. Drug Deliv. Rev.* **2002**, *54*, 631.

[248] A. M. Pourrahimi, D. Liu, V. Ström, M. S. Hedenqvist, R. T. Olsson, U. W. Gedde, *J. Mater. Chem. A* **2015**, *3*, 17190.

[249] J. K. Park, K. Y. Park, C.-B. Song, *Aerosol Sci. Technol.* **2004**, *38*, 827.

[250] L. J. Thomas Jr, S. P. Bessman, **1976**.

[251] W. J. Spencer, W. T. Corbett, L. R. Dominguez, B. D. Shafer, *IEEE Trans. Sonics Ultrason.* **1978**, *25*, 153.

[252] J. G. Smits, *Sensors Actuators A Phys.* **1990**, *21*, 203.

[253] L. P. Raman, M. Cheryna, N. Rajagopalan, *Chem. Eng. Progress; (United States)* **1994**.

[254] G. Chao, Y. Shuili, S. Yufei, G. Zhengyang, Y. Wangzhen, R. Liumo, *IOP Conf. Ser. Earth Environ. Sci.* **2018**, *128*, 012150.

[255] M. Frank, G. Bargeman, A. Zwijnenburg, M. Wessling, *Sep. Purif. Technol.* **2001**, *22–23*, 499.

[256] A. W. Mohammad, Y. H. Teow, W. L. Ang, Y. T. Chung, D. L. Oatley-Radcliffe, N. Hilal, *Desalination* **2015**, *356*, 226.

[257] S. P. Adiga, C. Jin, L. A. Curtiss, N. A. Monteiro-Riviere, R. J. Narayan, *WIREs Nanomedicine and Nanobiotechnology* **2009**, *1*, 568.

[258] T. R. Gaborski, J. L. Snyder, C. C. Striemer, D. Z. Fang, M. Hoffman, P. M. Fauchet, J. L. McGrath, *ACS Nano* **2010**, *4*, 6973.

[259] P. Guo, C. R. Martin, Y. Zhao, J. Ge, R. N. Zare, *Nano Lett.* **2010**, *10*, 2202.

[260] Y. Eygeris, E. V White, Q. Wang, J. E. Carpenter, M. Grünwald, I. Zharov, *ACS Appl. Mater. Interfaces* **2019**, *11*, 3407.

[261] W. Zhang, P. Cheng, J. Cheng, N. Li, Y. Wang, J. Yang, X. Qiu, H. Tan, H. Yu, *J. Memb. Sci.* **2019**, *570–571*, 427.

[262] M. Mabrouk, R. Rajendran, I. E. Soliman, M. M. Ashour, H. H. Beherei, K. M. Tohamy, S. Thomas, N. Kalarikkal, G. Arthanareeswaran, D. B. Das, *Pharmaceutics* **2019**, *11*, 294.

[263] Łącki Karol M., J. Joseph, K. O. Eriksson, in (Eds.: G. Jagschies, E. Lindskog, K. Łącki, P.B.T.-B.P. Galliher), Elsevier, **2018**, pp. 637–674.

[264] C. C. Striemer, T. R. Gaborski, J. L. McGrath, P. M. Fauchet, *Nature* **2007**, *445*, 749.

[265] Z. Wang, Z. Wang, S. Lin, H. Jin, S. Gao, Y. Zhu, J. Jin, *Nat. Commun.* **2018**, *9*, 2004.

[266] C.-Y. Li, F.-X. Ma, Z.-Q. Wu, H.-L. Gao, W.-T. Shao, K. Wang, X.-H. Xia, *Adv. Funct. Mater.* **2013**, *23*, 3836.

[267] L. Li, J. Zhang, A. Wang, *Chem. Rec.* **2018**, *18*, 118.

[268] A. B. Chin, I. I. Yaacob, *J. Mater. Process. Technol.* **2007**, *191*, 235.

[269] R. Massart, V. Cabuil, *J. Chim. Phys. Physico-Chimie Biol.* **1987**, *84*, 967.

[270] J. Zha, H. Roggendorf, *Adv. Mater.* **1991**, *3*, 522.

[271] S. Sultan, K. Kareem, L. He, *Surf. Coatings Technol.* **2016**, *300*, 42.

[272] J. M. Kim, S. M. Chang, S. M. Kong, K.-S. Kim, J. Kim, W.-S. Kim, *Ceram. Int.* **2009**, *35*, 1015.

[273] K.-S. Chou, C.-C. Chen, *Microporous Mesoporous Mater.* **2007**, *98*, 208.

[274] K.-S. Kim, J.-K. Kim, W.-S. Kim, *Ceram. Int.* **2002**, *28*, 187.

[275] G. H. Bogush, M. A. Tracy, C. F. Zukoski, *J. Non. Cryst. Solids* **1988**, *104*, 95.

[276] Y.-D. Chiang, H.-Y. Lian, S.-Y. Leo, S.-G. Wang, Y. Yamauchi, K. C.-W. Wu, *J. Phys. Chem. C* **2011**, *115*, 13158.

[277] K. Han, Z. Zhao, Z. Xiang, C. Wang, J. Zhang, B. Yang, *Mater. Lett.* **2007**, *61*, 363.

[278] P. Abdulkin, T. L. Precht, B. R. Knappett, H. E. Skelton, D. A. Jefferson, A. E. H. Wheatley, *Part. Part. Syst. Charact.* **2014**, *31*, 571.

[279] J. Dupont, J. D. Scholten, *Chem. Soc. Rev.* **2010**, *39*, 1780.

[280] C. Deraedt, L. Salmon, S. Gatard, R. Ciganda, R. Hernandez, J. Ruiz, D. Astruc, *Chem. Commun.* **2014**, *50*, 14194.

[281] D. G. Duff, A. Baiker, P. P. Edwards, *J. Chem. Soc. Chem. Commun.* **1993**, 96.

[282] J. L. Hueso, V. Sebastian, A. Mayoral, L. Uson, M. Arruebo, J. Santamaria, *RSC Adv.* **2013**, *3*, 10427.

[283] M. R. Rasch, K. V Sokolov, B. A. Korgel, *Langmuir* **2009**, *25*, 11777.

[284] A. Villa, D. Wang, D. S. Su, L. Prati, *Catal. Sci. Technol.* **2015**, *5*, 55.

[285] R. M. Pasternack, S. Rivillon Amy, Y. J. Chabal, *Langmuir* **2008**, *24*, 12963.

[286] M. S. Inkpen, Z. Liu, H. Li, L. M. Campos, J. B. Neaton, L. Venkataraman, *Nat. Chem.* **2019**, *11*, 351.

[287] J. Goldstein, *Practical Scanning Electron Microscopy: Electron and Ion Microprobe Analysis*, Springer Science & Business Media, **2012**.

[288] N. Raval, R. Maheshwari, D. Kalyane, S. R. Youngren-Ortiz, M. B. Chougule, R. K. Tekade, in *Adv. Pharm. Prod. Dev. Res.* (Ed.: R.K.B.T.-B.F. of D.D. Tekade), Academic Press, **2019**, pp. 369–400.

[289] P. S. Kumar, K. G. Pavithra, M. Naushad, in (Eds.: S. Thomas, E.H.M. Sakho, N. Kalarikkal, S.O. Oluwafemi, J.B.T.-N. for S.C.A. Wu), Elsevier, **2019**, pp. 97–124.

[290] P. D. Nellist, in *Springer Handb. Microsc.*, Springer, **2019**, p. 2.

[291] B. Fultz, J. M. Howe, *Transmission Electron Microscopy and Diffractometry of Materials*, Springer Science & Business Media, **2012**.

[292] J. Stetefeld, S. A. McKenna, T. R. Patel, *Biophys. Rev.* **2016**, *8*, 409.

[293] S. E. Harding, K. Jumel, *Curr. Protoc. Protein Sci.* **1998**, *11*, 7.8.1.

[294] W. Sutherland, *London, Edinburgh, Dublin Philos. Mag. J. Sci.* **1905**, *9*, 781.

[295] S. Myhra, J. C. Rivière, *Characterization of Nanostructures*, CRC Press, **2012**.

[296] V. Filipe, A. Hawe, W. Jiskoot, *Pharm. Res.* **2010**, *27*, 796.

[297] A. Zieba, S. Foner, *Rev. Sci. Instrum.* **1982**, *53*, 1344.

[298] R. L. Fagaly, *Rev. Sci. Instrum.* **2006**, *77*, 101101.

[299] P. A. Joy, P. S. A. Kumar, S. K. Date, *J. Phys. Condens. Matter* **1998**, *10*, 11049.

[300] J. L. Garc\'\ia-Palacios, F. J. Lázaro, *Phys. Rev. B* **1998**, *58*, 14937.

[301] W. F. Brown, *Phys. Rev.* **1963**, *130*, 1677.

[302] N. A. Usov, O. N. Serebryakova, V. P. Tarasov, *Nanoscale Res. Lett.* **2017**, *12*, 489.

[303] A. Vansteenkiste, J. Leliaert, M. Dvornik, M. Helsen, F. Garcia-Sanchez, B. Van Waeyenberge, *AIP Adv.* **2014**, *4*, 107133.

[304] W. Scholz, T. Schrefl, J. Fidler, *J. Magn. Magn. Mater.* **2001**, *233*, 296.

[305] N. A. Usov, M. S. Nesmeyanov, E. M. Gubanova, N. B. Epshtein, *Beilstein J. Nanotechnol.* **2019**, *10*, 305.

[306] M. N. Avadhanulu, *A Textbook of Engineering Physics*, S. Chand Publishing, **1992**.

[307] N. Jalili, K. Laxminarayana, *Mechatronics* **2004**, *14*, 907.

[308] A. Manz, D. J. Harrison, E. M. J. Verpoorte, J. C. Fettinger, A. Paulus, H. Lüdi, H. M. Widmer, *J. Chromatogr. A* **1992**, *593*, 253.

[309] A. T. Woolley, D. Hadley, P. Landre, A. J. deMello, R. A. Mathies, M. A. Northrup, *Anal. Chem.* **1996**, *68*, 4081.

[310] J. Khandurina, T. E. McKnight, S. C. Jacobson, L. C. Waters, R. S. Foote, J. M. Ramsey, *Anal. Chem.* **2000**, *72*, 2995.

[311] M. T. Taylor, P. Nguyen, J. Ching, K. E. Petersen, *J. Micromechanics Microengineering* **2003**, *13*, 201.

[312] R. A. Clark, P. B. Hietpas, A. G. Ewing, *Anal. Chem.* **1997**, *69*, 259.

[313] A. L. Grosvenor, A. Feltus, R. C. Conover, S. Daunert, K. W. Anderson, *Anal. Chem.* **2000**, *72*, 2590.

[314] P. C. H. Li, D. J. Harrison, *Anal. Chem.* **1997**, *69*, 1564.

[315] C. Qi, C. C. Striemer, T. R. Gaborski, J. L. McGrath, P. M. Fauchet, *Small* **2014**, *10*, 2946.

[316] M. Dehghani, K. Lucas, J. Flax, J. McGrath, T. Gaborski, *Adv. Mater. Technol.* **2019**, *4*, 1900539.

[317] F. G. Rinaldi, O. Arutanti, A. F. Arif, T. Hirano, T. Ogi, K. Okuyama, *ACS Omega* **2018**, *3*, 8963.

[318] E. V Miu, J. R. McKone, *J. Mater. Chem. A* **2019**, *7*, 23756.

[319] A.-M. Popa, P. Niedermann, H. Heinzelmann, J. A. Hubbell, R. Pugin, *Nanotechnology* **2009**, *20*, 485303.

[320] I. Vlassiouk, P. Y. Apel, S. N. Dmitriev, K. Healy, Z. S. Siwy, *Proc. Natl. Acad.*

Sci. **2009**, *106*, 21039.

[321] L. Cao, Q. Wen, Y. Feng, D. Ji, H. Li, N. Li, L. Jiang, W. Guo, *Adv. Funct. Mater.* **2018**, *28*, 1804189.

[322] J. P. S. DesOrmeaux, J. D. Winans, S. E. Wayson, T. R. Gaborski, T. S. Khire, C. C. Striemer, J. L. McGrath, *Nanoscale* **2014**, *6*, 10798.

[323] K. Hill, S. N. Walker, A. Salminen, H. L. Chung, X. Li, B. Ezzat, J. J. Miller, J.-P. S. DesOrmeaux, J. Zhang, A. Hayden, T. Burgin, L. Piraino, M. N. May, T. R. Gaborski, J. A. Roussie, J. Taylor, L. DiVincenti Jr., A. A. Shestopalov, J. L. McGrath, D. G. Johnson, *Adv. Healthc. Mater.* **2020**, *9*, 1900750.

[324] K. C. Briley-Saebo, L. O. Johansson, S. O. Hustvedt, A. G. Haldorsen, A. Bjørnerud, Z. A. Fayad, H. K. Ahlstrom, *Invest. Radiol.* **2006**, *41*.

[325] J. C. Trefry, J. L. Monahan, K. M. Weaver, A. J. Meyerhoefer, M. M. Markopolous, Z. S. Arnold, D. P. Wooley, I. E. Pavel, *J. Am. Chem. Soc.* **2010**, *132*, 10970.

[326] N. Alele, R. Streubel, L. Gamrad, S. Barcikowski, M. Ulbricht, *Sep. Purif. Technol.* **2016**, *157*, 120.

[327] G. Hemery, A. C. Keyes, E. Garaio, I. Rodrigo, J. A. Garcia, F. Plazaola, E. Garanger, O. Sandre, *Inorg. Chem.* **2017**, *56*, 8232.

[328] J. D. Winans, K. J. P. Smith, T. R. Gaborski, J. A. Roussie, J. L. McGrath, *J. Memb. Sci.* **2016**, *499*, 282.

[329] K. Kan-Dapaah, N. Rahbar, W. Soboyejo, *Med. Phys.* **2015**, *42*, 2203.

[330] A. Petryk, A. Giustini, P. Ryan, R. Strawbridge, P. Hoopes, *Proc. SPIE--the Int.*

Soc. Opt. Eng. **2009**, *7181*, 71810N.

[331] P. Allia, G. Barrera, P. Tiberto, *Phys. Rev. Appl.* **2019**, *12*, 34041.

[332] G. Baldissera, C. Persson, *Eur. Phys. J. B* **2013**, *86*, 273.

[333] M. Longmire, P. L. Choyke, H. Kobayashi, *Nanomedicine (Lond).* **2008**, *3*, 703.

[334] A. A. Ashkarran, A. I. zad, M. M. Ahadian, S. A. M. Ardakani, *Nanotechnology* **2008**, *19*, 195709.

[335] T. H. L. Nghiem, T. N. Le, T. H. Do, T. T. D. Vu, Q. H. Do, H. N. Tran, *J. Nanoparticle Res.* **2013**, *15*, 2091.

[336] S. I. C. de Torresi, A. Gorenstein, R. M. Torresi, M. V Vázquez, *J. Electroanal. Chem. Interfacial Electrochem.* **1991**, *318*, 131.

[337] O. Bohnke, M. Rezrazi, B. Vuillemin, C. Bohnke, P. A. Gillet, C. Rousselot, *Sol. Energy Mater. Sol. Cells* **1992**, *25*, 361.

[338] A. B. Serrano-Montes, J. Langer, M. Henriksen-Lacey, D. de Aberasturi, D. M. Solís, J. M. Taboada, F. Obelleiro, K. Sentosun, S. Bals, A. Bekdemir, F. Stellacci, L. M. Liz-Marzán, *J. Phys. Chem. C* **2016**, *120*, 20860.

[339] Y. He, S. Su, T. Xu, Y. Zhong, J. A. Zapien, J. Li, C. Fan, S.-T. Lee, *Nano Today* **2011**, *6*, 122.

[340] Y. Jun, Y.-M. Huh, J. Choi, J.-H. Lee, H.-T. Song, S. Kim, S. Yoon, K.-S. Kim, J.-S. Shin, J.-S. Suh, J. Cheon, *J. Am. Chem. Soc.* **2005**, *127*, 5732.

[341] E. D. Smolensky, M. C. Neary, Y. Zhou, T. S. Berquo, V. C. Pierre, *Chem. Commun.* **2011**, *47*, 2149.

[342] C. Hoskins, Y. Min, M. Gueorguieva, C. McDougall, A. Volovick, P. Prentice, Z.

Wang, A. Melzer, A. Cuschieri, L. Wang, *J. Nanobiotechnology* **2012**, *10*, 27.

[343] I. Fernández-Barahona, M. Muñoz-Hernando, J. Ruiz-Cabello, F. Herranz, J. Pellico, *Inorganics* **2020**, *8*, 28.

[344] C. Westbrook, *MRI at a Glance*, John Wiley & Sons, **2016**.

[345] K. Ge, W. Williams, Q. Liu, Y. Yu, *Geochemistry, Geophys. Geosystems* **2014**, *15*, 2021.

[346] A. I. Figueroa, J. Bartolomé, L. M. García, F. Bartolomé, A. Arauzo, A. Millán, F. Palacio, *Phys. Procedia* **2015**, *75*, 1050.

[347] C. Jiang, C. W. Leung, P. W. T. Pong, *Nanoscale Res. Lett.* **2016**, *11*, 189.

[348] F. Moro, R. de Miguel, M. Jenkins, C. Gómez-Moreno, D. Sells, F. Tuna, E. J. L. McInnes, A. Lostao, F. Luis, J. van Slageren, *J. Magn. Magn. Mater.* **2014**, *361*, 188.

[349] Q. Li, C. W. Kartikowati, S. Horie, T. Ogi, T. Iwaki, K. Okuyama, *Sci. Rep.* **2017**, *7*, 9894.

[350] Y. Prado, N. Daffé, A. Michel, T. Georgelin, N. Yaacoub, J.-M. Grenèche, F. Choueikani, E. Otero, P. Ohresser, M.-A. Arrio, C. Cartier-dit-Moulin, P. Sainctavit, B. Fleury, V. Dupuis, L. Lisnard, J. Fresnais, *Nat. Commun.* **2015**, *6*, 10139.

[351] G. P. Zhao, Y. Deng, H. W. Zhang, Z. H. Cheng, J. Ding, *J. Appl. Phys.* **2011**, *109*, 07D340.

[352] E. Navarro, F. Piccapietra, B. Wagner, F. Marconi, R. Kaegi, N. Odzak, L. Sigg, R. Behra, *Environ. Sci. Technol.* **2008**, *42*, 8959.

Appendix

*Furnace oven calibration: T*he differences in temperatures are plotted in 4.3 to evaluate the trend.

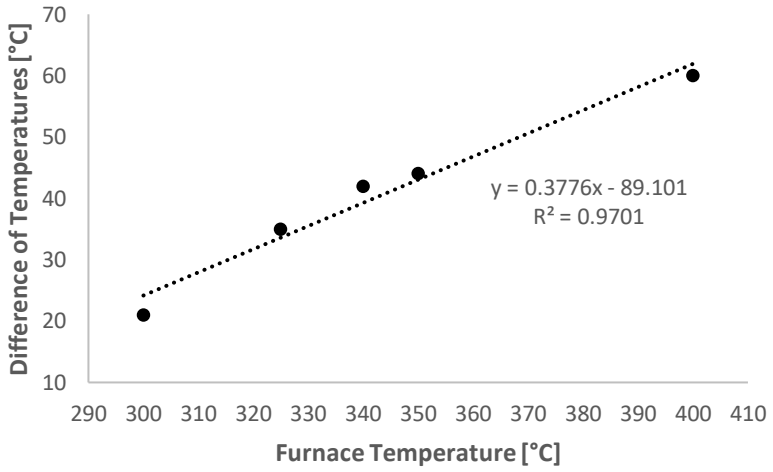

Figure A.1 | Contrast between the furnace temperature and the thermometer temperature.

Figure A.1 clearly concludes that there is approximately a linear correlation between the furnace temperature and measured with the thermometer. This to estimate the future temperatures along with ensuring reproducibility.

T1 and T2 calculations: T1 and T2 decay times calculations from converting the exponential decay formulas into a linear formula by applying a Napierian logarithmic reduction approach which then is adjusted into a linear regression to obtain both T1 and T2. The steps used are the following.

For T1 mode, T1 and S0 are calculated by using the following formula:

$$S = S0\left(1 - 2e^{-\frac{TI}{T1}} + e^{-\frac{TR}{T1}}\right) = S0(1 - 2e^{TI} + e^{TR})^{-T1^{-1}} \quad \text{(A.1)}$$

$$\underbrace{\ln(S)}_{y} = \frac{-1}{T1}\ln(-2e^{TI} + e^{TR}) = \underbrace{\ln(1 - 2e^{TI} + e^{TR})}_{x}\underbrace{(-R1)}_{slope} + \underbrace{\ln(S0)}_{b} \quad \text{(A.2)}$$

$$\frac{-\ln(1 - 2e^{TI} + e^{TR})}{\ln\left(\frac{S}{S0}\right)} = T1 \quad \text{(A.3)}$$

For T2, the analysis follows similar procedure:

$$\underbrace{\ln(S)}_{y} = \underbrace{TE}_{x}\ \underbrace{(-R2)}_{slope} + \underbrace{\ln(S0)}_{b} \quad \text{(A.4)}$$

$$\frac{-TE}{\ln\left(\frac{S}{S0}\right)} = T2 = \frac{1}{R2} \quad \text{(A.5)}$$

List of Publications:

- "Novel Au-SiO_2-WO_3 core-shell composite nanoparticles for surface-enhanced Raman spectroscopy with potential application in cancer cell imaging". P Martinez Pancorbo, K Thummavichai, L Clark, T A Tabish, J Mansfield, B Gardner, H Chang, N Stone, Y Zhu, 2019, *Adv. Funct. Mater* 1903549. https://doi.org/10.1002/adfm.201903549

- "Nanosized Selective Filtration of Commercial Polydisperse Magnetic Nanoparticles with Nanoporous Membranes in Normal and Tangential Flow Microfluidic Devices". P Martinez Pancorbo, K Lucas, J McGrath, I Rodriguez Diaz, K Webb, Y Zhu, N Stone (In preparation).

- “Development of magnetic-plasmonic core-shell nanoparticles for multifunctional cancer imaging and single-cell hyperthermia”. P Martinez Pancorbo, I Morales, P de la Presa, C McKeever, M Belal, D Ankrett, B Gardner, S Treves, Y Zhu, N Stone (In preparation).

List of Research Conference Presentations:

- Serendipity Workshop 2020 (#Serendipityworkshop2020) with the Twitter poster presentation (Participants’ Award Winner): “Finding and killing cancer cell by cell before it is too late”. https://twitter.com/SerendipityWrk/status/1275282225769005056
- Photonics Online Meet-up 2020 (#POM20Ju) with the Twitter poster presentation: “Finding and killing cancer cell by cell before it is too late”. https://twitter.com/PabloMPancorbo/status/1274878782076305408
- Organ-on-a-Chip: Current Gaps and Future Directions Conference, GSK’s Medicines Research Centre, Stevenage, 2019. Poster presentation: “In vitro human toxicity assessments of novel multifunctional nanoparticles for cancer theranostics”.
- GW4 3Rs Symposium, Exeter, 2019. Poster presentation: “In vitro human toxicity assessments of novel multifunctional nanoparticles for cancer theranostics”.
- RSC Twitter Poster Competition by Royal Society of Chemistry, March 2019. 1st Prize in the Chemical and Biology Interface (#RSCChemBio) category with the Twitter poster presentation: “Smart Nanoparticle Design for Finding and Killing Early-Stage Single Cancer Cells”.

https://blogs.rsc.org/rscpublishing/2019/03/12/2019-rscposter-twitter-conference-thank-you-for-participating/

- GW4 Nanomedicine Workshop, Exeter, 2019. Poster presentation: “Imaging and Treatment of Cancer Cells with smartly Designed Magnetoplasmonic Nanoparticles”.
- 14th International Conference on Materials Chemistry (MC14) 2019, Birmingham, United Kingdom. Poster presenter with a poster titled “Fe_2O_3-SiO_2-Au Composite Nanoparticles for Potential Cancer Theranostics”.
- 6th Nano Today Conference 2019, Lisbon, Portugal. Poster presentation Finalist Award: “Fe_2O_3-SiO_2-Au Composite Nanoparticles for Potential Cancer Theranostics”.
- Invited oral presentation: “Smartly designed composite nanoparticles for potential cancer therapy and diagnosis” by West of England Metals and Materials Association (WEMMA), 2018.
- NanoBio Conference 2018, Heraklion, Crete, Greece. Oral presentation: “Au-SiO_2-WO_3 Core-shell Nanoparticles for SERS Cancer Imaging”.
- STEM for Britain selected presenter representing Exeter at House of Parliament, Westminster, 2018. Poster presentation: “Novel Au-SiO_2-WO_3 Core-Shell Nanocomposites for Surface-Enhanced Raman Spectroscopy”.
- 13th International Conference on Materials Chemistry (MC13), 2017, Liverpool, United Kingdom. Poster presentation: “Novel Au-SiO_2-WO_3 Core-Shell Nanocomposites for Surface-Enhanced Raman Spectroscopy”.

ADVANCED FUNCTIONAL MATERIALS
www.afm-journal.de

Novel Au–SiO_2–WO_3 Core–Shell Composite Nanoparticles for Surface-Enhanced Raman Spectroscopy with Potential Application in Cancer Cell Imaging

*Pablo Martinez Pancorbo, Kunyapat Thummavichai, Louise Clark, Tanveer A. Tabish, Jessica Mansfield, Ben Gardner, Hong Chang, Nick Stone, and Yanqiu Zhu**

With the rapid development of nanotechnology during the last decades, the ability to detect and control individual objects at the nanoscale has enabled us to deal with complex biomedical challenges. In cancer imaging, novel nanoparticles (NPs) offer promising potential to identify single cancer cells and precisely label larger areas of cancer tissues. Herein, a new class of size tunable core–shell composite (Au–SiO_2–WO_3) nanoparticles is reported. These nanoparticles display an easily improvable ≈10^3 surface-enhanced Raman scattering (SERS) enhancement factor with a double Au shell for dried samples over Si wafers and several orders of magnitude for liquid samples. WO_3 core nanoparticles measuring 20–50 nm in diameter are sheathed by an intermediate 10–60 nm silica layer, produced by following the Stöber-based process and Turkevich method, followed by a 5–20 nm thick Au outer shell. By attaching 4-mercaptobenzoic acid (4-MBA) molecules as Raman reporters to the Au, high-resolution Raman maps that pinpoint the nanoparticles' location are obtained. The preliminary results confirm their advantageous SERS properties for single-molecule detection, significant cell viability after 24 h and in vitro cell imaging using coherent anti-stokes Raman scattering. The long-term objective is to measure SERS nanoparticles in vivo using near-infrared light.

1. Introduction

Cancer is the second main cause of death globally after cardiovascular diseases, which are preventable via low-fat diet. Currently, the approach for cancer diagnosis is still based on nineteenth and twentieth century methodologies, which were supported in a limited knowledge of the cancer biology. In the 2000s, positron emission tomography (PET) combined with computed tomography (CT) was commercialized and started to be used worldwide due to its enhanced precision in the location of areas with highly active cells compared to older techniques. Its appearance had a great impact on cancer diagnosis until today, remaining the main technique for precise tumor location in the clinical stage for most types of cancers.[1] Unfortunately, this technique does not provide single cell detection and involves radioactive agents. More recent advances in optical imaging techniques such as deep Raman spectroscopy-based approaches have enabled the potential to find single cancer cells inside of the human body without involving ionizing radiation. These novel techniques allow higher precision via light–molecule interactions by measuring biomarkers in the microscale, such as microcalcifications in breast cancer tissue.[2] More precise measurements using nanoscale objects labeled with Raman reporters could achieve single cell resolution for an optimal early stage cancer detection.[3]

In modern cancer imaging, the best personalized medical techniques are based on delivering nanoscale agents to cancer cells location while minimizing any undesirable interactions. However, many nanostructures do not arrive at the target and can induce toxicity. Hence, it is crucial to develop biocompatible nanoscale objects that contain clinically approved materials. Among many inorganic nanomaterials used, only iron-oxide (Fe_3O_4), silica (SiO_2), and gold (Au) NPs are currently clinically accepted.[4] Iron oxide is used in imaging and thermal ablation of tumors; silica for fluorescent cancer imaging;[5] and gold for both surface-enhanced Raman spectroscopy (SERS) and photothermal ablation of tumors.[6] Plasmonic nanoparticles (gold or silver) coated with Raman agents provide a platform for the emission of measurable Raman signals to optically locate the nanoparticles in the body, and therefore the cancer cells too.

The combination of different materials in the same particle to perform medical diagnosis and therapy in the same agent has become an important research topic, known as theranostics. The most extensively studied composite nanoparticles

P. Martinez Pancorbo, Dr. K. Thummavichai, Dr. L. Clark, Dr. T. A. Tabish, Dr. J. Mansfield, Dr. B. Gardner, Dr. H. Chang, Prof. N. Stone, Prof. Y. Zhu
College of Engineering, Mathematics and Physical Sciences
University of Exeter
Exeter EX4 4QF, UK
E-mail: Y.Zhu@exeter.ac.uk

The ORCID identification number(s) for the author(s) of this article can be found under https://doi.org/10.1002/adfm.201903549.

DOI: 10.1002/adfm.201903549

in medical diagnosis are the colloidal ferromagnetic Fe_3O_4 wrapped by functionalized Au core–shell NP for X-rays, SERS, and MRI imaging.[7] However, there are some important limitations in all these applications. Medium to high energy X-rays can penetrate through the soft tissue in the human body but can induce new tumors and have poor contrast between soft tissues.[8] MRI uses Fe_3O_4 as a contrast agent due to favorable superparamagnetic properties, biodegradability, and easily modified surface properties for improved in vivo kinetics and multifunctionality.[9] Although MRI has a penetration depth only limited by the magnetic field, it has a low contrast between bound and unbound water molecules.[10] Further contrast is typically provided by injecting gadolinium-based enhancing agents. However, gadolinium has shown certain mechanisms for cytotoxicity.[11] The alternative, Fe_3O_4, is noncytotoxic but carries the risk of magnetic aggregation, forming very large particles that will not be excreted.[12] Au SERS uses nonionizing radiation that requires specific wavelengths in the near-infrared to penetrate the soft tissue, but penetration depth is typically up to only several centimeters.[13] However, it is one of the few techniques that allow achieving single cancer cell detection.

On the one hand, Au NPs have been extensively used as nanoprobes for SERS cancer imaging.[14] Their recent extension to Au nanoshells (Au NSs) covering in a core–shell structure has shown rather promising results for future biosensing,[15] by using specific molecules with benzene rings on top as the Raman reporters.[16] Spherical Au NPs have a range of surface plasmonic resonance wavelength excitations ranging from 510 to 572 nm for particle sizes from 3 to 100 nm, and from 520 to 932 nm excitations for Au NSs with different combinations of internal diameters and external shell thickness, respectively.[17,18] Apparently, thinner shells and larger internal diameters of nanoshells bring redshifts in the plasmonic generation.[18–20] Both Au NPs and Au NSs are well known for their good biocompatibility, ready bioconjugation,[21] and optical properties via plasmons.[22] On the other hand, Fe_3O_4 presents a behavior from superparamagnetic to ferromagnetic for 20 nm size or above of the nanoparticles which leads to significant magnetic nanoparticle aggregation.[23,24] Therefore, there is a drive to develop new materials that integrate alternative cores for Au nanoshells core–shell nanoparticles without magnetic aggregation.

Here we have explored the use of tungsten trioxide (WO_3) that has excellent sensing properties,[25] including unique chromic behavior activated via thermal changes, electrical currents, and gases.[26] Additionally, some studies have previously shown potential oxygen vacancy induced ferromagnetism that brings magnetic hyperthermia capabilities,[27,28] and both biocompatibility and antibacterial properties.[29] Ultrasmall WO_{3-x} nanodots have also been used recently for in vivo studies for multimodality imaging tumor imaging through computed tomography and photoacoustic imaging, and effective cancer treatment combining both photothermal therapy and radiation therapy.[30] WO_3 and WO_2 transparency can be tuned by inducing a difference of electric potential or electric current, which can enhance or reduce the plasmonic generation of an external Au shell. However, Au and WO_3 are not easily bound together, therefore an intermediate interface that helps to bind both the Au NPs and the WO_3 core is needed. This intermediate layer needs to have low cytotoxicity for the human cells and should be able to accommodate the Au NPs easily. Porous silica (SiO_2) NPs have previously been utilized to accommodate Au and have shown very low toxicity in the human body.[31] The synthetic steps are displayed in Figure S1 (Supporting Information). To validate this design (**Figure 1**a), we will use the well-established Raman reporter on Au, 4-mercaptobenzoic acid (4-MBA), to acquire the SERS signals. The schematic of the SERS process in the Au shell surface is explained in Figure 1b. It also shows that 785 and 830 nm are the two wavelengths used to obtain the Raman signals and maps, which are in the near-infrared region of the electromagnetic spectra. These wavelengths allow human tissue penetration while standard SERS that uses visible light would be fully absorbed by the organic tissues.

2. Results and Discussion

2.1. Characterization of Au–SiO_2–WO_3 Nanocomposites

Figure 2a displays the X-ray powder diffraction (XRD) patterns of the nanoparticles from each synthesis step. The peaks in each XRD pattern reveal the crystal structure of these materials. Along with the progression, the original monoclinic WO_3 (Blue line) peaks are accompanied with lumps of the amorphous SiO_2 at 23.1° (002), 23.6° (020), and 24.4° (200) (Black line), and then the cubic Au peaks appear (Red line) in the composite, benchmarked against the plain Au NPs at 38.1° (111) and 44.3° (200) (Green line). The three main fingerprint peaks of monoclinic WO_3 at 23.1°, 23.6°, and 24.4° are always present. This result confirms the bulk composite phase structures.

The phases identified by XRD are also verified by high-resolution transmission electron microscopy (HRTEM) imaging. The lattice spacing is 0.265 nm (Figure 2b) for the monoclinic WO_3 (020) core, and 0.235 nm for the Au (111) on top of the intermediate SiO_2 shell (Figure 2b,c). Figure 2d–r shows the scanning transmission electron microscopy (STEM) images of the composite nanoparticles and their corresponding energy-dispersive X-ray spectroscopy (EDX) elemental mapping results. These maps reveal the detailed distribution features of each element at the nanoscale. Figure 2n–r represents the first step of the synthesis and shows that the core contains W and O, while the first shell being Si and O. This is consistent with the expected WO_3 wrapped by SiO_2. Figure 2i–m is the Au seeding step, in which Au in green color is found surrounding the SiO_2 shell with a homogeneous distribution of small Au seeds. Figure 2d–h demonstrates the thick Au shell growth in green color as compared with that shown previously for the attached Au nanoseeds. Finally, the STEM-EDX and HRTEM results both confirm an average diameter of 3.5 ± 1.0 nm for the particulate Au nanoseeds.

The WO_3 core used in this material is polydispersed and add a big uncertainty in the final shape and size, especially for thin layers of SiO_2 and Au. Also, the purity of the source can

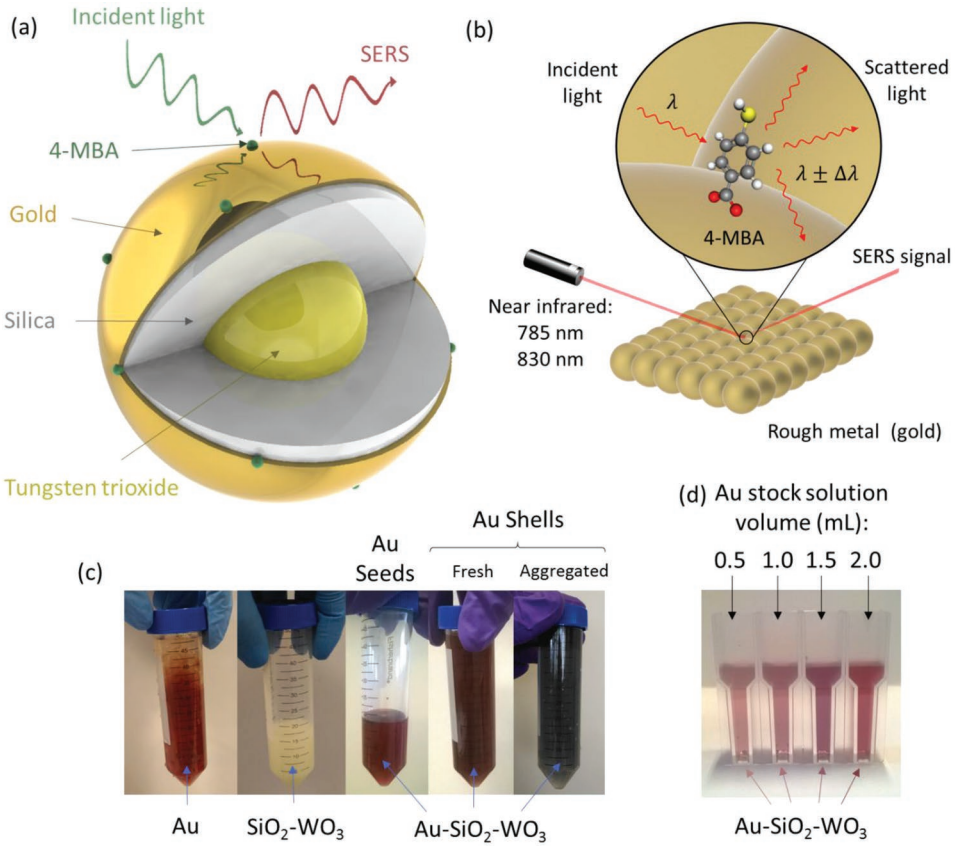

Figure 1. a,b) Schematic of the composite NP design and SERS effect over the gold nanoshell, respectively. c) Colloidal nanoparticles solutions made of Au, SiO_2–WO_3, and Au–SiO_2–WO_3 covered with Au seeds and Au shells within thick layers, respectively. d) Au–SiO_2–WO_3 nanoparticles solutions with various Au thickness obtained by using different Au stock solution during the shell formation.

be refined to avoid crosslinked WO_2 contamination or use WO_2 cores directly during the synthesis, which has smaller energy bandgap for displaying electrochromic behavior. The reduction of the final overall size can help to improve excretion rates of the nanoparticles after imaging.[32–35]

2.2. Control of SiO_2 Shell Thickness

Figure 3 shows the SiO_2 thickness dependency on the ratio of ammonia:TEOS. To achieve thickness control, the volume of ammonia remains constant at 1 mL for all the displayed coatings in Figure 3. This follows the principles of the Stöber process that describes the growth of SiO_2 NPs.[36] When the amount of TEOS increases over the ammonia, the coating is thicker, and vice versa (Figure 3a–f). This has been previously addressed using different cores by several authors.[37–39] The thickness of the SiO_2 can be minimized down to 3 nm. However, the relationship between the thickness and the concentration of TEOS is nonlinear. On the other hand, the current core has been found to exhibit some potential cytotoxicity for certain cells,[40–42] so it needs to be wrapped thick enough to ensure it never directly interacts with healthy cells. TEOS is the main parameter determining the SiO_2 layer thickness.

2.3. Attachment of Au NPs

There are several very important optical and chemical properties of Au NPs that depend strictly on the type of ligand and ligand-metal bond. 3-Aminopropyltrimethoxysilane (APTS) is one of the most common chemicals used to amine-functionalized surfaces for successive Au attachment due to its stable bonding with Au, fast attachment, and low cost.

Figure 4a displays the sample prepared with 4 times fewer APTS concentration than the one used to prepare the sample shown in Figure 4b during the amine functionalization process. Figure 4 shows that an increment of the APTS content leads to a more homogeneous Au seeding over the SiO_2 surface. The concentration of APTS used in this study produced Au NPs of 3.5 nm ± 1.0 nm in diameter.

2.4. Plasmonic Light Absorption

Figure 5a shows the ultraviolet–visible (UV–vis) absorption spectra of various synthesis stages, which reveals the plasmon excitation wavelengths and the maximum absorption peak of Au, and the visible color displayed by the colloidal. The plain Au colloidal appears as red, with maximum absorption

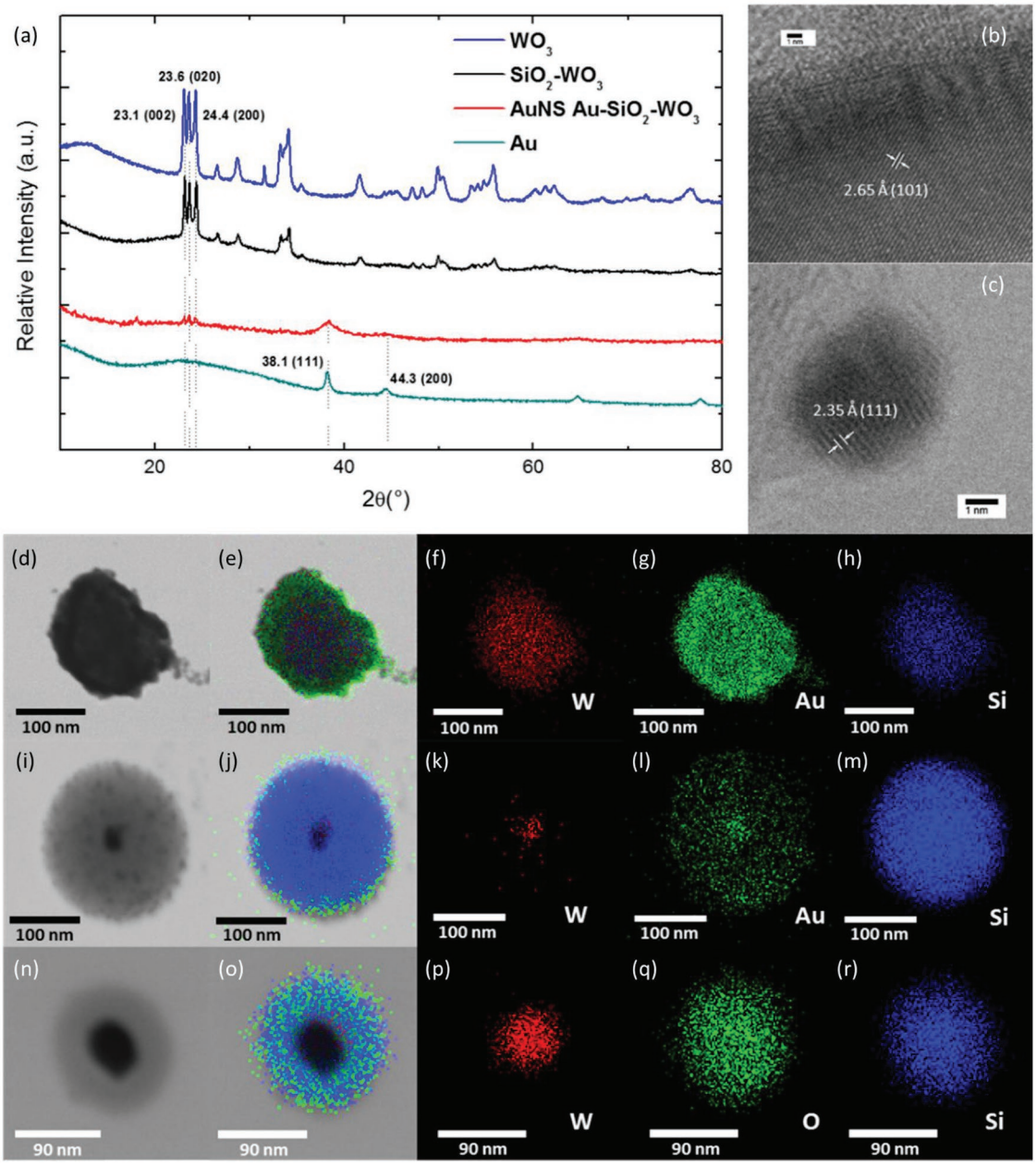

Figure 2. Characterization of the nanocomposites. a) XRD profiles of the WO_3, SiO_2–WO_3, Au–SiO_2–WO_3 and Au. b) HRTEM images of WO_3 and c) Au. d–h) STEM-EDX element mapping of Au nanoshell on Au–SiO_2–WO_3: STEM image, RGB overall, W, Au, and Si, respectively. i–m) STEM-EDX element mapping of Au nanoseeds on Au–SiO_2–WO_3: STEM image, RGB overall, W, Au, and Si, respectively. n–r) STEM-EDX element mapping of SiO_2–WO_3: STEM image, RGB overall, W, O, and Si, respectively.

at 510 nm; whilst the colloidal of nanoshell version of Au–SiO_2–WO_3 appears purple with an absorption peak at 532 nm.[43] Figure 5b, which corresponds to the colloidal nanoparticles displayed in Figure 1d, displays the evolution of the absorption spectra during the nanoshell formation in which X represents the volume of 25×10^{-3} M Au stock solution as explained in the methods section. Also, there is a clear redshift when the aggregation of the Au and Au–SiO_2–WO_3 NPs takes place. The optimal scenario is a maximum peak in the near-infrared regime to have the highest plasmonic oscillations for the SERS application with near-infrared laser illumination. There are no local maximum peaks for the nonmetallic materials, as expected since they do not have plasmon resonances. Also, the contribution of SiO_2 is negligible but starts to be relevant for increased wavelengths.

2.5. SERS Maps with 4-MBA Reporter

Figure 6a–c shows the Raman spectra of 4-MBA molecules bound to the shelled Au–SiO_2–WO_3, seeded Au–SiO_2–WO_3 and

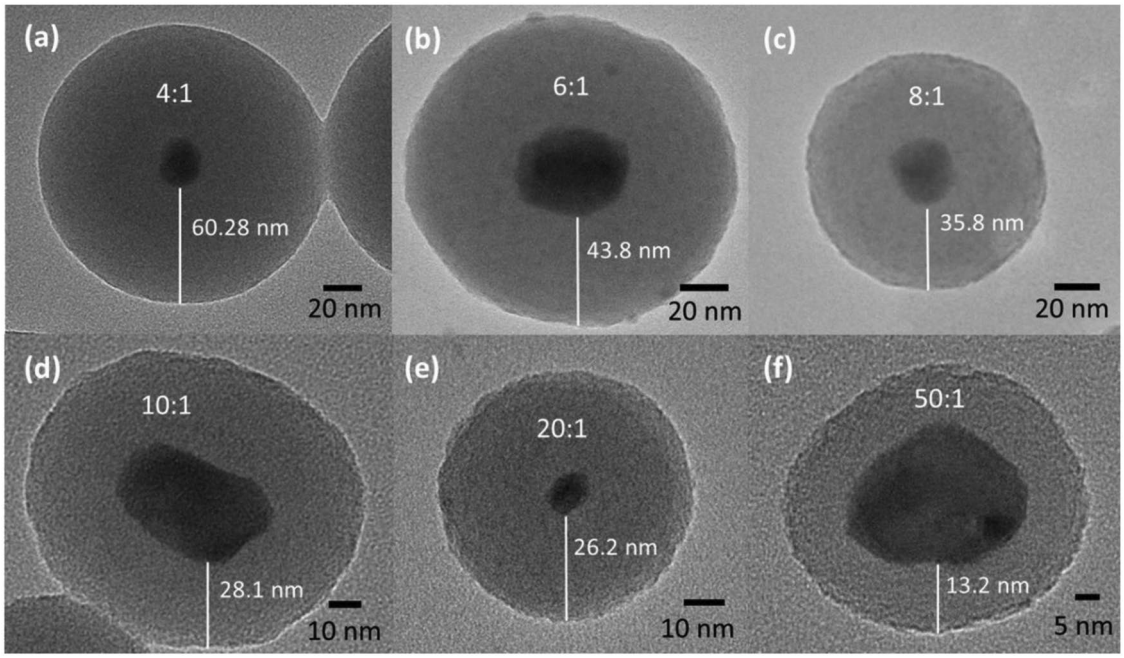

Figure 3. TEM images of SiO_2–WO_3 samples with different ratios of ammonia:TEOS. a) 4:1, b) 6:1, c) 8:1, d) 10:1, e) 20:1, and f) 50:1.

4-MBA alone, respectively. The substrate that holds the samples is a Si wafer and acts as a reference to control the intensity performance of the vibrational resonance peaks from the fixed concentration and volume of 4-MBA molecules, and therefore, the SERS effect quality. It is clear from Figure 6a–c that for Au content there is a boost in these peaks against the 4-MBA molecule alone in Figure 6c.[44] The maximum enhancement of 771 times over the original signal is achieved for the core–shell NPs nanoshelled with Au twice as shown in Figure S2b (Supporting Information). This factor is more than four times achieved value with the 3.5 nm Au nanoseeds on the SiO_2 surface from Figure 6b. This implies that for higher resolution and detection power, the complete nanoshell is essential. All the enhancement factor calculations have been carried out using the same Raman reporter molecule concentrations. A quick comparison with previous results using bare Au nanoparticles for the same overall size shows that these composite nanoparticles achieved lower enhancement factors, mainly due to the bluer maximum absorption peak position.[45,46] Smaller monodispersed cores and thinner silica shells can be the key for a substantial improvement to match the surface plasmon resonance wavelength. Larger enhancements can be easily achieved by increasing the gold nanoshell thickness while keeping nonsmooth surfaces. It can also be improved with the addition of another external Au layer on top of the Raman molecules to create hot spots.

4-MBA is a thiol that contains a benzene ring in the R part, which forms the aromatic ring. This ring provides a strong Raman scattering cross-section with characteristics peaks of 1078 cm^{-1} and 1589 cm^{-1} (see Figure 6). We chose this molecule due to its features of stable sulfur bond with Au, easy attachment, and pH sensitivity in the Raman spectra.[47]

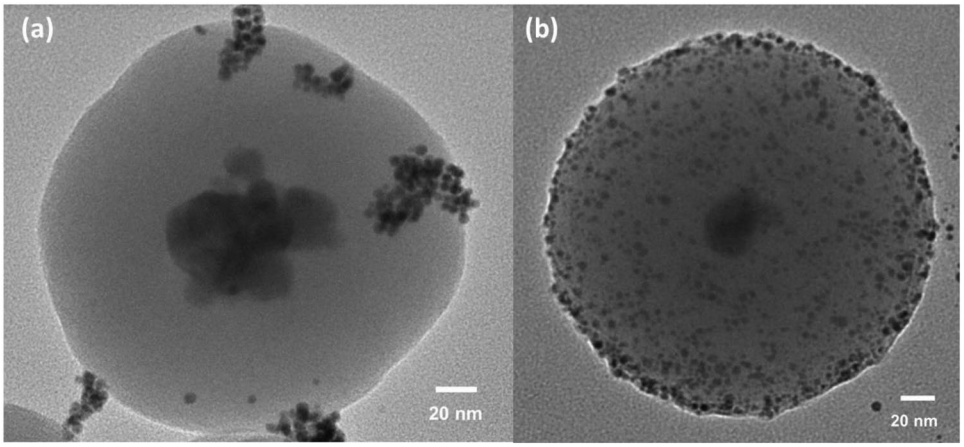

Figure 4. TEM images of Au nanoseeds attachment. Au–SiO_2–WO_3 NPs synthesized with different APTS additions: a) 50 µL. b) 200 µL.

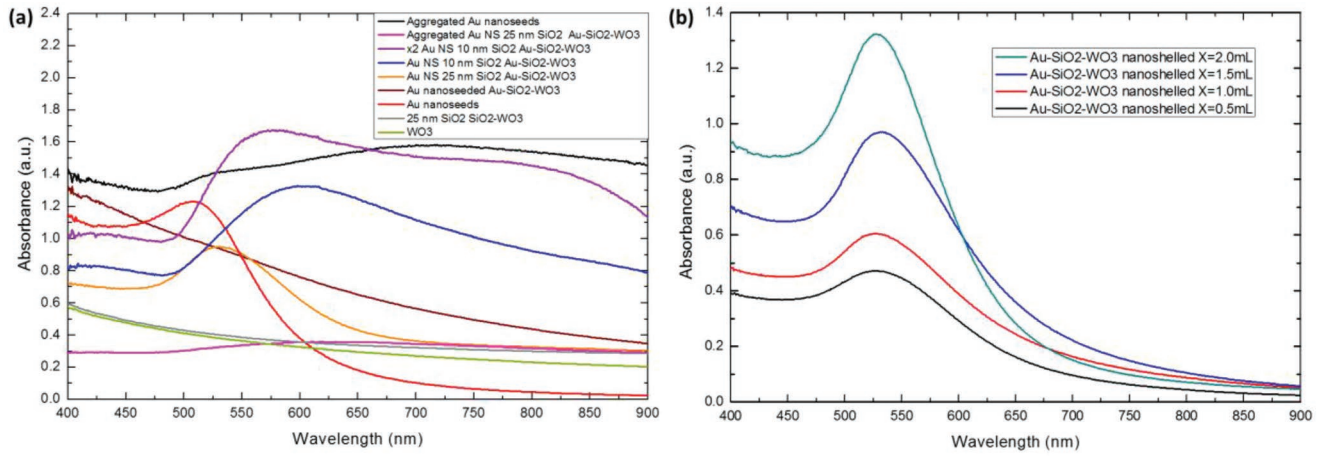

Figure 5. UV–vis absorption spectra of various colloidal nanoparticles: a) WO_3, SiO_2–WO_3, Au seeded Au–SiO_2–WO_3, Au shelled Au–SiO_2–WO_3 (and aggregated batch, after 2 weeks stored in room temperature) and Au alone (and aggregated batch, after 2 weeks stored in room temperature). b) Au–SiO_2–WO_3 shelled with different Au stock solution (X) used during the shell formation.

Depending on the intensity and position of the peaks, different thiolated reporter molecules can be investigated to find the most suitable Raman reporters for potential use when labeling specific cell types such as cancer cells. The nanoparticles synthesized in this paper achieve easily improvable 10 and 10^3 SERS EFs for one Au shell and double Au shell, respectively, in dried samples over Si wafers (see Figure 6a and Figure S2b, Supporting Information). Also, several orders of magnitude were found for the double Au layer for liquid samples (see Figure S2a, Supporting Information), which is very promising for future in vivo applications due to including optical absorption similar to organic human soft tissue. All these values were obtained by diving the SERS signal by the background silicon peak to normalize them and subsequently measuring the ratio of the SERS peak versus the molecule without plasmonic enhancement. Moreover, we have not displayed the Raman enhancement from the Au seeds without attaching to the silica shell because the intensity of the 4-MBA peaks was as strong as the molecules alone for both near-infrared lasers.

Principal component analysis (PCA) is an adaptive data analysis technique that combines conventional imaging and spectroscopy to simultaneously obtain both spatial and spectral information from an object by reducing a large set of possibly correlated variables to a small set of uncorrelated variables, called principal components that still contains most of the relevant information from the large set.[48,49] The origin of the new coordinate system is located in the center

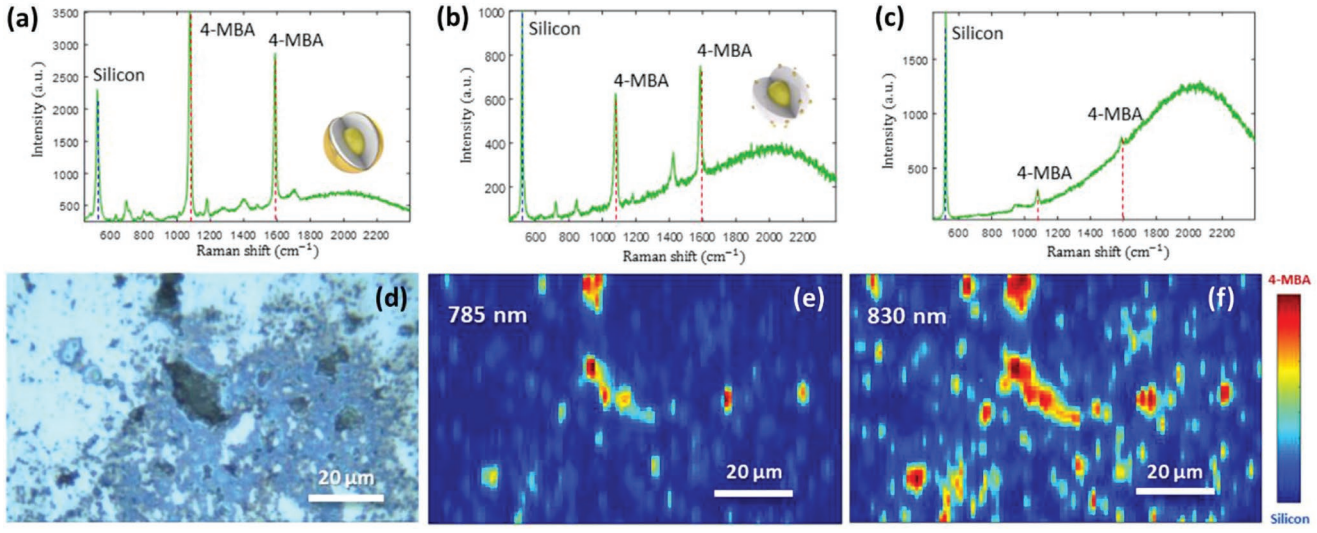

Figure 6. a–c) SERS spectra of 4-MBA molecule peaks at 1078 and 1589 cm^{-1} with 830 nm laser and d–f) Raman maps with 785 and 830 nm of different samples with 4-MBA Raman reporter over a silicon wafer with its characteristic reference peak at 520 cm^{-1}. a) Au shelled Au–SiO_2–WO_3. b) Au seeded Au–SiO_2–WO_3. c) Plain 4-MBA molecules. d–f) Optical microscopy image, Raman maps under PC1 (66.09%) taken with 785 nm and 830 nm lasers, respectively.

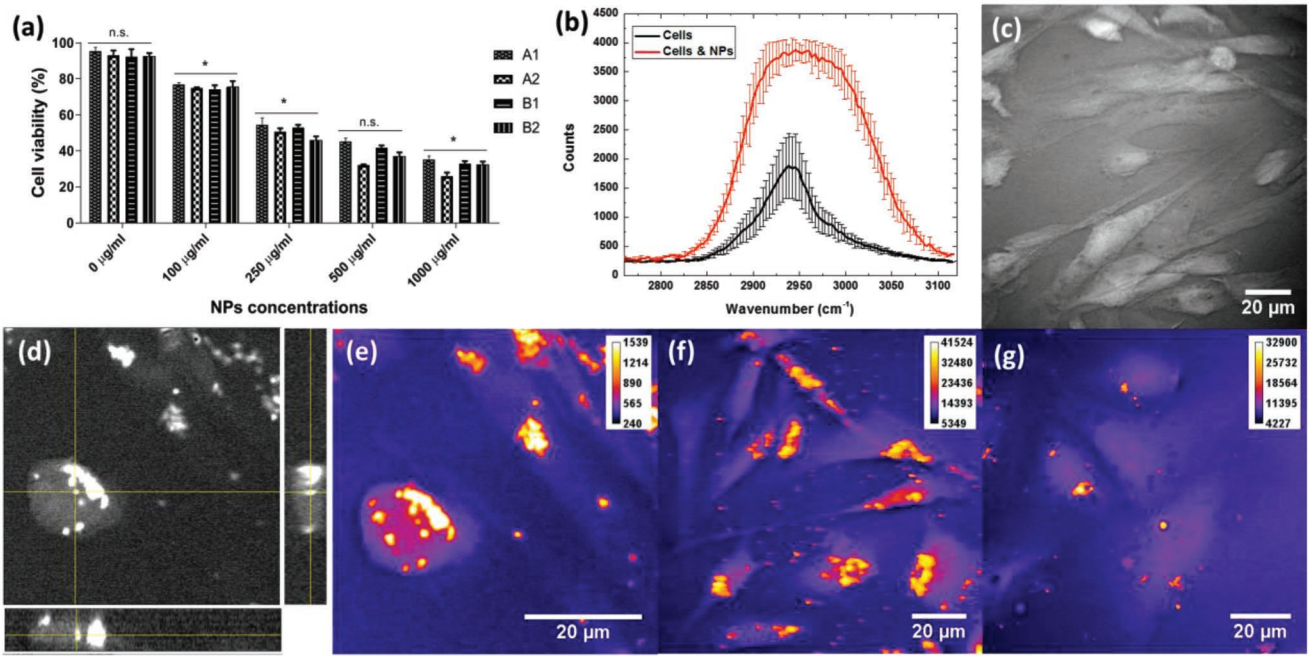

Figure 7. a) Cytotoxicity tests after 24 h of samples A1 (single layer of Au), A2 (single layer of Au coated with 4MBA), B1 (double layer of Au) and B2 (double layer of Au coated with 4MBA). The values represent the mean ± standard deviation of three experiments; * denotes $p < 0.05$ (statistical significance) and ns represents $p \geq 0.05$ (nonstatistical significance). b) Average values and standard deviations errors from CARS spectra from cells alone and cells with nanoparticles. c) Control cells CARS stack—z-projection image in grayscale. d) CARS 3D demonstration of nanoparticles B1 within the cell in grayscale and e) its z-projection of the entire stack (recolored intensity-dependent with fire LUT in ImageJ). f) Nanoparticles A2 in cells CARS imaging (recolored intensity-dependent with fire LUT in ImageJ). g) z-stacking of CARS images from cells and nanoparticles stack A1 (recolored intensity-dependent with fire LUT in ImageJ).

of the data points, the first PCA step includes the points in the direction of the highest variance, the second PCA step includes the ones for the second-highest variance and the rest follow this trend. Using the first PCA, which describes the greatest variance in the dataset (66.09%) in the Raman maps, we can find where the 4-MBA molecules are located: dark red means 4-MBA and dark blue represents the Si wafer (Figure 6e,f). This information is not obvious from the optical image (Figure 6d); however, the Raman maps are able to identify the locations of these reporters. The SERS intensity of the aggregated areas is not only due to the 2D spatial distribution of the materials but also due to having several layers that lead to stronger hot spots[50] and cannot be seen with the optical microscope. After subsequent attachment of the nanoparticles to or uptake into cancer cells, the cancer cells will be precisely located.

Targeting and localization of cancer cells can be achieved by functionalizing the Au nanoshell with cancer ligands such as antibodies, which are customized for each type of cancer. One type of promising ligand is the anti-HER monoclonal antibodies for the treatment of various types of cancers including HER-2^+ metastatic breast, colorectal, NSCLC, pancreatic, breast, HNSCC, ovarian and renal tumors.[51,52] Should these core–shell nanoparticles provide sufficient signals in combination with bright Raman reporters in the near-infrared, the SERS signals could be readout using microscopy in individual cancer cells. Moreover, they also could visualize in vivo tissues with Raman fiber probes or surface-enhanced spatially offset Raman spectroscopy (SESORS).

2.6. Cytotoxicity Profile in a Triple-Negative Human Breast Cancer Cell Line MDA-MB 231

Figure 7a shows the in vitro cytotoxicity profile of the selected concentrations (100, 250, 500, and 1000 µg mL^{-1}) of four different batches (A1, A2, B1, B2) of Au–SiO_2–WO_3 nanoparticles in a triple-negative human breast cancer cell line MDA-MB 231. A1, A2, B1, B2 represent single layer of Au, single layer of Au coated with 4MBA, double layer of Au and double layer of Au coated with 4MBA, respectively. The NPs concentration range was selected from the minimum concentration showing low toxicity to concentration showing maximum toxicity. A live–dead assay for a period of 24 h was performed to confirm the suitability of the nanoparticles for biomedical applications. Statistical analysis was performed with three batches per sample and concentration of which the mean and standard deviation were calculated. The results show no statistical significance (ns, $p \geq 0.05$) for concentrations 500 µg mL^{-1}, while for concentrations of 100, 250, and 1000 µg mL^{-1} the results are statistically significant (*, $p < 0.01$ to 0.05) as shown in Figure 7a. Among the statistically significant results, low cytotoxicity (>75% alive cells) after 24 h was found for concentrations of 100 µg mL^{-1} indicating their suitability for cell imaging purposes.

2.7. Cell Imaging in Human MDA-MB 231 Breast Cancer Cells

The cancer cells were visualized by imaging the CARS signal generated from the CH molecular vibrations within the

cells, this signal was chemically specific with a peak around 2940 cm^{-1}. The nanoparticles within the cells also exhibited a very strong signal within the CARS channel, however, this was from a four-wave mixing process, which was not chemically specific. Figure 7b compares the spectra of the cells to the spectral of the Au–SiO_2–WO_3 NPs within the cells. The average value and standard deviation of three measurements were taken and plotted for both the cells only and the cells with the NPs. The intensity of the signal in cells with NPs is a few times higher than cells alone, which indicates high sensitivity to locate the NPs. Figure 7c–g shows the cell imaging results obtained with CARS. The control label-free human MDA-MB 231 breast cancer cells without nanoparticles are shown in Figure 7c, this image is a z-projection of a CARS image stack and the contrast is from the CH vibrations within the cells. Then, in Figure 7d, CARS 3D cross-sections of NPs with a double layer of Au (white color) within the cells (gray color) in gray confirms that the nanoparticles were uptaken by the cells and can be seen from the inside of the cells. Additionally, the z-projection of the entire stack of CARS images was implemented in Figure 7e by applying the color filter fire look-up-tables (LUT) in ImageJ over the original intensity-dependent greyscale. This recolored image shows the nanoparticles (white) located inside the cells (purple) at different z-positions. Similarly, Figure 7f,d shows the z-projection of the entire stack with fire LUT recoloration for nanoparticles with a single layer of Au coated with 4MBA and without 4MBA, respectively. These results along with the cytotoxicity profiles confirm the viability for these nanoparticles to be used in cancer cell imaging.

3. Conclusion

In summary, we have demonstrated a size tunable synthesis method to obtain novel Au–SiO_2–WO_3 NPs. Higher APTS concentrations result in attachment of larger numbers of seeding Au NPs over the SiO_2 layer. Along with the synthesis, modifications in the intensity of the ultrasonication and speed in the centrifugation can be introduced to refine the washing process and avoid nanoparticles agglomerations. On the one hand, by repeating the Au shell growth step, several gold shells are created and stronger SERS is achieved as displayed in Figure S2a (Supporting Information). This ability to increase the enhancement factor is crucial for translational biomedical applications that involve media that attenuates the near-infrared laser intensity. On the other hand, the main parameter for the SiO_2 thickness growth is the ratio between TEOS and ammonia. Higher ratios of ammonia:TEOS lead to thinner SiO_2 thickness, which reduces the potential toxicity in the human body through a faster excretion. However, it could increase the risk of displaying cytotoxicity related to partially uncoated WO_3 cores. The final Au–SiO_2–WO_3 NPs have been systematically obtained in more than 10 batches by following the synthetic procedure, this reflects the high reproducibility of the synthesis. The optimal thickness of the SiO_2 and Au nanoshells for both strong SERS and low toxicity has yet to be determined. However, preliminary results from various configurations show highly reproducible accurate nanoparticles detection in 2D human breast cancer cell culture and liquid media which leads to believe in vivo cell imaging can be achieved. Moreover, cytotoxicity tests after 24 h show >75% alive cells from statistically significant cell viability at concentrations of 100 μg mL^{-1}. This is a very promising translational result that encourages the use of these nanoparticles in future live human cancer cells imaging and 3D human cell culture models such as spheroids, organoids and organ-on-a-chip technologies to have the full picture of how beneficial these nanoparticles can be in the clinical stage.

4. Experimental Section

Materials: All the following reagents were purchased from Sigma-Aldrich: gold(III) chloride hydrate ($HAuCl_4.xH_2O$, 99.999% trace metals basis M_W 339.79 g mol^{-1}), tetrakis (hydroxymethyl)phosphonium chloride solution (THPC, 80% in H_2O), (3-aminopropyl)triethoxysilane (APTS), potassium carbonate (K_2CO_3, 99.995% trace metals basis M_W 138.21 g mol^{-1}), sodium hydroxide (NaOH, Sigma-Aldrich), potassium carbonate (K_2CO_3), formaldehyde (CH_2O (H—CHO)), 4-mercaptobenzoic acid (MBA), deionized water, ethanol, formaldehyde solution, Dulbecco's modified Eagle's medium (DMEM), trypsin–EDTA solution, and cell proliferation reagent WST-1. The WO_3 nanoparticles were purchased from China, Chang Sha Na Ro Mei Nanomaterials Ltd, with a purity of 99.9% and an average size of 40 nm. Culture cell serum-supplement and penicillin–streptomycin were purchased from Gibco.

Cell Culture: The MDA-MB 231 human breast cancer cells were cultured in DMEM with 10% serum-supplement and 1% penicillin–streptomycin. Cells were grown under standard conditions of 5% CO_2 and 37 °C in a controlled humidified incubator to reach 70–80% confluence. Cells were routinely subcultured using 0.25% trypsin–EDTA solution.

Characterization Instruments and Conditions: The nanoparticles were characterized by using the Thermo Scientific Evolution Array UV–vis spectrophotometer to obtain the light absorption spectra of the colloidal composite nanoparticles suspended in ethanol at mild conditions. For the electron microscopy images and the EDX element maps, the JEOL 2100 TEM/STEM system was used. The XRD patterns were obtained with the Bruker D8 advanced XRD machine working at 0.03° step per second of 2θ from 10° to 80° at room temperature. Raman signals, maps, and optical images for dried samples were obtained from samples dried on top of silicon wafers by using 785 and 830 nm lasers integrated into the Renishaw Invia Raman system and with its internal optical microscope at standard room conditions.

Silica Nanoshell Formation: The first step was the synthesis of the SiO_2–WO_3 core–shell nanocomposites (Figure S1, Supporting Information), NP following the Stober process. A liquid suspension made of 10 mL deionized (DI) water, 20 mL ethanol, and 0.015 g WO_3 NPs was first prepared, then a modified Stöber process promoted the formation of the SiO_2 shell via the sol–gel method. In this method, consecutive hydrolysis and condensation of alkoxysilanes in an aqueous-alcoholic solution in the presence of a base catalyst were involved, using tetraethyl orthosilicate (TEOS) as alkoxysilane and ammonia as the base catalyst.

In this paper, a different route from other Stöber-based versions was taken to perform the silica synthesis while in parallel coating the core. WO_3 NPs were coated with SiO_2 by adding 1 mL ammonia and 5 drops of TEOS while stirring the WO_3 suspension with a time interval of 10 s between each TEOS drop. This was the key to create the SiO_2 coating because by changing the concentration of TEOS the SiO_2 thickness could be modified. After that, the mixture was stirred continuously for 30 more min. The ammonia concentration catalyzed this reaction by increasing the reaction rate. Finally, the suspension was washed with deionized water and Ethanol by centrifugation to separate the nanoparticles from the liquid in 50 mL Eppendorf tubes.

Amine Functionalization: The SiO_2–WO_3 core–shell nanocomposite surfaces were functionalized with an amine group. First, 0.015 g

SiO_2–WO_3 core–shell nanocomposites (Figure S1, Supporting Information) was dispersed in 20 mL of ethanol in a beaker and subjected to 30 min ultrasonic probe treatment. Then, 500 µL of APTS was added to the suspension, which was heated to 70 °C under the magnetic stirring for 5 h. To remove the excess reactants, the suspension of 25 mL ethanol was centrifuged for three times (10 min per cycle at 6 000 rpm) without washing and redispersed by ultrasonic probe treatment.

The key aspect of this functionalization was the NH_2 ending on top.[53] These NH_2 ligands reacted with Au after breaking it in two parts by heating. On the one hand, H_2 was released on one side when the H atoms absorbed higher energy than the bond. On the other hand, a very strong bond was created between the N and the Au atoms that were close enough to be attracted by the electric force of the N^{2-} ions and the Au electron cloud. This fact made it possible to attach Au nanoseeds and to stable subsequent Au growth on top with homogeneous distribution.

Colloidal Au–SiO_2–WO_3 NPs Fabrication: Colloidal Au NPs can be obtained following different methods, which are based on the work of Turkevich et al.[54] Herein they were NP obtained by reducing Au salts ($HAuCl_4$) in the presence of surfactants, tetrakis (hydroxymethyl) phosphonium chloride (THPC, $C_4H_{12}ClO_4P$).[55] During the formation of the metallic solution, a huge excess of NaOH was formed. The reactions between THPC and NaOH produced formaldehyde as the reducing agent for Au. After the amine functionalization, the gold coating process is implemented.

By dissolving 0.098 g of $HAuCl_4{\cdot}3H_2O$ in 10 mL of deionized water,a 25.0×10^{-3} M Au stock solution was prepared, called chloroauric acid. By typical reducing the chloroauric acid with THPC, the colloidal Au NPs (13×10^{-9} M) was prepared. In detail, 3 mL of 1 M NaOH (0.2 g in 5 mL deionized water) and 1 mL of diluted THPC (12 µL of 80% THPC per 1 mL of deionized water, 50×10^{-3} M) were added to 44 mL of deionized water while being stirred. The solution was magnetically stirred for 5 min and 2 mL of the 25×10^{-3} M Au stock solution was rapidly added in and the color quickly changed to dark red or brown. The final Au colloidal was stored at 5 °C for 12 h, prior to being used for later Au coating process.

5 mL of the amine-functionalized SiO_2 core–shell nanocomposites suspension of 70 °C was added to 20 mL of magnetically stirred Au colloidal NP of 100 °C, and then continuously stirred for 10 min. The resulting colloidal suspension NP was washed with deionized water under centrifugation for three times at 6000 rpm for 10 min each time, to remove the excess of reactants.

Au Shell Synthesis: Once the Au nanoseeds were attached to the SiO_2 nanoshell, the Au started to grow to form the final out layer.[56] The alkaline growth solution was prepared by dissolving 0.025 g potassium carbonate (K_2CO_3) in 100 mL deionized water (0.18×10^{-3} M). Then 1.5 mL of 25×10^{-3} M (1% w/v) of the Au stock solution was added to the growth solution, and the mixture was stirred until the yellow colloidal suspension became clear (transparent). 20 mL of this clear solution was injected with 1 mL of the Au–SiO_2–WO_3 NPs suspension, then 100 µL of formaldehyde was added, and a color change from colorless to purple was observed which is characteristic of the Au nanoshell formation. The resultant suspension was then centrifuged and redispersed in water, for later UV–vis spectrophotometry and Raman spectroscopy characterization.

Adding Reporter Molecule for SERS: The Au nanoshell bioconjugation was achieved by mixing 4-mercaptobenzoic acid (4-MBA) diluted in ethanol with the Au–SiO_2–WO_3 nanocomposites.[57] After these synthesis steps, thiolated Au–SiO_2–WO_3 core–shell nanocomposites were obtained. Figure S1 (Supporting Information) describes the entire synthesis steps. 1×10^{-3} M of 4-MBA solution was prepared by diluting an appropriate mass of the solid in ethanol (or aqueous). For the collection of SERS spectra, 100 µL of 1×10^{-3} M solution of 4-MBA was mixed with 1 mL of colloidal Au NPs. After 5 min stirring, the mixture was centrifuged three times for 7 min at 4000 rpm in 1.5 mL Eppendorf tubes, and the supernatant was redissolved in deionized water.

Cell Viability: Cell viability experiments were performed in 96-well plates and imaging experiments were performed in six-well plate. Cells were seeded in a 96-well plate at the density of 1×10^4 cells per well while cells were seeded onto the six-well plates at a density of 1×10^6 cells per well and incubated for 24 h prior to the experiments. After overnight incubation, cells were treated with and without 100, 250, 500, and 1000 µg mL^{-1} of four types of NPs for 24 h. Cell viability after nanoparticle treatment was determined using WST-1 assay (Roche Applied Biosystems) according to the manufacturer's instructions with modifications to adapt for nanoparticle-treated cells. Briefly, cells were seeded in a 96-well plate with a density of 1×10^4 cells per well, differentiated and incubated with nanoparticles (three replicates per concentration). After 24 h, WST-1 reagent was added to the cells, and after the color reaction, the plate was then kept for shaking and then absorbance was measured at a wavelength of 450 nm using a plate reader (Clariostar plate reader, BMG labtech). The results were expressed as percentage cell viability. Three independent experiments were performed for each study and all measurements were performed in triplicate.

Statistical Analysis: The data were statistically analyzed using GraphPad Prism 5.04 to assess the effects of NPs treatment on cell viability and were expressed as % cell count ± SD, Mann Whitney. *($p < 0.05$) was considered statistically significant. Results were presented as the mean ± standard deviation (SD).

Cell Imaging Using Coherent Antistokes Raman Spectroscopy: Coherent anti-Stokes Raman scattering (CARS) imaging was carried by using dual-wavelength output from an InSight X3 ultrafast fs laser (Newport SpectraPhysics) with 800 nm for the pump and probe beam and 1045 nm as the Stokes beam. The beams where chirped to produced ps pulses and spatially overlaid in the Spectral Focusing Timing and Recombination Unit (SF-TRU, Newport SpectraPhysics). The temporal overlap between the pump and Stokes beams was scanned via the SF-TRU unit to allowing us to rapidly change which Raman vibration was probed, and acquire spectral data.[58] 3D submicron resolution imaging was performed on a modified confocal microscope (Olympus FV3000), with a 60× water-immersion objective (1.2NA, UPlanSApo, Olympus). The anti-Stokes light at 648 nm from CARS was collected in the forward direction using a water immersion objective (Olympus LUMPlanFLN 60X). The anti-Stokes light was separated from the laser fundamentals by using a long pass dichroic beamsplitter (Chroma DC/T760lpxr) followed by two filters (Chroma ET650/45x) and detected using a PMT (Hamamatsu R3896). The samples were mounted between two coverslips. To avoid photodamage to the samples, the laser intensities were attenuated to give 9 and 18 mW for the pump and Stokes beams in the sample plane, respectively.

Supporting Information

Supporting Information is available from the Wiley Online Library or from the author.

Acknowledgements

P.M.P., K.T., and Y.Z. designed the nanocomposites. P.M.P. and H.C. characterized the nanocomposites. P.M.P., L.C., and N.S. designed the 4-MBA functionalization. P.M.P. and L.C. measured the Raman maps on silicon wafers and the SERS effect. B.G. and P.M.P. obtained the nanoparticles SERS Raman spectra in liquid samples. T.A.T. and P.M.P. designed and performed the cytotoxicity studies. J.M., P.M.P., and T.A.T. designed and carried out the cell imaging. P.M.P. drafted the manuscript, and all co-authors contributed to modification. P.M.P., Y.Z., and N.S. led the project. Thank Ellen Green and Pascaline Bouzy for technical supports in Raman measurements. The authors acknowledge Professor Julian Moger for providing access to the CONTRAST facility for the CARS imaging (this facility was funded by the Engineering and Physical Sciences Research Council (EPSRC) grant number (EP/5009957/1). P.M.P. acknowledge financial support from the EPSRC of the United Kingdom, via the EPSRC Centre for Doctoral Training in Metamaterials (Grant No. EP/L015331/1). All data created during this research are openly available from the University of Exeter's institutional repository.

Conflict of Interest

The authors declare no conflict of interest.

Keywords

cancer imaging, core–shell, gold, SERS, tungsten oxide

Received: May 3, 2019
Revised: August 14, 2019
Published online: September 9, 2019

[1] M. D. Farwell, D. A. Pryma, D. A. Mankoff, *Cancer* **2014**, *120*, 3433.
[2] D. I. Ellis, D. P. Cowcher, L. Ashton, S. O'Hagan, R. Goodacre, *Analyst* **2013**, *138*, 3871.
[3] J. P. B. O'Connor, E. O. Aboagye, J. E. Adams, H. J. W. L. Aerts, S. F. Barrington, A. J. Beer, R. Boellaard, S. E. Bohndiek, M. Brady, G. Brown, D. L. Buckley, T. L. Chenevert, L. P. Clarke, S. Collette, G. J. Cook, N. M. deSouza, J. C. Dickson, C. Dive, J. L. Evelhoch, C. Faivre-Finn, F. A. Gallagher, F. J. Gilbert, R. J. Gillies, V. Goh, J. R. Griffiths, A. M. Groves, S. Halligan, A. L. Harris, D. J. Hawkes, O. S. Hoekstra, E. P. Huang, B. F. Hutton, E. F. Jackson, G. C. Jayson, A. Jones, D.-M. Koh, D. Lacombe, P. Lambin, N. Lassau, M. O. Leach, T.-Y. Lee, E. L. Leen, J. S. Lewis, Y. Liu, M. F. Lythgoe, P. Manoharan, R. J. Maxwell, K. A. Miles, B. Morgan, S. Morris, T. Ng, A. R. Padhani, G. J. M. Parker, M. Partridge, A. P. Pathak, A. C. Peet, S. Punwani, A. R. Reynolds, S. P. Robinson, L. K. Shankar, R. A. Sharma, D. Soloviev, S. Stroobants, D. C. Sullivan, S. A. Taylor, P. S. Tofts, G. M. Tozer, M. van Herk, S. Walker-Samuel, J. Wason, K. J. Williams, P. Workman, T. E. Yankeelov, K. M. Brindle, L. M. McShane, A. Jackson, J. C. Waterton, *Nat. Rev. Clin. Oncol.* **2016**, *14*, 169.
[4] A. C. Anselmo, S. Mitragotri, *Bioeng. Transl. Med.* **2016**, *1*, 10.
[5] K. Ma, H. Sai, U. Wiesner, *J. Am. Chem. Soc.* **2012**, *134*, 13180.
[6] F.-Y. Cheng, C.-T. Chen, C.-S. Yeh, *Nanotechnology* **2009**, *20*, 425104.
[7] K. Kan-Dapaah, N. Rahbar, W. Soboyejo, *Med. Phys.* **2015**, *42*, 2203.
[8] J. F. Hainfeld, D. N. Slatkin, T. M. Focella, H. M. Smilowitz, *Br. J. Radiol.* **2006**, *79*, 248.
[9] Z. R. Stephen, F. M. Kievit, M. Zhang, *Mater. Today* **2011**, *14*, 330.
[10] J. Zhao, J. Chen, S. Ma, Q. Liu, L. Huang, X. Chen, K. Lou, W. Wang, *Acta Pharm. Sin. B* **2018**, *8*, 320.
[11] M. Rogosnitzky, S. Branch, *BioMetals* **2016**, *29*, 365.
[12] N. Singh, G. J. S. Jenkins, R. Asadi, S. H. Doak, *Nano Rev.* **2010**, *1*, 5358.
[13] V. Tuchin, *Tissue Optics: Light Scattering Methods and Instruments for Medical Diagnosis*, Vol. *PM166*, 2nd ed., SPIE Press Book, Bellingham, WA **2007**, p. 882.
[14] L. Fabris, *J. Opt.* **2015**, *17*, 114002.
[15] D. Gontero, A. V Veglia, A. G. Bracamonte, D. Boudreau, *RSC Adv.* **2017**, *7*, 10252.
[16] J. H. Kim, P. P. Pompa, H. G. Baek, B. H. Chung, *Nanotechnology* **2016**, *27*, 175704.
[17] S. J. Oldenburg, R. D. Averitt, S. L. Westcott, N. J. Halas, *Chem. Phys. Lett.* **1998**, *288*, 243.
[18] M. Hu, J. Chen, Z.-Y. Li, L. Au, G. V Hartland, X. Li, M. Marquez, Y. Xia, *Chem. Soc. Rev.* **2006**, *35*, 1084.
[19] Z. Qiao, G. Jianping, G. James, H. Yongxing, S. Yugang, Y. Yadong, *Adv. Mater.* **2010**, *22*, 1905.
[20] R. Ashayer, S. H. Mannan, S. Sajjadi, *Colloids Surf., A* **2008**, *329*, 134.
[21] K. Sokolov, M. Follen, J. Aaron, I. Pavlova, A. Malpica, R. Lotan, R. Richards-Kortum, *Cancer Res.* **2003**, *63*, 1999.
[22] D. Barchiesi, *J. Opt. Soc. Am. A* **2015**, *32*, 1544.
[23] P. J. Vikesland, R. L. Rebodos, J. Y. Bottero, J. Rose, A. Masion, *Environ. Sci. Nano* **2016**, *3*, 567.
[24] E. C. Abenojar, S. Wickramasinghe, J. Bas-Concepcion, A. C. S. Samia, *Prog. Nat. Sci.: Mater. Int.* **2016**, *26*, 440.
[25] S. F. Chen, A. Aldalbahi, P. X. Feng, *Sensors* **2015**, *15*, 27035.
[26] H. Zheng, J. Z. Ou, M. S. Strano, R. B. Kaner, A. Mitchell, K. Kalantar-zadeh, *Adv. Funct. Mater.* **2011**, *21*, 2175.
[27] R. Chatten, A. V Chadwick, A. Rougier, P. J. D. Lindan, *J. Phys. Chem. B* **2005**, *109*, 3146.
[28] G. Baldissera, C. Persson, *Eur. Phys. J. B* **2013**, *86*, 273.
[29] G. Duan, L. Chen, Z. Jing, P. De Luna, L. Wen, L. Zhang, L. Zhao, J. Xu, Z. Li, Z. Yang, R. Zhou, *Chem. Res. Toxicol.* **2019**, *32*, 1357.
[30] L. Wen, L. Chen, S. Zheng, J. Zeng, G. Duan, Y. Wang, G. Wang, Z. Chai, Z. Li, M. Gao, *Adv. Mater.* **2016**, *28*, 5072.
[31] H. Yang, C. Liu, D. Yang, H. Zhang, Z. Xi, *J. Appl. Toxicol.* **2009**, *29*, 69.
[32] J. Lu, S. Yang, K. M. Ng, C.-H. Su, C.-S. Yeh, Y.-N. Wu, D.-B. Shieh, *Nanotechnology* **2006**, *17*, 5812.
[33] R. Hardman, *Environ. Health Perspect.* **2006**, *114*, 165.
[34] M. Arruebo, R. Fernández-Pacheco, M. R. Ibarra, J. Santamaría, *Nano Today* **2007**, *2*, 22.
[35] M. Longmire, P. L. Choyke, H. Kobayashi, *Nanomedicine* **2008**, *3*, 703.
[36] W. Stöber, A. Fink, E. Bohn, *J. Colloid Interface Sci.* **1968**, *26*, 62.
[37] M. Ohmori, E. Matijević, *J. Colloid Interface Sci.* **1992**, *150*, 594.
[38] A. Guerrero-Martínez, J. Pérez-Juste, L. M. Liz-Marzán, *Adv. Mater.* **2010**, *22*, 1182.
[39] A. Vanderkooy, Y. Chen, F. Gonzaga, M. A. Brook, *ACS Appl. Mater. Interfaces* **2011**, *3*, 3942.
[40] A. M. Yassin, M. Elnouby, N. M. El-Deeb, E. E. Hafez, *Appl. Biochem. Biotechnol.* **2016**, *180*, 623.
[41] Z. Zhou, B. Kong, C. Yu, X. Shi, M. Wang, W. Liu, Y. Sun, Y. Zhang, H. Yang, S. Yang, *Sci. Rep.* **2014**, *4*, 3653.
[42] A. L. Popov, N. M. Zholobak, O. I. Balko, O. B. Balko, A. B. Shcherbakov, N. R. Popova, O. S. Ivanova, A. E. Baranchikov, V. K. Ivanov, *J. Photochem. Photobiol., B* **2018**, *178*, 395.
[43] B. G. Prevo, S. A. Esakoff, A. Mikhailovsky, J. A. Zasadzinski, *Small* **2008**, *4*, 1183.
[44] M. M. Y. Chen, A. Katz, *Langmuir* **2002**, *18*, 8566.
[45] J. D. Driskell, R. J. Lipert, M. D. Porter, *J. Phys. Chem. B* **2006**, *110*, 17444.
[46] H. J. Butler, S. W. Fogarty, J. G. Kerns, P. L. Martin-Hirsch, N. J. Fullwood, F. L. Martin, *Analyst* **2015**, *140*, 3090.
[47] S. Jung, J. Nam, S. Hwang, J. Park, J. Hur, K. Im, N. Park, S. Kim, *Anal. Chem.* **2013**, *85*, 7674.
[48] I. T. Jolliffe, J. Cadima, *Phil. Trans. R. Soc. A* **2016**, *374*, 20150202.
[49] A. A. Gowen, C. P. O'Donnell, M. Taghizadeh, P. J. Cullen, J. M. Frias, G. Downey, *J. Chemom.* **2008**, *22*, 259.
[50] T. Chen, H. Wang, G. Chen, Y. Wang, Y. Feng, W. S. Teo, T. Wu, H. Chen, *ACS Nano* **2010**, *4*, 3087.
[51] F. J. Esteva, *Oncologist* **2004**, *9*, 4.
[52] T. Carter, P. Mulholland, K. Chester, *Immunotherapy* **2016**, *8*, 941.
[53] A. Cossaro, M. Dell'Angela, A. Verdini, M. Puppin, G. Kladnik, M. Coreno, M. de Simone, A. Kivimäki, D. Cvetko, M. Canepa, L. Floreano, *J. Phys. Chem. C* **2010**, *114*, 15011.
[54] J. Turkevich, P. C. Stevenson, J. Hillier, *Discuss. Faraday Soc.* **1951**, *11*, 55.
[55] J. L. Hueso, V. Sebastian, A. Mayoral, L. Uson, M. Arruebo, J. Santamaria, *RSC Adv.* **2013**, *3*, 10427.
[56] M. L. Brongersma, *Nat. Mater.* **2003**, *2*, 296.
[57] A. B. Serrano-Montes, J. Langer, M. Henriksen-Lacey, D. de Aberasturi, D. M. Solís, J. M. Taboada, F. Obelleiro, K. Sentosun, S. Bals, A. Bekdemir, F. Stellacci, L. M. Liz-Marzán, *J. Phys. Chem. C* **2016**, *120*, 20860.
[58] A. Zeytunyan, T. Baldacchini, R. Zadoyan, *Proc. SPIE* **2018**, *10498*, 104980K-1.